# Mechanical and fatigue properties of bellows determined with Integrated DIC and IR Thermography

Morgan Bertin

université PARIS-SACLAY

école normale supérieure paris—saclay

NNT : 2016SACLN031

# THESE DE DOCTORAT
# DE
# L'UNIVERSITE PARIS-SACLAY
# PREPAREE A
# L'ECOLE NORMALE SUPERIEURE DE CACHAN

ECOLE DOCTORALE N° 579
Sciences Mécaniques et Energétiques, Matériaux et Géosciences

Spécialité Mécanique des Solides

Par

**Morgan Bertin**

# Mechanical and Fatigue Properties of Bellows Determined With Integrated DIC and IR Thermography

**Thèse présentée et soutenue à l'Ecole Normale Supérieure de Cachan le 12/09/2016:**

**Composition du Jury :**

| | | | |
|---|---|---|---|
| Bouvier, Salima | Professeur des Universités, Université de tech. de Compiègne | France | Présidente du jury |
| Habraken, Anne-Marie | Directrice de Recherche, Université de Liège | Belgique | Rapporteur |
| Périé, Jean-Noël | Maître de conférence, Institut Univ. de tech. de Toulouse | France | Rapporteur |
| Willner, Kai | Professor, Friedrich-Alexander Universität | Allemagne | Rapporteur |
| Aubin, Véronique | Professeur des Universités, Ecole Centrale Paris | France | Examinateur |
| Hild, François | Directeur de Recherche, LMT Cachan | France | Directeur de thèse |
| Hoefnagels, Johan | Assistant Professor, Technische Universiteit Eindhoven | Pays-Bas | Co-directeur de thèse |

université PARIS-SACLAY
ÉCOLE DOCTORALE
Sciences mécaniques et énergétiques, matériaux et géosciences (SMEMAG)

**Titre :** Identification du comportement mécanique et des propriétés en fatigue d'un soufflet à l'aide de l'identification intégrée à la corrélation d'images et de la thermographie infra-rouge.

**Mots clés :** Acier inoxydable, Expérience multiaxiale, Photomécanique, Elasto-plasticité

**Résumé:** Afin de participer à l'émergence de technologies innovantes et contribuer aux objectifs de développement durable, un consortium composé de 13 partenaires (3 laboratoires académiques et 10 entreprises industrielles) a été formé. Le projet Thermofluide-RT consiste à développer un système de refroidissement à boucle de fluide diphasique à pompage mécanique. Le LMT-Cachan contribue à la conception de l'élément essentiel de la pompe, à savoir, le soufflet. Celui-ci est obtenu en soudant des feuilles d'acier inoxydable à durcissement structural très mince (70 µm) et doit fonctionner sans défaillance pendant 20 ans. Un dimensionnement fiabiliste du soufflet basé sur la théorie du maillon le plus faible est réalisé.
Une méthode d'optimisation basée sur la technique d'identification intégrée à la corrélation d'images numériques aboutit à une géométrie d'éprouvette qui minimise l'incertitude des paramètres recherchés.
La géométrie optimisée est testée sur Mini-Astrée, la nouvelle machine biaxiale du LMT. Plusieurs lois de comportements sont identifiées et testées sur le matériau étudié. Toutes les données brutes sont combinées à leur juste valeur grâce à une formulation bayésienne basée sur l'hypothèse de bruits blanc gaussiens.
De très fines feuilles du même acier sont également testées à l'aide d'essais uniaxiaux et multiaxiaux. Une loi de plasticité anisotrope est identifiée.
Une analyse microscopique est conduite au travers d'un micro-essai de traction sur 2 grains et l'identification de paramètres d'une loi de plasticité cristalline est menée.
Enfin, le dimensionnement probabiliste du soufflet est validé à partir de plusieurs mesures expérimentales infra-rouges sur un nouveau banc d'essai. Un modèle probabiliste à deux échelles permet la caractérisation des phénomènes observés sur le matériau d'étude et le composant lui-même.

**Title:** Mechanical and fatigue properties of bellows determined with Integrated DIC and IR Thermography

**Keywords**: Stainless steel, Multi-axial experiment, Photomechanics, Elasto-plasticity

**Abstract:** In the context of leveraging and accelerating innovative technological solutions that contribute to meeting sustainable goals, a consortium composed of 13 partners (3 academic laboratories and 10 industrial companies) has been formed. The Thermofluide-RT project consists in developing a two-phase fluid loop driven by a mechanical pump. LMT-Cachan contributes to the design of the critical component of the pump, *i.e.,* bellows. This component, which is obtained by welding very thin (70 µm) pre-deformed sheets made of precipitation-hardened stainless steel, is expected to operate without failure for 20 years.
First, a probabilistic design methodology, which is based on the weakest link theory, allows for the fatigue design of the component.
Second, an optimization methodology based on full-field measurements and Integrated Digital Image Correlation (IDIC) allows the sample geometry to be designed with the least uncertainty of the sought parameters.
Third, the optimized cruciform geometry has been tested in a new compact biaxial machine, mini-Astrée, that allows for a fast, yet robust identification. Several elasto-plastic models with increasing complexity are investigated to probe the material behavior. All data account for the latter thanks to a Bayesian foundation that equitably weights all measurements. Ultra-thin sheets are also tested in uniaxial and biaxial experiments thanks to an anti-wrinkling setup. An anisotropic plasticity model is calibrated.
Fourth, a microscopic analysis is performed via quasi-3D IDIC and a uniaxial micro-specimen allow a crystal plasticity law to be characterized.
Last, the probabilistic fatigue design of the bellows based upon a two-scale probabilistic model is validated with infrared measurements in the high cycle fatigue regime.

# Remerciements

Je n'aurais jamais imaginé, il y a de cela trois années, que ma vie aurait tant changé. Je n'ai que peu de souvenirs de mes premiers instants comme jeune doctorant, mis à part le sentiment d'un travail conséquent mais nécessaire. J'ai néanmoins profité de ces années au delà de ce que j'avais imaginé.

Professionnellement, j'ai appris au contact de personnalités enthousiastes, cordiales et passionnées. Á tout seigneur tout honneur, je remercie Franois H. et Stéphane R. qui m'ont guidé avec justesse et liberté. L'association de ces deux personnalités fut une expérience enrichissante dont je garderai longtemps la trace. Je remercie Johan H., Marc G. et Chaowei. D. pour l'experience scientifique offerte à Eindhoven. Je remercie aussi Xavier P. pour son aide lors des campagnes expérimentales. Je remercie enfin largement toutes celles et tous ceux que j'ai eu le plaisir de côtoyer au LMT.

Personnellement, je me suis aventuré et développé sur tous les fronts. Je pense à l'Aero Touring Club de France où j'ai été chaleureusement accueilli et à tous les hussards que j'ai côtoyé ces 4 dernières années. Je pense aux clubs d'athlétisme que j'ai fréquenté en France et aux Pays-Bas. Enfin, je remercie toutes les parties de ma famille qui ont su m'accompagner et me soutenir.

Finalement, je remercie mon épouse, Larissa, pour laquelle je suis tombé follement amoureux un soir de décembre. Larissa, tu m'as apporté l'amour, une nouvelle famille, la patience, le portugais et tant d'autres choses. Je te remercie de tout mon coeur, pour tout cela et pour tout ce qui suivra.

**Cher ami, je nous souhaite d'avoir bon vent !**

# Contents

**1 Introduction . . . . . 1**
1.1 Motivation . . . . . 1
1.2 Goal . . . . . 2
1.3 Strategy . . . . . 3
1.4 Scope of the thesis . . . . . 5
**2 Probabilistic Fatigue Design of Bellows . . . . . 7**
2.1 Introduction . . . . . 7
2.2 Component . . . . . 8
2.3 Numerical model . . . . . 10
2.4 Probabilistic design . . . . . 12

A Material Parameter Identification . . . . . 19

**3 Optimization of a cruciform geometry . . . . . 21**
3.1 Introduction . . . . . 21
3.2 Optimization strategy . . . . . 23
3.3 Elastic law with different parameterizations . . . . . 33
3.4 Geometry optimization . . . . . 36
3.5 Conclusion . . . . . 47
**4 Elasto-plastic identification with IDIC in a biaxial experiment . . . . . 49**
4.1 Introduction . . . . . 49
4.2 Experimental protocol . . . . . 51
4.3 Identification strategy . . . . . 53
4.4 Identification results . . . . . 59
4.5 Conclusion . . . . . 69
**5 Anisotropic plasticity identification with IDIC . . . . . 71**
5.1 Introduction . . . . . 71
5.2 Theoretical and methodological framework . . . . . 73
5.3 Parameter identification with uniaxial test . . . . . 75
5.4 Analysis of a biaxial experiment . . . . . 82
5.5 Conclusion . . . . . 91

**6 Crystal plasticity parameter identification with quasi-3D IDIC . . . . . 93**
6.1 Introduction . . . . . 93
6.2 Coupled experimental/numerical procedure . . . . . 96
6.3 Experimental results . . . . . 105
6.4 Boundary conditions and material parameter identification . . . . . 109
6.5 Conclusion . . . . . 112

B Validation of Probabilistic Fatigue Design . . . . . 115

**7 Self-heating experiments and bellows design optimization . . . . . 117**
7.1 Introduction . . . . . 117
7.2 Thermomechanical background . . . . . 118
7.3 Uniaxial ultra-thin specimens . . . . . 122
7.4 Fatigue analysis of bellows . . . . . 128
7.5 Conclusion . . . . . 138
**8 General conclusions and recommendations . . . . . 141**
8.1 Conclusions . . . . . 141
8.2 Recommendations . . . . . 143
**A Operation manual of mini-Astrée and its environnement . . . . . 163**
A.1 Installation instructions . . . . . 163
A.2 Digital camera instructions . . . . . 171
A.3 Load cell calibration procedure . . . . . 172
A.4 Experimental instructions . . . . . 173
A.5 Digital Image Correlation . . . . . 177
**B Draft of a fatigue testing machine for bellows . . . . . 179**

He could feel his heart beating against the pine needle floor of the forest.

Ernest Hemingway, *For Whom the Bell Tolls*, (1940)

# Main notations

| | |
|---|---|
| $\gamma_f$ | standard deviation of gray levels |
| $\gamma_F$ | standard resolution of the load measurement |
| $\chi_f$ | digital image correlation residual |
| $\chi_U$ | finite element method updating objective function based on displacement fields (FEMU-U) |
| $\chi_F$ | finite element method updating objective function based on force measurements (FEMU-F) |
| $\chi_{UF}$ | finite element method updating objective function based on displacement fields and force measurement (FEMU-UF) |
| $\chi_{\boldsymbol{I}}$ | Integrated Digital Image Correlation objective function (IDIC) |
| $\chi_{\boldsymbol{R}}$ | Regularization objective function |
| $\Omega$ | region of interest |
| $\boldsymbol{u}(\boldsymbol{x})$ | displacement field vector |
| $[\boldsymbol{M}]$ | global correlation matrix |
| $[\boldsymbol{S}_U]$ | displacement sensitivity matrix |
| $[\boldsymbol{S}_F]$ | force sensitivity matrix |
| $[\boldsymbol{C_U}]$ | covariance matrix of measured nodal displacements |
| $[\boldsymbol{C_F}]$ | covariance matrix of measured load |
| $[\boldsymbol{C}_p^{\bullet}]$ | covariance matrix of identified material parameters using a method labeled by $\bullet$ |
| $[\boldsymbol{H}_U]$ | kinematic Hessian |
| $[\boldsymbol{H}_F]$ | static Hessian |
| $[\boldsymbol{H}_{UF}]$ | combined Hessian |
| $[\boldsymbol{M}_{IDIC}]$ | Hessian matrix of the displacement IDIC approach |
| $[\boldsymbol{H_F}]$ | Hessian matrix of the *FEMU-F* approach |
| $[\boldsymbol{H}_{IFDIC}]$ | Hessian matrix of the global IDIC approach |
| $f(x), g(x)$ | pictures in the reference and deformed configurations, respectively |
| $\boldsymbol{e}_\alpha$ | unit vector along direction $\alpha = 1, 2$ |
| $\boldsymbol{x}$ | 2D or 3D coordinates in normal space |
| $\boldsymbol{\psi}(\boldsymbol{x})$ | vectorial shape functions |
| $\boldsymbol{\xi}$ | 2D or 3D coordinates in reference space |
| $\{\boldsymbol{p}\}$ | vector gathering constitutive parameters |
| $\boldsymbol{u}_c$ | computed displacement field |
| $\boldsymbol{u}_m$ | measured displacement field |
| $\delta_{ij}$ | Kronecker operator |
| $\langle\bullet\rangle$ | mean value of $\bullet$ |
| $G_f = \langle\nabla^2 f\rangle^{1/2}$ | root mean square gray level gradient |

# Chapter 1
# Introduction

## 1.1 Motivation

For about half a century, the world has experienced an extraordinary period of growth and prosperity. However, these changes have led to hazardous consequences and the need to address them in the short term has become urgent and vital. First initiated in 1992 at Rio de Janeiro [1] and pursued in 2015 in Paris [2], governments have set goals and rules for the forthcoming decades and beyond that account for all society aspects. The sole and unique objective is to spur and sustain our *well-being* [3]. To that end, countries have initiated strategies that are both environmentally sustainable and socially inclusive. They embody numerous aspects as civil society, economic stability, education, transportation and their implementations are garnering greater public attention and debate. Only regarding the technological and scientific contributions, countries have decided to actively manage them as steered by Article 10 of the Paris Agreement [2]: “accelerating, encouraging and enabling innovation is critical for an effective, long-term global response to climate change and promoting economic growth and sustainable development. Such effort shall be, as appropriate, supported [...] for *collaborative approaches to research and development*, and facilitating access to technology, *in particular for early stages of the technology cycle*".

This imperious will generates new challenges for industry where sustainability maters and gains more and more importance [4]. Various external forces are acting to that end, namely, government legislation, consumers or employees concerns, environmental pollution, social pressure, and climate change. To ensure that companies follow a more sustainable path, governments are providing conditions to help technological advances to be developed and concrete applications to be effective in the short-term in all industrial domains [3, 2]. It has been shown that the companies that are acting are the ones that are winning and all parties benefit from such behaviors [5].

The contribution on the climate change of the transportation sector is under increasing scrutiny and must reach in the forthcoming decades ambitious objectives for reducing noise and pollutant emissions [6]. The first European Aviation Environmental Report [7] issued in 2016 and some compagnies [8, 9] have pointed out the importance to uphold a strong commitment to the development of new technologies to enhance competitive-

ness and reach sustainability standards. Aircraft engines emit various pollutants of which carbon dioxide ($CO_2$) is the most significant greenhouse gas (GHG) influencing climate change. In the context of international efforts to limit climate changes, the transportation sector is expected to reduce its GHG emissions by 20% in 2030 compared to 2008 levels, and by 70% in 2050 [10].

To meet these ambitious standards automotive [11] and aircraft [8] manufacturers lead the way to embrace electrical technology that drastically lessens the $NO_x$ emission levels. However, adding more electrical components dramatically raises the amount of dissipated heat that cannot be coped with existing embedded cooling technologies. This observation requires a new paradigm regarding this vital function and one solution arises from the liquid enthalpy of vaporization. This endothermic process leverages the fluid heat-transfer capacity. Four technologies exist but only a mechanically pumped two-phase fluid loop solution is able to cope with accelerated environments as encountered in aircraft or automotive applications.

A consortium composed of 13 partners (3 academic laboratories and 10 industrial companies) has been formed. Funded by public agencies and industry, the THERMOFLUID-RT project [12] consists in developing a two-phase fluid loop driven by a mechanical pump. The industrial partners seek to meet their goals in terms of thermal control regarding their applications whereas the laboratories focus on more fundamental aspects. Two laboratories aim to model and optimize the two-phase fluid loop whereas LMT-Cachan contributes to the design of the critical component of the pump, *i.e.,* bellows. This component obtained by welding very thin (70 $\mu$m) pre-deformed sheets made of precipitation hardened stainless steel (17-7 PH grade) is expected to operate without failure for 20 years. The project will contribute to sustain the leadership of the European Air and Space industry and will serve the Île-de-France region by socially contributing to the economic situation with 35 engineers and researchers employed for four years.

The pump is the critical component of the two-phase fluid loop and a non-removable and non-repairable system. Therefore, the present work aims to contribute to the success of the mechanically pumped two-phase fluid loop by providing an understanding and prediction of the welded bellows mechanical and fatigue properties. The study proposes and discusses several scientific aspects that are needed to address the investigated problem. New tools are designed and exploited to give insights into the mechanical properties of very thin sheets and aim to enhance the technological transfer capability from academic findings to industrial applications.

## 1.2 Goal

The goal of the study is to investigate and predict the mechanical and fatigue behavior of welded bellows, and to optimize their lifetime. To reveal the mechanisms that are

of the basis of the sought behaviors a two-step investigation is set forth. The strategy originates from the fact that the High Cycle Fatigue (HCF) mechanical properties can be evaluated based on the evaluation of the dissipated energy [13, 14, 15]. This phenomenon is the macroscopic thermal response of micro-plastic activity that can be modeled by an elastoplastic law with kinematic hardening [16, 17]. Therefore, the first part of the thesis investigates the elastoplastic behavior at the macroscopic and the microscopic scales. Second and in the light of the evaluated mechanical behaviors, self heating experiments and numerical analyses both on the material and the component are carried out and lead to the determination of their fatigue properties. To meet these goals, a set of novel experimental and numerical tools are developed and validated.

## 1.3 Strategy

### 1.3.1 Part A: Material Parameter Identification

In the first part of the thesis, the elasto-plastic behavior is investigated following two separate scales (macroscopic and microscopic) at which mechanical tests are performed (see Figure 1.1) and several constitutive laws are probed.

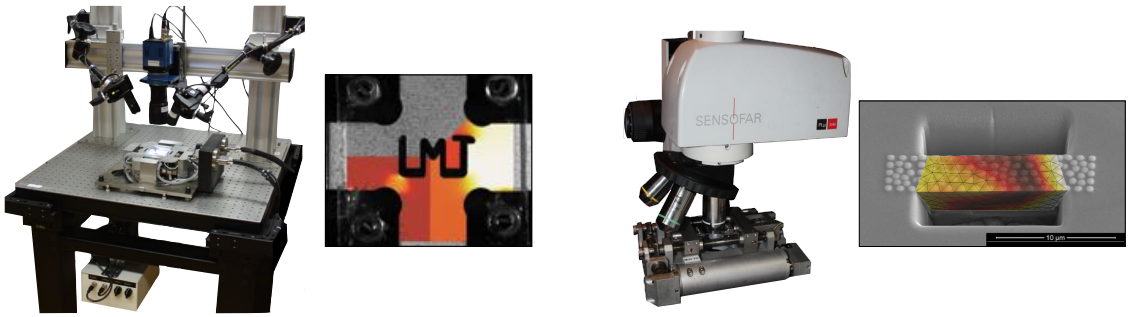


(a) (b)

**Figure 1.1:** (a) Multiaxial testing machine, mini-ASTREE and an ultra-thin biaxial specimen, and (b) the microscopic tensile apparatus and the triangular prism micro-specimen

To ensure the most relevant identification of the mechanical properties, it is crucial to optimize the specimen geometry based on an accurate definition of the sought objectives (*i.e.,* material parameters and constitutive laws). Furthermore, all raw data, even if their nature differ, must contribute to enhance identification robustness and accuracy. Experimental investigations on ultra-thin sheet will be performed with the new multiaxial testing machine, mini-ASTREE (Chapter 3) to address their elasto-plastic anisotropic properties. The microscopic investigation aims to assess the kinematic hardening properties of a crystal plasticity law [18] with Integrated DIC. The experiment relies on a triangular prism

micro-specimen machined via focused ion beam (FIB) and gathers height profile images with a confocal microscope. It will be shown that the boundary conditions are crucial to assess the sought micromechanical properties and all experimental data (reaction forces and displacement fields) need to be combined (Chapter 6). Figure 1.1 shows two experimental setups and the experimental results used to characterize the elastoplastic behavior at (a) the macroscopic scale and (b) the microscopic scale.

### 1.3.2 Part B: Fatigue Characterization

In the second part of the thesis, the fatigue properties of the studied material and the bellows are investigated. The approach relies on the self-heating concept [15, 17] and assumes a probabilistic multi-scale model to the dissipated energy [19, 20]. First, experiments on ultra-thin and uniaxial specimens are performed on a servohydraulic tension/-compression testing machine. Second, the HCF response of the bellows is monitored with a newly designed testing machine (see Figure 1.2). The experimental results are combined with their numerical counterparts to assess the sought fatigue properties.

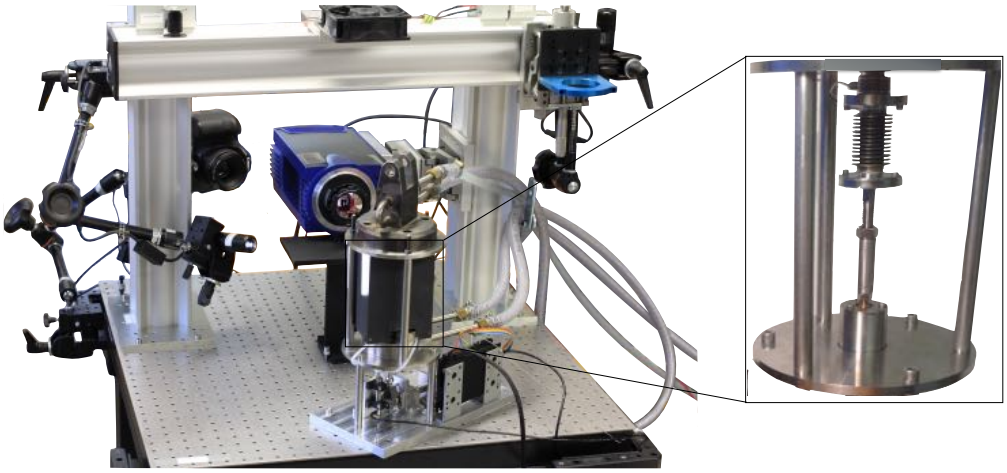

**Figure 1.2:** Experimental device for the fatigue investigation of welded bellows

## 1.4 Scope of the thesis

Chapter 2 introduces the investigated component and its material, and gives an initial probabilistic fatigue design based on the weakest link theory [21]. In Part A, the tools, methodologies, and results about the mechanical behavior characterization of the studied material are discussed in Chapters 3, 4, 5, and 6. In Part B, the results of the fatigue investigation both on the material and the bellows are reported in Chapter 7. The thesis ends with a reflection about the results and the proposed methodology that evaluates and validates an optimal fatigue design of the welded bellows. Further recommandations and challenges are mentioned in Chapter 8.

# Chapter 2
# An initial probabilistic fatigue design of welded bellows


## Abstract

The study aims to optimize the fatigue life of a mechanical deformable component made of stainless steel without experimental data about its material fatigue behavior. First, a representative Finite Element model is designed with optical microscopy photography and Computed Axial Tomography scan. Second, a crack initiation index based on the weakest link theory that assumes a Weibull probability density function is proposed [22]. The results lead to an optimal use of the bellows. It is shown that the solution of the probabilistic model varies as a function of the material properties.


## 2.1 Introduction

An engineering company wants to design welded bellows for aerospace applications. The component is used as a mechanical actuator of a mechanically pumped two-phase fluid loop that delivers a constant fluid volume per cycle. The latter is an assembly of numerous diaphragms made of stainless steel that are welded. Its geometry is given by the existing stamping tools and the process aims to create a very strong, yet flexible mechanical conduit compatible with liquids and gases. Regarding its use, the stroke is equal to $\delta_z = 8$mm and the liquid is in contact with the outer face with a standard differential pressure equal to $\Delta p = 1$ bar. The manufacturer wants to identify the minimum number of diaphragms and the location of the mid-stroke that maximizes its life. No investigation on the fatigue properties of the material has been performed and only the material parameters for an isotropic linear elastic model are available [23]. To address the second issue without any fatigue results, a numerical model of the bellow is designed and a probabilistic approach is carried out to minimize its fatigue failure probability.

The chapter is organized as follows. Section 2.2 analyzes the mechanical component with tomographic scans and optical microscopy photographs. Section 2.3 shows the Finite Element model. Section 2.4 introduces the probabilistic model and the so-called *Weibull crack initiation index* and gives the results of the optimization procedure.

## 2.2 Component

The bellows is a component manufactured by assembling several stamped metal diaphragms from a 70-$\mu$m thick sheet of precipitate hardened stainless steel (17-7 PH grade [23]). The plate originates from a 300-$\mu$m thick sheet that has been cold rolled. The diaphragms are them stamped and welded without additional elements on their inner and outer radii. The assembly is then heat treated to obtain the TH 1050 mechanical properties [23]. The bellows operates with a 1-bar differential pressure on its outer side and an 8mm stroke. Table 2.1 gathers the material characteristics of the studied precipitate hardened stainless steel (17-7 PH grade in TH1050 condition [23, 24]).

**Table 2.1:** Material parameters relative to the isotropic linear elastic model and the yield stress from litterature data [23]

| Name | $E$ (GPa) | $\nu$ (—) | $\sigma_y$ (MPa) |
|---|---|---|---|
| Value | 200 | 0.30 | 1300 |

Two experimental investigations have determined the major geometrical features of the mechanical component. Figure 2.1(a) shows a Computerized Axial Tomography scan (CAT-scan) with a voxel size of 30 $\mu$m with, *i*) the geometry of the diaphragms and *ii*) the inner and outer welds. However, this observation at this magnification has not revealed defects and more investigations are carried out on the welded regions. One bellows is vertically cut and analyzed with an optical microscope. Figure 2.1(b) shows an optical micrograph of an inner weld region and indicates that the Electron Beam Welding (EBW) process generates welds with a circular shape. Furthermore, the two diaphragms are separated by about 10 $\mu$m, which is unexpected since the two diaphragms are maintained in contact during the welding process.

Figure 2.2 shows an EBSD pole figure that reveals the material microstructure with the measured individual crystal orientations for the material in TH1050 condition. The grains are small with an average size below 1 $\mu$m that helps to enhanced fatigue properties [25].

For the sake of simplicity two key assumptions are made, *i*) the mechanical behavior is assumed homogeneous over the entire volume (welds included) and *ii*) the geometrical discontinuities in the welds are not modeled because of their complexity. No residual stresses are accounted for.

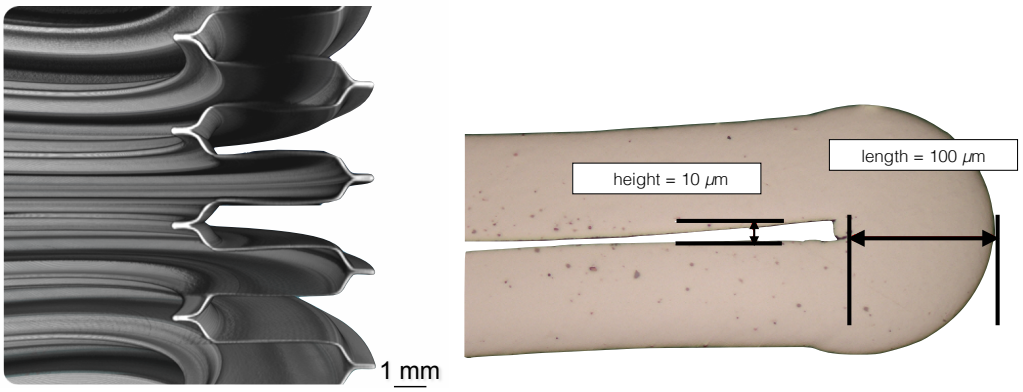


(a) (b)

**Figure 2.1:** (a) Computerized Axial Tomography scan (CAT-scan) of one bellows and (b) optical micrograph of a welded area on the outer radius (note the circular shape and the gap equal to 10 $\mu$m that separates the two diaphragms)

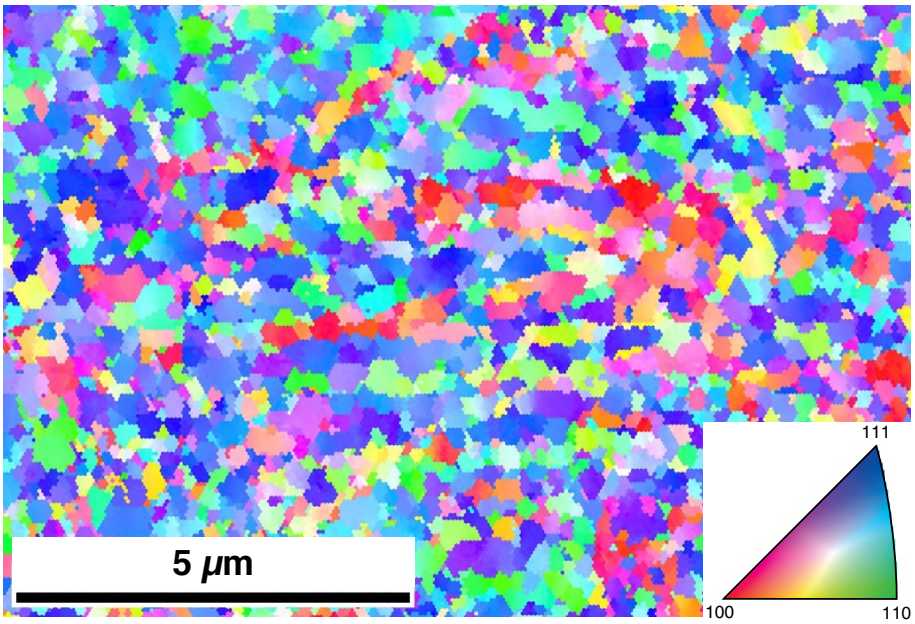


**Figure 2.2:** EBSD pole figure of the material in TH1050 condition

## 2.3 Numerical model

The last investigation has provided key features to design the Finite Element model. The latter is defined by its geometry and its boundary conditions. First, Figure 2.3 shows the FE model at an inner weld (see the corresponding geometry as experimentally observed in Figure 2.1(b)). The model is axisymmetric (note that the abscissa refers to the center axis coordinates) and composed of 37,000 four-noded QUAD elements with bilinear displacement interpolation (Q4). The mesh size is adapted to the specific regions to improve the quality of the computation and only 6 diaphragms are modeled to minimize the computation time.

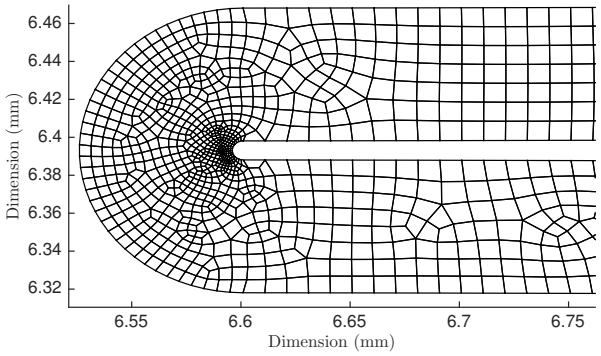


**Figure 2.3:** Finite Element model of an inner weld region where the mesh size is adapted to improve the quality of the numerical computations

Second, the boundary conditions are divided into two parts, namely, the nature of the contacts between the bellows and interface pieces, and the prescribed loading history. The lower interface is assumed to be clamped whereas the upper one undergoes the prescribed displacement. Furthermore, the tangential displacement on the upper interface is free. Figure 2.4 shows the kinematic response of the bellows for various levels of prescribed displacement $\delta_z$.

An initial numerical analysis shows that for 6 diaphragms the minimum displacement amplitude where the Von Mises stress is lower than the yield stress is equal to 2.7 mm. Therefore, 18 is the minimum number of diaphragms that ensures that the macroscopic mechanical behavior remains linear elastic for an 8 mm stroke. Because of the observations of severe geometrical discontinuities, the decision is made to increase the final design to 24 diaphragms. In the following the prescribed amplitude on the model (*i.e.,* made of 6 diaphragms) is adapted to the real number of diaphragms (24) and equal to 2 mm (ratio of 4 between the numerical model and the real bellows).

Last, to correspond to the real application, the numerical model relies on several loading phases: $i$) gradually apply the pressure on the outer surface, $ii$) reach the mid-stroke,

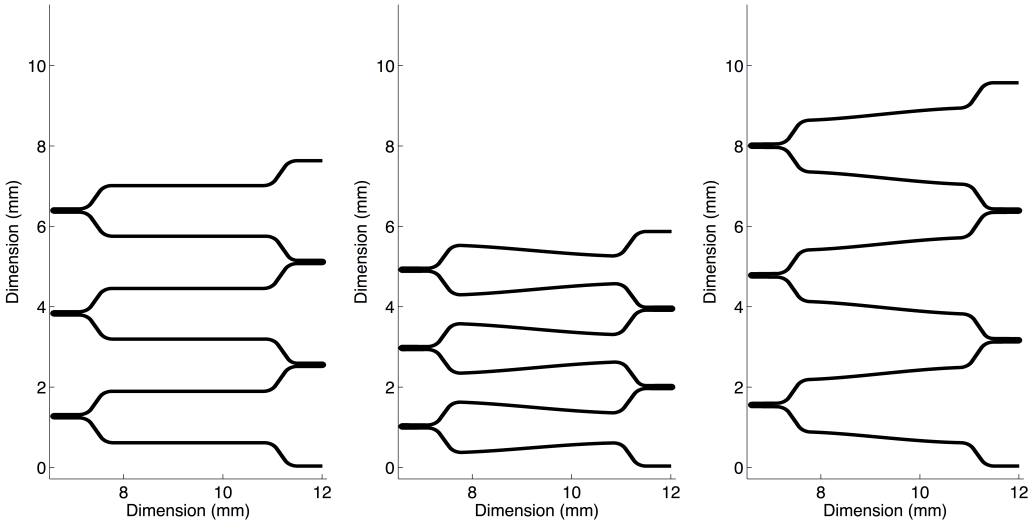


(a) (b) (c)

**Figure 2.4:** Deformed geometries for three prescribed displacements and a 1-bar differential pressure; (a) $\delta_z = 0$ mm, (b) $\delta_z = -4$ mm, and (c) $\delta_z = 4$ mm

and *iii*) prescribe three cycles of an equivalent 8-mm stroke. Figure 2.5 shows the steps for numerous mid-strokes.

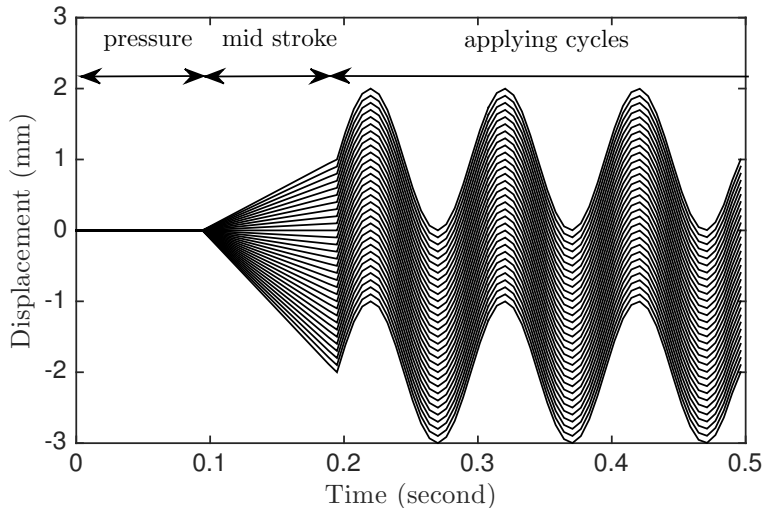


**Figure 2.5:** Prescribed loading history with its three steps, namely, pressure, reaching the mid-stroke, and applying a cyclic loading

## 2.4 Probabilistic design

This section aims to design a bellows for fatigue purposes before any experimental results. This preliminary design will be experimentally validated in Section 7.4. A deterministic design of the fatigue limit of the component would minimize the maximum principal stress on the location where its value is the highest. This criterion assumes that a fatigue crack will always initiate at the latter location. But experimental investigations have shown for identical specimen geometry stressed with identical loading history that fatigue cracks do not initiate in such deterministic way [26]. To account for this scatter a probabilistic approach based on the weakest link theory [21] is applied. This theory has been initially employed to predict the failure of this type of materials for numerous experiments [27]. The results revealed 5 key concepts about the failure mechanisms: *i*) the failure probability denoted $P_f$ associated with a failure stress denoted $\sigma_f$, *ii*) the correlation between this failure stress and the initial size of the initiating defect, *iii*) the influence of the volume size, *iv*) the influence of the stress heterogeneity quantified with a quantity coined stress heterogeneity factor, and *v*) the influence of the defect distribution.

The failure probability as defined for quasi-brittle materials has no physical meaning when applied to ductile material except if they behave elastically (*e.g.,* high cycle fatigue). Physically, the initiation occurs locally in regions where initial defects or heterogeneities lead to intense microplastic activities. Therefore, the material is assumed to be macroscopically homogeneous (and elastic) but microscopically heterogeneous. A Weibull probability function is chosen to provide an explicit mathematical formulation of the random distribution of activation sites. The crack initiation probability that is the equivalent of the failure probability in quasi-brittle materials is introduced ($P_f$) to account for the non deterministic initiation of cracks in HCF for metallic materials [26].

Let $D$ be the damage variable that models the state of the material in a elementary volume. For a damage equal to zero, the crack initiation stress $\sigma_f$ is equal to a defect-free material stress $\sigma_{f_0}$. Conversely, if the crack initiation stress is equal to zero the volume is fully damaged and $D = 1$,

$$\frac{\sigma_f}{\sigma_{f_0}} = 1 - D \tag{2.1}$$

where $\sigma_f$ is the crack initiation stress for a damage $D \in [0;1]$. Let $P_{f_0}$ be the crack initiation probability such that $\sigma \geqslant \sigma_f$ in a volume $V_0$ with $\sigma$ the applied stress. A crack initiates when the initial damage $D_0 \geqslant 1 - \sigma/\sigma_{f_0}$. The threshold damage for a stress $\sigma$ that leads to the initiation of the first crack in an elementary volume is $D_{0_c} = 1 - \sigma/\sigma_{f_0}$. To account for the damage variability within the volume its distribution follows a probability density function $f_0$,

$$\int_0^1 f_0(\delta t) d\delta t = 1 \;\text{ such that }\; f_0(\delta t) \geqslant 0 \;\forall\; \delta t \in [0;1], \tag{2.2}$$

which defines the elementary crack initiation probability in the elementary volume,

$$P_{f_0} = \int_{D_0 \geqslant D_{0_c}} f_0(\delta t) d\delta t \Rightarrow P_{f_0} = \int_{D_{0_c}}^{1} f_0(\delta t) d\delta t \tag{2.3}$$

Assuming that all $n$ elementary volumes that compose the structure are independent the survival probability of the structure ($P_s = 1 - P_f$) becomes

$$1 - P_f = \prod_{i=1}^{n} \left(1 - P_{f_i}\right) \tag{2.4}$$

and applying to the last expression the natural logarithm yields,

$$\lim_{n \to +\infty} \frac{1}{n} \sum_{i=1}^{n} \ln\left(1 - P_{f_i}\right) = \frac{1}{V} \int_{\Omega} \ln\left(1 - P_{f_0}\right)\right) dV \tag{2.5}$$

the crack initiation probability $P_{f_i}$ reads,

$$P_{f_i} = 1 - \exp\left[\frac{1}{V} \int_{\Omega} \ln\left(1 - P_{f_0}\right)\right) dV\right] \tag{2.6}$$

To extend this expression for a multiaxial stress state, a first crack initiation equivalent stress $\sigma_{eq}$ defined by the maximum value of the positive principal stresses is chosen. The latter has to be positive as prescribed by the definition of the crack initiation stress,

$$\sigma = \underbrace{\sigma_{f0}}_{>0} \underbrace{(1 - D_0)}_{\geqslant 0} \tag{2.7}$$

therefore,

$$\sigma = \sigma_{eq} = \max\left(\langle \sigma_1 \rangle_+, \langle \sigma_2 \rangle_+, \langle \sigma_3 \rangle_+\right) \tag{2.8}$$

where $\langle \bullet \rangle$ denotes the positive part of $\bullet$. A power law probability density is chosen,

$$f(D_0) = m k_0 \left(1 - D_0\right)^{m-1} \tag{2.9}$$

where $m$ is the exponent and $k_0$ a scaling parameter of the distribution. The modulus is a dimensionless parameter used to describe the variability of the strength of materials [27, 28]. The elementary crack initiation probability becomes,

$$P_{f_0} = \int_{D_{0c}}^{1} m k_0 \left(1 - \delta t\right)^{m-1} d\delta t \tag{2.10}$$

Using Equation (2.1) and using the new notation $\sigma_0^m = \sigma_{f_0}^m / k_0$, the crack initiation probability of an elementary volume reads,

$$P_{f_0} = \left( \frac{\sigma_{eq}}{\sigma_0} \right)^m \tag{2.11}$$

Using Equation (2.6) and assuming that $P_{f_0} \ll 1$ leads to the Weibull law that describes the crack initiation probability in HCF

$$P_{f_i} = 1 - \exp\left[ -\frac{1}{V_0} \int_\Omega \left( \frac{\sigma_{eq}}{\sigma_0} \right)^m dV \right] \tag{2.12}$$

where the Weibull law parameters are $m$ and $V_0(\sigma_0)^m$. This expression assumes that the more heterogeneous the stress field the higher the crack initiation stress for a given crack initiation probability. This effect originates from the stress heterogeneity in the material and it is described by the stress heterogeneity factor [22],

$$H_m = \frac{1}{V} \int_\Omega \left( \frac{\sigma_{eq}}{\sigma_f} \right)^m dV \tag{2.13}$$

that leads to a new expression of the crack initiation probability,

$$P_{f_i} = 1 - \exp\left[ -\frac{V H_m}{V_0} \left( \frac{\sigma_F}{\sigma_0} \right)^m \right] \tag{2.14}$$

where $\sigma_F = \max_\Omega \sigma_f$ where $\sigma_F$ is the maximum value of the crack initiation stress. The concept of stress heterogeneity factor is related to the volume of the studied structure and their product is called the effective volume ($V_{eff}$),

$$V_{eff} = V \times H_m \tag{2.15}$$

So far, no experimental investigations have been performed to assess the Weibull parameters. Therefore, the Weibull crack initiation index ($I_i$) is introduced to deal with this lack of data. It enables the probabilistic design of a structure to be investigated without the Weibull parameters (particularly $V_0 \sigma_0^m$) being known. This index is defined as,

$$I_i = V_{eff} (\sigma_F)^m = V_0 \sigma_0^m \left[ -\ln(1 - P_f) \right] \tag{2.16}$$

The next part aims to evaluate this index and to minimize this value as it is directly related to the crack initiation probability ($P_{f_i}$).

The following analysis aims to maximize the bellows life by optimizing the location of its mid-stroke. The numerical analysis shown Figure 2.5 is carried out. Various mid-

strokes are investigated and an external differential pressure of 1 bar is prescribed. The probabilistic methodology is applied to the numerical results to evaluate the stress heterogeneity factor ($H_m$) and the Weibull crack initiation indice ($I_i$). However, the prescribed displacement being cyclic, the maximum amplitude of the equivalent stress $\Sigma_{eq}$ is the quantity of interest

$$\Sigma_{eq}(\boldsymbol{x}) = \max\langle\Sigma_1,\Sigma_2,\Sigma_3\rangle_+ \quad \text{such that} \quad \boldsymbol{\Sigma}(\boldsymbol{x}) = \boldsymbol{\sigma}(t_{T.D.C.},\boldsymbol{x}) - \boldsymbol{\sigma}(t_{B.D.C.},\boldsymbol{x}) \tag{2.17}$$

where $\boldsymbol{x}$ is the local coordinates, ($\Sigma_1,\Sigma_2$, and $\Sigma_3$) the eigenvalues of the strain tensor $\boldsymbol{\Sigma}$, and $t_{T.D.C.}$ and $t_{B.D.C.}$ the top dead center ($T.D.C.$) and bottom dead center ($B.D.C.$) strokes. The maximum amplitude of the crack initiation stress $\Sigma_F$ is equivalent to the maximum equivalent stress amplitude over the volume for the entire loading history,

$$\Sigma_F = \max_{\boldsymbol{x}} \left(\Sigma_{eq}(\boldsymbol{x})\right) \tag{2.18}$$

Figure 2.6 shows the maximum principal stress field for a positive prescribed displacement. Two regions exhibit important levels of the principal stress, namely, the inner side of the weld and the two faces of the diaphragm elbow.

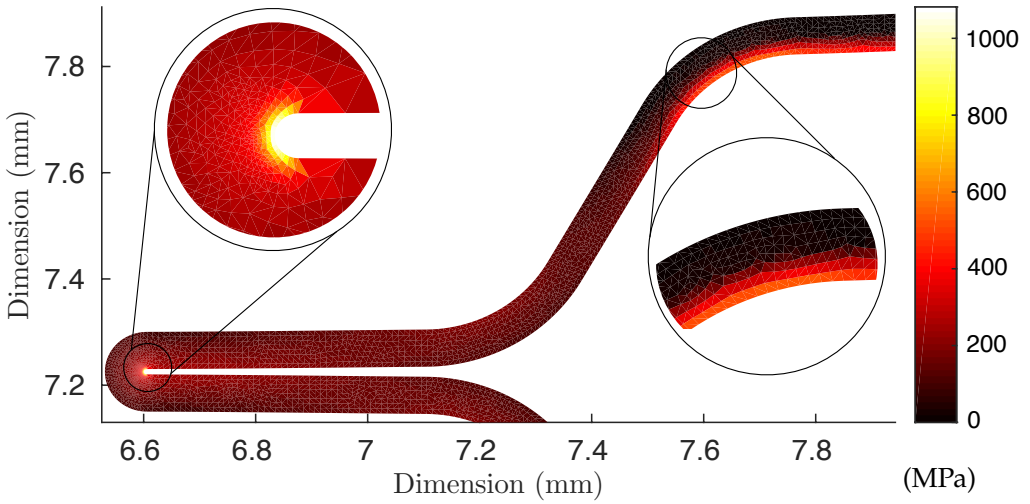


**Figure 2.6:** Maximum principal stress field (in MPa) evaluated for a positive displacement

The new expression of the stress heterogeneity factor $H_m$ (*i.e.,* associated with the equivalent stress amplitude) reads,

$$H_m = \frac{1}{V}\int_\Omega \left(\frac{\Sigma_{eq}(\boldsymbol{x})}{\Sigma_F}\right)^m d\boldsymbol{x} \tag{2.19}$$

Figure 2.7 shows the stress heterogeneity factors ($H_m$) for a Weibull modulus $m \in [1;15]$

in a semi-log plot for all the studied mid-strokes. First, the larger the Weibull modulus the smaller the stress heterogeneity factor. The larger the Weibull modulus the more homogeneous the material and less scattered damage initiations. Second, the minimum value of $H_m$ varies as the Weibull modulus increases. Last, a significant variation is encountered for a mid-stroke equal to -4 mm that originates from contact between two neighboring diaphragms.

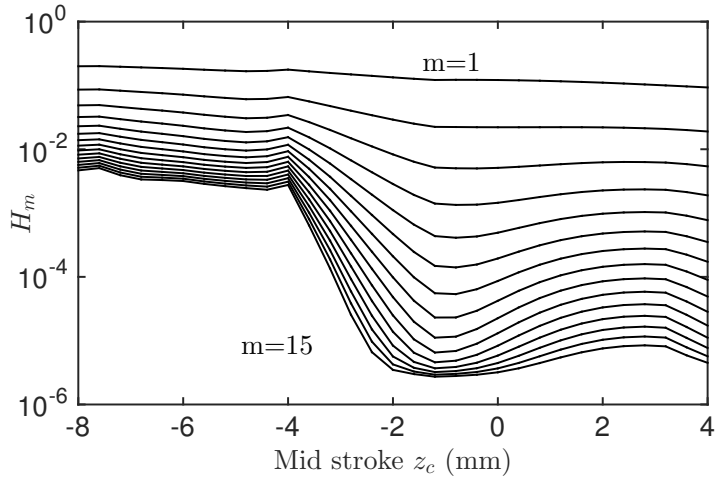


**Figure 2.7:** Stress heterogeneity factor ($H_m$) for a Weibull modulus $m \in [1;15]$ evaluated on all the structures for different mid-strokes ($z_c \in [-8,4]$ mm)

The Weibull crack initiation index considers the cyclic aspect of the problem with the maximum amplitude value of the first crack initiation stress $\Sigma_F$,

$$I_i = V_{eff} \left(\Sigma_F\right)^m \tag{2.20}$$

Figure 2.8 shows the crack initiation Weibull index $I_i$ for different mid-strokes and a Weibull modulus equal to 12 in a semi-log plot. For other Weibull moduli the trend is similar but the value changes. A global minimum is found.

Figure 2.9 shows the optimal mid-stroke obtained for the minimum value of the Weibull crack initiation index ($I_i$) as a function of the modulus $m$. The optimal value varies with the Weibull modulus. When $m \to \infty$ the initiation will always occur at the location of the maximum principal stress as a deterministic approach would predict.

A standard value of Weibull modulus for a stainless steel is $m = 12$ [19]. Based on this value, the optimal mid-stroke is equal to $z_c = -1.6$ mm and corresponds to a displacement variation $\delta_z \in [-5.6;2.4]$ mm.

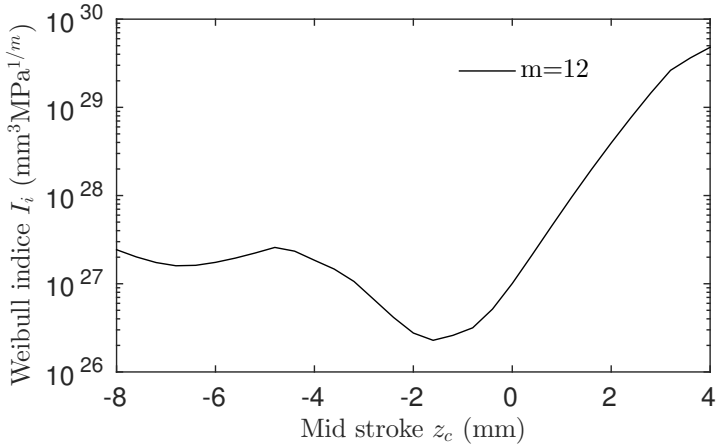


**Figure 2.8:** Weibull crack initiation index for a Weibull modulus $m = 12$ evaluated on the whole bellows for different mid-strokes ($z_c \in [-8,4]$ mm)

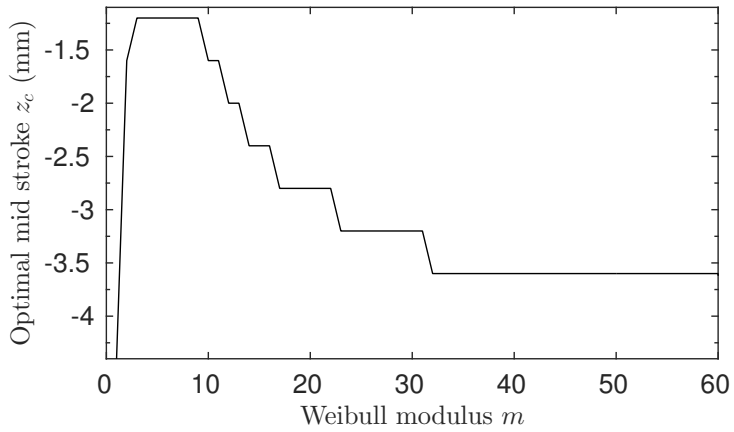


**Figure 2.9:** Optimized mid-stroke for a Weibull modulus $m \in [1;60]$ evaluated on the whole bellows for different mid-stroke ($z_c \in [-8,4]$ mm)

### 2.4.1 Conclusion

An initial probabilistic design has led to the optimization of the mid-stroke ($z_c$) of welded bellows. First, experimental investigations have assessed the key geometrical features leading to a representative numerical model. Second, the weakest link theory has been applied to the concept of crack initiation in high cycle fatigue. That path has led to the introduction of the Weibull crack initiation index. Based on numerical results, the index has been evaluated for numerous mid-stroke configurations. The results have shown a unique minimum value for each mid-stroke. However, this analysis has been achieved without experimental data of the material fatigue behavior. Therefore, the optimal mid-stroke value has been evaluated for numerous Weibull moduli. A standard value for stainless

steel has been chosen [19] to give an initial answer. This answer is crucial for the design of the pump because it enables for a more compact design that minimizes the mass of the total component. Experimental investigations on fatigue in particular must be undertaken to assess the key properties and validate this initial probabilistic fatigue design.

Two pieces of information are needed. First, the mechanical behavior of the material needs to be assessed and second, its fatigue properties and those of the component need to be determined. Therefore, Chapter 3 aims to design an optimized cruciform geometry to reveal and assess the mechanical properties. The designed procedure fully exploits the wealth of information provided by full-field measurement.

# Part A

# Material Parameter Identification

# Chapter 3
# Optimization of a cruciform geometry for the identification of constitutive parameters

Reproduced from: Morgan Bertin, François Hild and Stéphane Roux, *Optimization of a cruciform specimen geometry for the identification of constitutive parameters based upon full-field measurements*, Strain, 2016, doi: 10.1111/str.12178

## Abstract

A methodology is proposed to optimize a specimen shape in a biaxial testing machine for the identification of constitutive laws based on full-field measurements. Within the framework of Finite Element Model Updating (FEMU) and Integrated Digital Image Correlation (IDIC), the covariance matrix of the identified material parameters due to acquisition noise is computed and its minimization is the basis of the proposed shape optimization. Two models are investigated; first, a linear elastic law, and second, an elastoplastic law with linear kinematic hardening. Two optimal fillet radii sets are assessed for the two investigated laws based on the minimization of the identification uncertainty.

## 3.1 Introduction

One of the main issues of mechanical engineering is to understand, describe and predict how materials behave and fail. For many industrial applications, the optimization with respect to mass for instance pushes toward accurate and hence complex constitutive laws. Just to mention a very early example, elastoplastic flow in sheet metal forming prompted Hill [29] to emphasize on the need for properly describing anisotropy to account for the influence of the orientation of the sheet with respect to the rolling direction. Together with the complexity of constitutive laws comes a rapid increase in the number of material parameters to be identified in order that the model matches the load / displacement relationship as observed in either one or several mechanical test(s). This inflation of parameters implies an increased difficulty to measure them in well-suited experiments. In particular, plastic anisotropy calls for *multiaxial testing*.

Due to the complexity of designing multiaxial testing devices, one compromise was to consider flat cruciform specimens [30]. The authors showed the benefit provided by

such samples for biaxial fatigue studies with numerical simulations. However, only theoretical and modeling approaches were performed [31]. Kelly [32] carried out "virtual experiments" to characterize materials with multiaxial loadings. Finally, the first in-plane biaxial loading system has been proposed by Makinde *et al.* [33, 34, 35]. The authors proposed an original experimental device to prescribe biaxial tension in the plane of a cruciform specimen to study plasticity. Afterward, *ad hoc* systems were proposed to perform biaxial tension [36, 37, 38] using uniaxial testing machines [39].

Other authors [34, 40, 41, 42, 39] studied plasticity under biaxial loading and applications to constitutive modeling [43]. Eftis *et al.* [44] studied crack propagation under biaxial loadings. Kuwabara [36] prescribed different loading paths with both cruciform specimens and bending tests. It appears that the most flexible and versatile experimental system is related to in-plane biaxial tests of cruciform specimens [35, 42, 45] among different systems [46, 40, 45]. Some of them involve complex loading conditions [47, 48, 49, 50, 51].

Two main issues raised by the above-cited authors were *i)* How to reveal specific material behaviors? and *ii)* How to quantify and identify material parameters? The first issue deals with the design of experimental systems. The second one is related to measurement and identification procedures. These two aspects (*i.e.,* measurement and identification) are linked. For example, in the case of the identification of constitutive parameters, the main guide to the design of cruciform specimens, namely homogeneity, was motivated by the measurement methods (*e.g.,* strain gauges or extensometers).

Even if innovative sensors were proposed [52], the total number of sensors remained fairly small. This constraint has led to specific optimization criteria [53]. They accounted for three aspects, namely, the homogeneity of the zone over which the phenomena occur and the level of strains and stresses in order to have good measurements with strain gauges [40, 36, 54, 42]. The homogeneity requirement led for instance to specific features such as slits to cancel out Poisson's effect occurring on specimen arms and yielding larger homogeneous zones [53, 55, 56], a thinner central zone to concentrate the strains [47, 17] and a minimum number of discontinuities [41, 57] were also considered.

However, the stress and strain uniformity is not necessarily required when identification techniques accounting for heterogeneous fields are considered. First introduced by Kavanagh and Clouth [58] the so-called "Finite Element Model Updating" (FEMU) technique aims to identify the constitutive parameters while updating the numerical model to the experimental data. Lecompte *et al.* [41] proposed a mixed numerical-experimental technique to identify orthotropic parameters of metals based on full-field measurements. With a biaxial tensile test the FEMU technique was used to compare measured and computed strain fields (*i.e.,* FEMU-$\mathfrak{E}$). This method is one out of several procedures based on full-field measurements [59, 60]. Similarly, Schmaltz *et al.* [61] made use of stereo-DIC measurements and FEMU-U (*i.e.,* comparison between measured and computed displacement fields) to identify plastic laws for four different cross-shaped geometries. The key

point here was the introduction of full-field measurements, that is, a considerable increase in the density of measurement points. This abrupt transition from sparse to dense measurements is a major change of perspective.

FEMU can be extended to Integrated Digital Image Correlation (IDIC [62, 63]) to couple measurement and identification procedures. Unlike other identification techniques such as FEMU, IDIC relies directly on the images to determine material parameters. It allows standard finite element codes to be used in a non-intrusive way [64]. Further, when properly weighted it can be shown that for small noise levels weighted FEMU and IDIC lead to similar covariance matrices of the sought parameters [64].

The fact that full-field measurements are performed will lead to new approaches to mechanical test design. The geometry and load history will be chosen to optimize the sensitivity of the test with respect to the sought constitutive parameters. The present chapter aims to pave the way to a systematic optimization of test design tailored for an anticipated constitutive law. Here only the specimen geometry is optimized for the sake of simplicity and the loading path is considered as fixed. The target is formulated in terms of the quality of the measurement of constitutive parameters (*i.e.,* the least uncertainty is sought). After presenting the theoretical background, a single parameter optimization will be performed, based on the radius of a cruciform specimen fillet. An artificial (*i.e.,* numerical) case will be studied where the uncertainty is computed from an experimentally representative noise level in the entire data acquisition and treatment chain. Linear elasticity and elastoplasticity (with linear kinematic hardening) will be discussed to highlight the key role played by the formulation of the sought objective, and henceforth the constitutive law parameterization. The formalism proposed herein is transparent to more complex constitutive (*e.g.,* including various hardening postulates). To illustrate this test case, constitutive parameters are chosen as representative of $17-7$ PH (Precipitation-Hardened) stainless steel [23], which is known for its very good fatigue properties [24, 65]. Let us stress however that the present optimization is based on noise uncertainty and omits possible bias due to model error, which can hardly be addressed *a priori* (or very artificially).

## 3.2 Optimization strategy

To optimize the geometry of cross-shaped samples, Schmaltz *et al.* [61] propose to use so-called stress-stress and major-minor strain graphs. The first ones are determined via numerical simulations, whereas the second ones can be assessed experimentally via full-field measurement techniques. The present optimization is based on the covariance matrix of the identified material parameters, which indicates the identification uncertainty associated with a chosen constitutive law. The identifiability of constitutive parameters is estimated using the quantification of their influences on experimentally observable (*i.e.,* measured) quantities (*e.g.,* displacement or temperature fields, resultant forces).

Their influences are expressed with quantities called *sensitivity fields* [66, 41], *i.e.,* gradients of the observables with respect to the to-be-identified parameters. Considering one parameter variation and identical boundary conditions, there exists one sensitivity field for each material parameter. The latter ones are collected in a vector $\{\boldsymbol{p}\}$ whose components are conveniently designed to be dimensionless. This can always be performed through a normalization with the expectation values of the parameters (*i.e.,* nominal values). For convenience, it is possible to define as constitutive parameters logarithms of moduli scaled by nominal values.

The sensitivity fields are to be computed numerically based on the current determination of the constitutive parameters as well as with boundary conditions that are obtained from DIC analyses. In the present study, the identification is based on full-field measurements and two related techniques, namely, FEMU and integrated DIC [64]. Within those approaches, it is possible to track down the uncertainty from the measurement step down to the identification step. This uncertainty is collected into a global covariance matrix $[\boldsymbol{C_p}]$

$$[\boldsymbol{C_p}] = \langle \{\delta \boldsymbol{p}\} \otimes \{\delta \boldsymbol{p}\} \rangle \tag{3.1}$$

where the angular brackets $\langle ... \rangle$ denote the mathematical expectation of the enclosed argument. $[\boldsymbol{C_p}]$ deals with all facets of the problem, namely, the geometry of the studied structure, the chosen constitutive law, the set of parameters, the boundary conditions, the measurement uncertainties and the identification method. This is important since it provides an estimate of the quality of the identified parameters through an uncertainty, and also because it gives a handle on how to optimize a mechanical test (in the present case through the shape of the specimen). The lower the value of this covariance, the more reliable the identification. The objective is to minimize the covariance matrix components with respect to the optimization parameters (here chosen to be associated with the specimen shape). However, because this covariance is a second order tensor, some more discussion is required on what is really meant by minimization, and this issue and some of its consequences will be discussed and illustrated below.

### 3.2.1 Test and observables

#### Specimen geometry

The testing machine is biaxial, which has the ability to prescribe an arbitrary tensile strain in two orthogonal directions, $\boldsymbol{e_1}$ and $\boldsymbol{e_2}$, with opposite actuators that behave in a symmetric fashion so that the specimen center is motionless. The specimen shape is thus naturally cruciform (Figure 3.1). In the following, the four fillets are first assumed to have the same radius. The fillet radius will be the argument of the optimization problem. The region of interest is a square of area $30 \times 30$ mm$^2$. Figure 3.1 shows the triangular mesh used for

the numerical simulation and the specimen geometry for a fillet radius equal to $r = 2$ mm.

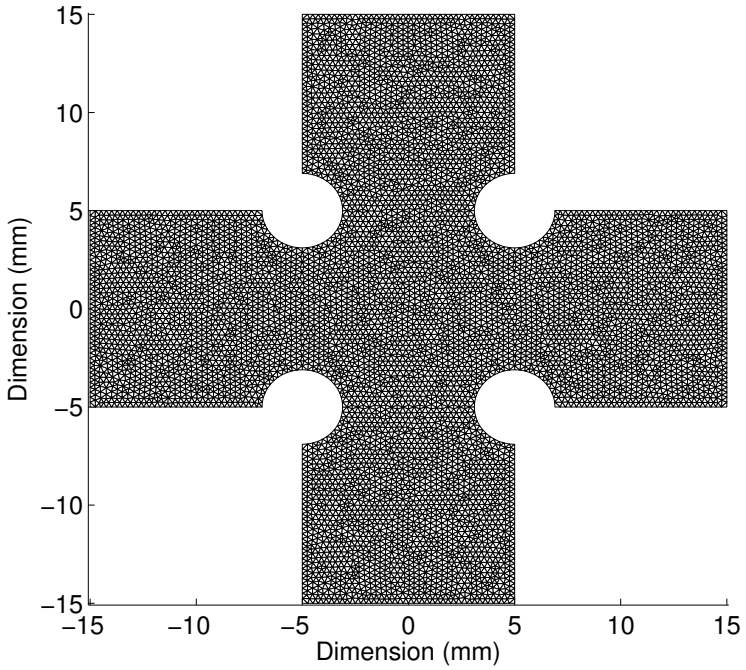


**Figure 3.1:** Mesh and geometry of the analyzed specimen with a fillet radius $r = 2$ mm

This type of geometry will be used to perform biaxial experiments on 17-7 PH stainless steel. It has been chosen regarding the manufacturing process and the machine capabilities, namely, *i*) Electrical Discharge Machining (EDM), *ii*) flat and thin biaxial specimens, *iii*) the largest arm width available to ensure the largest observable surface, and *iv*) a sufficiently simple geometry with a small number of parameters to optimize. However, other optimization parameters could be investigated such as adding a hole to the specimen. It is worth noting that other geometries have been proposed, *e.g.,* by Schmaltz *et al.* [61].

### Loading history

As shown in Figure 3.2, a "nonproportional" loading path is prescribed. First a displacement along direction $\boldsymbol{e}_1$ is applied up to a maximum value $d_1 = d^*$ while the transverse displacement is kept equal to 0 ($OA$). Then, at fixed displacement $d_1$, the displacement $d_2$ is raised to reach an equibiaxial strain state, $d_1 = d_2 = d^*$ (point $B$) and finally both displacement amplitudes are reduced to zero at the same rate ($BO$) so that in the displacement plane $(d_1, d_2)$ the loading path is a triangle.

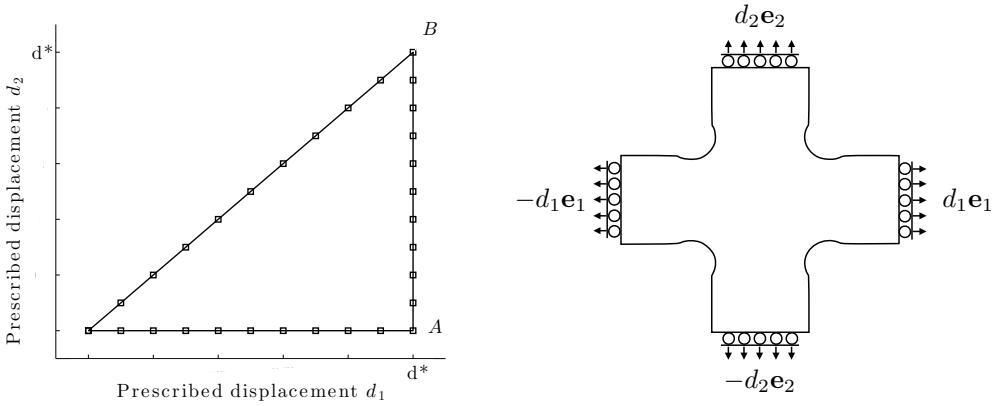


**Figure 3.2:** (a) Triangular loading history prescribed in the simulation. The squares depict the computed steps. (b) Boundary conditions prescribed on the sample in terms of longitudinal displacements. With the chosen loading history the center of the specimen is motionless

The tested specimens are 0.3 mm thick (Chapter 4). Thus, forces in both directions are chosen greater than or equal to zero to avoid buckling. The measured quantities are of two types. First, reaction forces in each arm are measured using load sensors. Second, at prescribed stages, images of the specimen surface are captured. They will be processed to measure displacement fields using DIC techniques discussed in detail below. The simulated digital camera is able to acquire 16-bit gray scale images. The physical size of one pixel is $a = 13.5$ $\mu$m.

Each measurement is performed with a specific uncertainty. $\gamma_F^2$ denotes the variance of the force measurement, where all load cells are independent of each other. Similarly, images are subjected to a noise that will be considered to be Gaussian and white (*i.e.,* uncorrelated). One key feature of the used DIC methodology is the fact that the effect of image noise on displacement uncertainty can be explicitly characterized. This is an extremely important feature as it allows for the design of the appropriate norm to be used in the FEMU identification procedure, and thereby to follow the impact of noise coming from either images or force sensors onto the uncertainty of the identified parameters [64]. It is because of this complete chain that the optimization of the specimen shape can be addressed even when the specimen has not been tested yet.

### 3.2.2 Covariance matrices

The aim of this subsection is to introduce the general framework to estimate the covariance matrix $[\boldsymbol{C_p}]$, which is the basis of the optimization procedure proposed herein. Two

different routes will be followed.

### Global DIC

In the following, global DIC is considered. It relies on the registration of an image $f(\boldsymbol{x})$ in the reference configuration and a series of pictures $g(\boldsymbol{x},t)$ in the deformed configurations indexed by time $t$. The gray level conservation is assumed

$$f(\boldsymbol{x}) = g(\boldsymbol{x}+\boldsymbol{u}(\boldsymbol{x},t),t) \tag{3.2}$$

where $\boldsymbol{u}(\boldsymbol{x},t)$ is the sought displacement field. The problem consists of minimizing the norm of the gray level differences over the whole Region of Interest (ROI)

$$\begin{aligned} \chi^2_{of} &= \|g(\boldsymbol{x}+\boldsymbol{u}(\boldsymbol{x},t),t) - f(\boldsymbol{x})\|^2_{C_n} \\ &\equiv \sum_{\Omega}\sum_{\Omega}(g(\boldsymbol{x}+\boldsymbol{u}(\boldsymbol{x},t),t) - f(\boldsymbol{x}))[\boldsymbol{C_n}(\boldsymbol{x},\boldsymbol{\xi})]^{-1}(g(\boldsymbol{\xi}+\boldsymbol{u}(\boldsymbol{\xi},t),t) - f(\boldsymbol{\xi})) \end{aligned} \tag{3.3}$$

where $[\boldsymbol{C_n}(\boldsymbol{x},\boldsymbol{\xi})]$ denotes the covariance matrix of gray level noise for pixels $\boldsymbol{x}$ and $\boldsymbol{\xi}$. In this expression $\Omega$ denotes the ROI. Although seldom used, it can be shown that this norm is the best suited one. At convergence the residual $(g(\boldsymbol{x}+\boldsymbol{u}(\boldsymbol{x},t),t) - f(\boldsymbol{x}))$ should be a statistically representative sampling of the noise for which the covariance has been computed.

Assuming that acquisition noise is Gaussian and white induces that the covariance matrix $[\boldsymbol{C_n}(\boldsymbol{x},\boldsymbol{\xi})]$ is equal to $\gamma_f^2[\delta(\boldsymbol{x},\boldsymbol{\xi})]$, where $[\delta(\boldsymbol{x},\boldsymbol{\xi})]$ is the Kronecker delta matrix, and $\gamma_f$ the standard deviation (expressed in gray levels) of noise. Equation (3.4) then reduces to the sum of squared differences between the deformed image corrected by the measured displacement $\boldsymbol{u}(\boldsymbol{x},t)$ and the reference image (written for each time $t$ independently)

$$\chi^2_f(t) = \frac{1}{2\gamma_f^2 N_\Omega}\sum_{\Omega}((g(\boldsymbol{x}+\boldsymbol{u}(\boldsymbol{x},t),t) - f(\boldsymbol{x}))^2 \tag{3.4}$$

that is minimized with respect to the sought displacement fields $\boldsymbol{u}(\boldsymbol{x},t)$. $N_\Omega$ denotes the area in terms of the number of pixels the ROI contains. Noise is assumed to affect each image independently (including the reference one, which is responsible for the factor of $1/2$ coming as a multiplicative term in this functional).

In the following, the noise amplitude $\gamma_f$ will be considered as constant in space and time, and independent of gray level so that it could have been dropped from the expression of the functional $\chi^2_f(t)$ without consequences. However, it is introduced here [67, 64] so that at optimal registration, acquisition noise will be responsible for an expectation value of this functional equal to unity. A similar strategy will be followed in the sequel. Let us note that although time (indexing an image series) is an important aspect of identification

because it is crucial to access the different stages of loading that will be sensitive to different features of the constitutive law, this section presents tools that are relative to image pairs. Treating a complete image series will simply consist of summing the different contributions of image pairs. Thus, the time parameter $t$ is dropped for the remainder of this section to simplify the notations.

The displacement field is decomposed onto a basis of functions $\boldsymbol{\psi}_n(\boldsymbol{x})$ that is selected at will

$$\boldsymbol{u}(\boldsymbol{x}) = \sum_n u_n \boldsymbol{\psi}_n(\boldsymbol{x}) \tag{3.5}$$

where $\boldsymbol{\psi}_x$ are shape functions in the present case, and $u_n$ the unknown degrees of freedom. Ideally, the number of these fields should be kept as small as possible (to reduce uncertainty on their amplitude) yet large enough to capture the anticipated variety or heterogeneity of the actual experimental field. The minimization of $\chi^2_f$ is achieved by successive linearizations and corrections, using Gauss-Newton scheme

$$[\boldsymbol{M}]\{\delta\boldsymbol{u}\} = \{\boldsymbol{b}^{(i)}\} \tag{3.6}$$

where $[\boldsymbol{M}]$ is the DIC matrix, $\{\delta\boldsymbol{u}\}$ the vector gathering all increments of measured displacement amplitudes, and $\{\boldsymbol{b}^{(i)}\}$ the residual column vector at iteration $i$. The DIC matrix reads

$$M_{ij} = \sum_\Omega \left(\boldsymbol{\nabla} f(\boldsymbol{x}) \cdot \boldsymbol{\psi}_i(\boldsymbol{x})\right) \left(\boldsymbol{\nabla} f(\boldsymbol{x}) \cdot \boldsymbol{\psi}_j(\boldsymbol{x})\right) \tag{3.7}$$

and the right hand side term

$$b_i = \sum_\Omega \left(\boldsymbol{\nabla} f(\boldsymbol{x}) \cdot \boldsymbol{\psi}_i(\boldsymbol{x})\right) \left(f(\boldsymbol{x}) - g(\boldsymbol{x} + \tilde{\boldsymbol{u}}(\boldsymbol{x}))\right) \tag{3.8}$$

where $\tilde{\boldsymbol{u}}(\boldsymbol{x})$ is the current estimate of the displacement field.

The DIC matrix is of importance when evaluating the covariance matrix of the measured degrees of freedom due to image noise, $[\boldsymbol{C_U}] = \langle \{\delta\boldsymbol{u}\} \otimes \{\delta\boldsymbol{u}\} \rangle$ [68, 67]

$$[\boldsymbol{C_U}] = 2\gamma_f^2 [\boldsymbol{M}]^{-1} \tag{3.9}$$

When a specific random pattern is known then the above equations are to be used. In the present case, the design is to be done without a specific speckle pattern in hand. For this reason, it is useful to resort to a "mean-field" assumption for the estimation of the DIC matrix $[\boldsymbol{M}]$, and derived quantities such as the covariance matrix of the kinematic degrees of freedom $[\boldsymbol{C_U}]$. This approximation is based on a scale separation of shape functions $\boldsymbol{\psi}(\boldsymbol{x})$ and random pattern $f(\boldsymbol{x})$ and their statistical independence. If the expectation value of the gray level gradient in the reference image, $G_f^2 = \langle (\boldsymbol{\nabla} f)^2 \rangle$, is introduced the mean-

field approximation of $[\boldsymbol{M}]$ reads

$$M_{ij} \approx \frac{G_f^2}{2} \sum_{\Omega} \boldsymbol{\psi}_i(\boldsymbol{x}) \cdot \boldsymbol{\psi}_j(\boldsymbol{x}) \tag{3.10}$$

Many choices of basis fields $\boldsymbol{\psi}_n$ are possible within the above framework of global DIC. Two specific choices will be considered hereafter. First, a finite element representation of the displacement [68]. For instance, a triangular mesh with finite elements that are three-node triangles with linear displacement interpolation (T3) is the simplest and offers both flexibility for meshing and robustness for DIC. Second, FEMU, which is detailed in the next subsection, can be transported into the global DIC framework with basis functions that are computed numerically from parameter sensitivity fields [64]. This procedure, which is called integrated DIC (or IDIC), is detailed after the FEMU method.

The output of this first processing of images is *i)* a series of displacement fields (one for each acquired image past the reference one) as amplitudes $\{\boldsymbol{u}(t)\}$ of the chosen kinematic basis and *ii)* the complete covariance matrix $[\boldsymbol{C_U}]$ due to noise. (Note that the latter is independent of time.) It will be the input of the following identification procedure.

### Weighted FEMU

FEMU is a classical identification strategy that is based on the minimization of the differences between measured quantities (*i.e.,* forces and displacements where the latter ones are obtained from DIC analyses) on the one hand, and the corresponding quantities that are computed from a numerical simulation exploiting a constitutive model and boundary conditions of Dirichlet type extracted from the DIC analysis. One key feature needed to obtain the most reliable estimate is to weigh the used information according to its value. This weight is coming from the covariance matrix of the measurement.

Weighted displacement-based Finite Element Model Updating (FEMU-U) consists of computing the set of (dimensionless) constitutive parameters, $\{\boldsymbol{p}\}$, that minimizes $\chi^2_U$ [69, 64]

$$\chi^2_U = \frac{1}{N_U} \{\boldsymbol{u}_m - \boldsymbol{u}_c\}^t [\boldsymbol{C_U}]^{-1} \{\boldsymbol{u}_m - \boldsymbol{u}_c\} \tag{3.11}$$

where $\chi^2_U$ is the weighted squared differences between measured, $\{\boldsymbol{u}_m\}$, and computed, $\{\boldsymbol{u}_c\}$, nodal displacements and $N_U$ the total number of kinematic degrees of freedom. Once again, the prefactor has been chosen so that, at convergence, noise in the measured displacement should, by itself, endow $\chi^2_U$ with a unitary value. Because the displacement field has generically a nonlinear behavior with respect to the constitutive parameters, an iterative scheme is implemented for the minimization of $\chi^2_U$ with respect to $\{\boldsymbol{p}\}$

$$\{\delta \boldsymbol{p}\}^{(i+1)} = \left( ([\boldsymbol{S}_U]^{(i)})^t [\boldsymbol{C_U}]^{-1} [\boldsymbol{S}_U]^{(i)} \right)^{-1} [\boldsymbol{S}_U]^{(i)} [\boldsymbol{C_U}]^{-1} \{\boldsymbol{u}_m - \boldsymbol{u}_c^{(i)}\} \tag{3.12}$$

where $[\boldsymbol{S}_U]^{(i)}$ is defined as the displacement sensitivity matrix with respect to material parameters $\{\boldsymbol{p}\}$

$$[\boldsymbol{S}_U]^{(i)} = \frac{\partial\{\boldsymbol{u}_c^{(i)}\}}{\partial\{\boldsymbol{p}\}} \tag{3.13}$$

that is expressed in pixels as the parameters $\{\boldsymbol{p}\}$ have been chosen dimensionless.

At convergence, the displacement sensitivity matrix does not depend any longer on the iteration number and hence, in the following, the index $(i)$ will be omitted whenever one does not refer to the practical numerical implementation where sensitivities have to be updated through iterations as the constitutive parameters are evolving. In particular, assuming that the noise level is small, the linearized relationship is used between the increments in $\{\boldsymbol{p}\}$ and the remaining discrepancy $\{\boldsymbol{u}_m - \boldsymbol{u}_c\}$ at convergence to interpret the displacement difference as the fluctuation in measured displacement induced by noise $\{\delta\boldsymbol{u}\}$. The resulting $\{\delta\boldsymbol{p}\}$ will be nothing but the fluctuating part of the identified parameters due to noise. The expectation value of $[\boldsymbol{C}_{\boldsymbol{p}}^{\boldsymbol{U}}] = \langle\delta\boldsymbol{p}\otimes\delta\boldsymbol{p}\rangle$ is the corresponding covariance matrix that contains the full characterization of the statistical variability (within the present framework of Gaussian noise and small perturbations).

Using the expression of the covariance of the displacement field from global DIC, Equation (3.12) at convergence becomes

$$\{\delta\boldsymbol{p}\} = 1/(2\gamma_f^2)[\boldsymbol{H}_U]^{-1}[\boldsymbol{S}_U][\boldsymbol{M}]\{\delta\boldsymbol{u}\} \tag{3.14}$$

where the Hessian $[\boldsymbol{H}_U]$ is introduced

$$[\boldsymbol{H}_U] = [\boldsymbol{S}_U]^t[\boldsymbol{C}_{\boldsymbol{U}}]^{-1}[\boldsymbol{S}_U] = 1/(2\gamma_f^2)[\boldsymbol{S}_U]^t[\boldsymbol{M}][\boldsymbol{S}_U] \tag{3.15}$$

The covariance in the constitutive parameters due to the image noise is expressed as [64]

$$[\boldsymbol{C}_p^U] = [\boldsymbol{H}_U]^{-1} \tag{3.16}$$

The reaction forces may also be measured and compared with the computed resultants, which themselves incorporate *i)* a constitutive law whose parameters will at convergence be adjusted to those of the material to be identified, and *ii)* displacement boundary conditions that are provided by DIC measurements on the boundary. Thus, the same approach is followed with the reaction forces for which $\chi_F^2$ is minimized

$$\chi_F^2 = \frac{1}{N_F}\{\boldsymbol{F}_m - \boldsymbol{F}_c\}^t[\boldsymbol{C}_{\boldsymbol{F}}]^{-1}\{\boldsymbol{F}_m - \boldsymbol{F}_c\} \tag{3.17}$$

where $N_F$ is the number of load cells, $\{\boldsymbol{F}_m\}$ the measured forces, $\{\boldsymbol{F}_c\}$ the computed reaction forces with respect to the chosen material parameter set, $[\boldsymbol{C}_{\boldsymbol{F}}]$ the covariance matrix

of the measured loads (in the present case it is assumed that the load measurements are uncorrelated so that $[\boldsymbol{C_F}] = \gamma_F^2[\boldsymbol{I}]$. However, it is assumed that the load uncertainty is proportional to the magnitude of the load, $\gamma_F^2 = \rho_1^2|F|^2$. Moreover, it is easy at this stage to incorporate a minimum measurement uncertainty for the load cells by including an additional noise term whose variance $\rho_0^2$ is independent of the load level. This practically disqualifies all measurements of forces below $F_{min} = \rho_0/\rho_1$. Thus, it is assumed that (Chapter 4)

$$\gamma_F^2 = \rho_1^2|F|^2 + \rho_0^2 \tag{3.18}$$

The minimization of $\chi_F^2$ leads to the variation of the identified set of material parameters

$$\{\delta \boldsymbol{p}\}^{(i+1)} = \left(([\boldsymbol{S}_F]^{(i)})^t[\boldsymbol{S}_F]^{(i)}\right)^{-1}[\boldsymbol{S}_F]^{(i)}\{\boldsymbol{F}_m - \boldsymbol{F}_c^{(i)}\} \tag{3.19}$$

where

$$[\boldsymbol{S}_F]^{(i)} = \frac{\partial\{\boldsymbol{F}_c^{(i)}\}}{\partial\{\boldsymbol{p}\}} \tag{3.20}$$

are the reaction force sensitivities.

Using the same analogy between the algorithmic solution to the problem and the small perturbation computation of the effect of noise, the covariance matrix of the identified parameters with respect to the reaction forces reads

$$[\boldsymbol{C}_p^F] = [\boldsymbol{H}_F]^{-1} \tag{3.21}$$

where $[\boldsymbol{H}_F] = [\boldsymbol{S}_F]^t[\boldsymbol{C}_F]^{-1}[\boldsymbol{S}_F] = \gamma_F^{-2}[\boldsymbol{S}_F]^t[\boldsymbol{S}_F]$ is the reaction force Hessian.

The identification based on the *combined* displacement fields and reaction forces is achieved by minimizing the global functional $\chi_{UF}^2$ [64]

$$\chi_{UF}^2 = \frac{N_U}{N_U + N_F}\chi_U^2 + \frac{N_F}{N_U + N_F}\chi_F^2 \tag{3.22}$$

where the displacement and reaction force functionals have been introduced in Equations (3.11) and (3.17) respectively. The reason for the specific weight of the two functionals originates from a Bayesian foundation for using a weighted quadratic difference including noise covariance. The underlying hypothesis is that the noise is Gaussian and remains so at all stages of its manifestation. The quadratic form is in fact the argument of the exponential in this Gaussian probability distribution. The additivity of the functionals is the counterpart of the statistical independence of the two measurements (*i.e.,* load and images), which implies that probabilities are to be multiplied. The chosen normalization by the noise amplitude in all functionals $\chi$ considered up to now guarantees that no additional prefactors are to be considered herein. Consistently, if only noise is present (*i.e.,* no model error), the expectation value of $\chi_{UF}^2$ amounts to unity.

The minimization leads to the iterative computation of the parameter increment $\{\delta \boldsymbol{p}\}^{(i)}$

$$\{\delta \boldsymbol{p}\}^{(i+1)} = [\boldsymbol{H}_{UF}]^{-1} \left( \frac{1}{2\gamma_f^2} [\boldsymbol{S}_U][\boldsymbol{M}](\{\boldsymbol{u}_m\} - \{\boldsymbol{u}_c\}^{(i)}) + \frac{1}{\gamma_F^2} [\boldsymbol{S}_F](\{\boldsymbol{F}_m\} - \{\boldsymbol{F}_c\}^{(i)}) \right) \tag{3.23}$$

where the global (*i.e.,* kinematic and static) Hessian is considered $[\boldsymbol{H}_{UF}] = ([\boldsymbol{H}_U] + [\boldsymbol{H}_F])$. The covariance matrix of the identified parameters becomes

$$[\boldsymbol{C}_{\boldsymbol{p}}^{UF}] = \langle \{\delta \boldsymbol{p}\} \otimes \{\delta \boldsymbol{p}\} \rangle = [\boldsymbol{H}_{UF}]^{-1} \tag{3.24}$$

The above sections have underlined the similarity of principles at play for extracting information with the least uncertainty from noisy data, both for DIC moving from images to displacement fields, and FEMU going from displacement fields (and load measurements) to material parameters. In this two-step process, one may note that displacement data are only an intermediate quantity, whose computation may imply constraints (*e.g.,* coarse mesh for DIC to be well-conditioned) that are not ideally suited to FEMU. It is thus desirable to merge these two processes into one. This is known as Integrated-DIC, or IDIC, and is now presented.

### Integrated DIC (IDIC)

Integrated digital image correlation (IDIC) is a global DIC technique that relies on a mechanical choice for the measured displacement field. It allows the user to perform the measurement and identification of the sought parameters in only one step. The displacement field is approximated as

$$\boldsymbol{u}(\boldsymbol{x}, t, \{\boldsymbol{p}\}) = \boldsymbol{u}(\boldsymbol{x}, t, \{\boldsymbol{p}\}^{(i)}) + \left[ \frac{\partial \boldsymbol{u}}{\partial \{\boldsymbol{p}\}^{(i)}} (\boldsymbol{x}, t, \{\boldsymbol{p}\}^{(i)}) \right] \{\delta \boldsymbol{p}\} \tag{3.25}$$

at iteration $i$, and the reaction forces

$$\{\boldsymbol{F}_c\}(t, \{\boldsymbol{p}\}) = \{\boldsymbol{F}_c\}(t, \{\boldsymbol{p}\}^{(i)}) + \left[ \frac{\partial \{\boldsymbol{F}_c\}}{\partial \{\boldsymbol{p}\}^{(i)}} (t, \{\boldsymbol{p}\}^{(i)}) \right] \{\delta \boldsymbol{p}\} \tag{3.26}$$

where the corrections $\{\delta \boldsymbol{p}\}$ to the sought parameters become the unknowns.

In theory, if the same mesh is used in DIC and for the computation of the sensitivity fields, there should be no difference between a two-step determination and an integrated procedure [64]. However, this is valid only for small amplitudes of noise and identical meshes. There are many cases where one can resort to a very fine mesh for the mechanical computation that would not be acceptable for DIC. This very fine mesh is not a problem with respect to IDIC as only a few search directions are chosen, and hence the modeling

error due to a coarse mesh can be avoided.

If the same mesh is used and the DIC matrix has been computed as $[\boldsymbol{M}]$, and residuals $\{\boldsymbol{b}\}$, IDIC simply consists of projecting the nodal displacement field onto the sensitivity fields. The Hessian becomes

$$[\boldsymbol{M}]_{IDIC} = [\boldsymbol{S}]^t[\boldsymbol{M}][\boldsymbol{S}] \tag{3.27}$$

and hence the amplitudes that can still be read as the increments in the constitutive parameters assume the following expression

$$\{\delta \boldsymbol{p}\}^{(i)} = [\boldsymbol{M}]^{-1}_{IDIC}[\boldsymbol{S}]^t\{\boldsymbol{b}\} \tag{3.28}$$

In the following, artificial (*i.e.,* computed) cases will be dealt with and hence one may question the added value of using IDIC. In fact it will mostly allow us to check that intermediate ill-conditioning does not interfere with the effect of noise to prevent convergence on the one hand, and it will lead to a realistic treatment of noise irrespective of its value. The level of noise indicated in Table 3.1 has been chosen as representative of actual experimental conditions.

**Table 3.1:** Displacement and load resolutions, and other characteristic features (Chapter 4)

| Quantity | $\rho_0$ | $\rho_1$ | $\gamma_f$ | $G_f = \langle(\boldsymbol{\nabla} f)^2\rangle^{1/2}$ | $a$ |
|---|---|---|---|---|---|
| Value | 2.5 N | $4\times10^{-4}$ | 233 gray levels | 3800 gray levels/pixel | 13.5 $\mu$m |

## 3.3 Elastic law with different parameterizations

For the identification involving multiple parameters, it is somewhat subjective to choose a given criterion to express the quality of identification by a single number to be optimized. It is desirable that all parameters be determined accurately. However when increasing the quality of one determination degrades that of another one, expressing a preference is difficult. Because of this freedom, one cannot pretend to provide a universal answer. The choice made herein is to focus on the "worst" determination, namely, the one that has the largest uncertainty due to noise, and the optimization is designed to reduce this uncertainty to its minimum. However, it is to be noted that even such a choice is fragile. A nonlinear transformation of parameters may lead to a different optimization criterion and hence a different answer.

It is important to note that changing parameters is simple and the above formalism may show that this change can be done before or after the identification, and get the very same result. The difficulty rather lies in the formulation of a relevant criterion. In many cases, an easy way out of this debate is to focus on a specific application (*e.g.,* a part with a given shape subjected to prescribed loads and for which one is interested in a deflection at a particular location) and for which one could reformulate an uncertainty criterion suited to the targeted application, which has no chance of coinciding with any other a priori choice.

The chosen objective is from now on to get the smallest level of the largest eigenvalue of the parameter covariance matrix. Equivalently, the largest level of the smallest eigenvalue of the Hessian is sought. Let us introduce the notation of $\{\lambda_U\}$ for the eigenvalues of the Hessian $[\boldsymbol{H}_U]$, and similarly $\{\lambda_F\}$, $\{\lambda_{UF}\}$ for $[\boldsymbol{H}_F]$ and $[\boldsymbol{H}_{UF}]$ respectively.

The choice of the constitutive law parameterization is important [66]. Two parameterizations will be considered in isotropic elasticity. One writing is based on the shear, $\mu$, and bulk, $K$, moduli. The stress-strain relationship reads

$$\boldsymbol{\sigma} = 2\mu(\boldsymbol{\epsilon} - \frac{1}{3}\mathrm{tr}(\boldsymbol{\epsilon})\boldsymbol{I}) + K\,\mathrm{tr}(\boldsymbol{\epsilon})\boldsymbol{I} \tag{3.29}$$

where $\boldsymbol{\sigma}$ and $\boldsymbol{\epsilon}$ are the stress and strain tensors, respectively, and $\boldsymbol{I}$ the identity tensor. Lamé coefficients are related to Young's modulus $E$ and Poisson's ratio $\nu$ by

$$E = \frac{9K\mu}{3K+\mu} \qquad \text{and} \qquad \nu = \frac{3K-2\mu}{2(3K+\mu)} \tag{3.30}$$

The values of the parameters in the example discussed in the following section are given in Table 3.2.

**Table 3.2:** Elastic parameters representative of 17-7 PH steel

| State | $E$ (GPa) | $\nu$ (—) | $K$ (GPa) | $\mu$ (GPa) |
|---|---|---|---|---|
| Reference ($p_0$) | 200 | 0.3 | 166.7 | 76.9 |
| Sensitivity analysis ($p$) | 204 | 0.306 | 175.3 | 78.5 |

Two optimizations will be studied. Because of the requirement to use a dimensionless set of parameters, the first chosen parameterization is based on $\{\log(E/E_0), \log(\nu/\nu_0)\}$ collectively denoted $\{\boldsymbol{p}\}$, and the second on $\{\log(K/K_0), \log(\mu/\mu_0)\}$ denoted $\{\boldsymbol{q}\}$. Here $E_0$, $\nu_0$, $K_0$ and $\mu_0$ are nominal values of the chosen parameters. The choice of using a log scale for the moduli is to favor *relative* uncertainties. Within this configuration the local

tangent map between the two bases reads

$$\left\{\begin{matrix}\frac{\mathrm{d}K}{K}\\ \frac{\mathrm{d}\mu}{\mu}\end{matrix}\right\} = \begin{bmatrix}1 & \frac{2\nu}{(1-2\nu)}\\ 1 & \frac{-\nu}{(1+\nu)}\end{bmatrix}\left\{\begin{matrix}\frac{dE}{E}\\ \frac{d\nu}{\nu}\end{matrix}\right\} \equiv [\boldsymbol{A}]\left\{\begin{matrix}\frac{dE}{E}\\ \frac{d\nu}{\nu}\end{matrix}\right\} \tag{3.31}$$

where $[\boldsymbol{A}]$ is the change of basis matrix. About a current point, the increments $\{\mathrm{d}\boldsymbol{q}\}$ and $\{\mathrm{d}\boldsymbol{p}\}$ are linearly related by the above $[\boldsymbol{A}]$ linear transformation. Figure 3.3 shows the incremental vectors $\{\mathrm{d}\boldsymbol{q}\}$ in the $\{\mathrm{d}\boldsymbol{p}\}$ plane. It is to be emphasized that these vectors are rotated and scaled differently so that the $\{\boldsymbol{p}\} \to \{\boldsymbol{q}\}$ mapping is not unitary (*i.e.,* norm of vectors will not be preserved). The consequences of this simple observation are now studied regarding the covariance matrices.

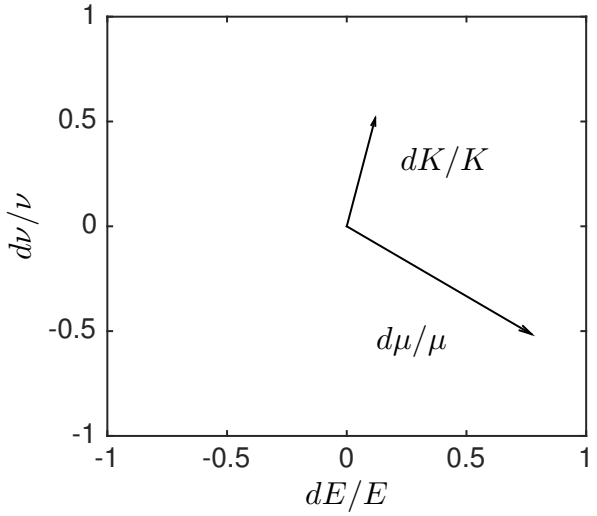


**Figure 3.3:** Local map of the $\{\log(K), \log(\mu)\}$ parameterization in the $\{\log(E), \log(\nu)\}$ basis

The covariance matrix in the first set of coordinates $\{\boldsymbol{p}\}$ may be diagonalized as

$$[\boldsymbol{C_p}] = \langle \{\delta\boldsymbol{p}\} \otimes \{\delta\boldsymbol{p}\} \rangle = [\boldsymbol{V}]^t [\boldsymbol{D}] [\boldsymbol{V}] \tag{3.32}$$

where $[\boldsymbol{V}]$ is the matrix gathering the eigenvectors and $[\boldsymbol{D}]$ the diagonal matrix of eigenvalues. In the second basis, the covariance matrix $[\boldsymbol{C_q}]$ reads

$$[\boldsymbol{C_q}] = \langle \{\delta\boldsymbol{q}\} \otimes \{\delta\boldsymbol{q}\} \rangle = [\boldsymbol{A}]^t [\boldsymbol{V}]^t [\boldsymbol{D}] [\boldsymbol{V}] [\boldsymbol{A}] \tag{3.33}$$

A singular value decomposition of $[\boldsymbol{A}]$ leads to the relationship $[\boldsymbol{A}] = [\boldsymbol{U}_1][\boldsymbol{S}][\boldsymbol{U}_2]$ where $[\boldsymbol{U}_1]$, $[\boldsymbol{U}_2]$ are unitary, and $[\boldsymbol{S}]$ symmetric and positive-definite. Thus the covariance ma-

trix becomes

$$[\boldsymbol{C_q}] = [\boldsymbol{U}_2]^t[\boldsymbol{S}][\boldsymbol{U}_1]^t[\boldsymbol{V}]^t[\boldsymbol{D}][\boldsymbol{V}][\boldsymbol{U}_1][\boldsymbol{S}][\boldsymbol{U}_2] \tag{3.34}$$

$$= [\boldsymbol{U}_2]^t[\boldsymbol{S}][\boldsymbol{W_1}]^t[\boldsymbol{D}][\boldsymbol{W_1}][\boldsymbol{S}][\boldsymbol{U}_2] \tag{3.35}$$

where $[\boldsymbol{W_1}]$ is also unitary. In the present case, the matrix $[\boldsymbol{A}]$ is equal to

$$[\boldsymbol{A}] = \begin{bmatrix} 1 & 1.5 \\ 1 & -0.23 \end{bmatrix} \tag{3.36}$$

and its singular decomposition leads to the three matrices

$$[\boldsymbol{U}_1] = \begin{bmatrix} -0.96 & -0.27 \\ -0.27 & 0.96 \end{bmatrix} \qquad [\boldsymbol{S}] = \begin{bmatrix} 1.85 & 0 \\ 0 & 0.93 \end{bmatrix} \qquad [\boldsymbol{U}_2] = \begin{bmatrix} -0.66 & 0.75 \\ -0.75 & -0.66 \end{bmatrix} \tag{3.37}$$

The criterion was chosen earlier as being the largest eigenvalue of the covariance matrix. It is to be stressed that a change of basis will not preserve such a criterion (it would if $[\boldsymbol{A}]$ were unitary). The largest eigenvalue of $[\boldsymbol{C_q}]$ is less than or equal to the largest eigenvalue of $[\boldsymbol{C_p}]$ times the square of the largest eigenvalue of $[\boldsymbol{S}]$ (*i.e.,* this is only a bound). If a criterion based on the uncertainty "volume" $\det([\boldsymbol{C_p}])$ were chosen, then a deterministic relationship could have been derived

$$\det([\boldsymbol{C_q}]) = \det([\boldsymbol{C_p}])\det([\boldsymbol{S}])^2 \tag{3.38}$$

suggesting a more favorable look to represent the results in the basis corresponding to the $\{\boldsymbol{p}\}$ parameterization rather than the $\{\boldsymbol{q}\}$ one, since $\det([\boldsymbol{S}])^2 \approx 3$.

This example shows that although one can freely move from one representation to another one without loss of information, the choice of a specific form criterion and *a fortiori* of its quantitative value may convey different appreciations of the quality of the identification. It is not suggested here to use a specific form of criterion, but simply to underline its consequences. In other terms, if the user desires to focus on one or several parameters, a suitable parameterization should be chosen. Therefore the corresponding experimental and identification procedures will result from the above considerations.

## 3.4 Geometry optimization

The following section now reports on the shape optimization of the cruciform sample whose geometry is shown in Figure 3.1 and designed for biaxial experiments. Furthermore, the triangular loading path presented in Figure 3.2 is applied. The constitutive law of the specimen is assumed to be elastic.

### 3.4.1 Analysis of an elastic case

The IDIC procedure is discussed assuming a linear isotropic elastic constitutive law based on the $\{\boldsymbol{p}\}$ set of parameters, namely, $p_1 = \log(E/E_0)$ and $p_2 = \log(\nu/\nu_0)$ where $E_0$ and $\nu_0$ are chosen as representative of 17-7 PH stainless steel [23] and listed in Table 3.2. The sensitivity fields are first discussed. They are obtained in all the sequel from a numerical finite difference based on a 2 % variation of the parameters (Table 3.2).

First, let us note that the Young's modulus sensitivity field $[\boldsymbol{S}_U]_E$ is equal to zero in that case. This is in accordance with the fact that Dirichlet boundary conditions are prescribed and no load information is used. A change in Young's modulus would only affect the load but not the displacement field for such a linear behavior. In contrast, the sensitivity fields related to the Poisson's ratio $[\boldsymbol{S}_U]_\nu$ whose horizontal component is shown in Figure 3.4 is nontrivial. This sensitivity field is computed for a geometry such that $r = 2$ mm and at the maximum amplitude loading with equi-biaxial tension (point $B$ of the loading path of Figure 3.2). Due to the fact that the thickness is uniform over the whole sample, the sensitivity is low close to the center of the sample, but interestingly it varies more strongly across the vertical arm of the specimen (*i.e.,* close to uniaxial tension).

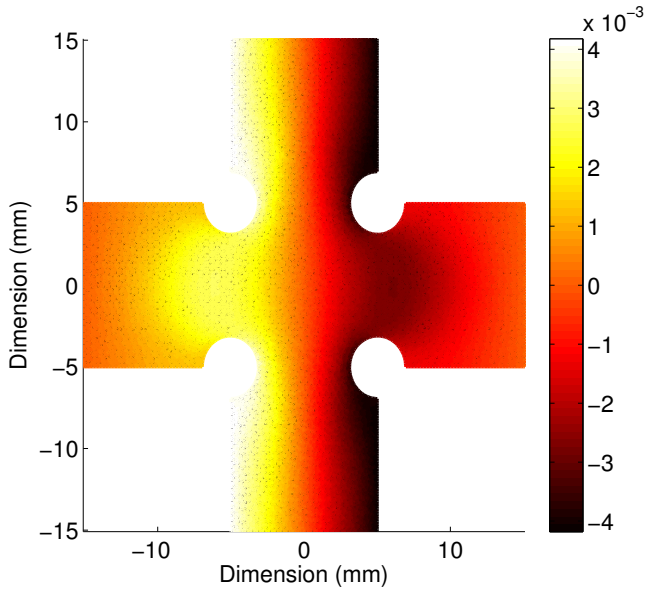


**Figure 3.4:** Sensitivity field $[\boldsymbol{S}_U]_\nu \cdot \boldsymbol{e}_1$ expressed in mm in the parameterization $\{\boldsymbol{p}\}$ related to Poisson's ratio

Using the second parameterization $\{\boldsymbol{q}\} = \{\log(K/K_0), \log(\mu/\mu_0)\}$, Figure 3.5 shows the horizontal component of the sensitivity fields $[\boldsymbol{S}_U]_K$ and $[\boldsymbol{S}_U]_\mu$ at point $B$. These fields are both non zero, as changing $K$ at fixed $\mu$ or $\mu$ at fixed $K$ does alter the Poisson's ratio. However, as only one degree of freedom matters, it is expected that $[\boldsymbol{S}_U]_K$, $[\boldsymbol{S}_U]_\mu$ and

$[\boldsymbol{S}_U]_\nu$ are all collinear

$$[\boldsymbol{S}_U]_K = a[\boldsymbol{S}_U]_\nu$$
$$[\boldsymbol{S}_U]_\mu = b[\boldsymbol{S}_U]_\nu \tag{3.39}$$

where $a$ and $b$ can be evaluated from the expression of matrix $[\boldsymbol{A}]$ (see Equation (3.31)) as $a = (A^{-1})_{21} \approx 0.58$ and $b = (A^{-1})_{22} \approx -0.58$.

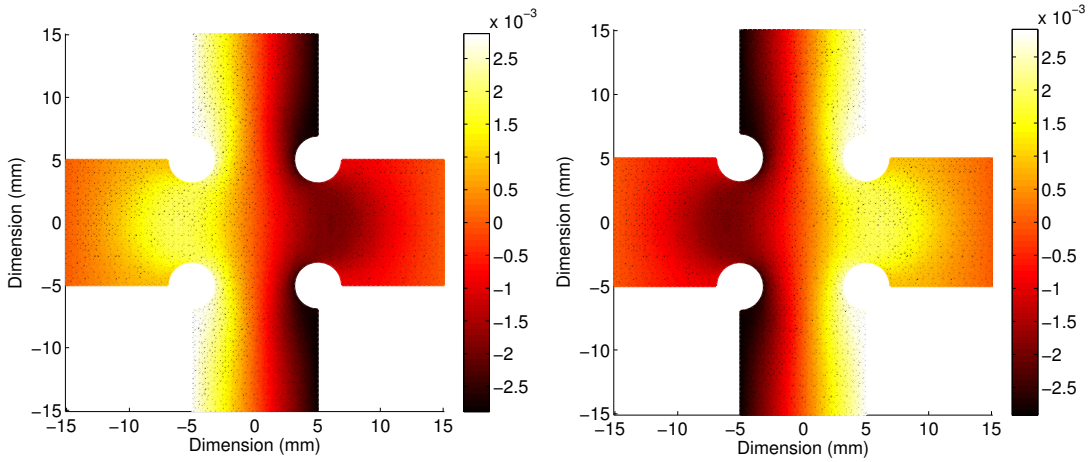


(a) (b)

**Figure 3.5:** (a) Horizontal component of the sensitivity field $[\boldsymbol{S}_U]_K$ relative to the bulk modulus and (b) of the sensitivity field $[\boldsymbol{S}_U]_\mu$ relative to the shear modulus at loading point $B$. The displacements are expressed in mm

Figure 3.6 shows the change of the only nonzero eigenvalue of the instantaneous Hessian along the loading path. Furthermore, this graph contains parabolas, of which two originate from O (OA and OB). This means that these two radial parts bring the same qualitative information, with an eigen value of the Hessian that scales as the square of the displacement amplitude (hence the parabolas). Along the AB path, the sensitivity fields do not preserve a fixed orientation through time, there is no simple relationship between instantaneous values and those of the radial parts of the load path, even though a single degree of freedom is sensitive.

Let us stress that this section illustrates the notion of sensitivity field through instantaneous loading stages. However, when performing an actual identification, the Hessian to be considered is the summation over time of the instantaneous Hessians, *i.e.,* over the entire loading path. Similarly right hand side members are to be summed over time.

Figures 3.6 and 3.7 show the level of the (nonzero) eigenvalues of instantaneous Hessians. It would be an exact property if the noise variance were constant, which is not true for the load uncertainty, but the deviation is almost negligible. The kinematic Hessian

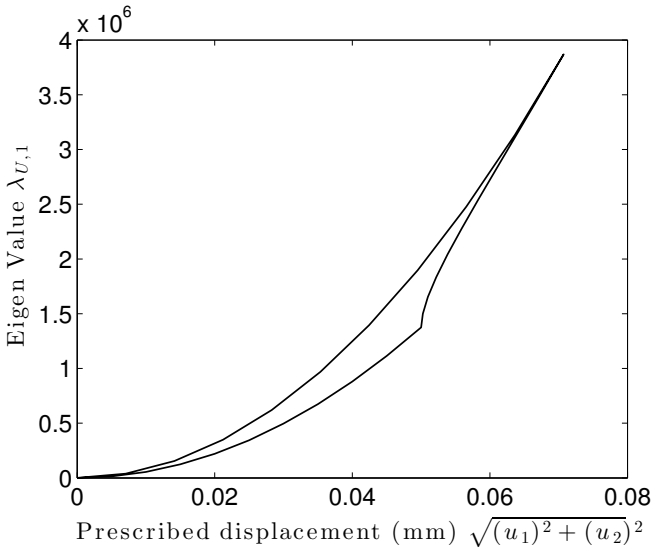


**Figure 3.6:** eigenvalue $\lambda_{U,1}$ of the Hessian $[\boldsymbol{H}_U]$ with the $\{\log(E/E_0), \log(\nu/\nu_0)\}$ parameterization. Point B corresponds to the right-top corner of the curve

$[\boldsymbol{H}_U]$ is evaluated at each step of the loading path. Figure 3.6 shows only the nonzero eigenvalue $\lambda_{U,1}$ of $[\boldsymbol{H}_U]$. The maximum level of $\lambda_{U,1}$ is reached for point *B*, but the behavior is different for the loading and unloading parts. The load dissymmetry reduces the value of $\lambda_{U,1}$. For an equivalent amplitude $\sqrt{U_1^2+U_2^2}$ the eigenvalue is lower for the asymmetric history.

Figure 3.7(a) shows the largest eigenvalue $\lambda_{F,1}$ related to $[\boldsymbol{H}_F]$. The maximum level of $\lambda_{F,1}$ is again reached for point *B*. However, a different behavior is observed for the second eigenvalue, $\lambda_{F,2}$ (Figure 3.7(b)). While the maximum level of the largest eigenvalue is reached for the maximum amplitude, the maximum level for $\lambda_{F,2}$ is reached for point *A*, *i.e.,* for the most asymmetric boundary condition. When the loads are equal in all branches of the sample, the second eigenvalue vanishes. Therefore, the equibiaxial loading history (in terms of loads *F*) only provides information for the dominant eigenvalue (whose eigenvector is essentially aligned with $\log(E)$). Furthermore, the different behaviors of the two eigenvalues originate from the two distinct material parameters. Last, let us stress that the ratio between the two eigenvalues related to $[\boldsymbol{H}_F]$ is in the range of a few hundreds. This important contrast leads to severe noise sensitivity issues when performing the inversion based on the static data only.

### 3.4.2 Geometry optimization in elasticity

Geometry optimization is now considered. Let us recall that the least uncertainty is sought, or with the criterion discussed in Section 3.3, the smallest eigenvalue of the Hes-

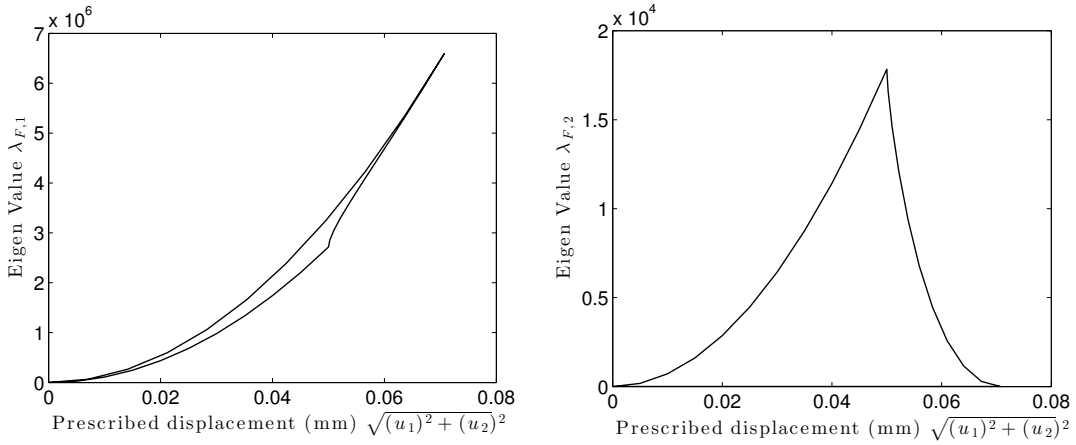


(a) (b)

**Figure 3.7:** Largest eigenvalue $\lambda_{F,1}$ (a) and smallest one $\lambda_{F,2}$ (b) of the Hessian $[\boldsymbol{H}_F]$ with the $\{\log(E/E_0), \log(\nu/\nu_0)\}$ parameterization

sian should be maximized. In order to be consistent it is important to ensure that the yield stress is not exceeded along the loading path. However, the highest stress depends critically on the geometry, namely, the smaller the fillet radius $r$ the higher the stress concentration. Hence it is decided to adjust the maximum displacement $d^*$ of the sample arms so that the maximum von Mises equivalent stress matches a lower bound on the yield stress, chosen to be $\sigma_y = 1300$ MPa, which is representative of 17-7 PH stainless steel in TH 1050 condition [23].

The eigenvalues of the kinematic, $[\boldsymbol{H}_U]$, and static, $[\boldsymbol{H}_F]$, Hessians, which are integrated over the whole loading history, for each studied geometry are displayed in Figure 3.8. As earlier noted in the purely kinematic case the Young's modulus cannot be determined, and hence $\lambda_{U,2} = 0$ (since $[\boldsymbol{H}_U]_{EE} = [\boldsymbol{H}_U]_{E\nu} = [\boldsymbol{H}_U]_{\nu E} = 0$). The other eigenvalue, $\lambda_{U,1}$, has a rather smooth variation with an optimal value at about $r = r^{opt} \approx 1.7$ mm for which the uncertainty on the Poisson's ratio is minimal.

Considering the reaction forces, Figure 3.8(b) shows the eigenvalues of the Hessian $[\boldsymbol{H}_F]$ with the fillet radius $r$. Both eigenvalues $\lambda_{F,1}$ and $\lambda_{F,2}$ display a similar behavior as that of $\lambda_{U,1}$ with a smooth maximum in the considered range. However, the maximum value of each eigenvalue is reached for a different radius, $r_1^{opt} = 1.7$ mm for $\lambda_{F,1}$ and $r_2^{opt} = 1.4$ mm for $\lambda_{F,2}$. If only reaction forces were considered in the identification, the criterion based on the largest value of the smallest eigenvalue would lead to a fillet radius $r_2^{opt}$.

It is worth noting that the largest eigenvalue takes a comparable value for the displacement-based and the load-based identification, stating that no obvious hierarchy is expected when using kinematic or static information. Rather they should complement each other. More-

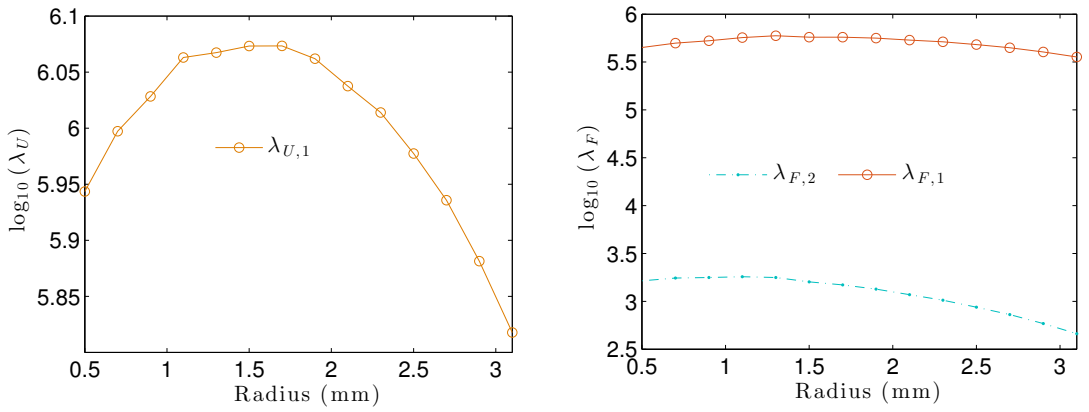


(a) (b)

**Figure 3.8:** Eigenvalue $\lambda_{U,1}$ of the Hessian $[\boldsymbol{H}_U]$ and $\lambda_{F,1}$ and $\lambda_{F,2}$ of the Hessian $[\boldsymbol{H}_F]$ in linear and isotropic elasticity for different fillet radii with the $\{\log(E/E_0), \log(\nu/\nu_0)\}$ parameterization

over, the influence of the loading history is not studied herein. However, it is worth noting that the latter would affect the eigenvalues, and thus, the value of the optimized fillet radius.

For a different parameterization $\{\log(K/K_0), \log(\mu/\mu_0)\}$, Figure 3.9 shows the eigenvalues of the two Hessians $[\boldsymbol{H}_U]$ and $[\boldsymbol{H}_F]$. As discussed above the second eigenvalue of $[\boldsymbol{H}_U]$ is null. Since a single eigenvalue remains, the optimal value of the fillet radius has to be identical to that observed with the $\{\boldsymbol{p}\}$ parametrization when dealing with $[\boldsymbol{H}_U]$. Considering the reaction forces, the behavior of the two eigenvalues is very close to that observed in Figure 3.8(b). Some slight changes of at most a factor of 4 could be anticipated due to the singular value decomposition of matrix $[\boldsymbol{A}]$.

Figure 3.10(a) shows the eigenvalues of the global Hessian $[\boldsymbol{H}_{UF}]$ using the $\{\log(E/E_0), \log(\nu/\nu_0)\}$ parameterization. The largest eigenvalue remains in the same range as previously observed with $[\boldsymbol{H}_U]$ and $[\boldsymbol{H}_F]$, $\lambda_1 \approx 10^6$. However, the most noticeable change lies in the second eigenvalue. From 0 with $[\boldsymbol{H}_U]$, and $10^3$ with $[\boldsymbol{H}_F]$ it now reaches about $3 \times 10^5$ when both static and kinematic data are combined at their best. This rise shows that these two sources of information are very complementary, and, schematically, if the load allows one to evaluate the Young's modulus, the DIC analysis captures the Poisson's ratio influence. The optimal fillet radius is again observed to be of the order $r^{opt} = 1.7 \pm 0.4$ mm.

Last, the influence of the parameterization can again be considered. Figure 3.10(b) is the equivalent for the $\{\boldsymbol{p}\}$ parameters of Figure 3.10(a) for $\{\boldsymbol{q}\}$. The comparison of both sub-figures shows that the $\{\log(E/E_0), \log(\nu/\nu_0)\}$ parameterization is more favorable since the lowest eigenvalue is higher compared with that obtained with $\{\log(K/K_0),$

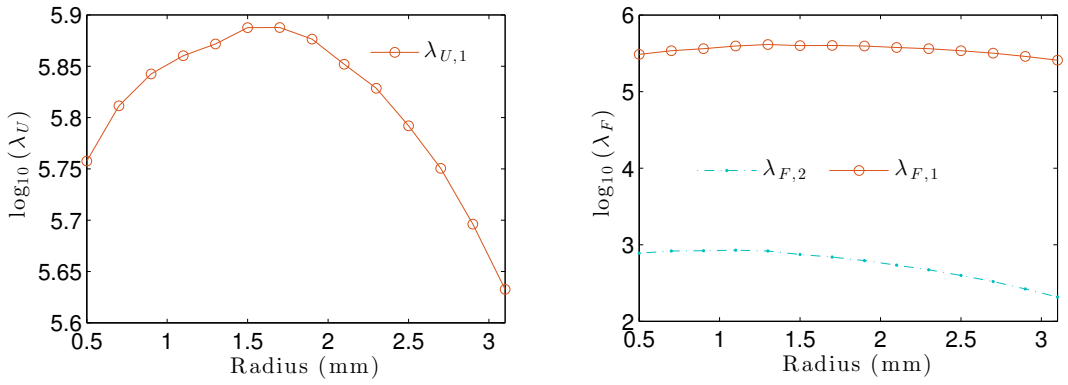


(a) (b)

**Figure 3.9:** Eigenvalue $\lambda_{U,1}$ of the Hessian $[\boldsymbol{H}_U]$ and $\lambda_{F,1}$ and $\lambda_{F,2}$ of the Hessian $[\boldsymbol{H}_F]$ in linear and isotropic elasticity for different fillet radii with the $\{\log(K/K_0), \log(\mu/\mu_0)\}$ parameterization. The second eigenvalue $\lambda_{U,2}$ is equal to zero

$\log(\mu/\mu_0)\}$ as could have been expected from the singular value decomposition of $[\boldsymbol{A}]$. This change is however marginal and simply shows the care with which the optimization criterion should be formulated. Fortunately, this change in the values of $\lambda$ does not affect much the optimal radius $r$, which remains of the order of $r^{opt} = 1.7 \pm 0.4$ mm.

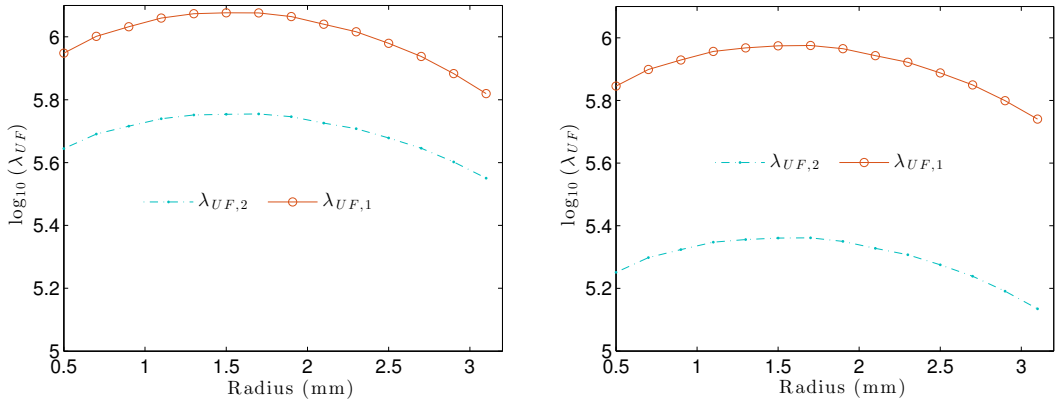


(a) $\{\log(E/E_0), \log(\nu/\nu_0)\}$ parameterization (b) $\{\log(K/K_0), \log(\mu/\mu_0)\}$ parameterization

**Figure 3.10:** Eigenvalues $\lambda_{UF}$ of Hessian $[\boldsymbol{H}_{UF}]$ with two different parameterizations

The above geometry optimization investigated a rather simple class with only one degree of freedom (*i.e.,* one fillet radius). The same principles can be applied to a larger class of variants. Practical restrictions may come from the computational cost of the study. The following subsection aims to illustrate an optimization procedure that allows a wider range of geometry variations to be considered at a modest additional cost.

### 3.4.3 Geometry optimization in elasticity with different fillets

The present section aims to investigate the influence of the four fillet radii and to propose a strategy to optimize their sizes. First, with all the fillet radii being equal an optimal value is obtained as shown previously. Second, the investigation is performed by only modifying three fillet radii with the same value and seeking the new optimal value while keeping one fillet radius equal to the previous optimal value. Then, the second fillet radius is also fixed with the new optimum value. This process is repeated until all the optimum fillet radii are found. The fillet radii are optimized in the trigonometric order from the top left corner. The same loading history is considered (Figure 3.2).

Figure 3.11 shows the eigenvalues $\lambda_{UF}$ of Hessian $[\boldsymbol{H}_{UF}]$ for the four optimization steps and for the $\{\log(E/E_0), \log(\nu/\nu_0)\}$ parameterization. The second optimization step does not strongly change the results and because less fillet radii are modified, the changes of the eigenvalues are less significant. Consequently, four identical fillet radii equal to $r = 1.7 \pm 0.4$ mm correspond to the optimal shape for the identification of elastic parameters.

### 3.4.4 Geometry optimization in elastoplasticity

Geometry optimization has been addressed up to now within the framework of linear elasticity. It has been emphasized that the entire optimization procedure as presented herein is transparent to the complexity of the parameters used in the modeling (although the cost of computing the sensitivity fields will be directly dependent on the sophistication of the chosen constitutive law). This statement also emphasizes that the "optimality" of a specimen geometry will never be universally optimal but only within a given framework. In this section, the initial geometry optimization (above shown to lead to an at least local optimum for a larger class of geometries) with a single degree of freedom (*i.e.,* four identical fillet radii) is reconsidered for an elastoplastic material. The chosen law is a standard one with linear kinematic hardening [70]

$$\dot{\boldsymbol{X}} = \frac{2}{3} C \dot{\boldsymbol{\epsilon}}_{pl} \tag{3.40}$$

where $C$ is a material parameter, $\dot{\boldsymbol{\epsilon}}_{pl}$ the plastic strain rate tensor, and $\boldsymbol{X}$ the back-stress. The yield surface $J_2(\boldsymbol{\sigma} - \boldsymbol{X}) = \sigma_0$ is defined such that $J_2$ is von Mises' equivalent stress and $\sigma_0$ the yield stress. The maximum amplitude prescribed displacement $d^*$ is defined such that the maximum equivalent plastic strain is equal to 10 %. The prescribed loading history is shown in Figure 3.2. The parameterization is identical to that chosen for the elastic case, namely, $\{\boldsymbol{q}\} = \{\log(E/E_0), \log(\nu/\nu_0), \log(\sigma/\sigma_0), \log(C/C_0)\}$. Table 3.3 gathers the reference values of the material parameters.

Figure 3.12 shows the eigenvalues of $[\boldsymbol{H}_{UF}]$ when the four fillet radii are equal. The two smallest eigenvalues have similar trends and values as the linear elastic case. The

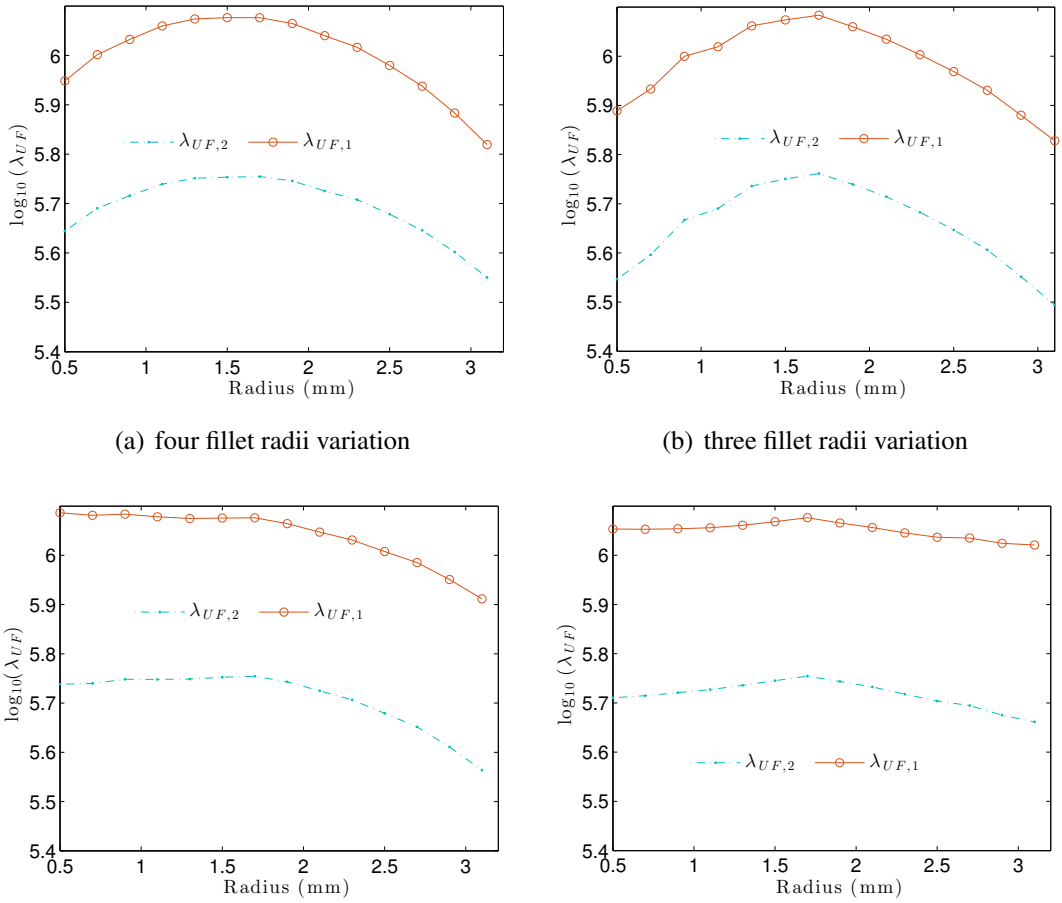


(a) four fillet radii variation

(b) three fillet radii variation

(c) two fillet radii variation

(d) one fillet radius variation

**Figure 3.11:** Eigenvalues $\lambda_{UF}$ of Hessian $[\boldsymbol{H}_{UF}]$ for the four optimization steps

**Table 3.3:** Value of the material parameters

| Parameter | $E$ | $\nu$ | $\sigma_0$ | $C$ |
|---|---|---|---|---|
| Value | 200 GPa | 0.3 | 1300 MPa | 10 GPa |

maximum level of the smallest eigenvalue $\lambda_{UF,4}$ is reached when $r = 1.5 \pm 0.3$ mm. This value is slightly less than that observed in elasticity. Although in the present case the optimal geometries for elasticity and elastoplasticity are quite close, it is worth emphasizing that different constitutive laws do not necessarily lead to the same optimal configuration.

Further, the fact that four material parameters are now investigated does not significantly alter the values of the smallest eigenvalues of the Hessian, even if the latter is slightly smaller than the linear elastic case at the initial step of the optimization. At the

end of the process their values are almost equal ($\log_{10}(\lambda_{min}^{elas}) \approx \log_{10}(\lambda_{min}^{plas}) \approx 5.8$). This result indicates that the elastic parameters are likely to be more difficult to identify than the hardening parameters. Consequently, an optimization only based on elastic parameters is already giving a good indication for the optimization. Its additional advantage lies in the fact that the simulations are much faster than for more complex constitutive equations.

Conversely, several orders of magnitude are observed between the four eigenvalues, which are significantly higher than in the elastic analysis (Figure 3.10). This observation shows that the hardening parameters are not as sensitive to noise as the elastic ones, which is to be expected since the strain levels (as displacement fluctuations) are more important in plasticity than in elasticity.

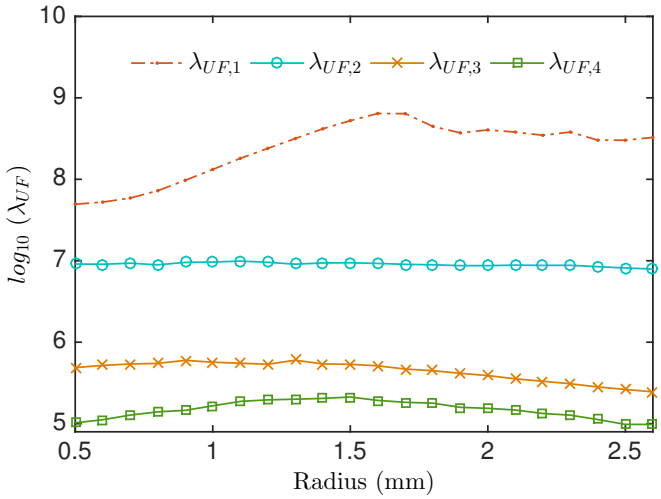


**Figure 3.12:** Eigenvalues $\lambda_{UF}$ of Hessian $[\boldsymbol{H}_{UF}]$ for an elastoplastic law with linear kinematic hardening when all the fillet radii are varying

### 3.4.5 Geometry optimization in elastoplasticity with different fillets

Figure 3.13(a) shows the eigenvalues of $[\boldsymbol{H}_{UF}]$ when one fillet radius is kept constant and equal to $r = 1.5$ mm (*i.e.,* the optimal case for four equal sizes). The other three fillet radii have the same value. The lowest eigenvalue becomes greater than what was achieved in the previous case. The optimal value is $r \approx 2.6$ mm for which $\lambda_{UF,3}$ and $\lambda_{UF,4}$ are identical. Last, it is noteworthy that several local minima are encountered. This originates from the elastoplastic kinematic behavior that influences the sensitivities that are no longer trivial and linear.

Last, Figure 3.13(b) shows the eigenvalues of $[\boldsymbol{H}_{UF}]$ when three fillet radii are kept constant. The maximum level of $\lambda_{UF,4}$ is achieved for a fillet radius equal to $r = 2.6$ mm

(at the intersection of $\lambda_{UF,4}$ and $\lambda_{UF,3}$). Furthermore, another maximum is reached for $r = 0.8$ mm. Contrary to elasticity, the present analysis shows that having various fillet radii is more favorable than having equal ones.

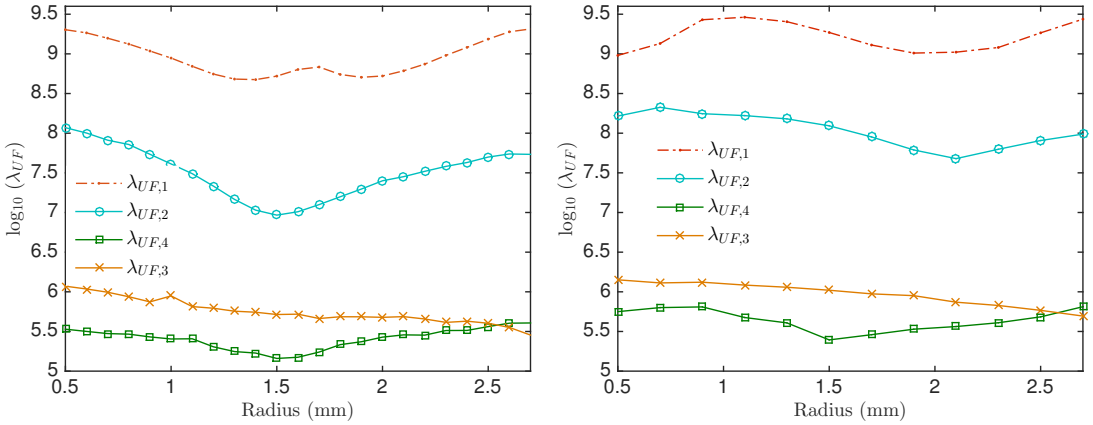


(a) one fillet radius variation

(b) three fillet radii variation

**Figure 3.13:** Eigenvalues $\lambda_{UF}$ of Hessian $[\boldsymbol{H}_{UF}]$ for the optimization steps 2 and 3

This result can be understood by analyzing the sensitivity fields. Figure 3.14 shows the sensitivity fields $[\boldsymbol{S}_U]_p \cdot \boldsymbol{e_1}$ for the four material parameters at loading point $B$. The sensitivity fields $[\boldsymbol{S}_U]_{\sigma_0}$ and $[\boldsymbol{S}_U]_C$ are not vanishing in the center of the specimen. This would occur in a fully symmetric geometry. In terms of levels, the two sensitivity fields are several orders of magnitude higher in plasticity in comparison with elasticity as was already observed when analyzing the eigenvalues of $[\boldsymbol{H}_{UF}]$ with four identical fillet radii (Figure 3.12).

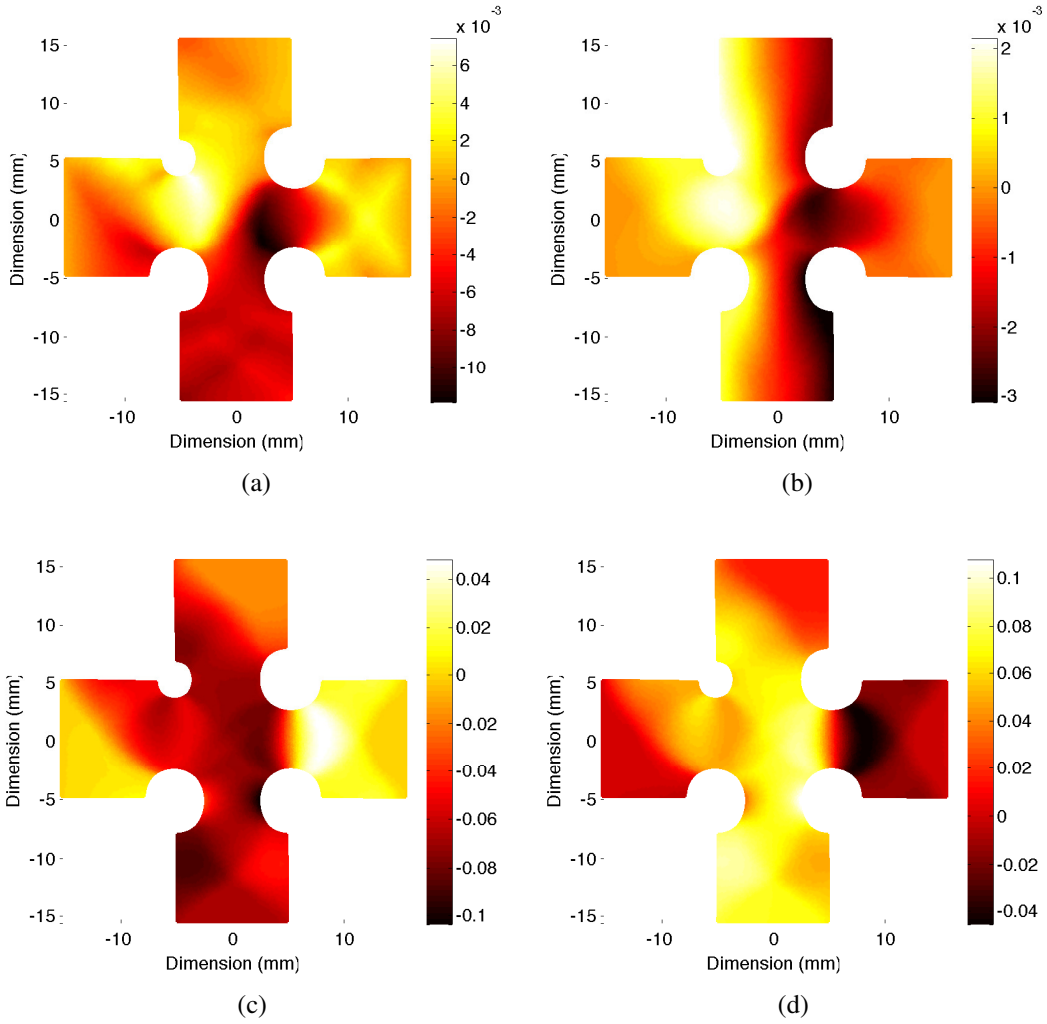


**Figure 3.14:** Sensitivity fields $[\boldsymbol{S}_U]_E \cdot \boldsymbol{e}_1$(a), $[\boldsymbol{S}_U]_\nu \cdot \boldsymbol{e}_1$(b), $[\boldsymbol{S}_U]_{\sigma_0} \cdot \boldsymbol{e}_1$(c), and $[\boldsymbol{S}_U]_C \cdot \boldsymbol{e}_1$(d) at point $B$. The displacements are expressed in mm

## 3.5 Conclusion

A complete identification procedure has been described, which starts from the acquisition of experimental data (*i.e.,* load levels and images) to the extraction of material parameters whereby uncertainties could be tracked all the way down to the identification step. It treats FEMU and DIC on the same footing and embraces both steps into a single one via IDIC. With this procedure in hand, the cruciform specimen geometry of a biaxial test could be optimized in such a way that the final uncertainty on the identified constitutive parameters is minimized.

The proposed procedure fully exploits the wealth of information provided by full-field measurements, and weighs this information according to its value, namely, its inverse un-

certainty. As emphasized in the introduction, the advent of full-field measurements allows to aim for the optimization directly to the final goal, and not to intermediate conditions (such as homogeneity) that were necessary for the exploitation of the test, as needed when strain gauges were to be used.

The optimization is based on the minimization of the worst uncertainty although different criteria may have been chosen. The present approach considers the entire metrological chain (*i.e.,* from the random pattern of DIC to finite element simulations for the computation of sensitivity fields) to account for the measurement resolution. As a result, the optimization is dedicated to a specific specimen and even more to its expected behavior. Different results are found for the two investigated laws. The optimization in linear elasticity leads to four identical fillet radii whereas the elastoplastic optimization leads to various fillet radii. However, the maximum level of the minimum eigenvalue is not significantly different between elastic and elastoplastic optimizations. The advantage of the former is that the computation time is significantly lower and provides a good first estimate (*i.e.,* 3 hours in comparison with 10-hour computation time on a PC with an 8-core Intel Xeon E5 processor). The result would presumably be different if the study would focus on a specific material parameter.

In the treated example, it is to be observed that sensitive regions are favored with respect to those where the strain field is the most uniform when the four fillet radii are identical. Such a marked difference implies that the here-derived optimized shape is significantly different from those obtained without resorting to full-field measurements. In particular the arms of the cruciform sample and the areas surrounding the fillet exhibit a greater sensitivity to the constitutive parameters than the center and hence are to be exploited. Conversely, when the radii are not identical, the central part of the sample is also contributing to the elastoplastic parameter sensitivity, which globally increases, thereby decreasing the overall sensitivity to noise.

Chapter 4 will exploit the optimized specimen geometry to assess the material mechanical properties in condition A (without heat treatment) of 17-7 PH. To that end, a new biaxial testing machine, mini-ASTREE, associated with an enhanced experimental environment is used.

# Chapter 4
# Integrated Digital Image Correlation applied to elasto-plastic identification in a biaxial experiment

Reproduced from: Morgan Bertin, François Hild, Stéphane Roux, Florent Mathieu, Hugo Leclerc and Patrick Aimedieu, *Integrated Digital Image Correlation applied to elasto-plastic identification in a biaxial experiment*, The Journal of Strain Analysis for Engineering Design, February 2016, (51) 118-131, doi: 10.1177/0309324715614759

## Abstract

The identification of the parameters of several constitutive laws is performed with the Integrated Digital Image Correlation (IDIC) technique in a biaxial experiment for a cruciform specimen made of stainless steel. The sought material parameters are assessed with the contribution of both reaction forces (from load sensors) and displacement fields (measured via digital image correlation). For each constitutive law a global residual quantifying the model error is assessed.

## 4.1 Introduction

The identification and validation of constitutive models are crucial issues for mechanical design. Challenges such as optimizing structures with respect to mass or using innovative materials, *e.g.,* high performance steels or composite materials push toward complex and multiaxial constitutive models. However, standard tests [71] related to the identification of material parameters require sample geometries for which the mechanical response must be homogeneous and uniaxial. Such limitations lead to numerous elementary tests even though more complex (*i.e.,* multiaxial) tests individually provide much more data. To characterize the latter ones, inverse identification methods based on full field measurements [59, 60] are developed. Since Hill [29] proposed to account for anisotropic plasticity, several identification strategies have been proposed. After briefly reviewing some of them, the paper seeks to solve the problematic of the identification of elastoplastic laws with Integrated Digital Image Correlation (IDIC).

First the simplest identification is performed by tuning the constitutive parameters with uniaxial strain-stress curves and least-squares fit [71]. However, this strategy does not provide internal checks of the accuracy of the resultant material parameters. Furthermore, it is assumed that the sample geometry behaves under statically determinate stress states [72]. This hypothesis is in opposition with the observed mechanical behaviors when complex and multiaxial experiments are performed.

Second approximately fifteen years after the appearance of the Finite Element Method, Kavanagh and Clough [58] proposed the Finite Element Model Updating (FEMU) technique. They focused their work on the characterization of nonlinear elastic materials. FEMU consists of minimizing the sum of squared residuals, a residual being the difference between the numerical and experimental displacement fields (*i.e.,* FEMU-U), strain data (*i.e.,* FEMU-ε), load levels (*i.e.,* FEMU-F), or combinations of the previous quantities (*e.g.,* FEMU-UF) [60]. This technique also provided new routes to tackle two main issues, namely, *i*) the internal validation of the identified parameters, and *ii*) the use of statically undeterminate stress conditions.

Some authors proposed strategies aiming to assess elastoplastic properties of aluminium alloys [73] and metals [74] while combining experimental load measurements and FE simulations. However, full-field measurement techniques were not used and only reaction forces were considered to solve the identification problem.

The advent of DIC as an experimental tool [75] has allowed elastic properties to be determined [76, 77, 41]. New strategies have been designed to tackle the increasing number of experimental data. Avril *et al.* [59] summarize several techniques based on full-field measurements to identify isotropic linear elastic properties. Some of these identification strategies have been extended to elastoplasticity and nonlinear mechanical behaviors. Lecompte *et al.* [78] identified Hill's parameters [29] with the FEMU technique under biaxial experiments. Conversely, Grédiac and Pierron [79] have used the virtual fields method. The constitutive error gap was also extended to plasticity [80]. Haddadi and Belhabib [81] have investigated the characterization of a hardening law on a heterogenous tensile test using the weighted-FEMU technique with both reaction force and strain field. Réthoré *et al.* [82] considered quasi-*3D* measurements with stereo-DIC to perform the identification of elasto-plastic constitutive parameters using the integrated digital image correlation technique. Schmaltz *et al.* [61] made use of stereo-DIC measurements and FEMU-U to identify a plastic law for four different biaxial cross-shaped geometries.

All the previous methods use as input the measured displacement fields or derived strain fields. However, these kinematic fields may be seen as parameterized by the sought material properties. Such observation enables the mechanical identification to be integrated within the digital image correlation procedure. This method is called Integrated-DIC [77, 62, 64]. The latter is a global DIC technique that relies on a mechanically driven choice for the kinematic basis. The measurement and identification of the sought param-

eters is thus performed in a single step. Since the identification is formulated at the pixel level, the process becomes mesh independent, provided the latter allows for a faithful description of the displacement fields as obtained from the mechanical modelling [83].

The same type of integrated strategy will be followed herein. In the sequel, a commercial FE package will be used in a non-intrusive way to estimate the displacement and load sensitivities to the sought material parameters. Consequently, any built-in or user-defined material model can be probed. This type of implementation makes the present work very generic. Consequently different constitutive postulates will be assessed hereafter (*e.g.,* linear and nonlinear kinematic hardening) to discuss model errors. The analysis will deal with a cruciform specimen in a biaxial experiment under load-controlled mode. The testing machine is a compact (2000 $cm^3$) biaxial device. The selected material is a precipitation-hardened stainless steel (*i.e.,* 17-7 PH grade [23]). It is used thanks to its excellent mechanical properties with respect to corrosion and fatigue [24, 65]. One key aspect of the present study is related to the small (*i.e.,* sub-millimetric) thickness of the tested sheet since it will be used to make bellows (Chapter 2) .

The chapter is divided into three main sections. In Section 4.2, the experimental tools and the theoretical background are presented. Integrated Digital Image Correlation (IDIC) and the chosen constitutive laws are also introduced. Section 4.3 deals with the experimental procedures. The sample geometry, the prescribed loads and the sources of uncertainties are assessed. Section 4.4 shows the identification results and a discussion based upon the identification residuals is proposed.

## 4.2 Experimental protocol

The experimental procedure utilizes an electromechanical testing machine, mini-ASTREE (Figure 4.1), and one digital camera with a telecentric lens. The machine prescribes arbitrary displacement and forces in two orthogonal directions, $\boldsymbol{e_1}$ and $\boldsymbol{e_2}$, with opposite actuators that can be controlled in a symmetric fashion so that the specimen center is motionless [84]. $F_1$ will denote the load amplitude applied by the two coupled actuators along direction $\boldsymbol{e_1}$, and $F_2$ for the other two coupled actuators. Biaxial compressive and tensile tests can be run with a load range $F_{1,2} \in [-2000; 2000]$ N. Furthermore the stroke rate varies from 30 $\mu$m/min to 5 mm/min. 16-bit gray scale images are captured with a pco.edge camera. The effective magnification is 13.5 $\mu$m per pixel or 74 pixel/mm.

The specimen is machined via Electrical Discharge Machining (EDM). Figure 4.2(a) shows the sample geometry. The holes in the four arms allow for the positioning of the sample in the grips. This geometry is different from those analyzed by Schmaltz *et al.* [61]. The machining process induces very small residual stresses in the specimen since no physical contact between the wire and the specimen is required. The sample is machined from a $300-\mu$m thick sheet made of precipitation hardened stainless steel

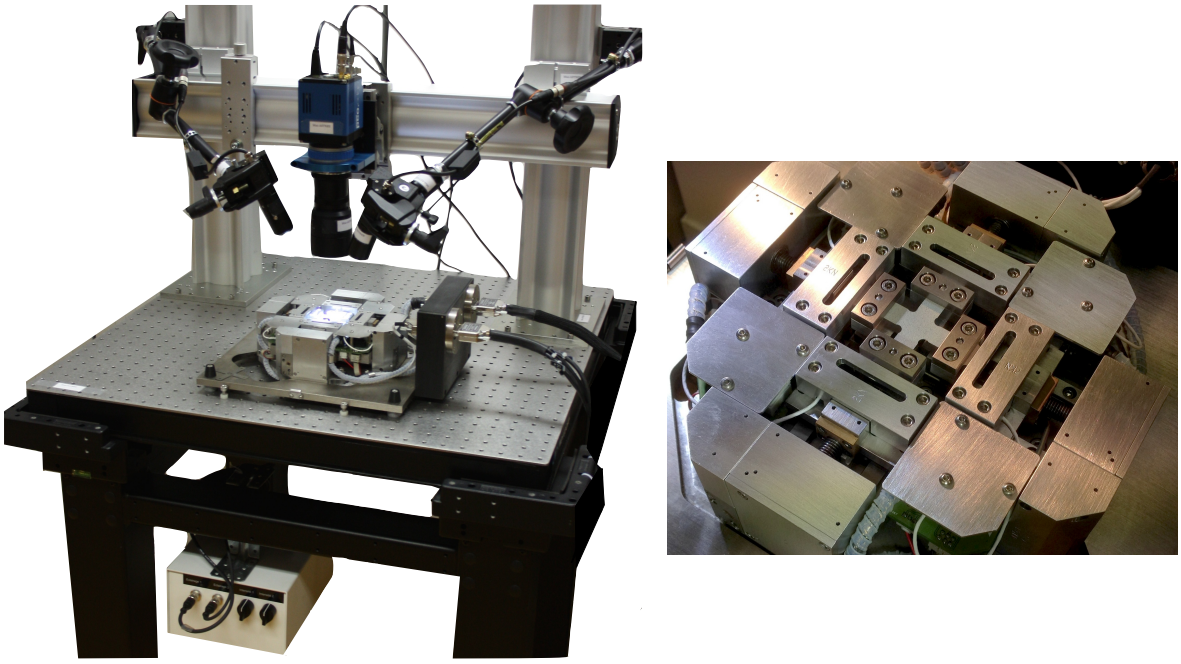

(a) (b)

**Figure 4.1:** (a) Mini-ASTREE and its environment and (b) the cross-shaped sample (center of picture) has been positioned after being patterned for DIC purposes

(*i.e.,* 17-7 PH grade), itself cut from a hot rolled 3-mm thick sheet. The chemical composition of the alloy is shown in Table 4.1. To avoid deflection during machining the sheet is maintained between two 3-mm thick aluminum sheets. The mechanical properties given by the manufacturer are the 0.2% yield stress ($\sigma_0^{0.2\%} = 300$ MPa) and Poisson's ratio ($\nu = 0.3$). The Young's modulus is not mentioned and its value is assumed to be equal to $E = 200$ GPa, which is the value of the untreated steel.

**Table 4.1:** Chemical composition of 17-7 PH grade [23]

| Composition | C | Mg | P | S | Si | Cr | Ni | Al |
|---|---|---|---|---|---|---|---|---|
| (wt %) | 0.09 | 1.00 | 0.040 | 0.030 | 1.00 | 16.00 - 18.00 | 6.50 - 7.75 | 0.75 - 1.50 |

The loading history may influence the identification results. A so-called triangular loading path is prescribed. Since the assessment of elastoplastic laws with kinematic hardening postulates is one of the present objectives, a cyclic loading history is prescribed. Figure 4.2(b) shows the $F_2$ versus $F_1$ cycles when the load amplitude is increased by 200 N between each of them. Furthermore, the load speed is constant and equal to $\dot{F}_1 = \dot{F}_2 =$ 3000 N/min when different from 0.

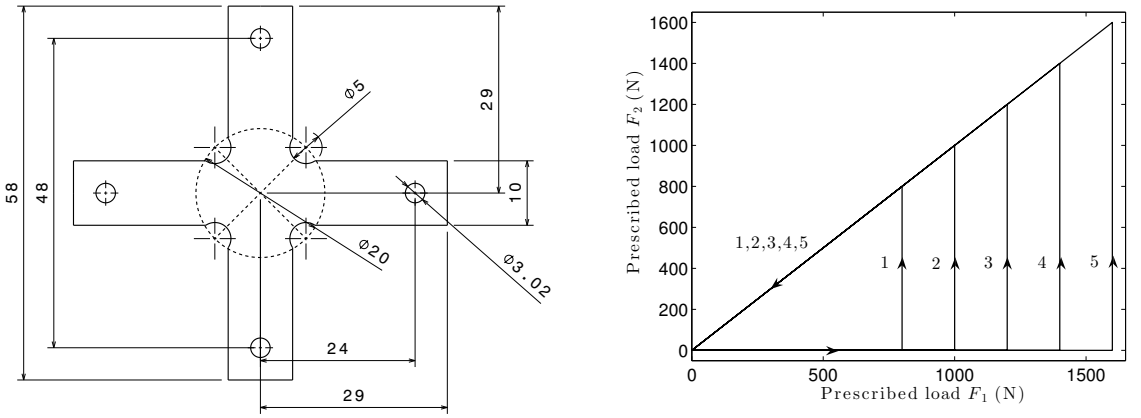


(a) (b)

**Figure 4.2:** (a) Specimen geometry (expressed in mm). (b) Prescribed loading history $F_2$ vs. $F_1$ consisting of successive triangles of increasing amplitudes, and where each triangle consists of a first increase of $F_1$ at $F_2 = 0$, followed by an equal increase of $F_2$ at fixed $F_1$, and finally and equibiaxial unloading down to $F_1 = F_2 = 0$

Figure 4.3(a) shows the Region Of Interest (ROI) that contains the specimen arms and the three-noded triangular mesh with linear interpolation (T3) used for DIC and IDIC purposes. Since FE-based DIC analyses are carried out, the mesh is constructed from the reference image. Consequently, it follows very faithfully the boundaries of the sample. Further, a small element size was selected (*i.e.,* 25 pixels) to capture the strain gradients as best as possible for regular T3-DIC. For the integrated approach, it could have been further refined [62, 83], but this option was not considered herein since both approaches are to be compared with the same underlying mesh. In the following the geometric coordinates shown in Figure 4.3(b) will be identical for any shown field.

## 4.3 Identification strategy

The numerical tools and the identification strategy are summarized hereafter. First, global DIC and Integrated-DIC are formulated. Second, the constitutive laws and their respective material parameters are introduced. Last, the numerical implementation of the identification scheme is briefly recalled.

### 4.3.1 Digital Image Correlation (DIC)

Global DIC will be used for comparison purposes with Integrated-DIC. Among various kinematic bases, finite element shape functions have initially been introduced to deal with regular meshes made of four-noded quadrilaterals [68]. It was subsequently generalized to

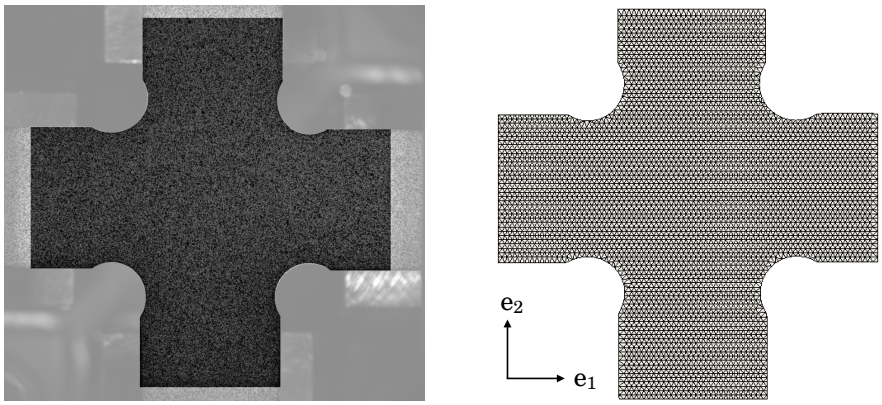


(a) (b)

**Figure 4.3:** (a) Reference image $f$ with the Region Of Interest (ROI) in dark and (b) mesh used for DIC and IDIC analyses (the characteristic element size is 25 pixel wide)

deal with unstructured meshes made of three-noded triangle (T3) elements [62]. DIC relies on the registration of an image $f$ in the reference configuration and a series of pictures $g$ in the deformed configurations. The problem consists of minimizing the global correlation residuals $\chi_f^2 = 1/N_t \sum_{t=1}^{N_t} \chi_f^2(t)$, which is the sum of squared differences between the deformed image corrected by the measured displacement $\boldsymbol{u}(\boldsymbol{x},t)$ and the reference image (written for each time $t$ independently) over the Region Of Interest

$$\chi_f^2(t) = \frac{1}{2\gamma_f^2 N_\Omega} \sum_\Omega ((g(\boldsymbol{x}+\boldsymbol{u}(\boldsymbol{x},t),t) - f(\boldsymbol{x}))^2 \tag{4.1}$$

with respect to the sought displacement fields $\boldsymbol{u}(\boldsymbol{x},t)$, where $\boldsymbol{x}$ is any considered pixel. In this expression $\Omega$ denotes the Region of Interest (ROI), $N_\Omega$ its area expressed in terms of the number of pixels it contains, $N_t$ the number of time steps, and $\gamma_f$ the standard deviation (expressed in gray levels) of the white noise assumed to affect each image independently (including the reference one, which is responsible for the factor of $1/2$ coming as a multiplicative term in this functional).

The displacement field is decomposed onto a basis of fields $\boldsymbol{\psi}_n(\boldsymbol{x})$ that is selected at will

$$\boldsymbol{u}(\boldsymbol{x}) = \sum_n u_n \boldsymbol{\psi}_n(\boldsymbol{x}) \tag{4.2}$$

where $\boldsymbol{\psi}_n$ are (vector) T3 shape functions in the present case ((*i.e.,* three noded triangles with a linear interpolation of displacements), and $u_n$ the unknown degrees of freedom. Ideally, the number of these fields should be kept as small as possible (*i.e.,* to reduce

the uncertainty[1] on their amplitude) yet large enough to capture the anticipated variety or heterogeneity of the actual experimental field. The minimization of $\chi_f^2$ is achieved by successive linearizations and corrections using Gauss-Newton scheme

$$[\boldsymbol{M}]\{\delta\boldsymbol{u}\} = \{\boldsymbol{b}\} \tag{4.3}$$

where $[\boldsymbol{M}]$ is the DIC matrix, $\{\delta\boldsymbol{u}\}$ the vector gathering all increments of measured displacement amplitudes, and $\{\boldsymbol{b}\}$ the residual column vector. In the present case, the minimization is performed independently for each considered time, *i.e.,* on $\chi_f^2(t)$.

### 4.3.2 Integrated DIC

The integration of the mechanical identification at the measurement step consists of choosing as the generalized degrees of freedom the sought parameters associated with a chosen constitutive law. Consequently, the kinematic basis is chosen as the set of sensitivity fields gathered in a matrix $[\boldsymbol{S}_U]$ [66] (see Chapter 3)

$$[\boldsymbol{S}_U] = \frac{\partial\{\boldsymbol{u}\}}{\partial\{\boldsymbol{p}\}} \tag{4.4}$$

where $\{\boldsymbol{u}\}$ is the computed nodal displacement vector, $\{\boldsymbol{p}\}$ the vector gathering the sought parameters in the computation via forward finite differences in the present case. One of the interests offered by an integrated approach is that the mesh size does not prevent the convergence of computations since the sought material parameters are significantly fewer in comparison with the degrees of freedom associated with the underlying FE discretization [62, 83]. Consequently, errors coming from a coarse mesh can be avoided (see Chapter 5).

If the same mesh is used, and the DIC matrix has been computed as $[\boldsymbol{M}]$ as well as the residual vector $\{\boldsymbol{b}\}$, the IDIC procedure simply consists of projecting the nodal displacement field onto the sensitivity fields [64]. One main difference with the previous T3-DIC procedure is that only one global minimization is performed in a single spatiotemporal analysis [86]. The identification of the sought parameters is achieved by solving iteratively until convergence linear systems

$$\{\delta\boldsymbol{p}\} = \frac{1}{2\gamma_f^2}[\boldsymbol{M}_{IDIC}]^{-1}[\boldsymbol{S}_U]^t\{\boldsymbol{b}\} \tag{4.5}$$

[1] 'The uncertainty [...] is a parameter, associated with the result of a measurement, that characterizes the dispersion of the values [...] [85].' In the present study, because the sole considered origin of uncertainty is that resulting from a Gaussian white noise, the uncertainty is quantified by the standard deviation of the concerned quantity.

where $[\boldsymbol{M}_{IDIC}] = 1/(2\gamma_f^2)[\boldsymbol{S}_U]^t[\boldsymbol{M}][\boldsymbol{S}_U]$ is the weighted kinematic Hessian. If this unique quantity $\chi_f^2$ is minimized, it can be shown that it is equivalent to a weighted FEMU-U procedure provided the noise level is small [64].

The applied load is also of importance for the identification because it provides an additional measured quantity, different in nature from the kinematics, and hence it contributes significantly to the identification and reduces the uncertainty of the determined material parameters. The reaction forces can also be computed. Thus, the same approach is followed with the reaction forces for which $\chi_F^2$ is minimized

$$\chi_F^2 = \frac{1}{N_F N_t}\{\boldsymbol{F}_m - \boldsymbol{F}_c\}^t[\boldsymbol{C}_{\boldsymbol{F}}]^{-1}\{\boldsymbol{F}_m - \boldsymbol{F}_c\} \tag{4.6}$$

where $\{\boldsymbol{F}_m\}$ are the measured reaction forces and $\{\boldsymbol{F}_c\}$ are the computed levels with respect to the chosen material parameter set, $[\boldsymbol{C}_{\boldsymbol{F}}]$ the covariance matrix of the measured loads (in the present case it is assumed that the load measurements are uncorrelated so that $[\boldsymbol{C}_{\boldsymbol{F}}] = \gamma_F^2[\boldsymbol{I}]$, and $N_F$ the number of load data.

It is assumed that the load uncertainty is proportional to the magnitude of the load, namely, $\gamma_F^2 = \rho_1^2|\boldsymbol{F}|^2$. Moreover, it is easy at this stage to incorporate a minimum measurement uncertainty for the load cells by including an additional noise term whose variance $\rho_0^2$ is independent of the load level. This practically disqualifies all measurements of forces below $F_{min} = \rho_0/\rho_1$. Thus, in the following it is assumed that

$$\gamma_F^2 = \rho_1^2|\boldsymbol{F}|^2 + \rho_0^2 \tag{4.7}$$

In the proposed procedure, the measured forces will be compared to the computed ones based on a numerical simulation that itself incorporates *i)* a constitutive law whose parameters will at convergence be adjusted to those of the material to be identified, and *ii)* Dirichlet (displacement) boundary conditions that are provided by the DIC measurements. The DIC measurement itself has an uncertainty that will induce an additional contribution, which is independent of the load magnitude as the DIC uncertainty is not dependent on the displacement amplitude, affecting computed forces rather than measured ones. However, as one will be interested in their differences, it is equivalent to transfer this additional force uncertainty on the measurement. The result is a term that cannot be distinguished from $\rho_0$. In practice, load cells are designed to have a dynamic range adapted to the geometry and mechanical properties of the specimen, and hence, the minimum and maximum values of these sensors are not limiting. In contrast, the identification of elastic properties requires sufficiently small strains to ensure the relevance of linear elasticity. In this case, the contribution of DIC uncertainty to the boundary conditions, and hence to the load level, is generally expected to provide a level for $\rho_0$ that may be limiting.

The minimization of $\chi_F^2$ leads to the variation of the identified set of material param-

eters

$$\{\delta \boldsymbol{p}\} = \frac{1}{\gamma_F^2}[\boldsymbol{H}_F]^{-1}[\boldsymbol{S}_{\boldsymbol{F}}]^t\{\boldsymbol{F}_m - \boldsymbol{F}_c\} \tag{4.8}$$

where $[\boldsymbol{H}_F] = \gamma_{\boldsymbol{F}}^{-2}[\boldsymbol{S}_{\boldsymbol{F}}]^t[\boldsymbol{S}_{\boldsymbol{F}}]$ is the static Hessian, and $[\boldsymbol{S}_{\boldsymbol{F}}] = \partial\{\boldsymbol{F}_c\}/\partial\{\boldsymbol{p}\}$ the reaction force sensitivities defined in the same way as the displacement field sensitivities (see Equation (4.4)). If $\chi_F^2$ is minimized alone, it corresponds to a load-based FEMU procedure, which is referred to as FEMU-F.

The identification based upon both observables, *i.e.,* displacement field *and* reaction force, is achieved by minimizing the global functional $\chi_I^2$

$$\chi_I^2 = \frac{N_\Omega}{N_\Omega + N_F}\chi_f^2 + \frac{N_F}{N_\Omega + N_F}\chi_F^2 \tag{4.9}$$

where the correlation and reaction force residuals have been introduced in Equations (4.1) and (4.6) respectively. The choice for the specific weight stems from a Bayesian foundation in the weighted quadratic difference including noise covariance. The minimization of the global residual (4.9) requires an iterative computation of the parameter increments $\{\delta \boldsymbol{p}\}$

$$\{\delta \boldsymbol{p}\} = [\boldsymbol{H}_{IDIC}]^{-1}\left(\frac{1}{2\gamma_f^2}[\boldsymbol{S}_U]^t\{\boldsymbol{b}\} + \frac{1}{\gamma_F^2}[\boldsymbol{S}_{\boldsymbol{F}}]^t\{\boldsymbol{F}_m - \boldsymbol{F}_c\}\right) \tag{4.10}$$

where the global (*i.e.,* kinematic and static) Hessian $[\boldsymbol{H}_{IDIC}]$ is the sum of kinematic $[\boldsymbol{M}_{IDIC}]$ and static $[\boldsymbol{H}_F]$ Hessians. The fact that images and load data are considered enables for the identification of the elastic parameters (*i.e.,* the Young's modulus in particular) contrary to what was performed by Schmaltz *et al.* [61].

The covariance matrix of the identified parameters reads

$$[\boldsymbol{C}_p^I] = \langle\{\delta \boldsymbol{p}\} \otimes \{\delta \boldsymbol{p}\}\rangle = [\boldsymbol{H}_{IDIC}]^{-1} \tag{4.11}$$

where $\langle\bullet\rangle$ is the mean value of $\bullet$. Another useful indicator is the correlation matrix (no index summation used)

$$(Cor_p)_{ij} = \frac{(C_p)_{ij}}{\sqrt{(C_p)_{ii}(C_p)_{jj}}} \tag{4.12}$$

The diagonal terms of the correlation matrix are equal to 1 since one parameter is perfectly correlated with itself and off-diagonal terms vary between -1 and 1.

### 4.3.3 Constitutive laws

The objective of the present work is to assess several parameters for three constitutive laws (*A*) linear and isotropic elasticity, and (*B*, *C*) two elastoplastic laws. The latter ones

correspond first to linear kinematic hardening with von Mises flow rule ($B$), and second to an exponential kinematic hardening ($C$) with von Mises flow rule. The total strain rate $\dot{\boldsymbol{\epsilon}}$ is written in terms of elastic and plastic strain rates $\dot{\boldsymbol{\epsilon}} = \dot{\boldsymbol{\epsilon}}_{el} + \dot{\boldsymbol{\epsilon}}_{pl}$ where $\dot{\boldsymbol{\epsilon}}_{el}$ is the elastic strain rate tensor and $\dot{\boldsymbol{\epsilon}}_{pl}$ the plastic strain rate tensor. The yield surface $J_2(\boldsymbol{\sigma} - \boldsymbol{X}) = \sigma_0$ is defined such that $J_2$ is von Mises' stress, $\boldsymbol{X}$ the back-stress, and $\sigma_0$ the yield stress. As a first approximation, a linear kinematic hardening model is chosen for the back-stress change [70]

$$\dot{\boldsymbol{X}} = \frac{2}{3} C \dot{\boldsymbol{\epsilon}}_{pl} \tag{4.13}$$

where $C$ is the hardening modulus. Under the assumption of exponential kinematic hardening, the back-stress becomes

$$\dot{\boldsymbol{X}} = \frac{2}{3} C \dot{\boldsymbol{\epsilon}}_{pl} - c \boldsymbol{X} \dot{p} \tag{4.14}$$

where $C$ and $c$ are material parameters, $p$ the cumulative plastic strain [87, 88].

### 4.3.4 Numerical implementation

The numerical procedure has been implemented in a C++framework, which computes the sensitivity fields from the finite element computations performed with the commercial code Abaqus [64]. The IDIC code provides to the latter the required input, namely, the finite element mesh, the current values of the material parameters, the chosen constitutive law and boundary conditions obtained from a DIC measurement. The parameterization is based on a log scale with a ratio between the current value of the parameter and its initial guess [69] (see also Chapter 3). It is defined such that the sought parameters in the new setting $\{\boldsymbol{q}\}$ are expressed from the initial basis as $\{\boldsymbol{q}\} = \log\{\boldsymbol{p}/\boldsymbol{p_0}\}$, where $\{\boldsymbol{p}\}$ is the vector gathering the values of the parameters and $\{\boldsymbol{p}_0\}$ their initial values. The procedure is considered to have converged when the change in the parameters reaches a chosen threshold

$$\|\{\delta \boldsymbol{q}\}\|_\infty \leq 10^{-4} \tag{4.15}$$

where $\|\{\bullet\}\|_\infty$ denotes the infinite norm of the vector $\{\bullet\}$. Finally, the numerical procedure uses a Levenberg-Marquardt regularization [89, 90], which is shown to be more robust than a pure Newton-based scheme [91, 73, 69] when seeking material parameters [90].

As proposed by Gras *et al.* [69], a regularization functional, namely $\chi_R$, is associated with the identification functional ($\chi_I$) to enable for the change of the sought parameters only if their corresponding sensitivities are higher than a specific bound. This regularization prevents meaningless identification when the influences of material parameters on

the observables are weak. $\chi_R$ is a convex function reaching its minimum equal to zero and reads

$$\chi_R^2 = \{q\}[C_q^R]^{-1}\{q\} \tag{4.16}$$

where $[C_q^R]$ is the covariance matrix of the material parameters. Because $\chi_I$, and $\chi_R$ are both dimensionless and normalized to one their summation is valid and the regularized functional becomes $\chi^2 = \chi_I^2 + \chi_R^2$. Finally, the regularization of the linear system reads

$$([H_{IDIC}] + \lambda^*[I])\{\delta q\} = \{b_{IDIC}\} - \lambda^*\{q\} \tag{4.17}$$

where $\lambda^*$ is the regularization parameter whose choice is performed to cancel out the influence of noise on the change of material parameters [69].

Most of the computational cost of such integrated procedures is associated with the computation of the various sensitivities, which each time requires an additional interrogation of the FE code. For the same number of iterations IDIC and FEMU procedures lead to very similar computation times [64]. In the present case, an analysis consisting of 365 pictures required 6 hours on a PC with an 8-core Intel Xeon E5 processor for the elastoplastic nonlinear kinematic hardening law (*i.e.,* five unknown parameters).

## 4.4 Identification results

This section presents the identification results and indicators of model errors. First, a resolution[2] analysis is carried out with an initial set of the sought parameters and the initial DIC solution. Second, the assessment of the material parameters is performed. Last, a discussion is conducted on the kinematic, static and global residuals.

### 4.4.1 Resolution analysis

This part aims to estimate *a priori* the procedure ability to perform an identification. The DIC measurement is used to prescribe in the FEM analysis the experimentally measured displacement (Dirichlet) boundary conditions and get the sensitivity fields. Table 4.2 gathers the initial values of the sought material parameters. For the computation of Hessians, the parameters are ranked in the same order except for the eigenvalues ranked from smallest to largest.

Load uncertainties are assessed for each iterations as discussed in Section 4.3.1 and the displacement uncertainty is evaluated since 10 images are acquired in the reference

[2] 'Resolution: smallest change in a quantity being measured that causes a perceptible change in the corresponding indication. [...] The resolution can depend on, for example, noise (internal or external) or friction.' [85]

**Table 4.2:** Initial value of the material parameters

| Parameter | $E$ | $\nu$ | $\sigma_0$ | $C$ | $c$ |
|---|---|---|---|---|---|
| Value | 200 GPa | 0.3 | 300 MPa | 10 GPa | 10 |

configuration before loading the sample. Once the pictures have been registered, the variance $\gamma_f^2$ is estimated as the root mean square of gray level differences at convergence (Table 4.3).

**Table 4.3:** Standard gray level and load uncertainties

| Quantity | $\rho_0$ | $\rho_1$ | $\gamma_f$ |
|---|---|---|---|
| Value | 2.8 N | $4\times10^{-4}$ | 302 gray levels |

The displacement uncertainty on the constrained boundaries is evaluated by measuring the displacement fields with DIC. The covariance matrix of the unknown degrees of freedom, namely $[\boldsymbol{C_u}]$ taken at the four boundaries provides this information. Furthermore, only the component in the displacement direction is kept. Therefore, the standard displacement uncertainty reads

$$\sigma_{BC}^2 = \frac{1}{N_{BC}\Delta t}\sum_t \{\boldsymbol{V}\}^t [\boldsymbol{C_U}]\{\boldsymbol{V}\} \tag{4.18}$$

where $\{\boldsymbol{V}\}$ is the vector that cancels out the values of the covariance matrix when they are not related to a constrained node in the prescribed displacement direction. $N_{BC}$ is the number of degrees of freedom corresponding to the boundaries. The standard uncertainty is evaluated as $\sigma_{BC} = 1.3\times10^{-4}$ pixel. In these experimental conditions with a Young's modulus equal to $E = 200$ GPa, the related uncertainty provides a standard load uncertainty equal to $\rho_0^{DIC} = 2.4$ N. Finally, the second parameter is evaluated while measuring the load with displacement control at several load levels $F \in [0;2000]$ N. The displacement is kept constant during 300 s. Figure 4.4 shows the experimental and interpolated standard load uncertainty. The latter depends on the applied load level and its maximum is reached for a load of 2 kN with $\gamma_F = 3.1$ N.

The evaluation of the covariance matrix (see Equation (4.11)) is the key quantity to study (see Chapter 3). The Hessians are evaluated with the linear elastic law over the first load cycle, which is assumed to be essentially in that regime

$$[\boldsymbol{H_F}] = \begin{bmatrix} 10 & 1.4 \\ 1.4 & 0.4 \end{bmatrix}\times10^3 \quad [\boldsymbol{M_{IDIC}}] = \begin{bmatrix} 0 & 0 \\ 0 & 8.2 \end{bmatrix}\times10^5 \quad [\boldsymbol{H_{IDIC}}] = \begin{bmatrix} 0.1 & 0.01 \\ 0.01 & 8.2 \end{bmatrix}\times10^5 \tag{4.19}$$

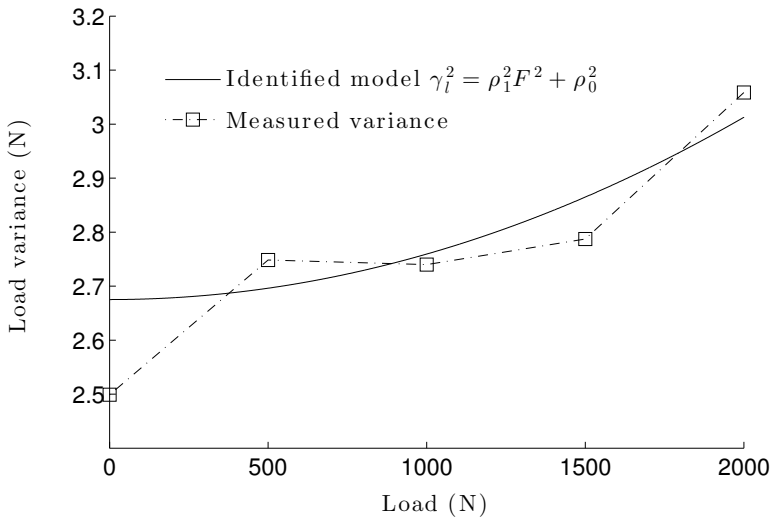


**Figure 4.4:** Measurement of the load variance under static conditions as a function of the load level. A quadratic interpolation is used [92]. The value of $\rho_0$ is obtained when adding the uncertainty from the load cells evaluated as $\rho_0^{LC} = 0.1$ N and that obtained from DIC $\rho_0^{DIC} = 2.4$ N

The diagonal terms of the static Hessian $[\boldsymbol{H}_F]$ are non-zero but separated by more than one order of magnitude. Since the Young's modulus does not influence the kinematic fields the corresponding diagonal term ($M_{11}$) in $[\boldsymbol{M}_{IDIC}]$ is equal to zero. The combination of both observables (see Equation (4.10)) leads to $[\boldsymbol{H}_{IDIC}]$, which has nonzero diagonal terms. This last result shows that the Young's modulus is significantly easier to determine than the Poisson's ratio even when static and kinematic data are coupled.

The correlation matrix and eigenvalues are evaluated for the coupled data by resorting to $[\boldsymbol{H}_{IDIC}]$

$$Cor([\boldsymbol{H}_{IDIC}]) = \begin{bmatrix} 1.00 & 0.02 \\ 0.02 & 1.00 \end{bmatrix} \quad ; \quad \log_{10}(\lambda_I) = \begin{Bmatrix} 4.0 \\ 5.9 \end{Bmatrix} \tag{4.20}$$

The off-diagonal terms denote a weak correlation between the two material parameters.

This first evaluation does not prove that the elastoplastic parameters can be assessed. The same approach is extended to the elastoplastic law with exponential kinematic hardening. The initial set of parameters is shown in Table 4.2. $[\boldsymbol{H}_{IDIC}]$ is evaluated for the

first loading cycle

$$[\boldsymbol{H}_{IDIC}] = \begin{bmatrix} 4.5 & 0.56 & -4.2 & -0.07 & 4\times10^{-4} \\ 0.56 & 0.87 & -0.52 & -0.01 & 6\times10^{-5} \\ -4.2 & -0.52 & 3.9 & 0.06 & -4\times10^{-4} \\ -0.07 & -0.01 & 0.06 & 0.003 & -3\times10^{-5} \\ 4\times10^{-4} & 6\times10^{-5} & -4\times10^{-4} & -3\times10^{-5} & 3\times10^{-7} \end{bmatrix} \times 10^5 \quad \textbf{4.21}$$

and the corresponding eigen values read

$$\log_{10}(\lambda_I) = \begin{Bmatrix} -1.75 \\ 3.23 \\ 4.59 \\ 5.90 \\ 6.93 \end{Bmatrix} \quad \textbf{4.22}$$

Since a plastic strain occurs a variation of the Young's modulus modifies the level of the plastic behavior (*i.e.,* for a smaller $E$ the elastic domain is greater since more strain is needed to reach the yield stress). Therefore both $[\boldsymbol{H}_F]$ and $[\boldsymbol{M}_{IDIC}]$ contribute for the identification of Young's modulus since both observables are influenced by the latter. Last the levels of the terms relative to $C$ and $c$ are very low denoting weak influences on the observables. The evolution of the corresponding material parameters will be avoided thanks to the regularized formulation. The corresponding correlation matrix reads

$$Cor([\boldsymbol{H}_{IDIC}]) = \begin{bmatrix} 1.00 & 0.28 & -0.99 & -0.58 & 0.34 \\ 0.28 & 1.00 & -0.28 & -0.18 & 0.12 \\ -0.99 & -0.28 & 1.00 & 0.61 & -0.36 \\ -0.58 & -0.18 & 0.61 & 1.00 & -0.93 \\ 0.34 & 0.12 & -0.36 & -0.93 & 1.00 \end{bmatrix} \quad \textbf{4.23}$$

In the early stages of plasticity the differentiation between the elastic and plastic regimes is not an easy task. Therefore when the boundary between elastic and plastic regimes is unclear the value of the yield stress depends on the Young's modulus. As a consequence, the two parameters are anticorrelated (*i.e.,* $Cor([\boldsymbol{H}_{IDIC}])(E,\sigma_0) \approx -0.99$). The resolution analysis over the first cycle shows that some parameters can be identified, especially elastic parameters. However, a small incursion in the plastic regime is not sufficient to identify $c$ and $C$ independently.

The same analysis is now applied for the evaluation of $[\boldsymbol{H}_{IDIC}]$ over the entire loading

history (Figure 4.2(a))

$$[\boldsymbol{H}_{IDIC}] = \begin{bmatrix} 89 & 4.8 & -118 & 28 & -20 \\ 4.8 & 4.0 & 4.4 & -9.3 & 2.6 \\ -118 & 4.4 & 275 & -154 & 72 \\ 28 & -9.3 & -154 & 125 & -51 \\ -20 & 2.7 & 72 & -51 & 28 \end{bmatrix} \times 10^5 \;\; ; \;\; \log_{10}(\lambda_I) = \begin{Bmatrix} 4.63 \\ 6.42 \\ 6.76 \\ 7.90 \\ 8.64 \end{Bmatrix} \quad (4.24)$$

The levels of the diagonal terms show that the influences of all material parameters have increased (elasto-plastic parameters included). The five eigenvalues have all their levels greater than the uncertainty and therefore can lead to the identification of all the parameters. Last the correlation matrix is evaluated from $[\boldsymbol{H}_{IDIC}]$

$$Cor([\boldsymbol{H}_{IDIC}]) = \begin{bmatrix} 1.00 & 0.26 & -0.75 & 0.26 & -0.40 \\ 0.26 & 1.00 & 0.13 & -0.41 & 0.25 \\ -0.75 & 0.13 & 1.00 & -0.83 & 0.82 \\ 0.26 & -0.41 & -0.83 & 1.00 & -0.87 \\ -0.40 & 0.25 & 0.82 & -0.87 & 1.00 \end{bmatrix} \quad (4.25)$$

still showing an important anti-correlation between the parameters $C$ and $c$. The correlation between $E$ and $\sigma_0$ has also been cut down.

Based on this resolution analysis two issues have been highlighted:

- Before performing the identification, it is known whether the test is discriminating to the sought parameters. In particular, it is shown that the five loading cycles are useful for the identification of the kinematic hardening parameters.
- The assessment of each parameter, its value and its uncertainty are related to the studied loading history.

In the following the results of the identifications over the first cycle and the entire loading history are analyzed for the three constitutive laws.

### 4.4.2 Parameter identification for the first loading step

The material parameters are assessed for the first cycle starting from the reference set of Table 4.2 and with the IDIC formulation (see Equation (4.9)). For comparison purposes, a global DIC analysis is also run. In the latter no hypothesis is made on the underlying material behavior. Table 4.4 gathers the corresponding values and the residuals for each law at convergence. The standard uncertainties $\gamma_p$ are obtained from the covariance matrices $[\boldsymbol{H}_{IDIC}]$.

The residuals $\chi_f$ are close to the initial DIC residual ($\chi_f = 2.06$), themselves very close to the lower limit (*i.e.,* 1) had the residuals only contained noise contributions. Figure 4.5 shows the change of IDIC residuals (color) and DIC residuals $\chi_f$ (black) with time.

**Table 4.4:** Identified parameters and identification residuals for the three laws for the first cycle ($\gamma_p$ is expressed in % of $p$)

| law | $\chi_I$ | $\chi_f$ | $\chi_F$ | $E$ GPa | $\gamma_E$ | $\nu$ | $\gamma_\nu$ | $\sigma_0$ MPa | $\gamma_{\sigma_0}$ | $C$ GPa | $\gamma_C$ | $c$ | $\gamma_c$ |
|---|---|---|---|---|---|---|---|---|---|---|---|---|---|
| $A$ | 2.10 | 2.10 | 15 | 174 | 0.4 | 0.31 | 0.09 | — | — | — | — | — | — |
| $B$ | 2.09 | 2.09 | 8.9 | 195 | 0.21 | 0.297 | 0.1 | 306 | 0.25 | 10 | — | — | — |
| $C$ | 2.09 | 2.09 | 8.9 | 195 | 0.25 | 0.297 | 0.1 | 306 | 0.3 | 10 | — | 10 | — |

After the first ten pictures captured before starting the experiment the residual levels increase. The level of DIC residuals can be explained by the mesh size equal to 25 pixels, which is a compromise between displacement resolution and spatial resolution [67]. The residual induced by the linear elastic law becomes slightly higher than the DIC residual for $t \geq 21$ s, and may point out the onset of plasticity. This is confirmed by analyzing the load residuals, which are 15 times higher than the levels expected from noise alone.

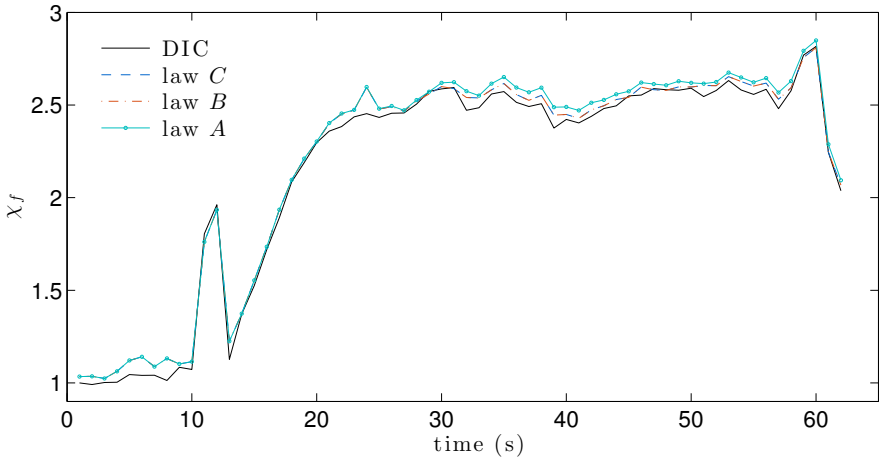


**Figure 4.5:** DIC and IDIC residuals for the three constitutive laws

Residuals induced by laws $B$ and $C$ are equivalent and marginally lower than those of law $A$. Consequently the exponential kinematic hardening does not improve the identification with respect to the experimental data. It is noteworthy that due to yielding the Young's modulus estimate is already 10 % lower than the levels observed for laws $B$ and $C$. A small rise in Poisson's ratio is also observed. The level of yield stress is found to be in accordance with known values [23].

Figure 4.6 shows the change of the parameters with the iterations. The convergence is reached after few iterations, namely, 5, 7 and 7 for laws $A$, $B$ and $C$ respectively. As observed in the resolution analysis, the kinematic hardening parameters keep their initial

values thanks to the Levenberg-Marquardt regularization. The corresponding standard uncertainty is significantly higher for the hardening parameters than those for the elastic parameters and the yield stress (Table 4.4)

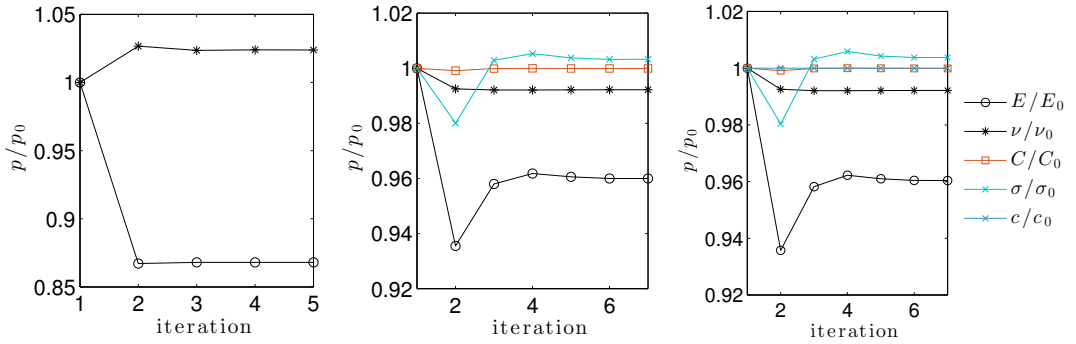


(a) Law *A* (b) Law *B* (c) Law *C*

**Figure 4.6:** Change of material parameters with the iteration number for the three investigated laws. Each parameter is normalized by its initial value

Figure 4.7 shows the displacement field $u_1$ and residual component, which is the difference between IDIC and DIC measurements at the last time step of the first load cycle ($t = 61$ s) for the different constitutive postulates. Non vanishing displacements exist, which indicate the presence of plastic strains (Figure 4.7(a)). This observation validates the results shown in Table 4.4. Figure 4.7(b) shows that law *A* induces very high differences in particular close to one of the connecting radii. This is an indication of plastic activity in the vicinity of stress concentration areas. When compared with Figures 4.7(c-d) there are significant differences, again validating the identification with elastoplastic postulates that lead to equivalent differences with raw DIC. The fact that there remain displacement residuals shows that the plastic behavior has been only partially captured.

### 4.4.3 Parameter identification for the whole history

The same analysis is now carried out over the entire loading history (Table 4.5). Even if the IDIC residual of law *C* ($\chi_I = 6.3$) is 2.5 times higher than the DIC residual ($\chi_f = 2.5$) it is the best of the three chosen postulates. The fact that the load residuals are still high is an indication that there remains a model error. This is particularly true for the elastic law that induces very high residual errors. The Young's modulus is found to be very small, and the Poisson's ratio tends to 0.5 (*i.e.,* incompressibility as expected from dominant isochoric plasticity).

All these trends clearly disqualify elasticity as a model able to describe the reported experiment. The latter was not the case for the first cycle because the mechanical behavior

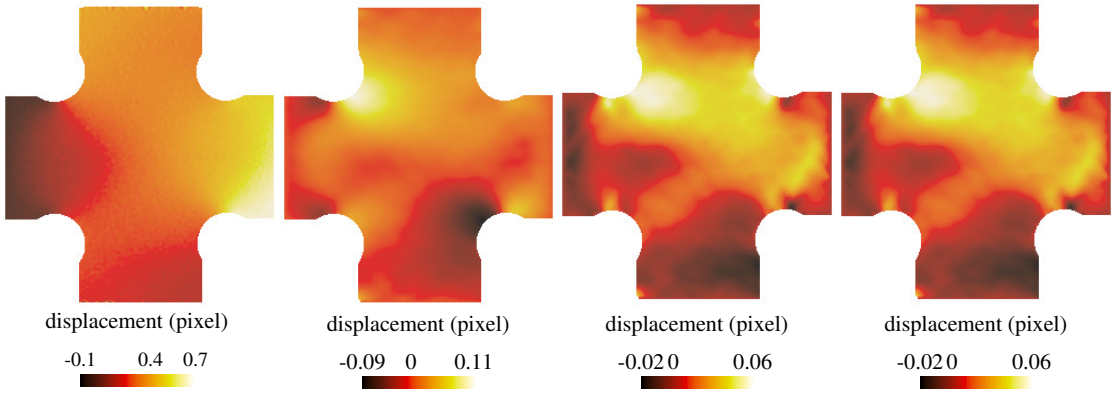


(a) DIC (b) DIC - IDIC (*A*) (c) DIC - IDIC (*B*) (d) DIC - IDIC (*C*)

**Figure 4.7:** Displacement field map $u_1$ measured by DIC and displacement differences between DIC and IDIC for the three investigated laws

**Table 4.5:** Identified parameters and identification residuals for the three laws for the whole loading history

| law | $\chi_I$ | $\chi_f$ | $\chi_F$ | $E$ GPa | $\gamma_E$ | $\nu$ | $\gamma_\nu$ | $\sigma_0$ MPa | $\gamma_{\sigma_0}$ | $C$ GPa | $\gamma_C$ | $c$ | $\gamma_c$ |
|---|---|---|---|---|---|---|---|---|---|---|---|---|---|
| *A* | 15 | 14.9 | 1820 | 8.8 | 0.25 | 0.499 | 0.002 | — | — | — | — | — | — |
| *B* | 7.1 | 7.1 | 113 | 157 | 0.15 | 0.31 | 0.04 | 480 | 0.15 | 6.7 | 0.15 | — | — |
| *C* | 6.3 | 6.3 | 100 | 148 | 0.16 | 0.30 | 0.04 | 423 | 0.16 | 8.6 | 0.16 | 10.8 | 0.03 |

was mainly elastically driven. This is confirmed by Figure 4.8 that shows the change of IDIC and DIC residuals over time. Unlike the previous results (Figure 4.5), gaps between IDIC and DIC residuals are much more pronounced, especially when the level of plastic strain increases. Furthermore, the gain offered by each law with respect to raw DIC results is also clarified.

For law *C*, all material parameters have been assessed with a low level of uncertainty. Regarding laws *B* and *C* all the parameters converge in few steps (see Figure 4.9). Unlike Figure 4.6 all the parameters are modified and no regularization is needed in the present case. It is worth noting that the more freedom the identification code has (*i.e.,* the number of unknowns is increased), fewer iterations are needed. Further, the converged solutions are rather far from the initial guesses, which shows the robustness of the procedure.

Figure 4.10 shows the displacement maps $u_1$ and $u_2$ at the last time step of the analysis. The permanent strains are important and the maximum measured eigen strain is equal to $\varepsilon_I = 18.7\%$. The normal strain map $\varepsilon_{11}$ is shown at the same time in Figure 4.10(c). The strain levels are the highest in the concentration zones induced by the fillets.

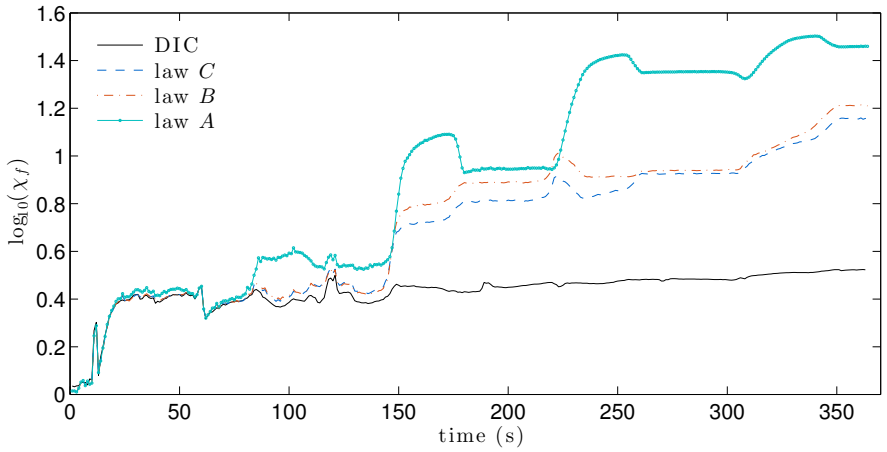


**Figure 4.8:** DIC and IDIC residual history for the three constitutive laws. Please note that a semi-logarithmic scale is used

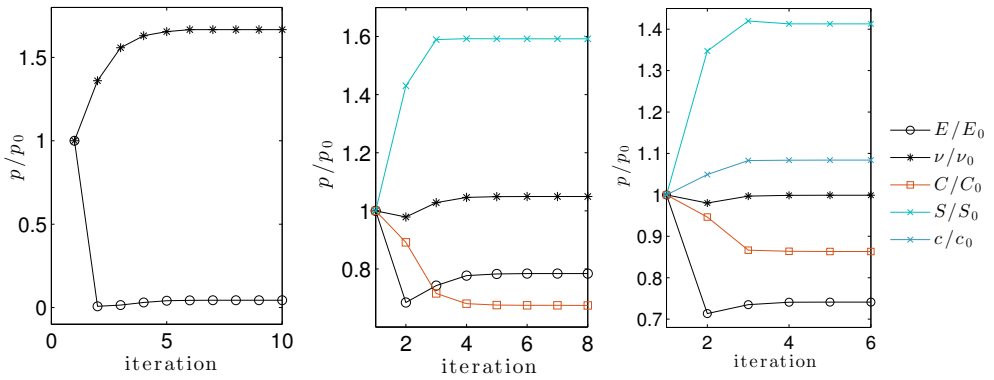


(a) Law *A* (b) Law *B* (c) Law *C*

**Figure 4.9:** Change of the material parameters for the three investigated laws during the identification iterations. Each parameter is normalized by its initial value

### 4.4.4 Comparison with FEMU-F results

Table 4.6 shows the parameters assessed only by considering the reaction forces (Equation (4.6)). It corresponds to a FEMU-F procedure [64]. To compare both approaches, the gray level and global residuals are also computed. As expected, the static residuals are lowered for all laws since the residuals only depend on reaction forces. Conversely, the overall quality degrades in addition to that associated with gray level residuals. More importantly, the standard uncertainties of the identified parameters are significantly higher, which is caused by the limited number of data used per analyzed time.

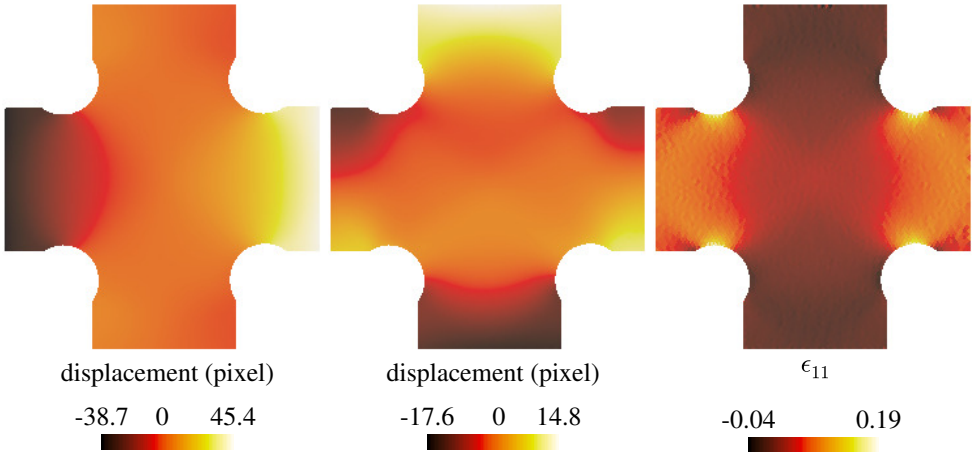


(a) Displacement $u_1$ (b) Displacement $u_2$ (c) Strain $\varepsilon_{11}$

**Figure 4.10:** (a-b) Measured displacement fields with DIC at the last experimental time step. (c) Corresponding strain field (normal component along direction 1)

**Table 4.6:** Identified parameters and identification residuals via FEMU-F for the three laws over the entire loading history cycle (no regularization prescribed)

| law | $\chi_I$ | $\chi_f$ | $\chi_F$ | $E$ GPa | $\gamma_E$ | $\nu$ | $\gamma_\nu$ | $\sigma_0$ MPa | $\gamma_{\sigma_0}$ | $C$ GPa | $\gamma_C$ | $c$ | $\gamma_c$ |
|---|---|---|---|---|---|---|---|---|---|---|---|---|---|
| *A* | 19.1 | 19 | 1732 | 10 | 0.4 | 0.19 | 4 | — | — | — | — | — | — |
| *B* | 8.1 | 8.0 | 11.9 | 188 | 0.7 | 0.23 | 4 | 330 | 0.4 | 3.7 | 1.2 | — | — |
| *C* | 7.5 | 7.5 | 9.6 | 191 | 0.7 | 0.25 | 4 | 300 | 0.5 | 8.5 | 3.7 | 29 | 11 |

Figure 4.11 shows the displacement field difference for component $u_1$ for the three constitutive laws with IDIC or FEMU-F approaches compared with DIC measurements at the end of the experiment. The choice of an elastoplastic law instead of an elastic law decreases the displacement difference, thereby decreasing the model error. The residual level is lower when the identification is performed with IDIC rather than FEMU-F. An overall residual remains because *i*) the model does not correctly predict the plastic strains, *ii*) localization phenomena occur.

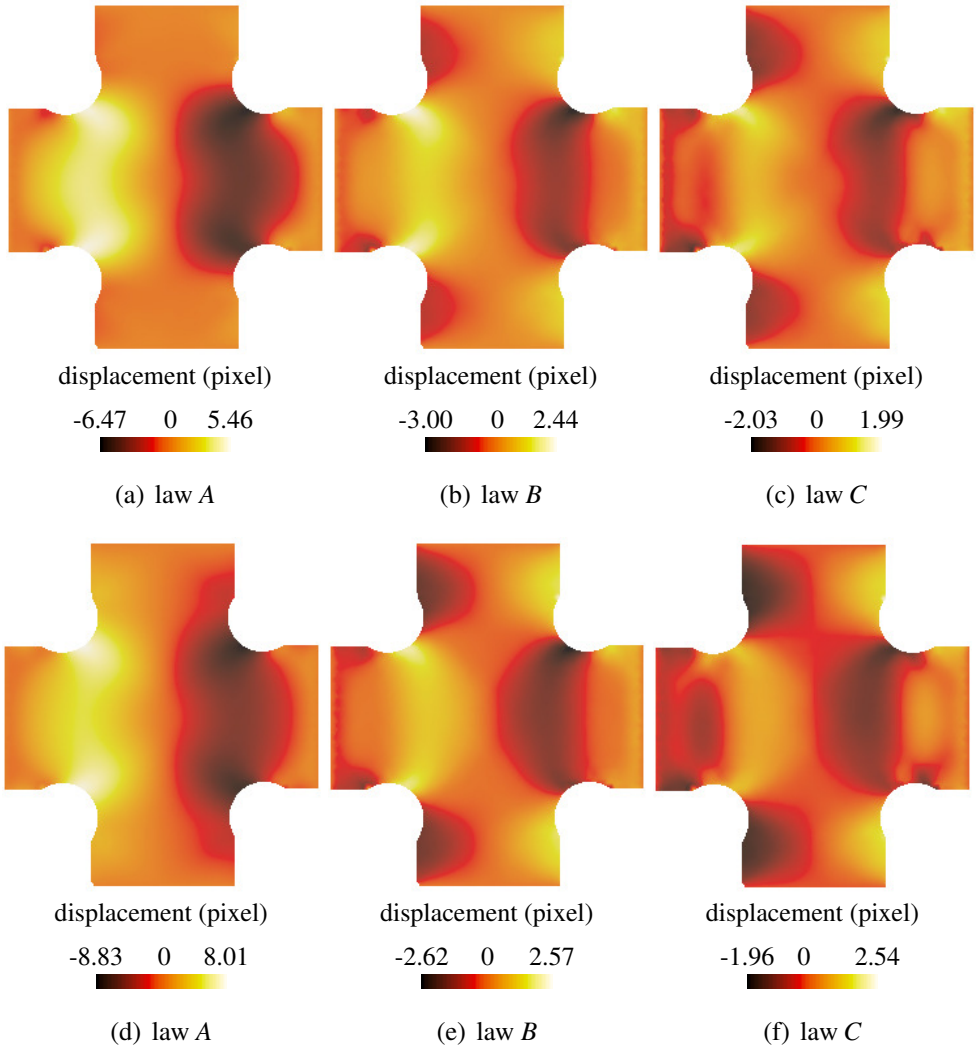


(a) law *A* (b) law *B* (c) law *C*

(d) law *A* (e) law *B* (f) law *C*

**Figure 4.11:** Displacement differences $u_1$ between DIC and IDIC (first row) or FEMU-F (second raw on the Figure) for the three investigated laws. The color bars correspond to the largest and lowest values of the corresponding residual map

## 4.5 Conclusion

Three constitutive laws have been investigated with Integrated Digital Image Correlation to analyze a biaxial test with a cruciform specimen of a thin sheet of precipitation hardened stainless steel. The Bayesian-based formulation presented in Chapter 3 has been implemented and employed to assess the sought material parameters.

An initial sensitivity analysis enables the impact of the loading history and the acquisition noise on the identification to be understood. It shows that the first loading cycle is

not sufficient to identify plastic laws but it is sufficient to detect its onset with the initial set of the material parameters. The corresponding identification leads to an IDIC residual with similar level as raw DIC. The identification is also performed over the entire loading history accounting for 5 loading/unloading cycles. Any of the chosen model does not match the available data with the same accuracy as observed for the first cycle. The three laws lead to three different residuals and the exponential kinematic hardening law provides the best results.

In the present study four different error indicators have been considered:

- When DIC and IDIC analyses are performed, the gap with respect to gray level conservation is computed. It estimates the registration quality when the pictures in the deformed configurations are corrected by the measured displacement field and subsequently compared with the picture of the reference configuration.

- DIC and IDIC can also be compared by computing the displacement differences measured by both approaches. When the mesh is identical, as in the present case, the comparison is straight forward.

- Load residuals are yet another way of characterizing the identification quality. In the present analyses, FEMU-F and IDIC could be compared since both included load residuals in their respective formulation.

- Last IDIC as developed herein has an overall quality indicator $\chi_I^2$ that compares all sensor information (be it gray levels for each pixel or load level for each load cell) in the same footing when normalized by the variance of corresponding noise.

This wealth of indicators allows the user to assess not only globally but also with each of the estimators the identification quality and the underlying model error (*i.e.,* choice of constitutive law, finite element discretization).

Now that the material in condition A has been modeled and the methodology has been introduced and validated Chapter 5 will investigate the material mechanical behavior in its final condition, namely TH1050. To that end a uniaxial experiment is performed on an ultra-thin (70 $\mu$m) 17-7 PH steel sheet and Integrated-DIC is again chosen. To prevent the specimen from buckling, a dedicated device is designed and enables the material to be successfully characterized.

# Chapter 5
# Identification of an anisotropic plasticity model with uniaxial and biaxial experiments via IDIC

Reproduced from: Morgan Bertin and François Hild, *Identification of an anisotropic plasticity model of 17-7 PH thin sheets with uniaxial and biaxial experiments via IDIC*, submitted 2016


## Abstract

Uniaxial and biaxial experiments are performed on ultra-thin specimens made of stainless steel. An anti-wrinkling setup allows for the characterization of the mechanical behavior with Integrated Digital Image Correlation (IDIC). The result shows that a simple uniaxial experiment investigated via IDIC possesses enough data (and even more) to characterize a complete anisotropic elastoplastic model. These results from uniaxial test are validated via biaxial experiments.


## 5.1 Introduction

For engineering design, Tresca [93] or von Mises [94] isotropic yield criteria are commonly used and give satisfactory results. However, a perfect isotropic plasticity assumption of industrially-manufactured materials is not common and anisotropy is the rule rather than the exception. It results that sheet metal anisotropy is a key issue to improve manufacturing processes and mechanical designs [95]. Therefore, authors have actively studied sheet anisotropy characterization. Experimental [96, 97, 98] and theoretical [29, 99] works have led to the first models of anisotropic plastic flow. They have been extended to describe more complex and challenging behaviors [100, 101]. Rolled sheet metal anisotropy originates in particular from a preferred orientation of polycrystalline grains. Two types of model corresponding to two separated scales address this phenomenon, *i*) macroscopic formulations and *ii*) microscopic analyses. Texture-induced anisotropy can be assessed by measuring the plastic anisotropy parameters from macroscopic analyses of the mechanical behavior, or can be predicted from texture measure-

ments [102, 103]. However, the more complex a constitutive law the more difficult and time-consuming the identification of its material parameters.

At the macroscopic scale, experiments have addressed two main issues, $i$) compare the theoretical results obtained from constitutive laws to their experimental counterparts, and $ii$) characterize and gather properties for numerous materials and engineering purposes. First, uniaxial tests [104, 105, 106] determined the so-called Lankford ratio. With the advent of strain gauges, the identification of Hill's anisotropic coefficient was achieved with numerous uniaxial specimens with the same geometry but with changing loading directions with respect to the rolling direction. Second, multiaxial tests were performed to challenge constitutive laws and complement the results of uniaxial tests. For instance, the bulge test allows for numerous anisotropic materials to be characterized [107, 108, 109]. Other materials such as pure aluminum, zinc and titanium have anisotropic behaviors not well predicted by these models [109, 108]. Lately, in-plane biaxial tensile setups allow for the anisotropic properties to be investigated via flat cruciform specimens [50].

Based on the use of standard experimental techniques [71], different approaches to optimize specimen geometry or experimental procedure were proposed [53, 54, 55, 56, 57]. The sought objective was to get the most homogeneous mechanical fields in a chosen region even though the to-be-characterized mechanical behaviors were plastically anisotropic. To analyze and extract parameters from large amounts of data, identification strategies based on inverse identification methods [110, 111, 112, 113, 73, 74] have enhanced the characterization capabilities.

With the advent of full-field measurement techniques and Digital Image Correlation in particular [75, 68], authors have investigated steel sheet anisotropy with heterogeneous mechanical fields. The wealth of data provided by such measurements has allowed for new insights but has also induced challenges [59] for identification and validation aspects. It also motivated a new approach of experimental design (see Chapter 3) that allows for the direct uncertainty minimization of the sought parameters. Remarkably, many works dedicated to characterize metal sheet anisotropy via full field measurement were performed with biaxial experiments and flat cruciform specimens [40, 39, 61, 52]. As a consequence, uniaxial specimens were almost entirely put aside abandoned in full-field characterized tests although they can still provide valuable information [114].

The present study aims for identification and validation of anisotropic plasticity model investigating Hill's quadratic yield function [29] via Integrated-DIC [77, 62, 63]. Two experiments on ultra-thin uniaxial and biaxial specimens are performed and four constitutive laws with increasing complexity are considered to challenge the sought behavior. The identification relies on Integrated-DIC that allows for measurement and identification of the sought properties in only one step. To enhance the relevance of the model, all data (displacement fields and reaction forces) are equitably weighted via a Bayesian foundation that assumes a white Gaussian noise (assessed prior to the experiment). Last,

the identified Hill's anisotropic parameters for the uniaxial experiment will initialize the identification routine for the biaxial investigation.

The paper is divided into three main sections. Section 5.2 introduces the chosen constitutive models and recalls the integrated-DIC identification methodology (see Chapters 3 and 4). Section 5.3 discusses the identification results for the uniaxial specimen and Section 5.4 addresses the biaxial experiment in a two-step strategy. Both sections address the issue of ultra-thin specimen and use an anti-wrinkling device.

## 5.2 Theoretical and methodological framework

### 5.2.1 Investigated constitutive laws

Four constitutive laws are investigated, namely, $(A)$ linear and isotropic elasticity (with Young's modulus $E$ and Poisson's ratio $\nu$), $(B)$ linear kinematic hardening with von Mises flow rule, $(C)$ exponential kinematic hardening with von Mises flow rule, and $(D)$ linear kinematic hardening with quadratic Hill [29] yield criterion. The total strain rate $\dot{\boldsymbol{\epsilon}}$ is written in terms of elastic and plastic strain rates $\dot{\boldsymbol{\epsilon}} = \dot{\boldsymbol{\epsilon}}_{el} + \dot{\boldsymbol{\epsilon}}_{pl}$ where $\dot{\boldsymbol{\epsilon}}_{el}$ is the elastic strain rate tensor and $\dot{\boldsymbol{\epsilon}}_{pl}$ the plastic strain rate tensor. The yield surface $J_2(\boldsymbol{\sigma} - \boldsymbol{X}) = \sigma_0$ is defined such that $J_2$ is the second invariant of the stress deviator tensor, $\boldsymbol{X}$ the back-stress, and $\sigma_0$ the yield stress. As a first approximation, a linear kinematic hardening model is chosen for the back-stress rate [70]

$$\dot{\boldsymbol{X}} = \frac{2}{3} C \dot{\boldsymbol{\epsilon}}_{pl} \tag{5.1}$$

where $C$ is the hardening modulus. Under the assumption of exponential kinematic hardening, the back-stress becomes

$$\dot{\boldsymbol{X}} = \frac{2}{3} C \dot{\boldsymbol{\epsilon}}_{pl} - c \boldsymbol{X} \dot{p} \tag{5.2}$$

where $C$ and $c$ are material parameters, $p$ the cumulative plastic strain [87, 88]. Last, the quadratic Hill [29] anisotropic yield criterion is associated with the linear kinematic hardening law $(B)$. The latter criterion is an extension of the von Mises criterion, and can be expressed in terms of rectangular Cartesian stress components as

$$f(\boldsymbol{\sigma}) = \sqrt{H_1(\sigma_{22} - \sigma_{33})^2 + H_2(\sigma_{33} - \sigma_{11})^2 + H_3(\sigma_{11} - \sigma_{22})^2 + 2H_4\sigma_{23}^2 + 2H_5\sigma_{31}^2 + 2H_6\sigma_{12}^2} \tag{5.3}$$

where $H_i$ are constants expressed with the normal yield stress ratio ($R_{11} = \sigma_0/\bar{\sigma_{11}}$, $R_{22} = \sigma_0/\bar{\sigma_{22}}$, $R_{33} = \sigma_0/\bar{\sigma_{33}}$) and those in shear ($R_{12}$, $R_{23}$, $R_{31}$) both with respect to the axes of

anisotropy

$$H_1 = \frac{1}{2}\left(\frac{1}{R_{22}^2}+\frac{1}{R_{33}^2}-\frac{1}{R_{11}^2}\right), \quad H_4 = \frac{3}{2}\frac{1}{R_{23}^2}$$
$$H_2 = \frac{1}{2}\left(\frac{1}{R_{33}^2}+\frac{1}{R_{11}^2}-\frac{1}{R_{22}^2}\right), \quad H_5 = \frac{3}{2}\frac{1}{R_{31}^2},$$
$$H_3 = \frac{1}{2}\left(\frac{1}{R_{11}^2}+\frac{1}{R_{22}^2}-\frac{1}{R_{33}^2}\right), \quad H_6 = \frac{3}{2}\frac{1}{R_{12}^2}$$

The computation being two dimensional, $R_{31}$ and $R_{23}$ are insensitive and set to 1 hereafter (and hence $H_4 = H_5 = 3/2$). One of the three parameters $H_1$, $H_2$, and $H_3$ must be chosen to decorrelate its value from the yield stress and hence $H_1 = 1$ is chosen. Therefore, only three additional material parameters, *i.e.,* $H_2$, $H_3$, and $H_6$, remain to be determined.

### 5.2.2 Integrated-DIC

In the following, the identification of the material parameters relies on Integrated Digital Image Correlation where the unknowns are no longer the displacement at each nodes but the sought parameters. It is based on the global DIC technique [68] that relies on the registration of an image $f$ in the reference configuration and a series of pictures $g$ in the deformed configurations. Assuming gray level conservation, the registration problem consists of minimizing the sum of squared differences between the deformed image corrected by the measured displacement $\boldsymbol{u}(\boldsymbol{x},t)$ and the reference image (written for each time $t$ independently)

$$\chi_f^2 = \frac{1}{2\gamma_f^2 N_\Omega N_t}\sum_t\sum_\Omega((g(\boldsymbol{x}+\boldsymbol{u}(\boldsymbol{x},t),t)-f(\boldsymbol{x}))^2 \tag{5.4}$$

with respect to the sought displacement fields $\boldsymbol{u}(\boldsymbol{x},t)$, where $\boldsymbol{x}$ is any considered pixel. In this expression $\Omega$ denotes the Region of Interest (ROI), $N_\Omega$ its area in terms of the number of pixels it contains, and $\gamma_f = 323$ gray levels is the standard deviation (*i.e.,* 2% of the dynamic range of $f$) of the white noise assumed to affect each image independently (including the reference one, which is responsible for the factor of $1/2$ coming as a multiplicative term in this functional). The load is also of importance for the identification because it increases the number of the measured quantities and as a consequence diminishes the relative uncertainty by enhancing the material parameters sensitivities (see Chapter 4). Thus, a second objective function, $\chi_F^2$, is introduced

$$\chi_F^2 = \frac{1}{N_F N_t \gamma_F^2}\{\boldsymbol{F}_m-\boldsymbol{F}_c\}^t\{\boldsymbol{F}_m-\boldsymbol{F}_c\} \tag{5.5}$$

where $\{\boldsymbol{F}_m\}$ are the measured reaction forces and $\{\boldsymbol{F}_c\}$ are the computed levels with respect to the chosen material parameter set, $N_F$ the number of load cells for each actuator, $N_t$ the number of steps and $\gamma_F^2$ the load variance. The identification based upon both observables, i.e., gray levels and reaction force, is achieved by minimizing the global functional $\chi_I^2$

$$\chi_I^2 = \frac{N_\Omega}{N_\Omega + N_F}\chi_f^2 + \frac{N_F}{N_\Omega + N_F}\chi_F^2 \tag{5.6}$$

where the DIC and reaction force functionals have been introduced in Equations (6.1) and (6.19) respectively. The choice for the specific weight is issued from a Bayesian approach whereby the noise characteristics imposes the appropriate weights to be given to quadratic differences (see Chapter 3). In particular, quadratic differences are to be evaluated with a metric equal to the inverse noise covariance.

In the following analyses, DIC measurements are based upon a global approach in which finite element discretizations are used to measure the displacement fields [68]. In the present case, meshes made of 3-noded triangles are considered. The displacement interpolation is linear within each element [62].

When using an integrated DIC approach, the kinematic basis is parameterized with the sought material parameters [77, 62, 63] that become the generalized degrees of freedom. When nonlinear behaviors are investigated, the dependence of the displacement fields with the material parameters are nonlinear as well. Consequently, sensitivity fields (*i.e.,* displacement and reaction force derivatives with respect to the sought parameters) are computed via finite element simulations (see Chapter 4). In the present case the commercial (implicit) finite element code used is Abaqus standard. It is driven by the measured displacements on the boundary of the considered region of interest to compute the displacement fields and reaction forces. A Gauss-Newton procedure is implemented to minimize to global functional by iteratively updating the material parameters. The interested reader will find additional details on the implementation of such procedures in Chapter 4.

## 5.3 Parameter identification with uniaxial test

The present study investigates the mechanical behavior of a 70-$\mu$m thick sheet of precipitation hardened stainless steel (17-7 PH grade) in TH1050 condition [23]. The specimen is loaded by a servo-hydraulic tension/compression testing machine (see Figure 5.1(a)). The experiment consists of three loading/unloading cycles in a displacement controlled mode with increased displacement amplitudes for each new cycle. The unloading phases are stopped when the measured load reaches 10 N to avoid compression. 14-bit gray scale images are captured with a digital camera (pco.pixelfly) and a telecentric lens. The effective magnification is 70 $\mu$m per pixel or 14 pixel/mm. Last, the load measurements and

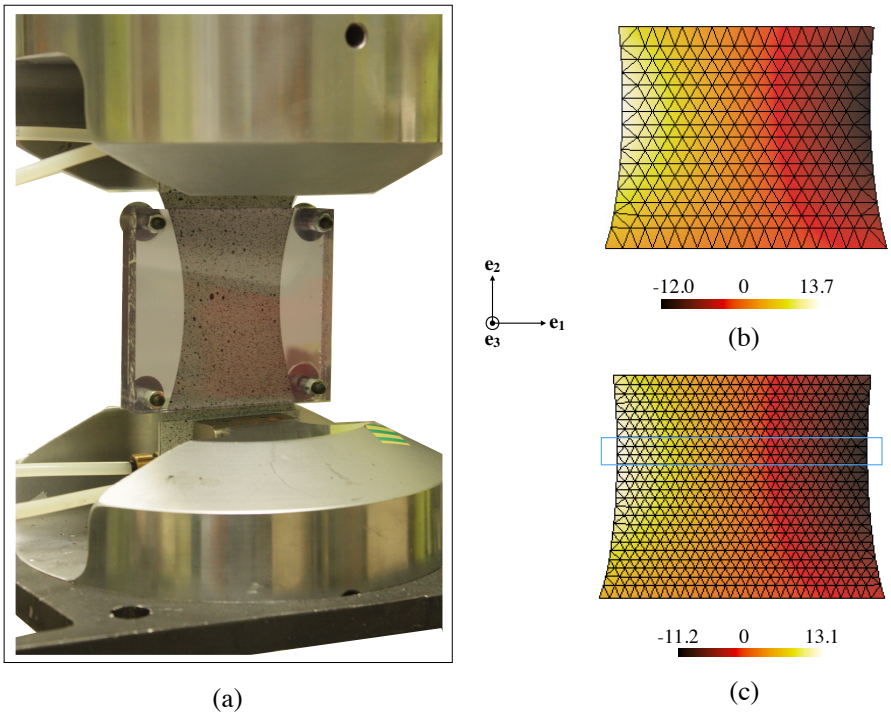


**Figure 5.1:** (a) Uniaxial specimen with dedicated anti-buckling device. (b) DIC and (c) IDIC displacement fields $u_1$ at the last experimental time step with two mesh sizes. (c) also shows the area that will be used to assess the Lankford coefficient. The displacements are expressed in pixels (1 pixel $\leftrightarrow$ 40 $\mu$m)

the image acquisitions are synchronized.

The main experimental challenge concerns the specimen thickness that prevents rough grips to be used. The solution relies on bonding the specimen ends to flat-surface aluminum alloy tabs with a 3M Scotch-Weld Structural Adhesive Film AF 126 [115]. Residual wrinkles are generated during this process near the edges. To maintain the surface flat in the center region (crucial to perform 2D-DIC analyses) an anti-wrinkling device is designed (see Figure 5.1). It consists in holding the specimen between two plexiglas sheets soldered with four screws. To perform DIC analyses a random speckle pattern is applied on the monitored surface and no paint loss was observed during the tests. Figure 5.1 shows the experimentally measured (b) and identified (c) (law $D$) displacement fields associated with the three-noded triangular mesh with linear interpolation (T3) at the last experimental time step.

Figure 5.2 shows the global residuals at each time step for the DIC (*i.e.*, $\chi_f$) and IDIC (*i.e.*, $\chi_I$) solutions. Prior to starting the experiment, 10 images and load measurements are acquired to assess the uncertainties. Then, the experiment starts and the residual increases to roughly four times the noise level. Whereas the DIC residual remains relatively

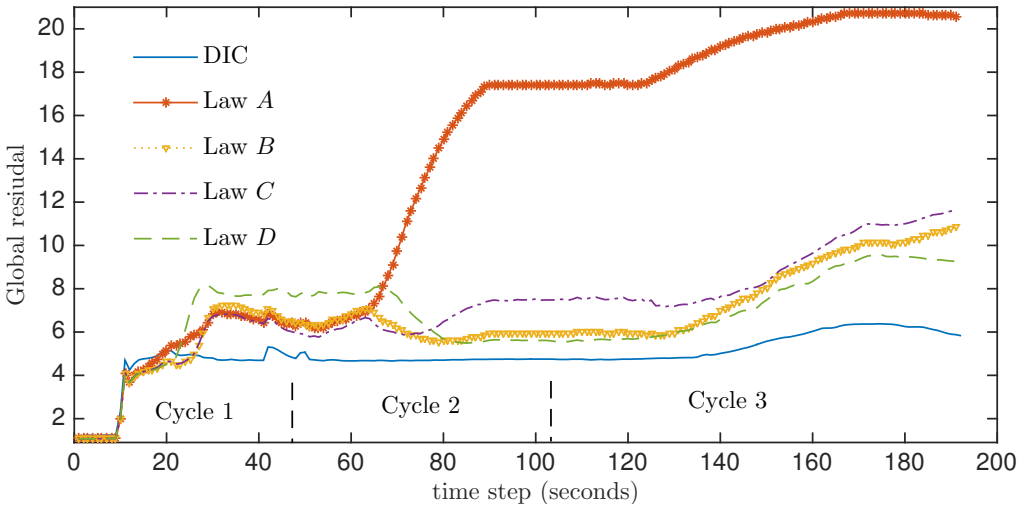


**Figure 5.2:** Global residual history for DIC and for the four constitutive models investigated with IDIC

constant over the experiment, the IDIC residuals increase. Let us stress that DIC is based on a number of degrees of freedom equal to 600 per image, or 114,600 for the entire experiment, whereas the IDIC approach has as many degrees of freedom as constitutive parameters to be identified ranging from 2 to 7 for laws A to C. This very drastic reduction incorporates many constraints due to a priori assumption on the material behavior. The difference in residuals from DIC to IDIC is a measurement of the model error that is due to the specific chosen constitutive law. Once the elastic regime ends ($t \geq 20$), the IDIC residuals increase and exceed the DIC residuals. At the end of the experiment, law *A* leads to the highest residual. It highlights that the mechanical behavior is mainly driven by plasticity. Second, law *D* is at the end of the experiment the best model to describe the observed mechanical behavior. However, law *D* is less suited to describe the mechanical behavior than laws *B* and *C* up to the middle of the second cycle. This result shows that the assumption of a constant anisotropic behavior, *i.e.,* constant anisotropic coefficients as a function of the plastic strain, is inaccurate.

Table 5.1 gathers the assessed material parameters for the four constitutive laws. Their initial values ($\boldsymbol{p_0}$) are chosen according to literature data [23, 24]. The initial and last values of the residuals are also shown ($1^{st}$ — last ) for all the investigated laws plus one identification with a coarser mesh $D^*$. All the parameters converge to a stabilized level while the residuals $\chi_I$ for each laws are minimized. First, all IDIC residuals are greater than the DIC residual but lower than the IDIC residual obtained when a coarse mesh (corresponding to DIC mesh) is used ($D^*$). This is an indication that model errors occur. It proves that refining the mesh (Figure 5.1) can enhance the identification quality by

decreasing the gray level residuals that are one of the basis of the present methodology. It also explains why the DIC residual is larger than the IDIC residuals during the first time steps ($t \in [10;20]$). The load residuals increase except for law $D$ thanks to the quadratic Hill yield criterion. This proves that an anisotropic behavior enables more freedom for the identification and helps to reconcile load and displacement data.

**Table 5.1:** Identified parameters and identification residuals via I-DIC for the four laws over the entire loading history cycle ($D^*$ corresponds to the coarse DIC mesh and "$1^{st}$ — last" corresponds to the first and last value of the residuals)

| law | $\chi_I$ $1^{st}$ — last | $\chi_f$ $1^{st}$ — last | $\chi_F$ $1^{st}$ — last | $E$ GPa | $\nu$ | $\sigma_0$ MPa | $C$ GPa | $c$ | $H_2$ | $H_3$ | $H_6$ |
|---|---|---|---|---|---|---|---|---|---|---|---|
| $p_0$ | 5.0 | | | 200 | 0.3 | 1300 | 10 | 10 | 1 | 1 | 1 |
| $A$ | 16.1 — 15 | 16.1 — 15 | 223 — 229 | 200 | 0.42 | — | — | — | — | — | — |
| $B$ | 11.3 — 7.0 | 11.3 — 7.0 | 15.6 — 33.8 | 157 | 0.18 | 1950 | 8.2 | — | — | — | — |
| $C$ | 10.3 — 7.6 | 10.3 — 7.6 | 13.6 — 26.1 | 142 | 0.17 | 1670 | 10.3 | 10.3 | — | — | — |
| $D$ | 11.3 — 7.0 | 11.3 — 7.0 | 15.5 — 9.30 | 202 | 0.30 | 1420 | 9.1 | — | 0.85 | 0.88 | 1.06 |
| $D^*$ | 11.1 — 7.8 | 11.1 — 7.8 | 15.5 — 10.8 | 202 | 0.3 | 1390 | 9.2 | — | 0.89 | 0.9 | 1.04 |

Second, the lowest residual (for law $D$) corresponds to 7 times the noise level, which indicates that the model does not fully capture all the experimental behavior. For law $A$, the Poisson's ratio increases because of plastic incompressibility and isotropy. For law $B$ and $C$ the Poisson's ratio and the Young's modulus are too small and only law $D$ achieves constitutive parameter values that are compatible with the literature [24, 23]. This result shows that a model accounting for an anisotropic behavior is necessary to achieve the identification of all the material parameters (in particular the elastic parameters).

Figure 5.3(a) shows the global Hessian ($H_{IFDIC}$) of the IDIC procedure for law $D$. The material parameters having the largest influence are $H_1$, $H_2$, and $H_3$ and account for the anisotropic plasticity behavior ($H_1$ is analyzed to show its correlations with other parameters but for identification purposes its value is kept equal to one). This result proves that a uniaxial experiment can lead to the characterization of an anisotropic behavior but also that this behavior must be accounted for. Figure 5.3(b) shows that the Poisson's ratio is correlated to $H_1$, $H_2$, and $H_3$, and explains why it is necessary to have a model that separates both contributions from the Poisson's ratio and the anisotropic coefficients (see corresponding values in Table 5.1). Figure 5.3(c,d) shows the static Hessian and that the reaction forces have a minor impact for the identification. The parameters $\nu$ and $H_6$ have almost no influences and it is clear that $H_1$ is correlated to all plastic parameters and explains why its value has been fixed. Furthermore, Figure 5.3 shows that many parameters are strongly correlated, which proves that the reaction forces cannot be the only data for identification purposes. Last, the global Hessian being the summation of the static and the kinematic Hessians, the latter is almost equal to the kinematic Hessian

$(M_{IDIC} \approx H_{IFDIC})$.

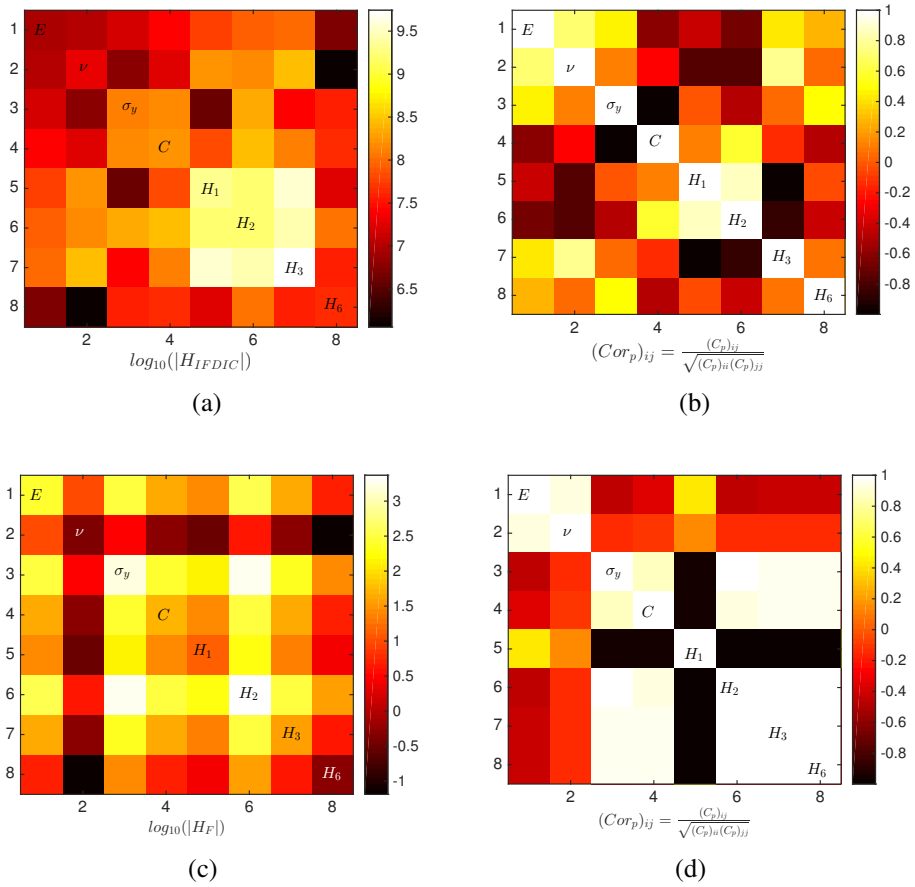


**Figure 5.3:** (a,b) Global Hessian ($\approx$ kinematic Hessian) and its corresponding correlation coefficient Matrix and (c,d) Static Hessian and its corresponding correlation matrix for law $D$. The absolute value of the Hessian is used

Figure 5.4 shows the displacement field residual for the $u_1$ component (difference between the IDIC and DIC displacement fields). The residuals corresponding to laws $B$ and $C$ are equivalent whereas the residual corresponding to law $D$ is twice as small thanks to the anisotropic plasticity model.

Figure 5.5 shows the shape of the sensitivity fields for all material parameters. The sensitivity fields corresponding to ν, $H_2$, and $H_3$ have an equivalent shape at the end of the test. This explains the Poisson's ratio identification issue if the constitutive model does not account for an anisotropic plasticity behavior. It is worth noting that the residuals of law $B$ and $C$, and the sensitivity fields obtained for the anisotropic parameters have a similar shape (see Figure 5.3). Therefore, it indicates that anisotropy can be captured, which will subsequently be proven. Last, even with the anisotropic plasticity model, a residual greater than the DIC residual remains.

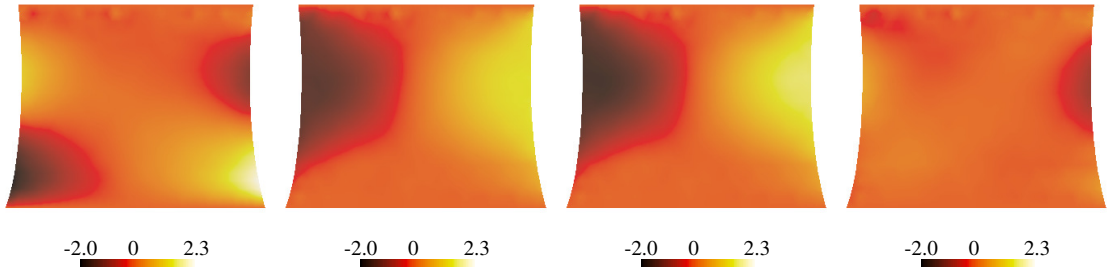


(a) $RMS(A) = 0.56$ (b) $RMS(B) = 0.74$ (c) $RMS(C) = 0.81$ (d) $RMS(D) = 0.19$

**Figure 5.4:** Transverse displacement field residuals (IDIC-DIC) and their corresponding root mean square levels (expressed in pixel) for the $u_1$ component for the four investigated constitutive models

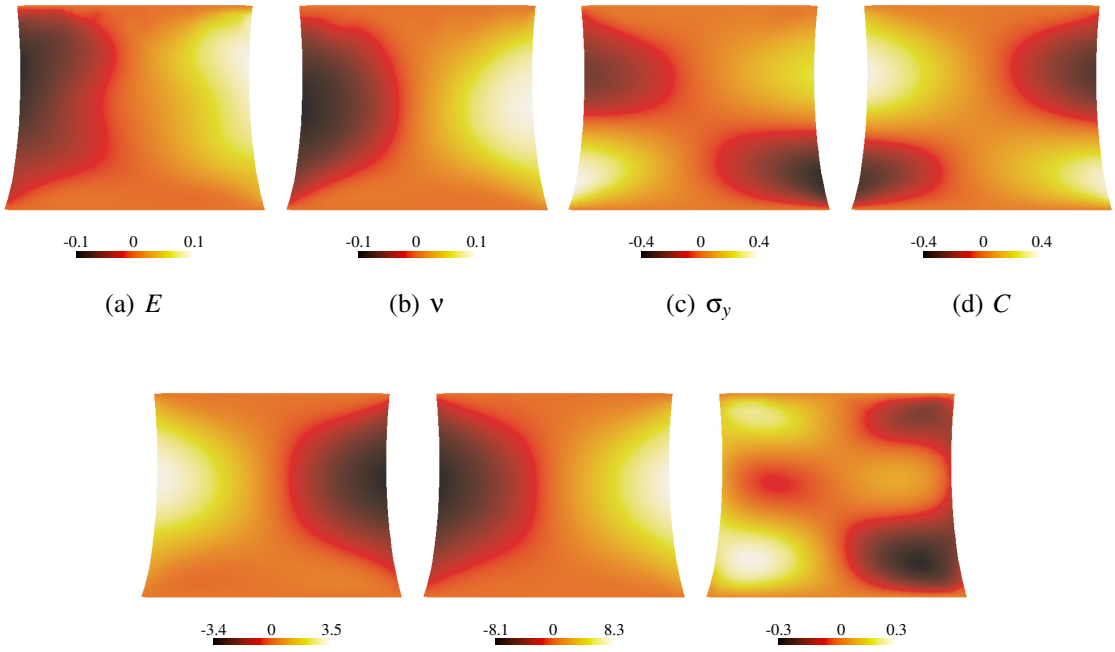


(a) $E$ (b) $\nu$ (c) $\sigma_y$ (d) $C$

(e) $H_2$ (f) $H_3$ (g) $H_6$

**Figure 5.5:** Sensitivity fields for all the material parameters of law $D$ (in $\mu$m) for a 2% variation of the parameters. One can see the similarity between the residuals of law $B$ and $C$ (Figure 5.4), and the sensitivity fields of $\nu$, $H_2$, and $H_3$ as mentioned and depicted in Figure 5.3

The Lankford coefficient [96] is an indicator used to describe the anisotropic plasticity behavior of sheet metals. The reported Lankford coefficient is equal to $r = \varepsilon^p_{33}/\varepsilon^p_{11}$ where $\varepsilon^p_{11}$ is the transverse plastic strain, $\varepsilon^p_{33}$ the out-of-plane plastic strain, which are computed

by assuming plastic incompressibility, and $\varepsilon^p_{22}$ the longitudinal plastic strain. This analysis is performed in the center area (see Figure 5.1(c)) of the specimen and the reported strains are the corresponding mean values. For elasto-plastic models B and C, the $r$-ratio is equal to 1. Only the anisotropic plasticity model (and the raw DIC results) allow for a ratio differing from 1.

Figure 5.6 shows the Lankford coefficients both for DIC and IDIC results (only for law $D$). The coefficient converges for both cases to a constant value as the level of plastic strain increases. The converged value of the Lankford coefficient is consistent with literature data of cold-rolled stainless steel [116]. Second, the model does not fully capture the experimentally observed anisotropy in the early stages of plasticity. This result shows that even if the identification of the anisotropic coefficients has been achieved, the assumption of a constant anisotropic behavior (Law $D$) is an approximation. This observation is consistent with the fact that the IDIC residuals are rather high at the end of cycle 1 and the beginning of cycle 2 compared to isotropic laws (see Figure 5.2).

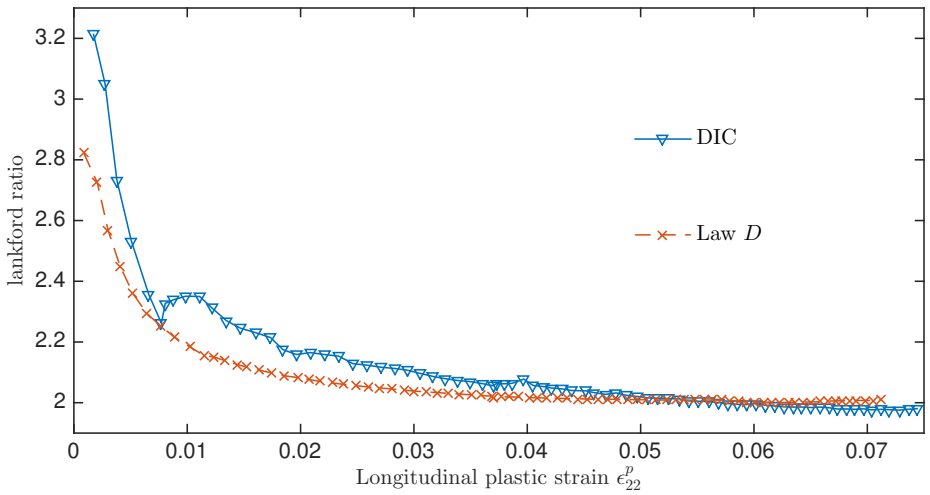


**Figure 5.6:** Lankford ratio evaluated from DIC and from the identified anisotropic elasto-plastic anisotropic (law $D$)

This section has shown that it is possible to determine *all* material parameters for an in-plane anisotropic plastic model in a *single* uniaxial experiment. This result has been achieved by combining kinematic and static measurements. The next section aims to validate the present results with a biaxial test.

## 5.4 Analysis of a biaxial experiment

This section investigates the mechanical behavior of a biaxial specimen, which is loaded with an electromechanical testing machine, mini-ASTREE (see Chapter 4). The sample thickness is 50 $\mu$m (*i.e.,* an additional pass was performed prior to final heat treatment in comparison with the previous case). 16-bit gray scale images are acquired with a digital camera (pco.edge) associated with a telecentric lens. The effective magnification is 12.5 $\mu$m per pixel or 80 pixels/mm. The gray level uncertainty is $\gamma_f = 233$ gray levels. The thickness of the specimen requires the surface to be maintained flat in the Region Of

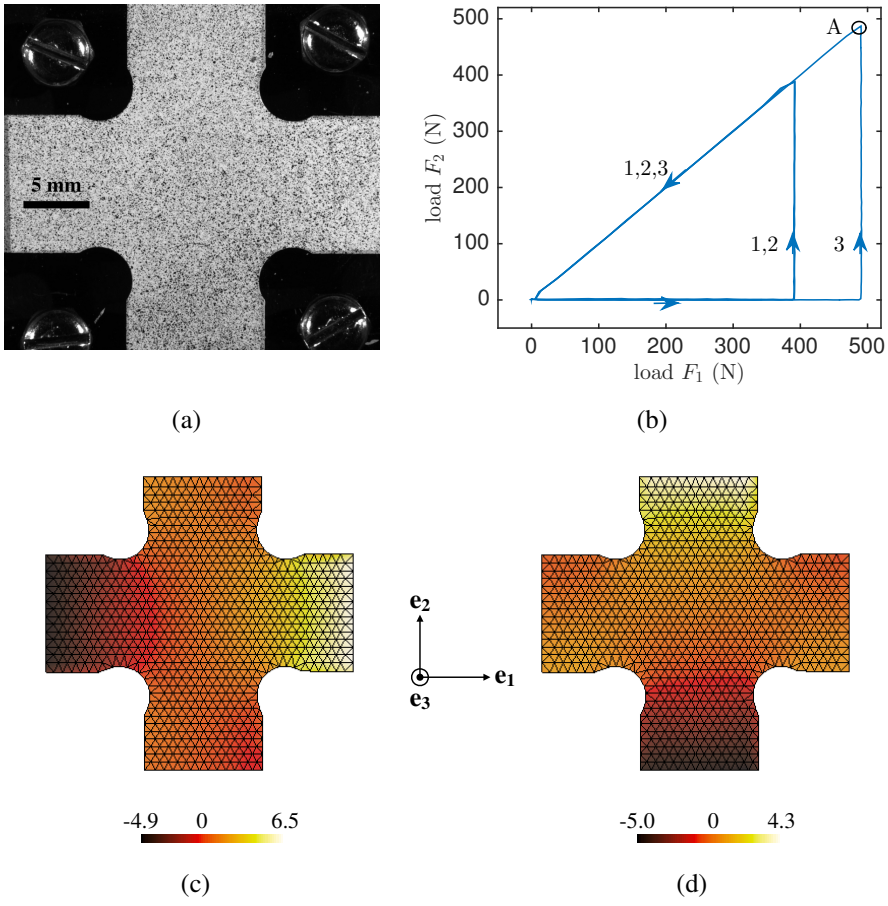


**Figure 5.7:** (a) Specimen and anti-wrinkling device (note the four screws on the four corners). (b) Prescribed loading history $F_2$ vs. $F_1$ consisting of successive triangles of increasing amplitudes. Displacement field components $u_1$ (c) and $u_2$ (d) at the maximum prescribed load amplitude corresponding to point $A$ of the loading path of Figure 5.7(b). The displacements are expressed in pixels (1 pixel $\leftrightarrow$ 12.5 $\mu$m)

Interest (which is crucial for 2D-DIC). An equivalent anti-wrinkling device as designed

for the uniaxial experiment is employed (Figure 5.7(a)). A triangular loading/unloading history is prescribed (Figure 5.7(b)) with load controlled mode. In the following analyses, the initialization of the sought parameters is based on the results obtained for the uniaxial specimen.

### 5.4.1 First identification: large ROI

Figure 5.7(c,d) shows the displacement field components $u_1$ and $u_2$ measured with 2D-DIC associated with the three-noded triangular mesh with linear interpolation (T3) at the maximum loading amplitude (point $A$, see Figure 5.7(b)). The same mesh is used for DIC and IDIC analyses. The maximum measured displacement is equal to 6.7 pixels corresponding to 83 $\mu$m. Figure 5.8 shows the strain field components $\varepsilon_{11}$ and $\varepsilon_{22}$ derived from the measured displacement field with DIC at point $A$ of the loading path (Figure 5.7(b)). As expected the strains are concentrated near the four fillet radii and their amplitudes remain small with a largest value of 1.2 % in accordance with the sought objective, namely less than 1.5 %. However, numerous fluctuations are seen in the vicinity of the four arms edges. An investigation of the DIC residual map reveals that this trend does not originate from the DIC routine (Figure 5.8(c)). The second hypothesis is that the anti-wrinkling system is not perfect.

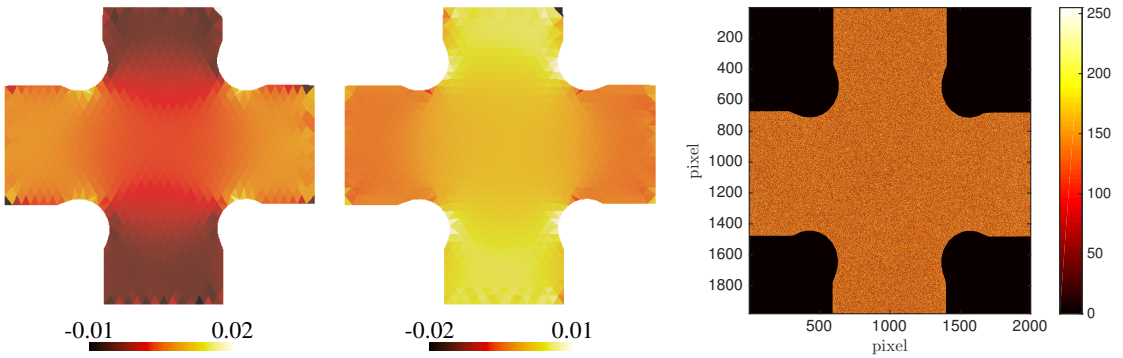


(a) $\varepsilon_{11}$ (b) $\varepsilon_{22}$ (c)

**Figure 5.8:** Strain fields $\varepsilon_{11}$ (a) and $\varepsilon_{22}$ (b), and residual map in gray level at point $A$ of the loading path of Figure 5.7(b) (the dynamic range of the pictures is 16 bits)

The identification is achieved by minimizing the global functional $\chi^2_I$. A sensitivity analysis is performed for law $D$ as it possesses the largest number of material parameters and the maximum strain level is lower than in the uniaxial case (*i.e.,* 8.8 %). Their initial values are gathered in Table 5.2 and correspond to the results obtained for the uniaxial specimen. The analysis consists of the evaluation of the kinematic ($[\boldsymbol{M}]_{IDIC}$), static

($[\boldsymbol{H}]_F$), and global ($[\boldsymbol{H}]_{IFDIC}$) Hessians with an initial numerical analysis associated with the same mesh and the measured boundary conditions with DIC.

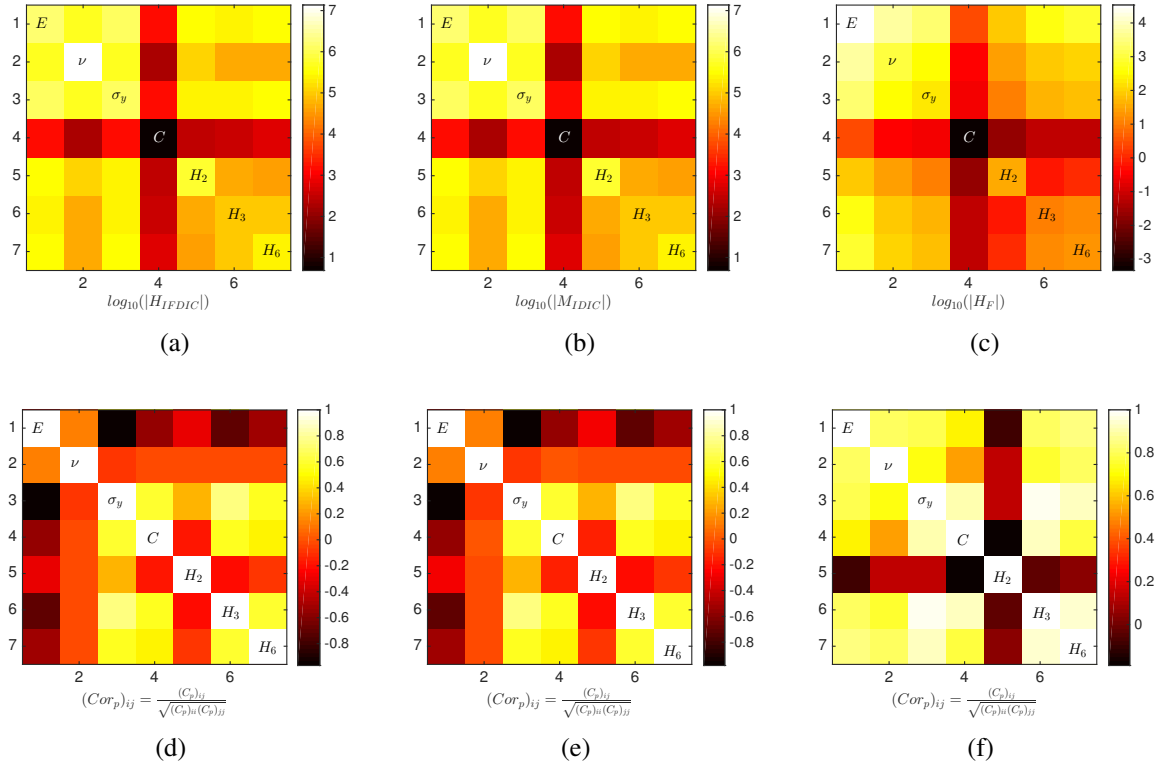


**Figure 5.9:** (a,b,c) Global ($[\boldsymbol{H}]_{IFDIC}$), kinematic ($[\boldsymbol{M}]_{IDIC}$), and static ($[\boldsymbol{H}]_F$) Hessians and (d,e,f) their corresponding cross-correlation matrices

Figure 5.9(a,b,c) shows the Hessians with a $\log_{10}$ scale and Figure 5.9(d,e,f) shows their corresponding cross-correlation matrices. First, the kinematic Hessian ($[\boldsymbol{M}]_{IDIC}$) has more influence on the identification than the static Hessian ($[\boldsymbol{H}]_F$) because their largest eigenvalues are separated by more than 3 orders of magnitude and $[\boldsymbol{H}]_{IFDIC} \approx [\boldsymbol{M}]_{IDIC}$. Second, the hardening modulus $C$ is insensitive for both kinematic and static Hessians. Conversely, the Poisson's ratio ($\nu$) has the highest sensitivity followed by $H_1$, $H_2$, and $H_3$ that account for the anisotropic plastic behavior. Regarding the cross-correlation matrices (Figure 5.9(d,e,f)), the Poisson's ratio has no correlation for the kinematic Hessian. Furthermore, the material parameters are more correlated to each other when looking at the static Hessian. In that case, the images are crucial for two reasons, namely, a greater sensitivity and less cross-correlations of the material parameters. To conclude on the sensitivity analysis, the behavior is mainly driven by an elastic behavior but small plastic strains occur near the four fillet radii. It worth noting that the material parameters $E$ and $\sigma_0$ are correlated only based on the kinematic data. The two parame-

ters affect the initiation of the plastic strain by two means, *i*) the higher the level of the Young's modulus the sooner the plastic regime sets in, *ii*) the lower the yield stress the sooner the plastic regime occurs as well.

Figure 5.10 shows the sensitivity maps for all material parameters associated with law $D$ at point $A$. First, the sensitivity map corresponding to the Poisson's ratio $\nu$ has the largest sensitive area. Second, the material parameters associated with the plastic behavior are only sensitive in the vicinity of the four fillet radii. These results are in agreement with the previous conclusion and show that the present approach is a powerful tool to summarize a large quantity of data.

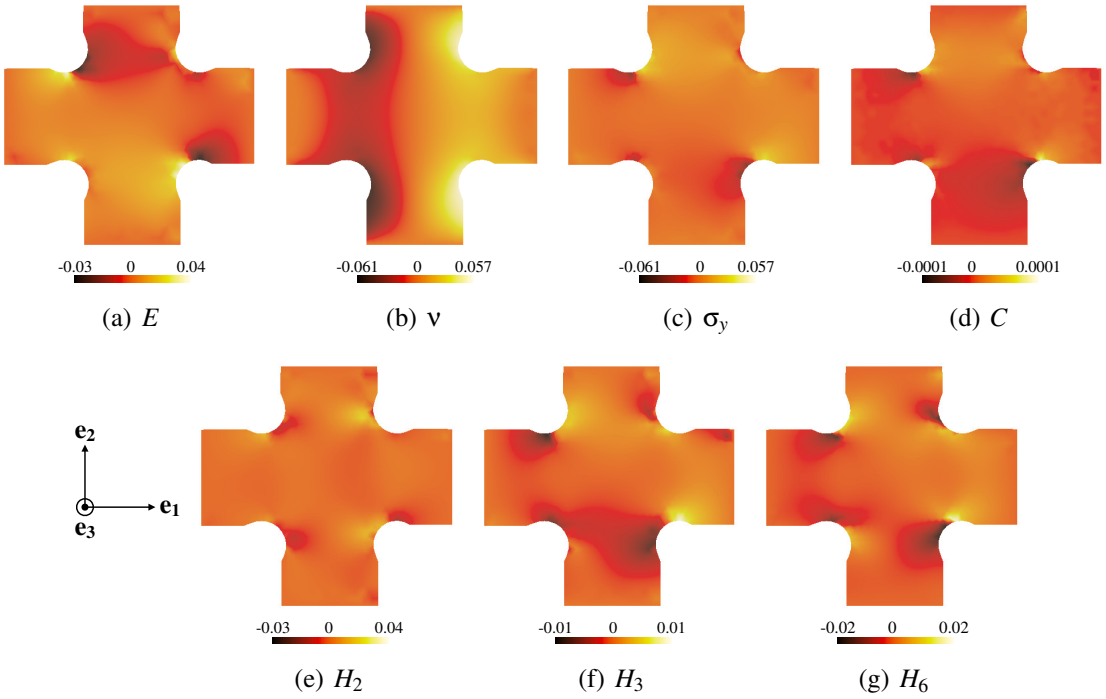


(a) $E$ (b) $\nu$ (c) $\sigma_y$ (d) $C$

(e) $H_2$ (f) $H_3$ (g) $H_6$

**Figure 5.10:** Sensitivity fields for all the material parameters of the law $D$ for the component $u_1$ (in $\mu$m) for a 2% variation of the parameters

The identification is performed with the four investigated laws and Figure 5.11 shows the registration residual history ($\chi_f$) for DIC and IDIC. The DIC residuals are smaller than the IDIC residuals, which are almost identical for the four investigated laws. The fact that the residuals decrease during unloading phases originates from the quasi-elastic behavior. After unloading, the material recovers almost everywhere its original shape.

Table 5.2 gathers the assessed material parameters for the four constitutive laws. The same Poisson's ratio value is obtained independently of the chosen constitutive model. The Young's modulus is affected when the model is elastoplastic. For the other material parameters, their values remain equivalent between the three elastoplastic models and

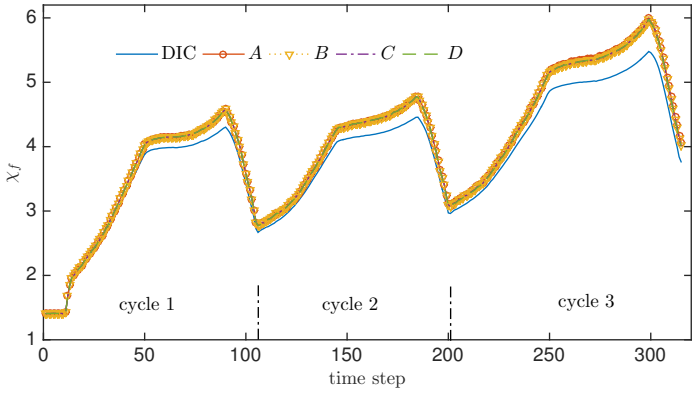


**Figure 5.11:** Global gray level residual history for DIC and for the four constitutive models investigated with IDIC

the assessed anisotropic coefficients reveal an anisotropic plastic behavior. Regarding the residuals, the indicators $\chi_I$ and $\chi_f$ are equal and the load residual $\chi_F$ decreases as the constitutive model becomes more complex. Using an elastoplastic model improves by 25 % the load residual. However, it remains large in comparison to the noise level (*i.e.,* 10 times higher). The change of global residual is small and there still is a model error. Last, the material parameters are different from the uniaxial identification, *i*) 10 % lower for the Young's modulus and *ii*) 10 % higher for the yield stress. Regarding the anisotropic parameters $H_2$ and $H_6$ are equivalent but $H_3$ has significantly changed.

**Table 5.2:** Identified parameters and identification residuals via IDIC for the four laws over the entire loading history cycle of the biaxial test

| law | $\chi_I$ $1^{st}$ — last | $\chi_f$ $1^{st}$ — last | $\chi_F$ $1^{st}$ — last | $E$ GPa | $\nu$ | $\sigma_0$ MPa | $C$ GPa | $c$ | $H_2$ | $H_3$ | $H_6$ |
|---|---|---|---|---|---|---|---|---|---|---|---|
| $p_0$ | 3.61 | | | 202 | 0.3 | 1420 | 9.1 | 10.3 | 0.88 | 0.86 | 1.06 |
| $A$ | 3.73—3.72 | 3.73—3.72 | 13.2—13.7 | 202 | 0.33 | — | — | — | — | — | — |
| $B$ | 3.75—3.71 | 3.75—3.71 | 11.9—10.6 | 181 | 0.33 | 1570 | 9.1 | — | — | — | — |
| $C$ | 3.75—3.71 | 3.75—3.71 | 11.8—10.6 | 181 | 0.33 | 1570 | 9.1 | 10.3 | — | — | — |
| $D$ | 3.76—3.71 | 3.76—3.71 | 11.4—10.3 | 177 | 0.33 | 1600 | 9.1 | — | 0.81 | 1 | 1.04 |

Figure 5.12 shows the measured and identified load histories for the four laws and for the two components $F_1$ and $F_2$. First, the loads do not return to zero as prescribed by the testing machine. Even if the assessed behaviors lead to an accurate description of the loading phases, the model is unable to capture the unloading phases. This error explains why the load residuals are large with respect to the noise level. The latter may originate from the anti-wrinkling system that prevents the material to return to a perfect unloaded

stage due to friction. However, qualitatively speaking, the biaxial trend is well captured by the elastoplastic models.

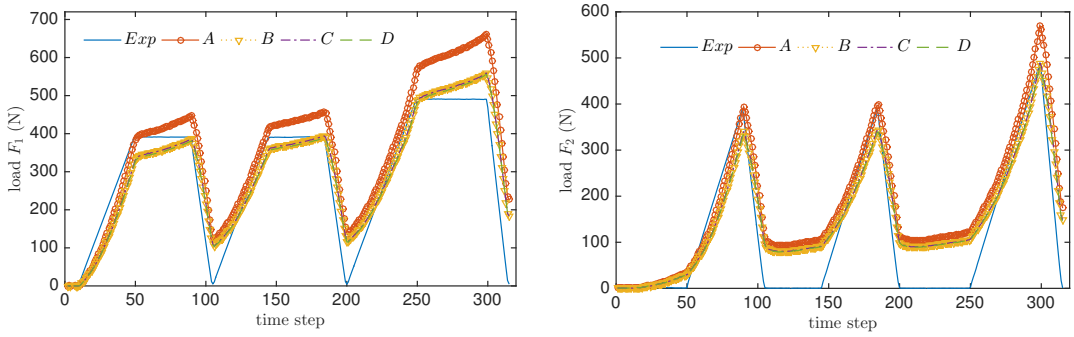


(a) (b)

**Figure 5.12:** Measured and computed load histories of (a) $F_1$ and (b) $F_2$

Figure 5.13 shows the two components $u_1$ and $u_2$ of the displacement field residual (difference between the IDIC and DIC displacement fields) at point A (Figure 5.7(b)). The highest differences are observed near the arm edges and the latter is stable and symmetrically distributed. It shows that the measured mechanical behavior does not correspond to the numerical solution. One possible explanation can be found in "line-tension theory," which is developed to account for the easy wrinkling of thin elastic membranes [117]. A theorem, which was initially formulated for masonry structures by Del Piero [118], can be extended to such a framework [119] showing that the convex envelope of connected components of traction-free boundaries are stress-free. Hence such regions, which coincide precisely with the support of the most salient displacement residuals, are not expected to be well described by the bulk constitutive law and the anti-wrinkling device cannot totally prevent such phenomena. However, after a redefinition of the effective free boundaries, the elastoplastic description should hold as long as no compressive stresses are generated. To test this hypothesis, a second analysis is performed [117, 118, 119].

### 5.4.2 Second identification: smaller ROI

A smaller ROI is investigated without the regions that are impacted by wrinkling. Figure 5.14 shows the component $u_2$ of the displacement field at point $A$ (Figure 5.7(b)) for (a) DIC, (b) IDIC with law $D$, and (c) the displacement field residual between the two. The IDIC analysis uses a refined mesh to capture more precisely the elastoplastic behavior in the vicinity of the four fillet radii. The results show that the maximum value of the residual is smaller by more than 1 order of magnitude than the solution given by the larger ROI.

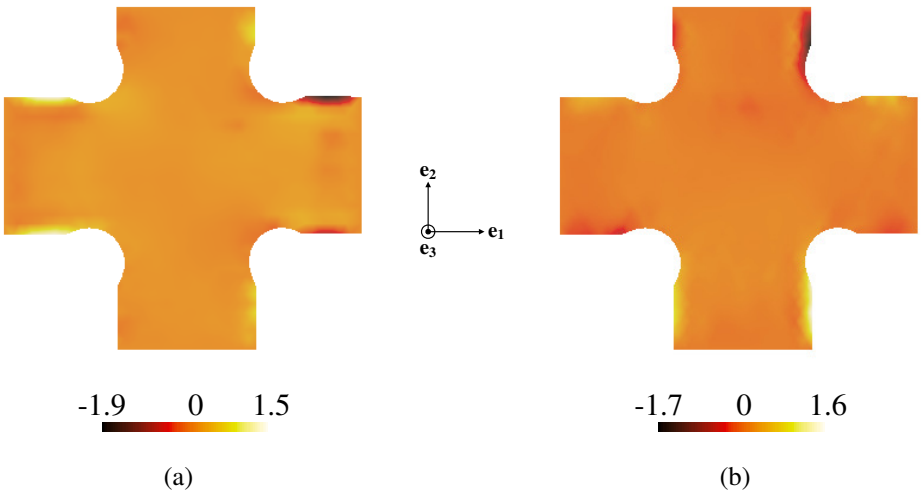


**Figure 5.13:** Components $u_1$ and $u_2$ of the displacement residuals (IDIC-DIC) for law $D$ (displacement differences are expressed in pixel)

This fact proves that the newly chosen region is less affected by wrinkles, which may prevent the identification of the material parameters.

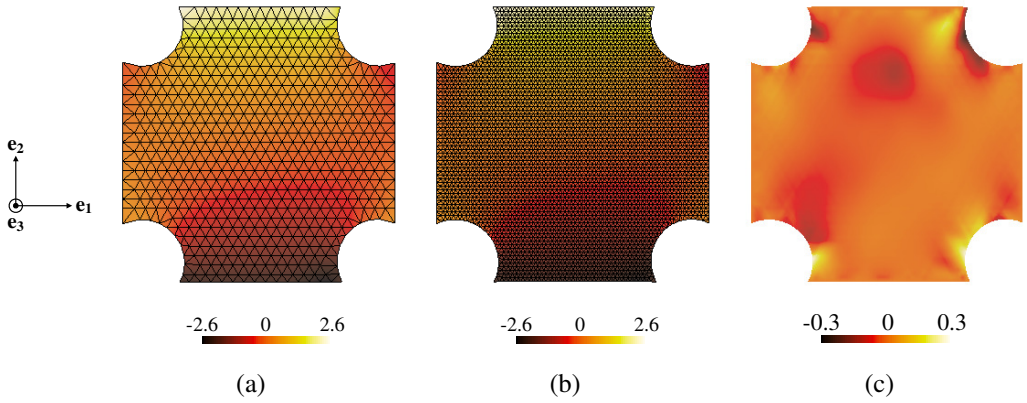


**Figure 5.14:** Displacement field component $u_2$ from (a) DIC, (b) IDIC with law $D$, and (c) the corresponding displacement residual at point $A$ of the loading path of Figure 5.7. The displacements are expressed in pixels (1 pixel $\leftrightarrow$ 12.5 $\mu$m)

Figure 5.15 shows the global Hessian ($[\boldsymbol{H}]_{IFDIC}$) and its cross-correlation matrix. The Poisson's ratio has no longer the largest level of sensitivity (see the results shown in Figure 5.9) but its influence is similar to the material parameters $E$, $\sigma_y$, and $H_2$. The smaller ROI corresponds to a smaller area that reduces the identifiability of the Poisson's ratio.

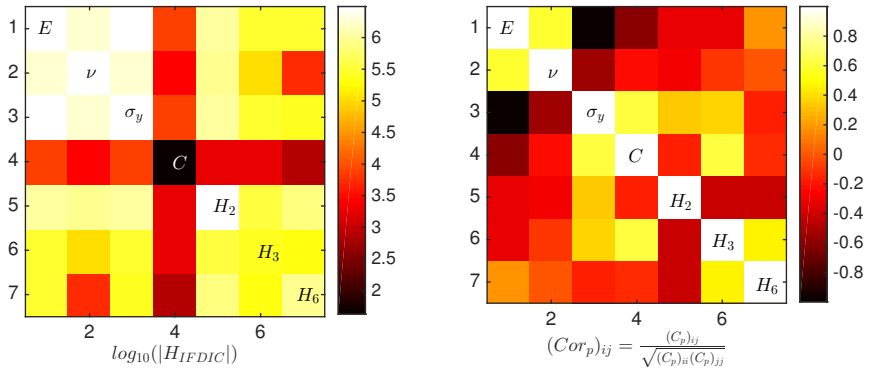


(a) (b)

**Figure 5.15:** (a) Global Hessian ($[\boldsymbol{H}]_{IFDIC}$) and (b) its cross-correlation matrix

Table 5.3 gathers the assessed material parameters for the four constitutive laws. Different Poisson's ratio values are obtained for the four constitutive models. Integrated DIC analyses are performed for law $D$ with $i$) a refined mesh with an average element size 20 % smaller than the standard IDIC mesh size ($D^*$) and $ii$) a coarser mesh equal to the one used for DIC ($D^{**}$). For the elastic model, (law $A$), the Poisson's ratio increases because a "compromise" is made between the truly elastic behavior and plasticity where the deformation is essentially isochoric (see Chapter 4). The Young's modulus is also in good agreement with literature data [23, 24]. The residuals slightly decrease as the law complexity increases and are smaller by 30 % than those with the larger ROI.

**Table 5.3:** Identified parameters and identification residuals via IDIC for the four laws over the entire loading history cycle and the smaller ROI. $D^*$ corresponds to the computation with a finer mesh and $D^{**}$ to the DIC mesh

| law | $\chi_I$ $1^{st}$ — last | $\chi_f$ $1^{st}$ — last | $\chi_F$ $1^{st}$ — last | $E$ GPa | $\nu$ | $\sigma_0$ MPa | $C$ GPa | $c$ | $H_2$ | $H_3$ | $H_6$ |
|---|---|---|---|---|---|---|---|---|---|---|---|
| $p_0$ | 2.56 | | | 202 | 0.3 | 1420 | 9.1 | 10.3 | 0.88 | 0.86 | 1.06 |
| $A$ | 2.71—2.70 | 2.71—2.70 | 11.8—13.0 | 202 | 0.35 | — | — | — | — | — | — |
| $B$ | 2.69—2.68 | 2.69—2.68 | 10.9—12.1 | 212 | 0.33 | 1350 | 9.1 | — | — | — | — |
| $C$ | 2.69—2.68 | 2.69—2.68 | 10.9—12.1 | 212 | 0.33 | 1350 | 9.1 | 10.3 | — | — | — |
| $D$ | 2.69—2.68 | 2.69—2.68 | 10.7—11.3 | 212 | 0.32 | 1350 | 9.1 | — | 0.86 | 0.84 | 0.96 |
| $D^*$ | 2.69—2.68 | 2.69—2.68 | 10.7—11.2 | 212 | 0.32 | 1350 | 9.1 | — | 0.86 | 0.84 | 0.96 |
| $D^{**}$ | 2.69—2.68 | 2.69—2.68 | 10.7—11.3 | 210 | 0.33 | 1370 | 9.1 | — | 0.88 | 0.84 | 1 |

Regarding the load residual ($\chi_F$), the same improvement is reached with an elasto-plastic law, but the newly chosen ROI does not improve their levels (*i.e.,* 10 times the noise level). In comparison with Section 5.3, the results obtained for the refined ROI are closer than those obtained from the larger ROI. Figure 5.16 shows the sensitivity fields

for law $D$. Their main contribution is close to the fillet radii. Thus, the mesh size is of importance for identification purposes but a strong refinement ($D^*$) does not improve the identification quality, even as compared to the coarse mesh ($D^{**}$), as shown in Table 5.3.

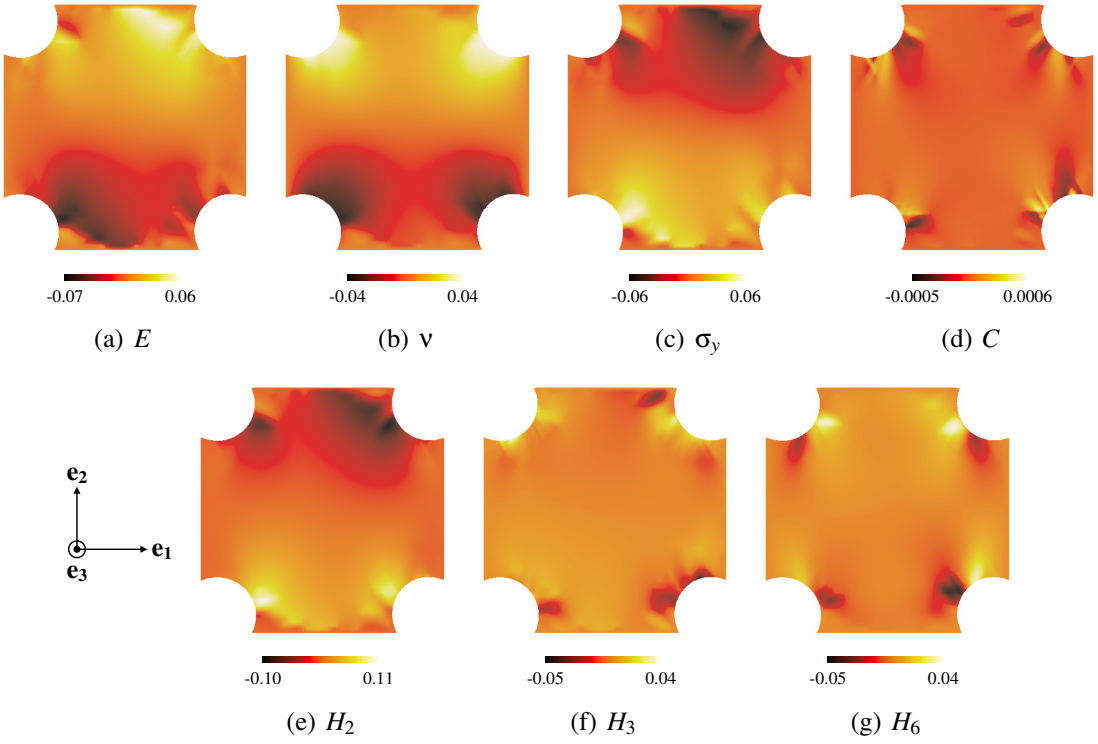


(a) $E$ (b) $\nu$ (c) $\sigma_y$ (d) $C$

(e) $H_2$ (f) $H_3$ (g) $H_6$

**Figure 5.16:** Sensitivity fields for all the material parameters of the law $D$ and the component $u_2$ ($\mu$m)

The anisotropic parameters are in good agreement with their uniaxial counterparts except for $H_6$ that differs by 10 %. The differences may originate from *i*) the plate itself that is thinner than its uniaxial counterpart by about 20 $\mu$m, *ii*) the biaxial test that reveals more of the mechanical behavior, and *iii*) the maximum strain which is significantly lower (8.8 % versus 1.2 %). To address this last point, the identification with the uniaxial experiment is carried out but for a lower longitudinal strain range (*i.e.,* 0-2 %), which corresponds to the first loading cycle. Table 5.4 shows the results of this new step, which is less stable in particular in terms of Young's modulus and yield stress, as they are more strongly correlated. Further, the set of parameters is not as close to the biaxial results as with the whole data set of the uniaxial experiment. It is believed that the main reason is due to the geometry of the uniaxial specimen where a more extended strain amplitude is needed to achieve a reliable identification. This final remark supports proposition *ii*).

**Table 5.4:** Identified parameters and identification residuals via I-DIC for the four laws over the first loading history cycle accounting for a 2 % maximum total strain value ($D^*$ corresponds to the coarse DIC mesh and "$1^{st}$ — last" corresponds to the first and last value of the residuals)

| law | $\chi_I$ $1^{st}$ — last | $\chi_f$ $1^{st}$ — last | $\chi_F$ $1^{st}$ — last | $E$ GPa | $\nu$ | $\sigma_0$ MPa | $C$ GPa | $c$ | $H_2$ | $H_3$ | $H_6$ |
|---|---|---|---|---|---|---|---|---|---|---|---|
| $p_0$ | 3.6 | | | 200 | 0.3 | 1300 | 10 | 10 | 1 | 1 | 1 |
| $A$ | 4.86 — 4.84 | 4.86 — 4.84 | 37.3 — 37.5 | 200 | 0.32 | — | — | — | — | — | — |
| $B$ | 5.48 — 3.88 | 5.48 — 3.88 | 9.65 — 11.7 | 130 | 0.26 | 124 | 15 | — | — | — | — |
| $C$ | 5.55 — 3.88 | 5.55 — 3.88 | 9.6 — 12.6 | 130 | 0.27 | 130 | 14 | 9.8 | — | — | — |
| $D$ | 5.5 — 3.9 | 5.5 — 3.9 | 9.0 — 20 | 170 | 0.27 | 1450 | 10.5 | — | 1.2 | 1.01 | 1.0 |
| $D^*$ | 5.8 — 4.0 | 5.8 — 4.0 | 9.1 — 21 | 166 | 0.27 | 1460 | 10.5 | — | 1.2 | 1.04 | 1.0 |

## 5.5 Conclusion

Four constitutive laws have been investigated with Integrated Digital Image Correlation to analyze a uniaxial test of an ultra-thin sheet of precipitation hardened stainless steel. A dedicated anti-wrinkling system is designed and employed to prevent non uniform out-of-plane displacements while loading and unloading the specimen. The identification is performed over the entire loading history accounting for 3 loading/unloading cycles. The four laws lead to different residuals and the anisotropic plastic law provides the best results and appears to be necessary to assess the material parameters. Thanks to full-field measurements, all the plain strain parameters could be calibrated with a *unique* uniaxial test.

The methodology is extended to a biaxial experiment with the objectives to assess the early plastic behavior of the material in TH1050 condition and to validate the "uniaxial" identification. The analysis of the experiment revealed that the specimen undergoes wrinkling on the connecting arms. The identification suffers from this effect as shown in the kinematic residual fields.

To address this issue a smaller region of interest that focuses on the specimen center but considers the four fillet radii where plasticity occurs is chosen. The results show that this choice allows for a better identification since the elastoplastic behavior is less corrupted by experimental errors. Plastic anisotropy provides the best result but does not appear as necessary to predict the mechanical response of the investigated material as for the uniaxial experiment because the strain range was significantly lower (*i.e.,* 1.2 % instead of 8.8 %). This study shows that experiments on ultra-thin specimens may easily be affected by wrinkling. Special care has to be exercised to avoid or minimize such effects.

Last, some small differences between the two sets of material parameters identified exist. Authors have already reported such differences between uniaxial and biaxial ex-

periments with respect to anisotropic behaviors [109, 107, 108]. Let us emphasize that possible causes for such a discrepancy may be the explored strain range but more importantly by the fact that the geometry of uniaxial test samples is less sensitive to material parameters (*e.g.,* associated with anisotropic plasticity).

Chapter 6 aims to assess the material parameters of a crystal plasticity law [18] with a micro experiment. Because 17-7 PH stainless steel has very fine grains (see Figure 2.2 in Chapter 2) an IF-steel, which has a similar microstructure but larger grains, is used.

# Chapter 6
# Crystal plasticity parameter identification with 3D measurements and IDIC

Reproduced from: Morgan Bertin, Chaowei Du, Johan P.M. Hoefnagels, and François Hild, *Crystal plasticity parameter identification with 3D measurements and Integrated Digital Image Correlation*, Acta Materialia, September 2016, (116) 321-331, doi: http://dx.doi.org/10.1016/j.actamat.2016.06.039

## Abstract

The present study unravels details of the micromechanical behavior of a microspecimen made of IF-steel. A triangular prism is machined via focused ion beam (FIB) and contains two ferritic grains. Four experimental tools are integrated to identify the material's crystal parameters: *i*) an optical confocal microscope captures height profile images, *ii*) an in-situ tensile stage prescribes the loading history to the macrospecimen, *iii*) a global Digital Image Correlation (DIC) algorithm measures the 3D surface displacement fields, and *iv*) an extension of Integrated-DIC for 3D displacement fields is implemented to assess the micromechanical behavior. It is demonstrated that with this methodology the identification of the boundary conditions and crystal plasticity parameters is successfully achieved.

## 6.1 Introduction

The mechanical properties of materials often originate from physical and multi-scale phenomena that are due to complex and heterogenous microstructures. One of the first method to consider heterogeneous media for computing macromechanical responses is based on homogenization [120]. In order to solve this problem micromechanical frameworks have been developed for elastic materials [121] and in elastoplasticity [100]. Due to complex behaviors and the difficulty to observe and measure at the microscale the main challenge remains the identification of the constitutive parameters.

The lattice structure (*e.g.,* FCC, BCC) is considered to derive the constitutive equations for single crystals [122, 123, 124]. The present study aims at coupling experimental and numerical results and provides a compromise between a reasonable computation time

and a sufficiently small scale to achieve the observation of the micromechanical behavior in a material with real engineering applications. Under the same assumptions, Raabe *et al.* [125] characterized the micromechanical behavior in polycrystalline aluminum with the measurement of the displacement on the observed surface. The authors demonstrated by 2-dimensional Finite Element analyses that the micromechanical response obtained from the crystal plasticity law was closer to the experimental observation and was able to predict the stress and strain heterogeneities. However, the underlying microstructure is a key feature and 3D orientation mapping has been performed by Musienko *et al.* [126] to compare experimental and numerical strains also on polycrystalline aluminum. Using a 3D analysis, Martins *et al.* [127] focused on the residual strain measured in a weld zone of 316L stainless steel.

Digital Image Correlation enables full displacement and strain fields to be measured and provides insight into the micromechanics of solids. Imaging systems capable of higher magnifications allow the heterogeneity of the micromechanical response to be evaluated. A first approach [128] using full field measurements obtained from SEM acquisitions has led to the identification of a single crystal plasticity law. Dmitrieva *et al.* [129] studied shear bands in a single copper crystal and Tasan *et al.* [130] characterized micromechanical banding effects. Other techniques may be used, *e.g.,* Raabe *et al.* [131] acquired pictures with a confocal microscope.

The combination of both experimental and numerical aspects has been investigated by Héripré *et al.* [132] while applying the Finite Element Model Updating technique (FEMU [58]). Tasan *et al.* [133] proposed an integrated experimental-numerical approach to investigate stress-strain partitioning in multiphase alloys, although, the mechanical properties of the material have been obtained with a separate technique, *i.e.,* nano indentation tests. Guery *et al.* [134] have identified constitutive parameters of the law proposed by Méric and Cailletaud [18] using full field measurement, SEM acquisitions and FEMU-UF. The results provide an internal check of the constitutive model with respect to the experiment with the identified parameters. However, several difficulties remain (*e.g.,* unknown underlying microstructure) and the specimen design is still one of the biggest challenges because it is hard to build and to test mechanically.

The objective of this chapter is to perform an investigation at the microscale and to identify the material parameters of a crystal plasticity model with Integrated Digital Image Correlation (IDIC [135, 86]). Figure 6.1 shows the designed identification procedure.

Initially, the crystallographic features, *i.e.,* phase, grain (size, number and orientation) and the geometry of the studied volume are assessed and lead to the design of a representative 3D numerical model. Secondly, the out-of-plane displacement holds essential information regarding the active slip systems. Therefore an experimental method is introduced that utilizes confocal microscopy combined with a 3D surface global DIC formulation to quantify full three-dimensional displacement fields of the specimen surface

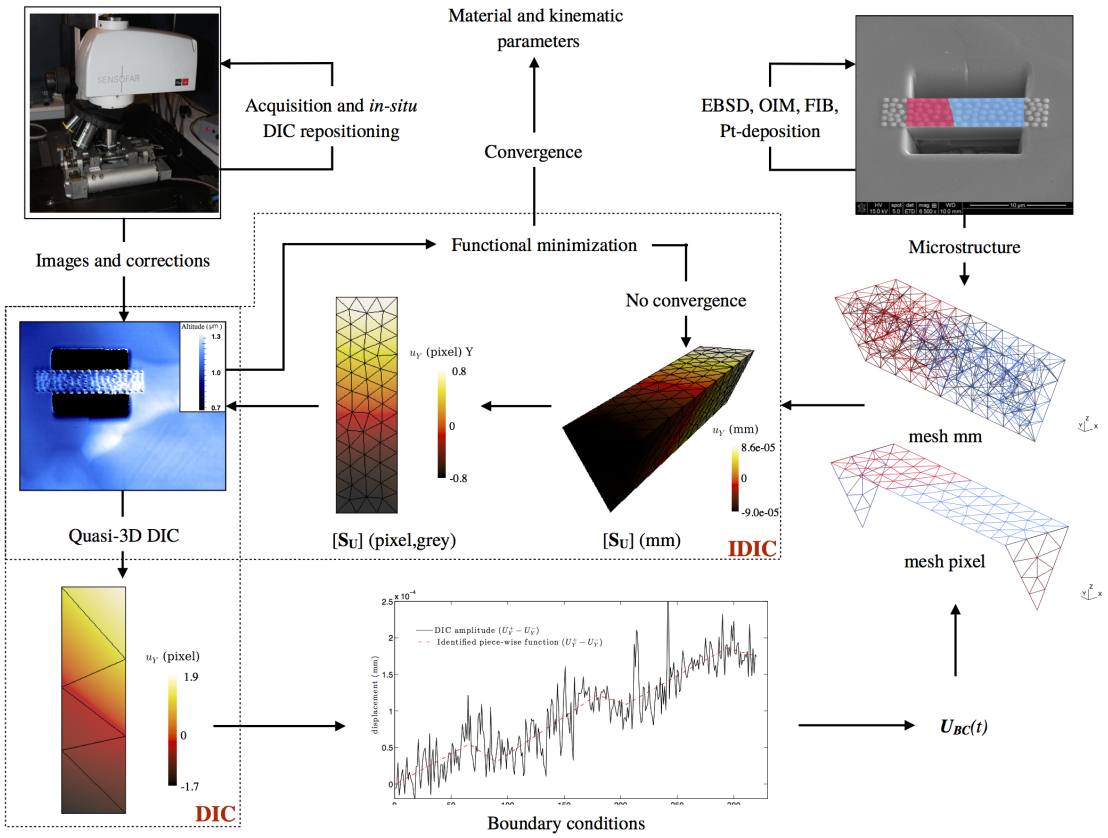


**Figure 6.1:** Schematic view of the methods used herein to extract boundary conditions and crystal plasticity parameters. The different steps of this methodology are explained in Section 2

and use these 3D data to extract boundary conditions and identify crystal plasticity parameters. Because of the relatively high noise level computations are run with stabilized boundary conditions. Finally, the sought parameters are identified with integrated-DIC that combines all experimental data, *i.e.,* the surface height profiles, constitutive model, and crystallographic features.

The chapter is organized as follows. Section 6.2 introduces the experimental and numerical tools utilized herein. Section 6.3 shows the experimental results prior to the identification discussed in Section 6.4.

## 6.2 Coupled experimental/numerical procedure

The objectives are *i*) to observe a crystal-specific micromechanical behavior under confocal microscopy, *ii*) to quantitatively measure the 3D surface displacement field at the grain scale with DIC, *iii*) to simulate the mechanical response with a representative model of the microstructure and the chosen crystal plasticity law, and *iv*) to couple experimental and numerical results in a single numerical framework to identify (as much as possible) the material and kinematic unknowns. The experimental methodology relies on the measurement of surface height profiles of a microspecimen ($\mu$-specimen) within a macroscopic sample that is mechanically loaded in tension.

### 6.2.1 Specimen

To demonstrate the potential of the proposed technique a relevant engineering material is chosen for this study, namely, 1-mm thick as-received IF-steel sheet. The latter possesses a very low carbon content and Table 6.1 gathers its chemical composition. IF steel is widely used, *e.g.,* in the automotive industry, for its deep drawability properties [136].

**Table 6.1:** Chemical composition of the studied IF-steel

| Composition | C | Mn | Al | Ti | Nb | Si | S | P | N(ppm) | Fe |
|---|---|---|---|---|---|---|---|---|---|---|
| (wt %) | 0.0022 | 0.09 | 0.015 | 0.033 | 0.008 | 0.003 | 0.007 | 0.012 | 28 | bal. |

The desired mechanical properties of IF-steels are, *a*) low yield stress, *b*) high hardening modulus resulting in stress levels after the material has been plastically deformed, *c*) high Lankford coefficients to improve deep-drawability capabilities and *d*) high fracture strain. The ferritic microstructure is body-centered cubic (BCC). The average grain size is of the order of 10 $\mu$m.

The preparation of the specimen requires four steps:

*i*. From the 1-mm thick sheet, a large specimen is cut (50 mm $\times$ 10 mm) and ground down to 0.3 mm thickness and polished on both sides, to yield a very flat specimen with the two surfaces parallel to each other.

*ii*. A large surface area of the large specimen is investigated using Orientation Imaging Microscopy (OIM, see Figure 6.2(a,b)). The location of the $\mu$-specimen is chosen to contain two grains that are larger than 15 $\mu$m having a clean grain boundary and a misorientation angle less than 1° within the grain so that both crystal and structure are relatively clean (Figure 6.2(c)).

*iii*. The $\mu$-specimen is milled using Focused Ion Beam technique (Figure 6.2(d)). The obtained $\mu$-specimen is 12 $\mu$m long and 4 $\mu$m wide with an equilateral triangular basis. Its length and depth are a compromise between a size consistent with the resolution of confocal microscopy and the milling speed of the FIB process.

*iv*. The last step is platinum deposition to create a random pattern for DIC purposes. The latter is obtained by depositing 20-nm high and 0.8 $\mu$m in diameter semi-spherical dots at specific locations. Their size has been adapted with respect to the confocal microscope features.

Figure 6.2 shows secondary electron images related to steps $(iii)$ and $(iv)$. Figure 6.2(d) shows the underlying microstructure and the grain boundary by observation from the side. Furthermore, it validates the assumption that the apex line of the $\mu$-specimen is entirely free. Figure 6.2(e) shows the pattern obtained after platinum deposition. The latter has also been deposited on the border of the $\mu$-specimen to perform DIC on a larger area.

Table 6.2 gathers the lattice orientations of the two grains identified from the OIM analysis.

**Table 6.2:** Euler angles of the two grains measured via OIM and maximum misorientation angle ($\delta$) within each grain

| | Euler angle (deg) | | | misorientation (deg) |
|---|---|---|---|---|
| Denomination | $\psi$ | $\theta$ | $\phi$ | $\delta$ |
| Grain 1 (red) | 281 | 8 | 47 | 0.70 |
| Grain 2 (blue) | 211 | 45 | 150 | 0.76 |

### 6.2.2 Experimental protocol

Figure 6.3 shows the experimental apparatus within the confocal microscope, *i.e.,* the large specimen clamped in the tensile stage. Before starting the experiment, the $\mu$-specimen is successively, $i$) positioned and aligned inside the tensile stage, $ii$) aligned with the translation and rotation stage, and $iii$) positioned in the center of the field of view of the sensor. During the experiment the large specimen is subjected to a velocity equal to 0.5 $\mu$m.s$^{-1}$ and at approximatively every 5 $\mu$m stopped while the image acquisition procedure is performed. Because the early stage of plastic strain and its corresponding kinematic hardening behavior are being sought, three cycles corresponding to 1 %, 2 % and 3 % global strain are applied without compression.

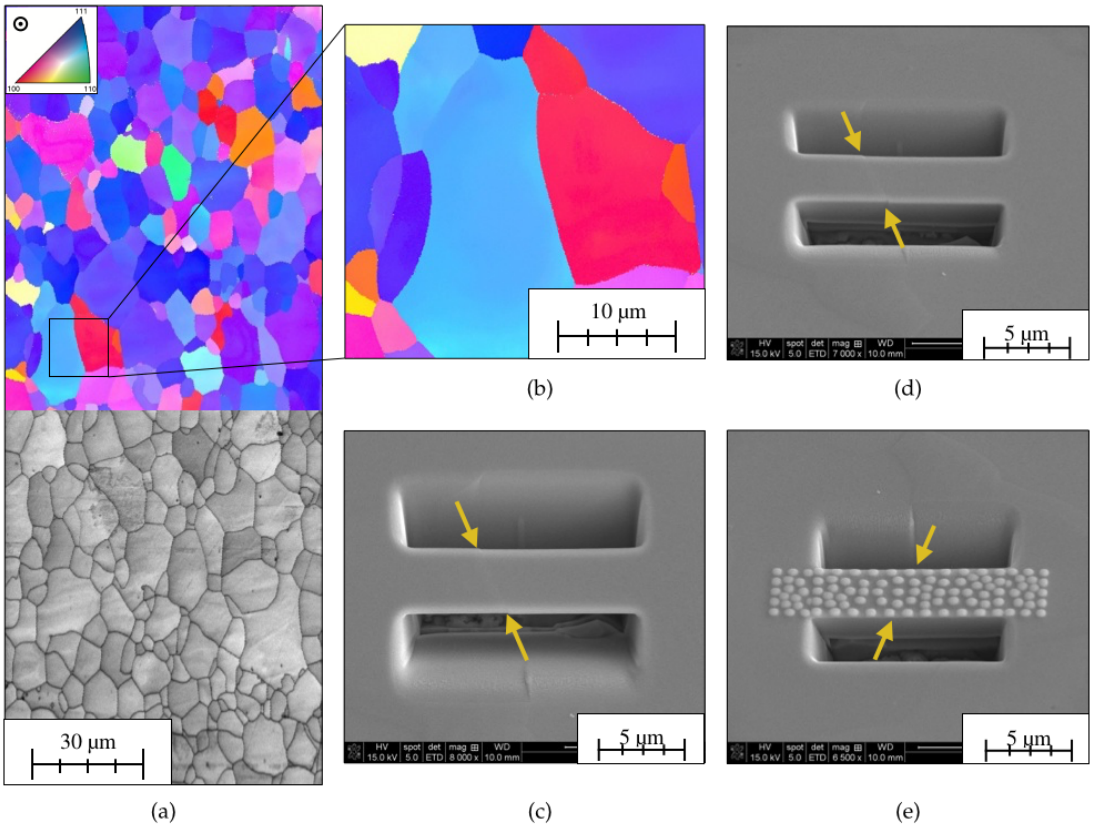


**Figure 6.2:** Image Quality (IQ) map (a) and Inverse Pole Figure (IPF) maps (a,b), resulting from the OIM measurement of the studied IF-steel. The longitudinal direction of the sample is the horizontal direction in all the figures. (b) Chosen location for the $\mu$-specimen and (c) $\mu$-specimen after the FIB process. (d) $\mu$-specimen observed with a tilt of 52°. The underlying microstructure and the grain boundary are observed. (e) $\mu$-specimen after platinum deposition. The arrows depict the location of the grain boundary

Since the $\mu$-specimen can never be perfectly centered on the microscale it moves in the field of view when strained. Therefore, an in-house routine was written to maintain the $\mu$-sample inside the field of view by correcting the rigid body motions using DIC and controlling the motorized $(x,y)$-sample accordingly.

The first image of the experiment corresponds to the reference, then for each load step, a first image is captured to evaluate the rigid body motions. The latter ones are applied as a correction by moving the motorized $(x,y)$-stage and finally a second image is captured. In the $z$-direction, the contraction of the large specimen will move the $\mu$-sample out of the depth of field. An auto-frontal procedure is used to address this issue.

Height profile images are captured in confocal profilometry mode by a Sensofar Pl$\mu$2300 Optical Confocal Microscope using a CCD camera (definition: $557 \times 557$ pixels) with a

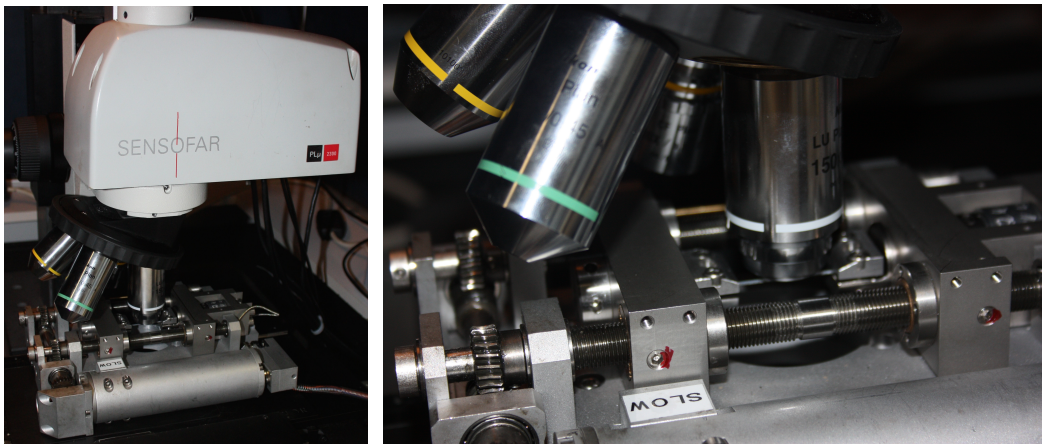


**Figure 6.3:** Experimental apparatus with the tensile stage on motorized $(x,y)$-sample positioning stage within a Sensofar optical profiler (150× magnification lens)

Nikon EPI 150× objective lens, resulting in a square field of view of $61 \times 61$ $\mu$m$^2$. This technique allows for a very small resolution in height (estimated to be 9 nm for this particular specimen configuration) whereas the in-plane resolution is limited by the diffraction limit of the blue light wavelength. However, a careful inspection of the height profiles revealed some artifacts caused by, *i*) lens defects and dust particles, and *ii*) the CCD pixel positions. Both errors were identified to be systematic because they remain at the same location on the images as long as the imaging parameters are fixed and the same lens is used.

Figure 6.4(a) shows an image with the systematic errors previously listed. The correction method consists of an acquisition under the identical parameters of 400 images at 400 random locations on a flat reference surface. All images are averaged, *i.e.,* added and normalized by the total number of images, and a plane is fitted and subtracted to this average profile to obtain a mean height level of zero mean with the corresponding root mean square error in the height level as small as possible. This process allows only the systematic error to be kept (Figure 6.4(b)) and by subtraction from all the experimental images the biases are almost completely removed without corrupting the experimental data. This procedure helps the DIC computation that needs reliable height levels over time. The loads are also measured and the standard resolution is evaluated as $\gamma_F = 1$ N.

### 6.2.3 3D Digital Image Correlation

Global DIC [68] relies on the registration of an image $f$ in the reference configuration and a series of pictures $g$ in the deformed configurations. The specific approach followed herein adds to the conventional 2D approach the out-of-plane displacement as an offset to the height conservation [137, 138, 139]. The registration problem consists of minimizing

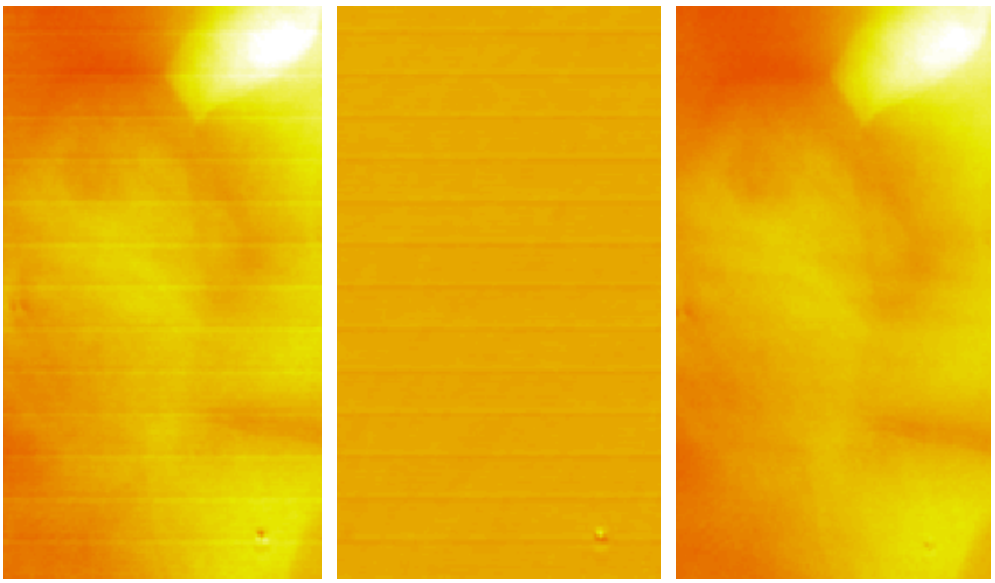

(a) (b) (c)

**Figure 6.4:** (a) Systematic errors on a profile image generated by the confocal microscope. Fringes and dust particles are present that are detrimental for the DIC computations. (b) Image correction obtained from the random acquisition of 400 images of a reference surface, and (c) profile image corrected from the systematic bias

the sum of squared differences between the deformed image corrected by the measured 3D displacements $\boldsymbol{u}(\boldsymbol{x},t) = u(\boldsymbol{x},t)\boldsymbol{e}_x + v(\boldsymbol{x},t)\boldsymbol{e}_y + w(\boldsymbol{x},t)\boldsymbol{e}_z$ and the reference image (written for each time $t$ independently) over the Region of Interest

$$\chi_f^2(t) = \frac{1}{2\gamma_f^2 N_\Omega} \sum_\Omega \left(g(\boldsymbol{x} + u(\boldsymbol{x},t)\boldsymbol{e}_x + v(\boldsymbol{x},t)\boldsymbol{e}_y, t) - f(\boldsymbol{x},t) - w(\boldsymbol{x},t)\boldsymbol{e}_z\right)^2 \tag{6.1}$$

with respect to the parameterization of the sought displacement fields $\boldsymbol{u}(\boldsymbol{x},t)$, where $\boldsymbol{x} = x\boldsymbol{e}_x + y\boldsymbol{e}_y$ is any considered pixel. Ten images have been acquired initially and the standard deviation is evaluated to be $\gamma_f = 9$ nm. The minimization of $\chi_f^2$ is achieved by successive linearizations and corrections, using a modified Gauss-Newton scheme

$$[\boldsymbol{M}]\{\delta\boldsymbol{u}\} = \{\boldsymbol{b}^{(i)}\} \tag{6.2}$$

where $[\boldsymbol{M}]$ is the DIC matrix, $\{\delta\boldsymbol{u}\}$ the vector gathering all increments of measured displacement amplitudes, and $\{\boldsymbol{b}^{(i)}\}$ the residual column vector at iteration $i$. The DIC matrix reads

$$M_{ij} = \sum_\Omega \left(\boldsymbol{\nabla} f(\boldsymbol{x}) \cdot \boldsymbol{\psi}_i(\boldsymbol{x})\right)\left(\boldsymbol{\nabla} f(\boldsymbol{x}) \cdot \boldsymbol{\psi}_j(\boldsymbol{x})\right) \tag{6.3}$$

and the right hand side term

$$b_i = \sum_{\Omega} \left(\boldsymbol{\nabla} f(\boldsymbol{x}) \cdot \boldsymbol{\psi}_i(\boldsymbol{x})\right) \left(f(\boldsymbol{x}) - g(\boldsymbol{x} + \tilde{\boldsymbol{u}}(\boldsymbol{x}))\right) \tag{6.4}$$

where $\tilde{\boldsymbol{u}}(\boldsymbol{x})$ is the current estimate of the displacement field and the image gradient is enriched with the variations of height levels, namely, $\boldsymbol{\nabla} f = \frac{\partial f}{\partial x}\boldsymbol{e}_x + \frac{\partial f}{\partial y}\boldsymbol{e}_y - \boldsymbol{e}_z$. A consequence of the addition of the out-of-plane displacement in the functional is that the problem has more degrees of freedom that might affect the minimization.

The integration of mechanical and kinematic constraints into the 3D-DIC problem, namely Integrated-DIC (IDIC), is performed by choosing as unknowns the sought parameters associated with a constitutive law or boundary conditions (Chapter 4). The sensitivity fields $\boldsymbol{S}_U(\boldsymbol{x})$ [41] are chosen as a basis of functions for the displacement field

$$[\boldsymbol{S}_U] = \frac{\partial \{\boldsymbol{u}\}}{\partial \{\boldsymbol{p}\}} \tag{6.5}$$

where $\{\boldsymbol{u}\}$ is the computed nodal displacement vector, $\{\boldsymbol{p}\}$ is the vector gathering the unknown parameters, *i.e.,* sought material parameters or boundary conditions. Furthermore, specific features of the loading history may or may not be sensitive. Treating an image series is equivalent to summing over the corresponding contributions at each time step: $\chi_f^2 = 1/N_t \sum_{t=1}^{N_t} \chi_f^2(t)$ to probe the sensitivities over the whole time domain. The solution at convergence gives an evaluation of the model error compared to the noise level. This indicator is useful because it allows the user to validate or not the investigated constitutive law(s) (see Chapters 4 and 5).

Last, if the same mesh is used, and the DIC matrix has been computed IDIC simply consists of projecting the nodal displacement field onto the sensitivity fields [62]. Thus, the sought parameters are identified by iteratively solving the linear system until convergence

$$\{\delta \boldsymbol{p}\} = \frac{1}{2\gamma_f^2} [\boldsymbol{M}]_{IDIC}^{-1} [\boldsymbol{S}_U]^t \{\boldsymbol{b}\} \tag{6.6}$$

where $[\boldsymbol{M}]_{IDIC} = 1/(2\gamma_f^2)[\boldsymbol{S}_U]^t[\boldsymbol{M}][\boldsymbol{S}_U]$ is the kinematic Hessian. The covariance matrix of the identified parameters is written as (Chapter 3)

$$[\boldsymbol{C}_p^I] = [\boldsymbol{M}]_{IDIC}^{-1} \tag{6.7}$$

where $\langle \bullet \rangle$ is the mean value of $\bullet$. Another useful indicator is the correlation matrix (no index summation used), where $i$ refers to the row number and $j$ the column number of the sought parameter

$$(Cor_p)_{ij} = \frac{(C_p)_{ij}}{\sqrt{(C_p)_{ii}(C_p)_{jj}}} \tag{6.8}$$

### Crystal plasticity model

To demonstrate the potential of the proposed technique to identify parameters of a crystal plasticity model, the Méric and Cailletaud [18] model is chosen. It is based on the decomposition of the total strain into an elastic and plastic strain. The elastic behavior assumes cubic symmetry in agreement with the BCC lattice. Using the *Kelvin-Voigt* notations, Hooke's fourth-order tensor $[\mathbb{C}]$ depends on three elastic constants of the material, namely $C_{11}$, $C_{12}$ and $C_{44}$. The plastic deformation initiates from crystallographic slip in the crystal lattice and satisfies incompressibility. A slip system ($\theta$) is defined by a slip plane $\boldsymbol{n}_0^\theta$ and a slip direction on the plane $\boldsymbol{s}_0^\theta$ in the initial configuration of the lattice ($\bullet_0$). In the case of a BCC crystallographic lattice, 24 slip systems are considered, namely 12 principal slip systems from $\langle 110 \rangle$ and 12 secondary systems from $\langle 112 \rangle$. The gradient tensor $\boldsymbol{F}^\theta = \boldsymbol{\nabla}_0^t \otimes \boldsymbol{x}$, where $\otimes$ is the dyadic product, corresponds to the lattice strain

$$\boldsymbol{F}^\theta = \boldsymbol{I} + \gamma^\theta \boldsymbol{s}_0^\theta \otimes \boldsymbol{n}_0^\theta \tag{6.9}$$

where $\gamma^\theta$ is the applied shear on the $\theta^{th}$ slip system, $\boldsymbol{I}$ is the second order identity tensor. The linear elasticity law relates the second Piola-Kirchhoff stress tensor $\boldsymbol{S} = J_e \boldsymbol{F}_e^{-1} \boldsymbol{\sigma} \left(\boldsymbol{F}_e^t\right)^{-1}$ where $\boldsymbol{\sigma}$ is the stress tensor and the Green-Lagrange strain tensor $\boldsymbol{E}_e = 1/2(\boldsymbol{F}_e^t \boldsymbol{F}_e - \boldsymbol{I})$; $\boldsymbol{S} = \mathbb{C} : \boldsymbol{E}_e$, where $\bullet : \bullet$ is the double inner product. Since an elasto-viscoplastic framework is assumed, the plastic strain rate is driven by the resolved shear stress on each slip system $\theta$. The gradient rate tensor reads

$$\boldsymbol{L}^\theta = \dot{\boldsymbol{F}}^\theta \boldsymbol{F}^{\theta-1} = \dot{\gamma}^\theta \boldsymbol{s}_0^\theta \otimes \boldsymbol{n}_0^\theta \tag{6.10}$$

where $\dot{\gamma}^\theta$ the resolved shear stress rate on the $\theta^{th}$ slip system. The orientation of the lattice is important with respect to the loading direction. Thus, for $\Theta$ slip systems the velocity gradient tensor reads

$$\boldsymbol{L} = \sum_{\theta=1}^{\Theta} \dot{\gamma}^\theta \boldsymbol{s}_0^\theta \otimes \boldsymbol{n}_0^\theta = \sum_{\theta=1}^{\Theta} \dot{\gamma}^\theta \boldsymbol{P}_0^\theta \tag{6.11}$$

where $\boldsymbol{P}_0^\theta = \boldsymbol{s}_0^\theta \otimes \boldsymbol{n}_0^\theta$ is the so-called non-symmetric Schmid tensor. The decomposition of the deformation gradient rate tensor becomes

$$\boldsymbol{L} = \boldsymbol{L}_e + \boldsymbol{F}_e \boldsymbol{L}_p \boldsymbol{F}_e^{-1} \tag{6.12}$$

where $\boldsymbol{L}_e$ and $\boldsymbol{L}_p$ are the elastic and plastic gradient rate tensors. To complete the constitutive description of the crystalline material, the plastic slip rates (6.10) rely on the resolved shear stress. The relationship between the resolved shear stress $\tau^\theta$ and the shear rate $\dot{\gamma}^\theta$ reads

$$\dot{\gamma}^\theta = \left\langle \frac{|\tau^\theta - cx^\theta| - \tau_0}{K} \right\rangle^n \eta^\theta \tag{6.13}$$

where $\tau_0$ is the critical resolved shear stress, $c$ is the hardening coefficient, $(K,n)$ are material constants related to Norton law, $\eta^\theta = \text{sign}(\tau^\theta - cx^\theta)$ and $\langle \bullet \rangle$ are Macauley brackets. Furthermore, the isotropic hardening behavior is not investigated, *i.e.,* only the kinematic hardening behavior is considered while assuming an exponential behavior

$$\dot{x}^\theta = \dot{\gamma}^\theta - d|\dot{\gamma}^\theta|x^\theta \tag{6.14}$$

where $d$ is a material parameter. Several slip systems may lead to the same plastic strain rate, thus the growth of the resolved shear stresses $\tau^\theta$ is governed by a phenomenological hardening law. From Equations (6.13), and (6.14), and by applying the consistency condition, it becomes

$$\dot{x}^\theta = \frac{1}{c}\sum_\kappa \boldsymbol{H}_{\theta\kappa}|\dot{\gamma}^\kappa| \tag{6.15}$$

where $[\boldsymbol{H}_{\theta\kappa}]$ is the interaction matrix, $\delta_{\theta\kappa}$ is the *Kronecker* operator and $H_{\theta\kappa} = c(\eta^\kappa - dx^\kappa)\delta_{\theta\kappa}$ the hardening moduli of the interaction matrix. Table 6.3 gathers all model parameters and their initial values chosen based on IF literature [140, 141].

**Table 6.3:** Parameters of the Méric and Cailletaud crystal plasticity model [140, 141]

| Mechanism | Elasticity | | | Viscosity | | Plasticity | | |
|---|---|---|---|---|---|---|---|---|
| Model parameter | $C_{11}$ | $C_{12}$ | $C_{44}$ | $K$ | $n$ | $\tau_0$ | $c$ | $d$ |
| Unit | GPa | GPa | GPa | MPa | (-) | MPa | GPa | (-) |
| Initial value | 233.5 | 135.5 | 118 | 12 | 10 | 40 | 40 | 1500 |

### C++ implementation

One of the main challenges is the coupling between experimental and numerical data in a single framework. An in-house C++ code dealing with all the facets of the problem from the acquired height profile images to the identification of parameters while computing the mechanical responses has been designed. Regarding the FE computations (performed in Code_Aster [142]), a C++ routine has been written to automatically generate the in-

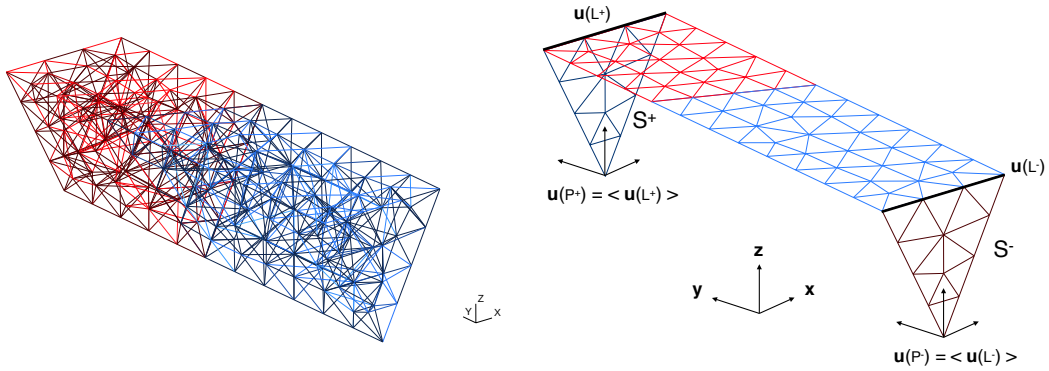


**Figure 6.5:** (a) 3D mesh of the $\mu$-specimen with the two grains visible (two different colors). (b) 2D mesh on the top surface used for IDIC, shown together with the sides where the boundary conditions are interpolated from the initial DIC computation

put files with all the necessary data, *i.e.,* the microstructure, the boundary conditions, the mesh, and the constitutive parameters. Simulations are automatically started and the results are sent back to the main code to iteratively solve the identification problem. This main code deals, with *i*) the surface profile images in height levels, *ii*) the 2D mesh (in pixels) related to the global DIC formulation, *iii*) the 3D mesh (in mm) used to solve the finite element problem, and *iv*) the 2D mesh (in pixels) where the sensitivity fields are projected on the DIC matrix to solve the Integrated DIC problem. As proposed in Chapter 3, the parameterization is based on a log scale of the ratio between the current value of the parameter and its initial guess. It is defined such that the sought parameters in the new setting $\{\boldsymbol{q}\}$ are expressed from the initial basis as $\{\boldsymbol{q}\} = \log\{\boldsymbol{p}/\boldsymbol{p_0}\}$, where $\{\boldsymbol{p}\}$ is the vector gathering the values of the parameters and $\{\boldsymbol{p}_0\}$ their initial values.

As a key feature, the measurement, the computation, and the identification steps rely on a 3D surface formulation where the out-of-plane displacements are also used to identify the micromechanical behavior of crystals. The simulations are performed on the measured 3D microstructures with their lattice orientation. Figure 6.5(a) shows the finite element model of the microstructure.

Furthermore, the applied boundary conditions are obtained from the displacements measured via DIC. The numerical simulations being 3D, the displacements of the triangular boundaries are obtained assuming a linear interpolation between the edge $L^+$ and $L^-$ (*i.e.,* intersection between the measured surface ($S^+$ and $S^-$) and the triangular boundary surface) and the apex ($P^+$ and $P^-$) where its displacement is equal to the mean value of the corresponding edge (respectively $L^+$ and $L^-$).

To conclude, a regularization method [69] is implemented to prevent meaningless

identification when the influences of material parameters on the observables are weak. Therefore, a functional ($\chi_R$) is associated with the identification functional ($\chi_f$) to enable for the changes of the sought parameters only if their corresponding sensitivities are higher than a specific bound. $\chi_R^2$ is a convex function reaching its minimum equal to zero and reads

$$\chi_R^2 = \{\boldsymbol{p}\}[\boldsymbol{C}_p^R]^{-1}\{\boldsymbol{p}\} \tag{6.16}$$

where $[\boldsymbol{C}_p^R]$ is the covariance matrix of the material parameters. The regularized functional is written as $\chi_I^2 = \chi_f^2 + \chi_R^2$ because both functionals are dimensionless and normalized to one. Finally, the regularization of the linear system reads

$$([\boldsymbol{M}]_{IDIC} + \lambda^*[\boldsymbol{I}])\{\delta\boldsymbol{p}\} = \{\boldsymbol{b}\} + \lambda^*(\{\boldsymbol{p}_0\} - \{\boldsymbol{p}\}) \tag{6.17}$$

where $\lambda^*$ is the regularization parameter whose choice is performed to cancel out the influence of noise [69].

## 6.3 Experimental results

320 profile images are acquired and 8-bit encoded such that the total range is used over the entire images set. The ratio between nm and pixels is equal to 110 nm/pixel, and the ratio between nm and height levels is constant and equal to 6.5 nm/(digital level). Figure 6.6

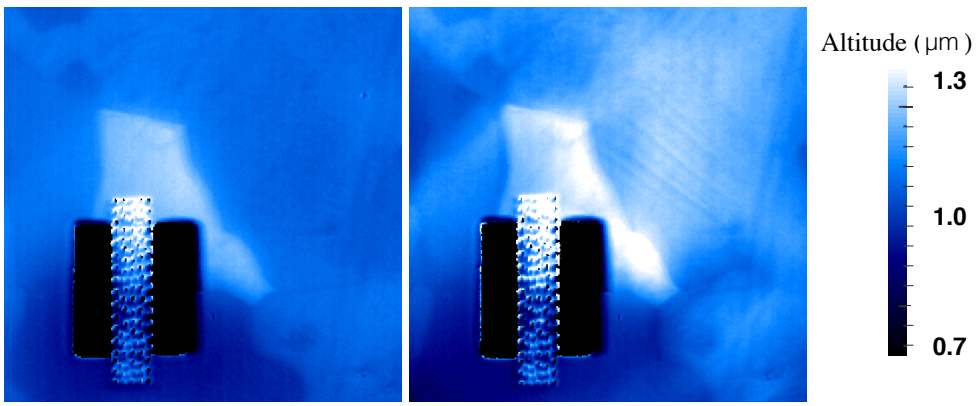


(a) (b)

**Figure 6.6:** (a) Reference image and (b) image at the last time step of the experiment after application of the systematic error correction

shows the reference image and the last image of the experiment after the application of the bias correction.

Figure 6.7 shows a Backscattered Electron (BSE) image of the $\mu$-specimen and its surrounding area where slip bands are revealed due to Electron Channelling Contrast. Furthermore plasticity has occurred during the experiment, as expected.

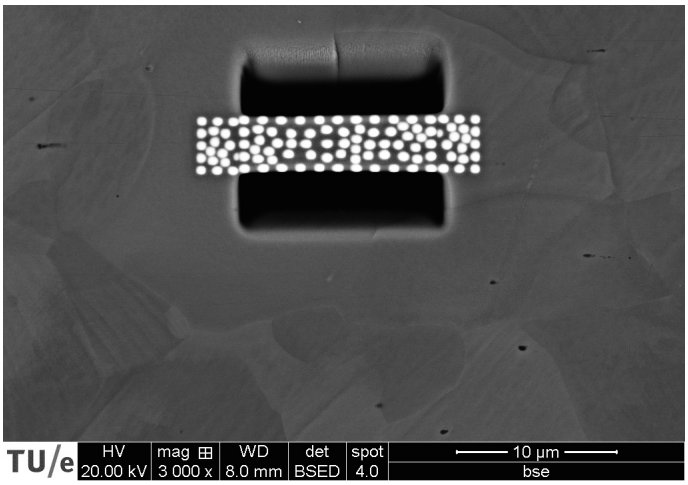


**Figure 6.7:** Backscattered electron (BSE) image of a larger view at the end of the experiment. The slip bands are observable around the $\mu$-specimen inside the grains

### 6.3.1 3D-DIC measurements

Figure 6.8(a) shows the $u_Y$ component of the displacement field obtained with the 3D-DIC algorithm at the last time step. The corresponding mesh is also shown. Because the displacements are very small and the specimen area contains only a limited amount of pixels ($120 \times 40$ pixels), the accuracy of the measured displacements over time is limited. Therefore, a coarse mesh is used to increase the robustness of the DIC procedure. Figure 6.8(b) shows the displacement amplitude $(u_Y^+(t) - u_Y^-(t))$ between the upper constrained surface ($S^+$) and the lower one ($S^-$) where $\gamma_u = 26$ nm is the standard displacement uncertainty. The signal possesses a notable amount of noise, which is challenging for further investigations. Figure 6.8(b) also shows the prescribed displacement on the boundary of the macroscopic specimen. The ratio between the two displacements (of the order of 5,000) is constant, as expected. The distance between the two grips is 32 mm and the $\mu$-specimen length 12 $\mu$m, is equal to $3.8 \times 10^{-4}$. However, the ratio experimentally observed is equal to $2 \times 10^{-4}$ and corresponds to a strain of the $\mu$-specimen of 1.6%. It is observed that that the microscopic strain is not equal to the global macroscopic strain. It originates from microscopic heterogeneities or small discontinuities of the macroscopic geometry.

Figure 6.9 shows the digital level residual fields reconstructed at the last time step of the experiment and the last iteration of the DIC procedure. The latter is obtained by computing the difference between each pixel of the reference image and the corrected

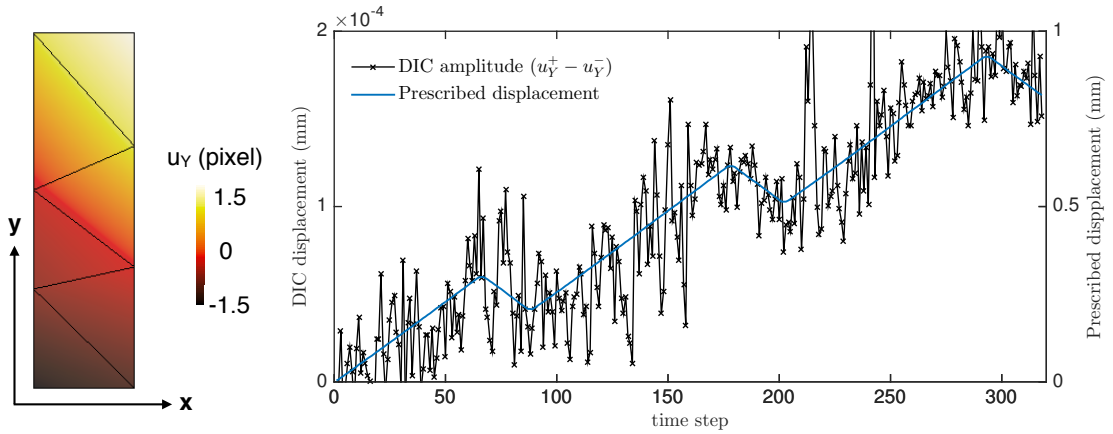


(a) (b)

**Figure 6.8:** (a) Component $u_Y$ of the displacement field at the last time step of the experiment evaluated via DIC. (b) Displacement amplitude $(u_Y^+(t) - u_Y^-(t))$ in the longitudinal direction and prescribed displacement with an adapted scale (see left size of the graph)

deformed image [62] and decreases by about 16 %. The gain originates from the vertical displacement determination that affects the entire ROI.

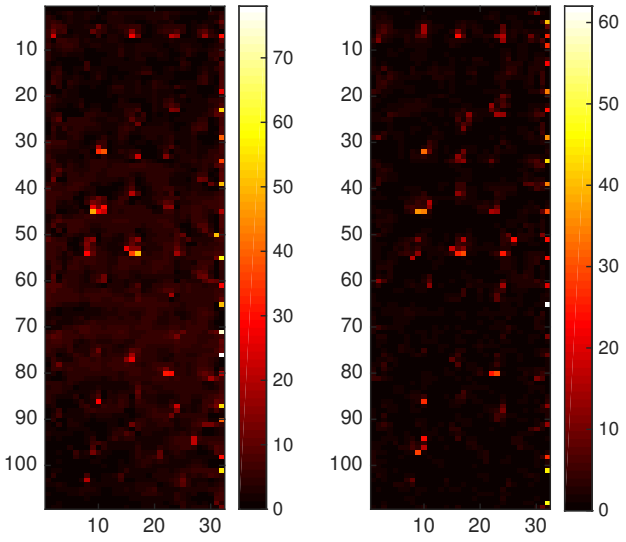

(a) $\chi_f = 3.9$ (b) $\chi_f = 3.2$

**Figure 6.9:** (a) Residual field at the last time step of the experiment for the first iteration and (b) at convergence. The fields are expressed in digital levels (*i.e.,* 1 digital level = 6.5 nm)

The main issue (see Figure 6.9) is that the signal to noise ratio is very small. To

overcome this challenge a new strategy is proposed, *i*) piecewise-linear time steps are assumed for each loading phase and for each considered surfaces ($S^+$ and $S^-$) for the components $u_Y$ and $u_Z$ (see Figure 6.10 in red), *ii*) the displacements of the apex (lines $L^+$ and $L^-$) of both boundary surfaces are identified with integrated 3D-DIC, and *iii*) the measured macroscopic loads are adapted to fit the section of the microscopic specimen and some material parameters are identified based on the minimization of the combination of the loads and image residuals. The $u_X$ component is not considered because of its larger noise level.

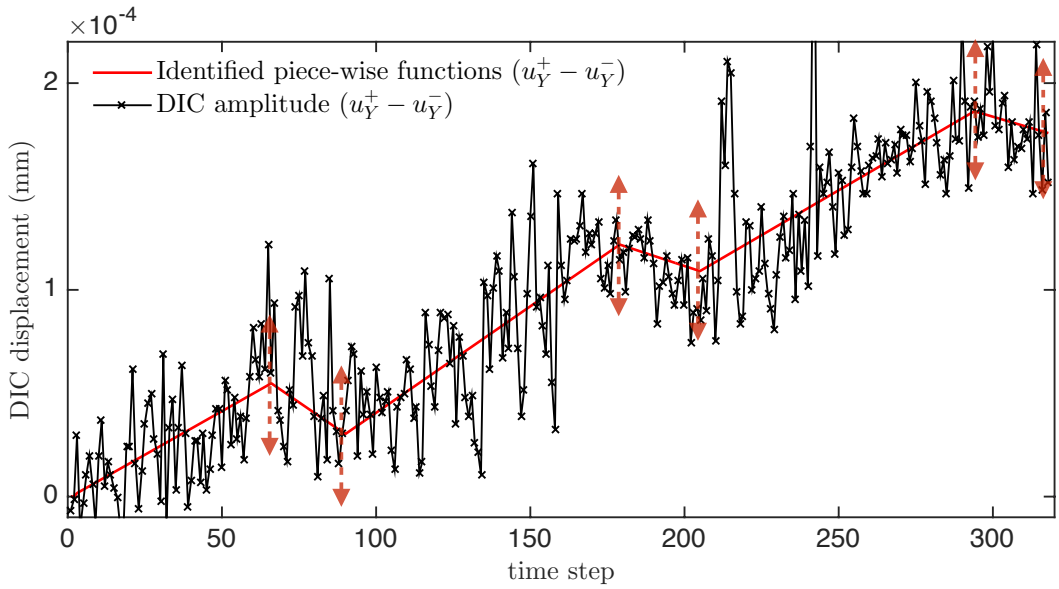


**Figure 6.10:** Displacement amplitude $(u_Y^+(t) - u_Y^-(t))$ in the longitudinal direction from DIC (the mean of the two extreme nodes) results and the corresponding piecewise-linear steps. The arrows denote the considered degrees of freedom

With this pre-processing strategy, two objectives have already been fulfilled, namely, *i*) the displacement fields have been measured over time and *ii*) the micromechanical plastic behavior and its evolution have been observed. The remaining objectives to achieve are *i*) the coupling between experimental and numerical solutions (with the selected crystal plasticity law), *ii*) the identification of the displacement of the apex of the boundary triangles and *iii*) the identification of the constitutive parameters.

## 6.4 Boundary conditions and material parameter identification

The identification is investigated with the 3D model and the measured microstructure. First, the in-depth displacements at the constrained boundaries are assessed. Four unknowns, namely $\lambda_Y^+$, and $\lambda_Z^+$, $\lambda_Y^-$, and $\lambda_Z^-$ are applied as an amplitude correction to $u_Y^+$ and $u_Z^+$ at point $P^+$ (apex of $S^+$), and to $u_Y^-$ and $u_Z^-$ at point $P^-$ (apex of $S^-$, see Figure 6.11).

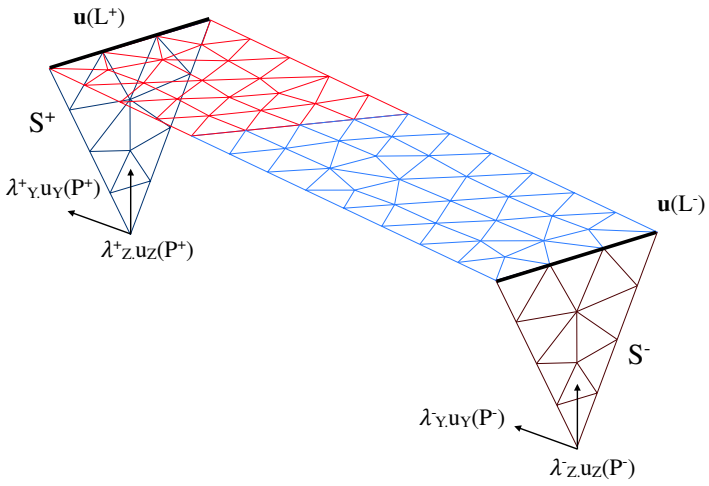


**Figure 6.11:** Kinematic unknowns corresponding to the boundary conditions on the bottom part of the specimen

### 6.4.1 Sensitivity analysis

A sensitivity analysis is carried out and the uncertainty is evaluated with the covariance matrix $[\boldsymbol{C}^p]_{IDIC}$ of the unknowns (Chapter 4). A 2% perturbation on each parameter is applied to compute the sensitivity fields. The vector of kinematic and material parameters reads $\{\boldsymbol{p}\} = \{\lambda_Y^+, \lambda_Z^+, \lambda_Y^-, \lambda_Z^-, \tau_0, c, d\}$. Figure 6.12(a) shows the kinematic Hessian for the entire loading history. The most influential parameters are $\lambda_Y^+$ and $\lambda_Y^-$ whereas the material parameters exhibit the smallest influences. This result shows that accurate identification of the boundary conditions is of paramount importance prior to any analysis of the material parameters. Figure 6.12(b) shows the corresponding correlation matrix. The high level of anti-correlation between the parameters $(c, d)$ will impact their identifications.

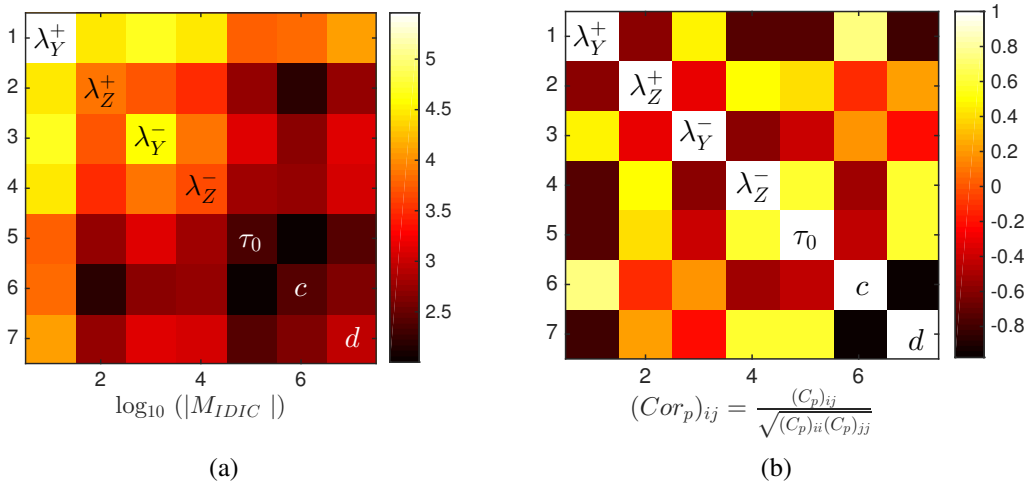


(a) (b)

**Figure 6.12:** (a) Kinematic Hessian $[M]_{IDIC}$ and (b) correlation matrix of the kinematic Hessian $[M]_{IDIC}$, both for the entire loading history

### 6.4.2 Identification

The underlying boundary conditions are now determined with Integrated-DIC by iteratively solving Equation (6.17). Figure 6.13(a) shows the change of the four kinematic parameters and Figure 6.13(b) shows that of the functional $\chi_I$. The converged solution is reached in 10 iterations. Furthermore, three kinematic parameters, namely $\lambda_Y^-$, $\lambda_Z^+$, and $\lambda_Z^-$ converged to a close solution with respect to their initial values. However, $\lambda_Y^+$ varies by about 20 %, which means that a significant shear strain occurs on the subsurface of the $\mu$-specimen during the experiment.

Table 6.4 gathers the measured values and compares the dimensionless residuals between the initial 3D-DIC solution, with more kinematic freedom and the integrated DIC solution, with only few degrees of freedom associated with boundary conditions. Therefore, the small residual increase is regarded as a validation of the integrated approach.

**Table 6.4:** Identified values of the kinematic parameters

| Name | $\chi_f$ | $\lambda_Y^+$ | $\lambda_Z^+$ | $\lambda_Y^-$ | $\lambda_Z^-$ |
|---|---|---|---|---|---|
| DIC | 3.7 | – | – | – | – |
| IDIC | 4.5 | 0.81 | 1.02 | 0.98 | 1.02 |

The monitored macroscopic loads are scaled to the specimen section and a combined

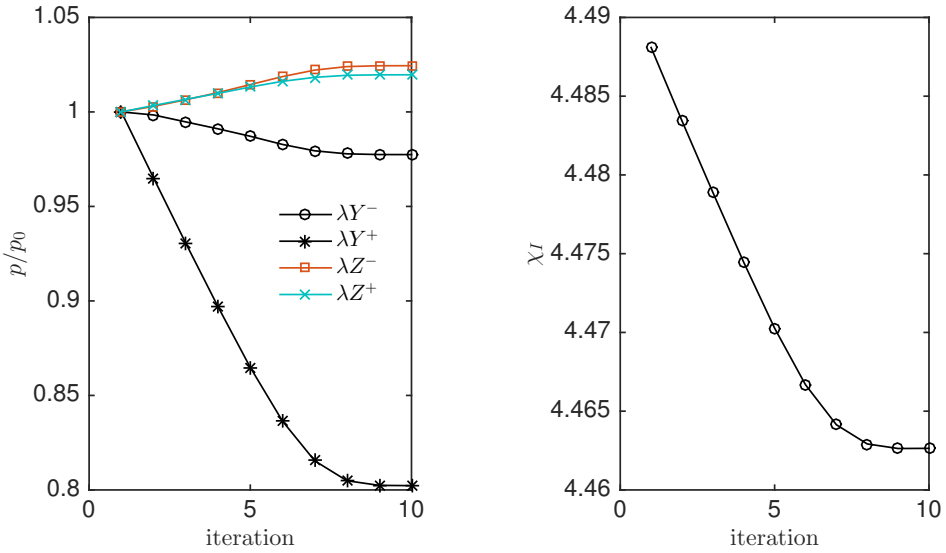


(a) (b)

**Figure 6.13:** (a) Parameter changes during the iterations of IDIC and (b) evolution of the dimensionless residual

image and load identification scheme is used, namely IF-DIC. The global cost function reads

$$\chi_I^2 = \frac{N_\Omega}{1+N_\Omega}\chi_f^2 + \frac{1}{1+N_\Omega}\chi_F^2 \tag{6.18}$$

where the weight of the two functionals originates from a Bayesian foundation (Chapter 3) to account in a fair manner for both sources of information. $\chi_F^2$ is the load residual

$$\chi_F^2 = \frac{1}{\gamma_F^2 N_t}\{\boldsymbol{F}_m - \boldsymbol{F}_c\}^t\{\boldsymbol{F}_m - \boldsymbol{F}_c\} \tag{6.19}$$

where $N_t$ is the number of time step, $\{\boldsymbol{F}_m\}$ and $\{\boldsymbol{F}_c\}$ the vectors gathering the measured and computed loads, respectively, and $\gamma_F = 5.97 \times 10^{-6}$ N is the standard load uncertainty [139]. The same choice of regularization methodology is made.As a first step, only the material parameters are sought, while the boundary conditions are the previously assessed ones. Figures 6.14(a) and 6.14(b) show the changes of the material parameters and residuals. The global residual ($\chi_I$) decreases by about 1 % and stabilizes after 4 iterations. Furthermore, while the load residual ($\chi_F$) is significantly minimized the kinematic residual remains approximately constant. Figure 6.14(c) shows the experimental, initial, and final computed load histories.

Table 6.5 gathers the constitutive parameters at convergence. Up to 50 % changes are observed with respect to the initial guess. The load residual has been decreased by 25 %,

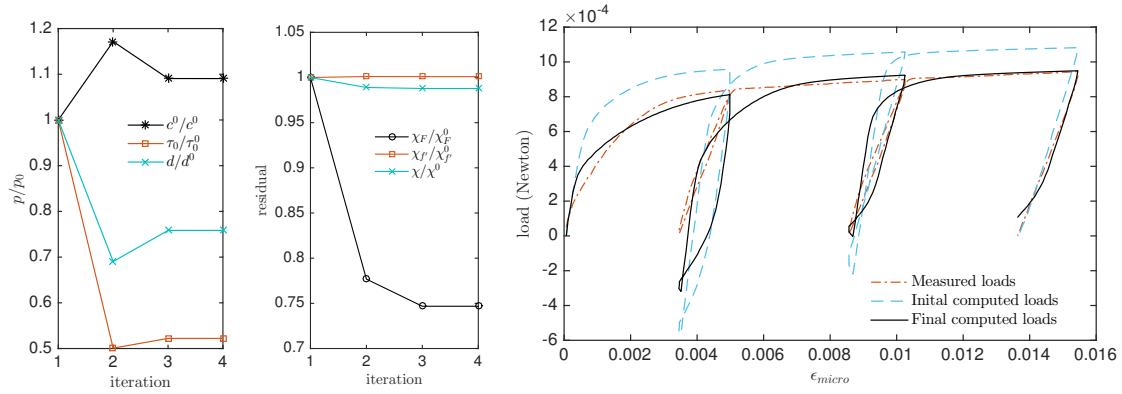


(a) (b) (c)

**Figure 6.14:** (a) Material parameters and (b) residuals as functions of iteration number. (c) Reaction forces on the $\mu$-specimen boundaries

**Table 6.5:** Identified parameters of the crystal plasticity model

| Name | $\chi_I$ | $\chi_f$ | $\chi_F$ | $\tau_0$ (MPa) | $c$ (GPa) | $d$ (-) |
|---|---|---|---|---|---|---|
| Initial value | 4.64 | 4.46 | 78 | 40 | 40 | 1600 |
| IF-DIC | 4.52 | 4.47 | 58 | 21 | 44 | 1140 |

which proves that it is sensitive to the sought parameters. However, its final value is still large, which is an indication of a model error associated with the constitutive law. Last, no changes in the kinematic parameters are obtained when a new identification is performed with the assessed material parameters. Reflecting on the influence of the unknown boundary conditions on the crystal plasticity parameter identification, one may consider a direct tensile test of a micro-specimen, *e.g.,* by employing the nano-force tensile stage proposed by Bergers *et al.* [139] to provide relevant data to perform a precise identification with accurate measurements of the load history at the scale of the $\mu$-specimen. Such a change of the methodology would, however, come at the expense of a more complex experimental procedure.

## 6.5 Conclusion

The investigation and the characterization of the micromechanical behavior of a microbeam made of two grains have been achieved. On the experimental side, two new procedures have been proposed, *i*) the design of a triangular prismatic shape micro-specimen with a known microstructure embedded in a macro-specimen and *ii*) the use of a global DIC algorithm to measure the 3D surface displacement field. On the identification side,

a novel strategy has been designed to overcome the encountered high noise level on the height profile images. The latter has prevented direct approaches such as Finite Element Method Updating to succeed because the initial 3D global DIC measurement is too noisy. The choice was made to use an integrated approach to work directly on the images but the scatter on the boundary conditions prevented a direct evaluation of the sensitivity fields.

Based on this limitation, a two-step identification strategy was adapted, *i*) estimation of the boundary conditions and *ii*) determination of the constitutive parameters. The boundary conditions were assumed to be piece-wise linear with time. First, the identification via integrated-DIC was performed only with the height profile images to assess the underlying boundary conditions. Subsequently, the macroscopic loads were adapted to the specimen section and both sources of information were combined to assess the sought constitutive parameters, which describe the kinematic hardening relationship in the crystal plasticity material model.

The investigated precipitate hardened 17-7PH grade stainless steel in TH1050 condition has now macroscopic and microscopic (assumed to be similar of an IF-steel) parameters. All necessary information has now been gathered to proceed to the determination of the fatigue properties of the studied material and the component. Chapter 7 investigates the latter based on self-heating experiment [15] and a probabilistic multi-scale model [19].

# Part B

# Validation of Probabilistic Fatigue Design

# Chapter 7
# Probabilistic fatigue design and validation of welded bellows with IR thermography measurements


## Abstract

The study aims to predict and optimize the endurance limit of welded bellows made of stainless steel and relies on the analysis and the modeling of the dissipated energy that occurs in the high cycle fatigue regime. Experimental investigations are carried out on ultra-thin (70 $\mu$m) uniaxial specimens and welded bellows and lead to the identification of their fatigue properties. However, the thinness of the uniaxial specimens and the bellows structural complexity generated by their manufacturing process induce uncommon behaviors. Last a modified Goodman diagram is constructed based on the evaluated material and bellows fatigue properties and validates the bellows design.


## 7.1 Introduction

Stromeyer [13] and Moore *et al.* [14] were the first scientists to propose that the change of dissipated power under cyclic loading as a function of the applied stress could lead to the fatigue limit determination of metals. Their idea assumed that the microstructure changes such as dislocations, persistent slip bands, and microstructural evolutions generate heat that can be macroscopically captured. Eight decades later, Luong *et al.* [15] and La Rosa *et al.* [143] proposed to monitor this phenomenon while applying numerous sets of repeated cycles with increasing amplitudes. One set corresponds to a number of cycles prescribed at a defined frequency and amplitude. They successfully confronted this methodology to standard fatigue investigations [144].

In order to model this phenomenon, a preliminary thermomechanical framework that assumes uniformly distributed heat sources in the material is proposed [16]. Then, to account for the material inhomogeneity, a multi-scale framework based on three separate scales is introduced [145]. The latter has been experimentally validated on metals [146, 147, 148] and the methodology has also been applied on one industrial com-

ponent [149] and composite materials [150]. Low Cycle Fatigue (LCF) regime has also been investigated by looking at the energy dissipation near a crack tip [151]. However, this framework does not address the scattered aspect of fatigue data and a uniaxial thermomechanical framework associated with a two-scale probabilistic model has been introduced [152, 17] and extended to multiaxial High Cycle Fatigue (HCF) regime [19, 20]. The results show that a probabilistic scenario based on the activation of microplasticity gives an accurate description of the observed fatigue behavior under proportional and non-proportional loadings.

Regarding the fatigue properties of the studied component, U-shape bellows with an elastoplastic behavior and linear kinematic hardening have been investigated and optimized [153]. An extended model that addresses stress and strain concentrations has been successfully designed [154]. Other bellows geometries have been investigated to predict their fatigue life [155, 156].

In the light of these investigations both on material and structure, the present goal is to investigate and optimize the fatigue life of bellows. First, the material is investigated with ultra-thin (70 $\mu$m) uniaxial specimens and their properties are assessed based on a probabilistic two-scale model [152] and the Weibull distribution that describes the variability of the strength of materials [27, 28] to assess the material fatigue properties. Second, the welded bellows are experimentally investigated with an ad hoc setup that prescribes cyclic loading and an infra-red camera to monitor the temperature fields.

The chapter is organized as follows. Section 7.2 introduces the theoretical background of the probabilistic two-scale model followed by experimental investigations on uniaxial specimen in Section 7.3 and bellows in Section 7.4.

## 7.2 Thermomechanical background

The material is assumed to be composed of numerous Representative Volume Elements (RVE). An RVE is composed of one spherical inclusion having a mesoscopic mechanical behavior ($\bullet^{\mu}$) embedded in an elastic matrix having a macroscopic mechanical behavior ($\bullet$). For one RVE without stress and material heterogeneities, the Helmotz state potential $\Psi$ is divided into two contributions accounting for the two domains of the RVE [157, 88],

$$\Psi = \frac{1}{V}\int_{RVE} \Psi(M)dV = (1-f_v)\Psi_m + f_v\Psi_i \tag{7.1}$$

where $f_v = V_0/V_{RVE}$ is the inclusion volume fraction, and $\Psi_i$ and $\Psi_m$ are respectively the state potentials of the inclusion and the matrix. Assuming an elastoplastic behavior with a linear isotropic elasticity and a linear kinematic hardening the local expression of the

mesoscopic dissipation power reads

$$\Delta_p = f_v \left[ (\boldsymbol{\sigma} - \frac{\partial \Psi_i}{\partial \boldsymbol{\epsilon}^p}) : \dot{\boldsymbol{\epsilon}}^p - \frac{\partial \Psi_i}{\partial p} \dot{p} \right] = f_v \left[ \boldsymbol{\sigma} - \frac{2}{3} C^\mu : \boldsymbol{\epsilon}^p \right] : \dot{\boldsymbol{\epsilon}}^p \tag{7.2}$$

where $\boldsymbol{\sigma}$ is the mesoscopic stress tensor, $\boldsymbol{\epsilon}^p$ the mesoscopic plastic strain, $C^\mu$ the mesoscopic kinematic hardening modulus, and $p$ the cumulative mesoscopic plastic strain. Equivalently, the thermoelastic dissipation generated in the matrix and the inclusions becomes

$$\Delta_e = (1 - f_v) \frac{\partial^2 \Psi_m}{\partial \boldsymbol{E} \partial T} : \dot{\boldsymbol{E}} + f_v \frac{\partial^2 \Psi_i}{\partial \boldsymbol{\epsilon}^e \partial T} : \dot{\boldsymbol{\epsilon}}^e = -T_0 \alpha \mathrm{tr}(\dot{\boldsymbol{\Sigma}}) \tag{7.3}$$

where $\boldsymbol{E}$ is the macroscopic strain tensor, $\boldsymbol{\Sigma}$ the macroscopic stress tensor, $\boldsymbol{\epsilon}^e$ the mesoscopic elastic strain, $T_0$ the initial material temperature and $\alpha$ the coefficient of thermal expansion. The dissipation per cycle reads

$$\mathcal{D}_{inc} = f_v \int_{cycle} \Delta_p \, dt = \frac{4}{h \rho c} f_v \Sigma_y^\mu \langle \Sigma_0 - \Sigma_y^\mu \rangle_+ \tag{7.4}$$

where $\Sigma_0 = 1/2(\Sigma_{max} - \Sigma_{min})$ is the stress amplitude in the inclusion and $\Sigma_y^\mu$ the mesoscopic yield stress. The heat equation of the studied problem is [158, 159, 160]

$$\dot{\theta} + \frac{\theta}{\tau_{eq}} = \frac{f_r \mathcal{D}}{\rho c} \tag{7.5}$$

where $c$ is the specific heat, $\rho$ the material mass density, $\tau_{eq}$ a time constant depending on the structure and the experimental conditions [159], and $f_r$ the applied loading frequency. A solution to the differential equation gives the temperature history [152]

$$\theta(t) = \frac{4 f_r \tau_{eq}}{h \rho c} f_v \Sigma_y^\mu \langle \Sigma_0 - \Sigma_y^\mu \rangle_+ \left[ 1 - \exp\left( -\frac{t}{\tau_{eq}} \right) \right] \tag{7.6}$$

where $h = C^\mu + 3\mu(1 - \beta)$, with $\beta = 2(4 - 5\nu)/15(1 - \nu)$, $\mu$ the shear modulus [120] (see Table 7.1 that gathers the material parameters). The value of the steady-state temperature reads

$$\Delta T = \eta f_v \Sigma_y^\mu \langle \Sigma_0 - \Sigma_y^\mu \rangle_+ \tag{7.7}$$

where $\eta = (4 f_r \tau_{eq})/(h \rho c)$ is a parameter that depends on both the material and the experimental conditions.

Microplasticity can also be described as a continuous process that exists even below the mesoscopic yield stress [17, 162]. A Poisson distribution is introduced to account for

**Table 7.1:** Physical properties of the studied precipitate hardened stainless steel (17-7PH grade) [23, 161]

| Name | $\rho$ | $\mu$ | $\alpha$ | $c$ |
|---|---|---|---|---|
| Dimension | $\mathrm{kgm}^{-3}$ | GPa | $\mathrm{C}^{-1}$ | $\mathrm{Jkg}^{-1}\mathrm{C}^{-1}$ |
| Value | 7650 | 79 | $11.2\times10^{-6}$ | 460 |

the mean number of active (*i.e.,* yielding) inclusions in a domain $\Omega$ of volume $V$ subjected to an activation stress $\Sigma_0$. The probability of finding $k$ active sites in a volume $V$ assuming this Poisson process reads

$$P_k(\Omega) = \frac{N(\Omega)^k}{k!}\exp(-N(\Omega)) \quad \text{where} \quad \lambda = \frac{1}{V_0}\left(\frac{\Sigma_0}{S_0}\right)^m \tag{7.8}$$

where $N(\Omega) = \lambda \times V$ is the mean number of active sites, with $\lambda$ the process intensity that relies on a power law and depends on the activation stress $\Sigma_0$, $m$ is the Weibull modulus, and $V_0 S_0^m$ is a material parameter. The global dissipation $\mathcal{D}$ is obtained with a point Point process that describes the mean number of activated sites in a domain $\Omega$ for an equivalent stress amplitude ranging from $\Sigma$ and $(\Sigma + d\Sigma)$

$$\mathcal{D} = \int_0^{\Sigma_0} \mathcal{D}_{inc}(\Sigma)\frac{d\lambda}{d\Sigma}d\Sigma \tag{7.9}$$

where $d\lambda/d\Sigma$ is the increase of the process intensity with respect to the applied stress level. The integration of Equation (7.9) yields the total dissipation $\mathcal{D}$

$$\mathcal{D} = \frac{4mV_0}{h\rho c(m+1)(m+2)}\frac{\Sigma_0^{m+2}}{V_0 S_0^m}, \tag{7.10}$$

and the corresponding steady-state mean temperature is determined by integrating the heat conduction equation (7.5)

$$\Delta T = \frac{\eta V_0 m}{(m+1)(m+2)}\frac{\Sigma_0^{m+2}}{V_0 S_0^m} \tag{7.11}$$

The fact that the study focuses on ultra-thin steel sheet prevents negative loads to be prescribed. It results that the mean stress will vary as the stress amplitude increases. To account for the influence of the mean stress, the intensity of the Poisson process is adapted

with the scale parameter $V_0 S_0^m$ that depends on the mean stress

$$\lambda = \frac{1}{V_0}\left(\frac{\Sigma_0}{S_0(\Sigma_m)}\right)^m \tag{7.12}$$

where $S_0(\Sigma_m)$ is a linear function [152]

$$S_0(\Sigma_m) = S_0 + \alpha\Sigma_m \tag{7.13}$$

and $\alpha$ a material parameter accounting for the dependence of the dissipation with respect to the loading level, and $\Sigma_{eq}$ the equivalent activation stress. The fatigue tests are performed for a given stress ratio between the maximum and the minimum stresses ($R = \Sigma_{min}/\Sigma_{max}$). It gives a relationship between the mean stress and the equivalent activation stress

$$\Sigma_m = \frac{1+R}{1-R}\Sigma_{eq} \tag{7.14}$$

The mean steady-state temperature reads

$$\Delta T = \frac{\eta m V_0}{(m+1)(m+2)} \frac{\Sigma_{eq}^{m+2}}{V_0\left[S_0 + \alpha\frac{1+R}{1-R}\Sigma_{eq}\right]^m} \tag{7.15}$$

Based on this framework and the weakest link theory [28], the failure probability $P_F$ of a domain $\Omega$, of volume $V$ is the probability of having at least one active site

$$P_F = P_{k\geq 1}(\Omega) = 1 - \exp\left[-\frac{V_{eff}}{V_0}\left(\frac{\Sigma_F}{S_0}\right)\right] \tag{7.16}$$

where $V_{eff} = V \times H_m$ is the effective volume [163], and $H_m$ the stress Heterogeneity factor [164]. The endurance behavior of the material is characterized by its mean endurance limit $\bar{\Sigma}_\infty$

$$\bar{\Sigma}_\infty = S_0\left(\frac{V_0}{V_{eff}}\right)^{1/m}\Gamma\left(1+\frac{1}{m}\right) \tag{7.17}$$

and its standard deviation $\bar{\bar{\Sigma}}_\infty$ [17]

$$\bar{\bar{\Sigma}}_\infty^2 = S_0\left(\frac{V_0}{V_{eff}}\right)^{1/m}\sqrt{\Gamma\left(1+\frac{2}{m}\right) - \Gamma^2\left(1+\frac{1}{m}\right)}. \tag{7.18}$$

where $\Gamma(x) = \int_0^\infty t^{x-1}\exp(-t)dt$ is the Euler (gamma) function. These equations show that the fatigue scatter ($\bar{\bar{\Sigma}}_\infty/\bar{\Sigma}_\infty$) only depends on $m$. The larger the value of $m$ the less scattered the fatigue limits. Wöhler's curve [144] can be determined based on these prob-

abilistic results and the assumption of a constant dissipated energy [19]

$$N = \frac{A}{\langle \Sigma_0 - \Sigma_\infty(P_F) \rangle \Sigma_\infty(P_F)} \tag{7.19}$$

where $N$ is the number of cycles to rupture, $A$ a material parameter, and $\Sigma_\infty(P_F)$ the endurance limit relative to a given failure probability $P_F \in [0;1]$. Table 7.2 gathers the assessed material parameters relative to the mechanical behavior evaluated in Chapters 5 and 6.

**Table 7.2:** Material parameters for the macroscopic and mesoscopic mechanical behavior. Both assume an elastoplastic behavior with a linear isotropic elasticity and linear kinematic hardening of 17-7 PH grade (Chapters 5, 6, and [24])

| Parameter | $E$ (GPa) | $\nu$ (—) | $\sigma_y$ (MPa) | $C$ (GPa) | $\sigma_y^\mu$ (MPa) | $C^\mu$ (GPa) |
|---|---|---|---|---|---|---|
| Value | 212 | 0.33 | 1370 | 9.1 | 550 | 44 |

## 7.3 Uniaxial ultra-thin specimens

### 7.3.1 Experimental results

An experimental investigation that aims to evaluate the dissipated energy on the specimen surface is carried out on four uniaxial specimens for various stress amplitudes. The procedure follows the so-called self-heating methodology [15, 143, 17]. Then, the four specimens are cyclically loaded at their highest amplitudes without monitoring the temperature. Three more samples are investigated only for the determination of their fatigue limit. The specimens are manufactured in a 70-$\mu$m thick sheet of precipitate hardened stainless steel (17-7 PH grade in TH1050 condition [23]). They are cyclically loaded ($f_r = 10$ Hz) on a servo-hydraulic tension/compression testing machine. Figure 7.1 shows the specimen geometry and the experimental setup with the black painted specimen and the infra-red camera. Two cooling systems are also associated (water and air) and two black painted boxes protect the specimen against external radiations.

Figure 7.2(a) shows one measured temperature difference (*i.e.,* the difference between the initial temperature field and another one acquired at instant $t$). The increase of temperature is relatively modest with a maximum difference equal to 1°C. Furthermore, the temperature field is not uniformly distributed over the specimen surface. A higher temperature is monitored on the boundaries of the median specimen region. This result originates from the heterogeneous stress field (stress concentration $K_t = 1.12$) and additional

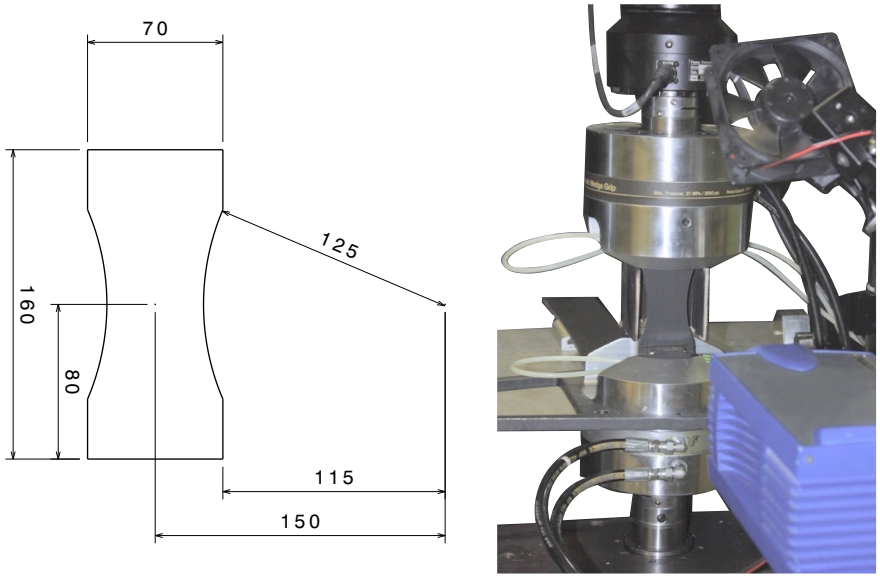


(a) (b)

**Figure 7.1:** (a) Specimen geometry (size in mm) and (b) experimental setup

conclusions will be drawn once the material parameters relative to the deterministic and probabilistic models will be assessed. The temperature field is also composed of numerous ripples generated by the out-of-plane motions (wrinkling) of the specimen. One technological solution would have been to use an anti-wrinkling device composed of an infra-red transparent material, which was not considered. We will thus concentrate on areas where these phenomena do not occur.

The identification of the characteristic time relative to the heat equation gives $\tau_{eq} = 4$ s. The steady-state temperature $\Delta T$ (*i.e.,* difference between the initial and the maximum steady-state temperature) is also determined. Figure 7.2(b) shows the assessed steady-state temperature gathered from the regions where the temperature increase is maximum. The thinness of the specimen leads to a greater interaction with the environnement that has increased the scatter of the results, although they are repeatable for the four tested samples.

Figure 7.3 shows three post-mortem micrographies obtained via Scanning Electron Microscopy (SEM) and enable for the observation of the fractographic features [165]. This analysis reveals that the fatigue crack initiates on one side, but not on the boundary itself, and traverses the sample in a straight path. In the crack initiation region, the surface fracture reveals numerous striations that are representative of brittle failures (consistent with a high cycle fatigue regime failure). Then, the surface features dimpled areas due to microvoid growth and coalescence and correspond to ductile tearing. Last, the specimen breaks by generating one important shear lip representative of a macroscopic ductile

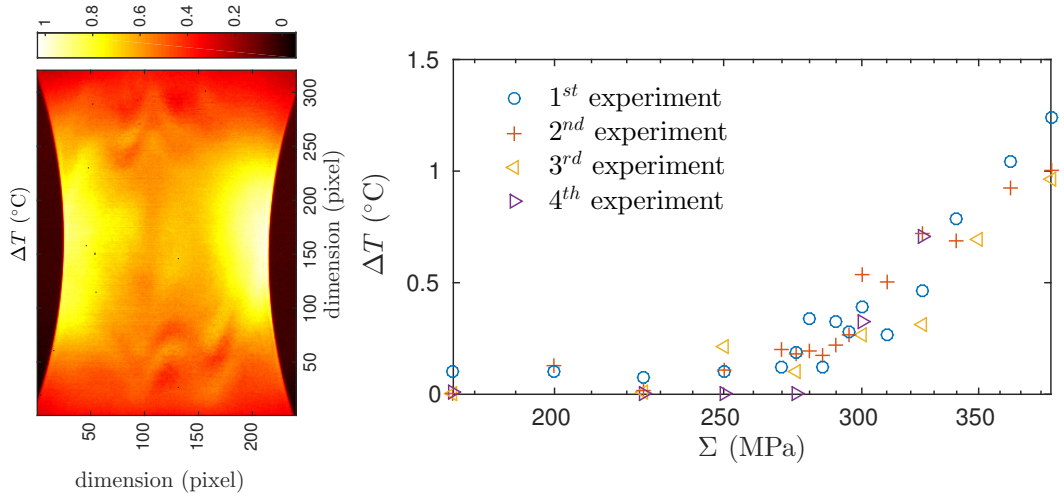


(a) (b)

**Figure 7.2:** (a) Temperature field and (b) steady-state temperatures for the four studied specimens and various stress amplitudes

fracture. The last two regimes induce a large amount of dissipated energy that is captured during the last cycles of the experiment (see Figure 7.4).

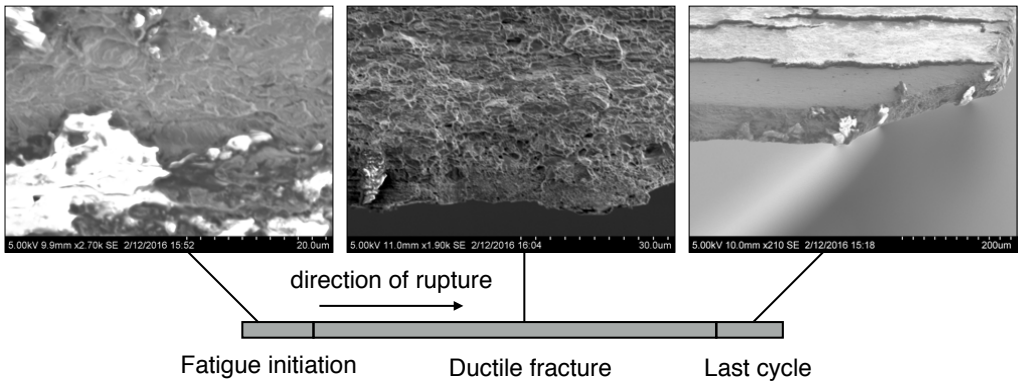


**Figure 7.3:** Failure history of the uniaxial specimen with (a) striations representative of a microscopic brittle fracture in HCF, (b) microscopic ductile fracture due to microvoid growth, and (c) macroscopic ductile tearing

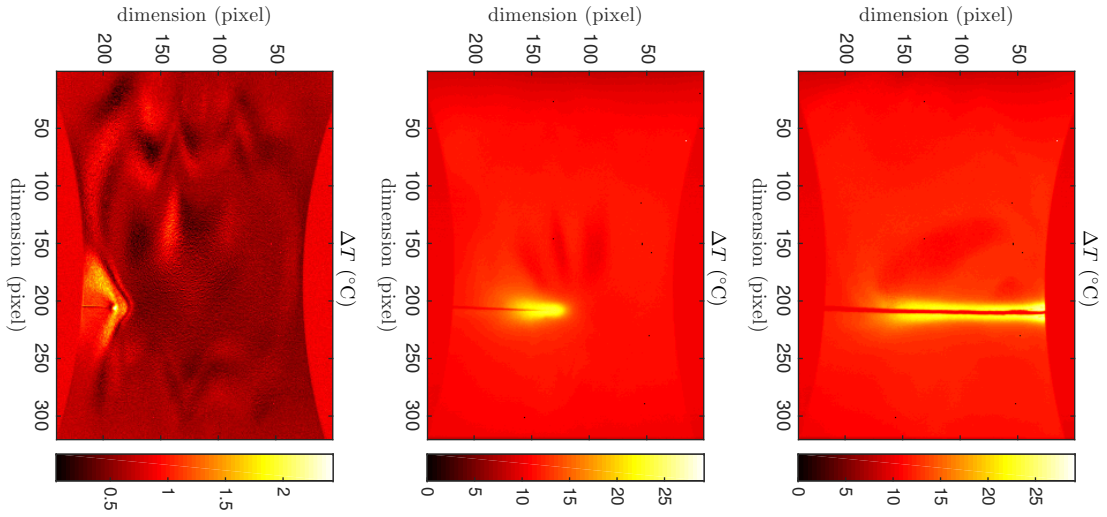


**Figure 7.4:** Temperature fields at (a) the initiation of the microscopic ductile fracture regime, (b) the ultimate monitored cycle before rupture, and (c) after rupture. For (b) and (c) the temperature calibration range is exceeded

### 7.3.2 Parameter identification

The objective is to assess the material parameters relative to the deterministic and the two-scale probabilistic models. Based on the experimental results and the numerical model the identification procedure consists of four steps:

1. the parameters $\eta f_v$ and $\Sigma_y^\mu$ relative to the deterministic model

$$\Delta T = \eta f_v \Sigma_y^\mu \langle \Sigma_0 - \Sigma_y^\mu \rangle_+ \tag{7.20}$$

2. the set $m$, $\alpha$, and $S_0$ associated with the two-scale probabilistic model [152] where $\Sigma_m = \Sigma_{eq} = \frac{1}{2}(\Sigma_{max} - \Sigma_{min}) \times K_t$

$$\Delta T = \frac{\eta m}{(m+1)(m+2)} \frac{(\Sigma_m)^{m+2}}{[S_0 + \alpha \Sigma_m]^m} \tag{7.21}$$

3. the fatigue limit $\Sigma_\infty$ and $A$ with the experimental Wöhler's curve (see Figure 7.6)

$$N = \frac{A}{\langle \Sigma_0 - \Sigma_\infty(P_F) \rangle \Sigma_\infty(P_F)} \tag{7.22}$$

4. the parameter $V_0$ where the stress heterogeneity factor $H_m$ and $V_{eff}$ the effective

volume are assessed with the numerical model

$$V_0 = \left[ \frac{1}{S_0 + \alpha \Sigma_m} \frac{\bar{\Sigma}_\infty \left(V H_m\right)^{1/m}}{\Gamma\left(1+\frac{1}{m}\right)} \right]^m \tag{7.23}$$

Figure 7.5 shows in a log-log plot the experimental steady-state temperatures with the two calibrated models. The RMS identification residuals are almost equal ($7.97 \times 10^{-2}$°C and $7.82 \times 10^{-2}$°C ) but the two models lead to two distinct trends when $\Sigma_m \to 0$. The deterministic model appears to be valid only for an equivalent stress above the mesoscopic yield stress whereas the two-scale probabilistic model is valid for any equivalent stress below the macroscopic yield stress in the investigated range. It is therefore of importance to represent these results in a log-log plot because a linear plot does not reveal this difference. The Weibull modulus $m$, $V_0$, and $\alpha$ are assessed based on the experimentally measured steady-state temperatures (Figure 7.5) and a least squares minimization.

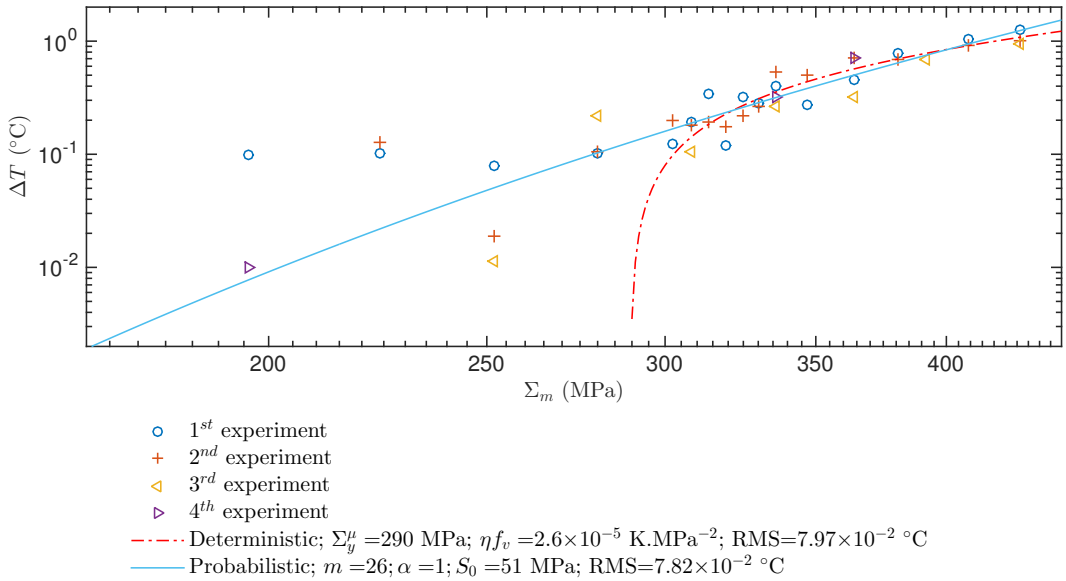


**Figure 7.5:** Experimentally measured steady-state temperature variations and the two evaluated models drawn in a log-log plot

Table 7.3 gathers the material parameters relative to the deterministic model. The inclusion volume fraction $f_v = V_0/V_{ref}$ is representative of this class of material and similar results corroborate this value [17].

Figure 7.6 shows the experimentally determined Wöhler's curve. The number of cycles to failure and the corresponding failure stress are depicted. The model is shown for three failure probabilities ($P_F = 95$ %, $P_F = 50$ %, and $P_F = 5$ %) based on the assessed

**Table 7.3:** Material parameters for the deterministic model

| Name | RMS (°C) | $\eta f_v$ | $\Sigma_y^\mu$ (MPa) |
|---|---|---|---|
| Value | $8.0 \times 10^{-2}$ | $2.6 \times 10^{-5}$ | 290 |

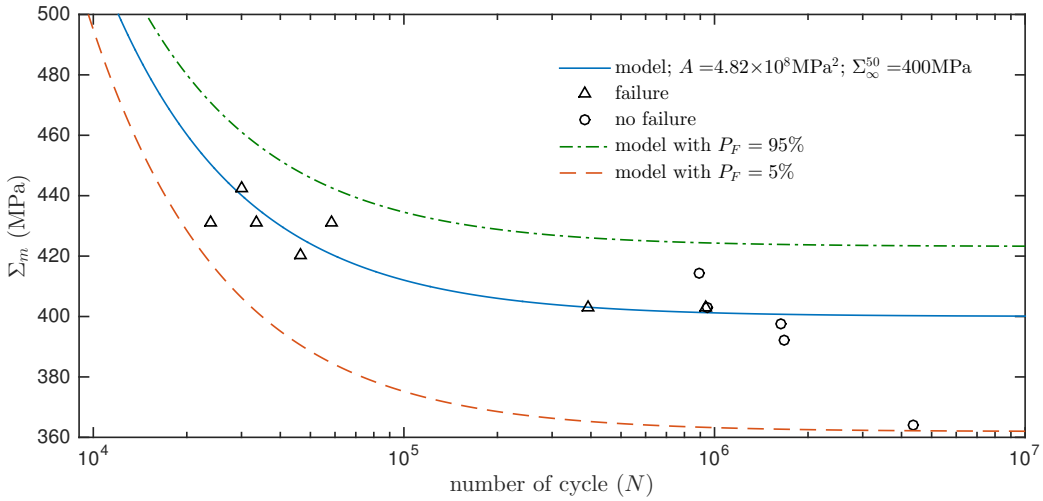


**Figure 7.6:** Wöhler's curve of ultra-thin sheets (70 $\mu$m) made of precipitate hardened stainless (17-7 PH grade) in TH1050 condition [23]

material parameters of the probabilistic two-scale model. The median ultimate tensile stress is evaluated as $\Sigma_\infty^{50} = 400$ MPa. This result is in contradiction with the evaluated fatigue limit based on the deterministic model and the self-heating experiment methodology. The gap is of the order of 100 MPa in the advantage of the standard (Wöhler) approach. First, specimen preparation, loading, handling and alignment in the testing set-up may cause modest variations in the experimental results. Second, the ultra-thin section of the specimen (70 $\mu$m) decreases the stresses in the specimen edges [166] as observed with a DIC analysis, which is not shown herein. This behavior prevents a crack from initiating on the specimen boundaries and enhances the fatigue strength of the material. This result is different from the one obtained with self-heating measurements.

Figure 7.7 shows the dissipation fields per cycle ($\mathcal{D}$) for (a) the deterministic model and (b) the two-scale probabilistic model for an applied equivalent stress amplitude equal to $\Sigma_{eq} = 350$ MPa. While the deterministic model leads to a localized dissipation in the regions where the stresses are greater than the mesoscopic yield stress, the probabilistic model generates heat in a larger area as the assumption of a continuous microplastic activity suggests. This result is in good agreement with the measured temperature fields. It also validates the location of fatigue crack initiation but does not account for the real

shape of the specimen (wrinkles) that affects the stress distribution through its section.

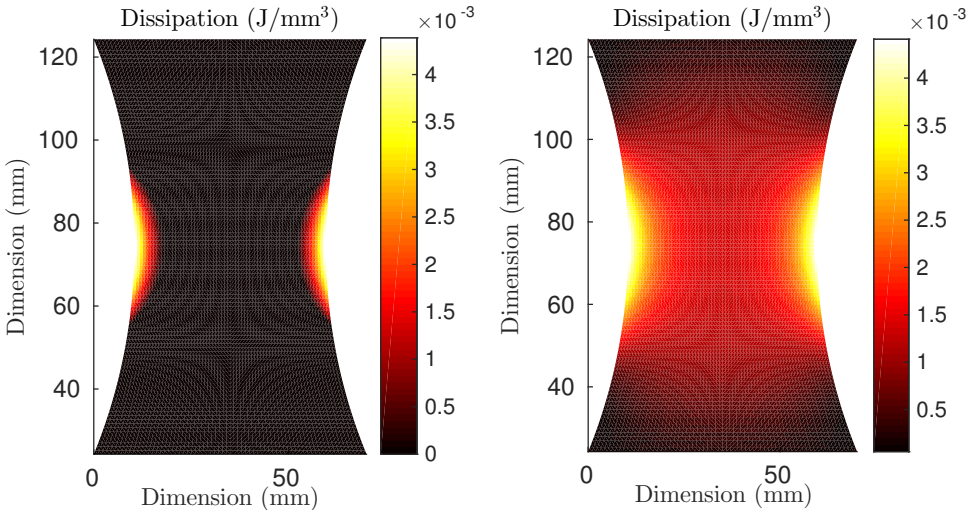


**Figure 7.7:** Deterministic (a) and probabilistic (two-scale model) dissipation maps for a maximum equivalent stress amplitude $\Sigma_{eq} = 350$ MPa

Last the parameter $V_0$ is assessed and Table 7.4 gathers the material parameters relative to the probabilistic two-scale model.

**Table 7.4:** Material parameters for the probabilistic model

| Name | RMS (°C) | $m$ | $S_0$ (MPa) | $\alpha$ | $V_0$ (mm$^3$) | $H_m$ | $V_{eff}$ (mm$^3$) |
|---|---|---|---|---|---|---|---|
| Value | $7.8 \times 10^{-2}$ | 26 | 51 | 0.9 | 8.83 | $2.94 \times 10^{-2}$ | 11.5 |

## 7.4 Fatigue analysis of bellows

### 7.4.1 Experiment

The experimental setup is composed of one infra-red camera, the specially designed fatigue testing machine (see Appendix B), a digital camera, and two cooling systems (see Figure 7.8). The water cooling system is composed of two parts (at the same temperature) positioned above and below the bellows. It allows for a temperature gradient close to zero in the bellows region as obtained for the uniaxial experiment with the two cold grips of the servohydraulic tension/compression testing machine. The air fan prevents the air to stagnate close to the bellows. A black matt painted box isolates the bellows from

environmental radiations. The bellows upper interface is bound to a load sensor (fixed on the machine) while its bottom counterpart is bound to the piston rod. The rotation speed of the electrical motor is synchronized to the acquisition rate of the infra-red camera to capture the bellows in the same configuration. The alternating displacement amplitude is applied at a 10 Hz frequency whereas the infra-red camera captures one image per second. The mid-stroke, that is the parameter to optimize (Chapter 2), is adapted by two means: *a*) a nut with two different threads at its ends is rotated while keeping fixed the two threaded shafts (the threads being different, the distance between the two changes as the nut is turned) and *b*) steel washers are added or removed on the three stainless steel columns that surround the bellows.

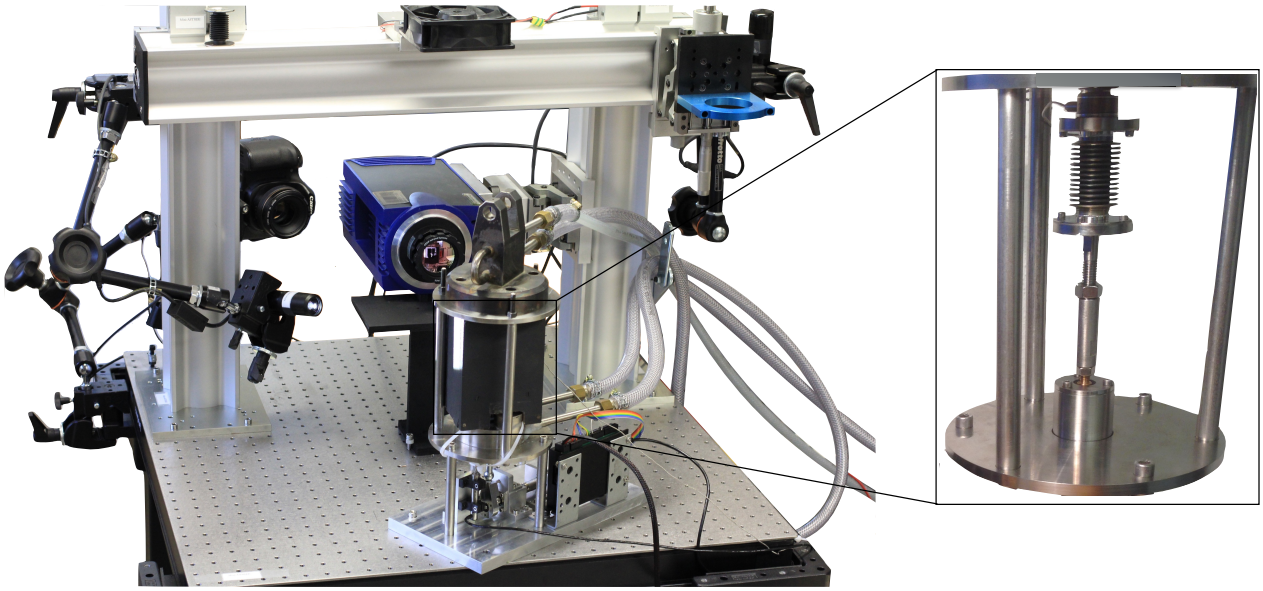

**Figure 7.8:** Experimental setup used to investigate and assess the fatigue properties of welded bellows

The experimental procedure for one bellows relies on 4 steps: *i*) the bellows is black matt painted, placed in the machine where the reference is defined such that the measured load is equal to zero, *ii*) the cyclic displacement and the measurement start when the temperature at rest is stable, *iii*) the loading ends when the temperature reaches a steady-state value (*i.e.,* the camera continues to monitor the temperature), *iv*) the acquisition stops when the temperature reaches a steady-state value.

Two sets of bellows respectively composed of 11 and 13 folds allow various stress amplitudes to be investigated. It is of importance to note that two identical bellows are necessary to investigate positive and negative mid-strokes. The macroscopic and microscopic plastic strains that occur for the first investigated direction (tension or compression) prevent a direct plastic-strain free material investigation for its opposite counterpart. Figure 7.9(a) shows a measured temperature field at time $t = 100$ s for an 11-fold bellows and

a mid-stroke positioned at $z_c = 0$ mm. Figure 7.9(b) shows the temperature history $\Delta T(t)$ processed from the thermal images. Solving the heat equation (7.5) gives the steady-state temperature and the constant $\tau_{eq}$ (roughly equal to 70 s). The same procedure is applied to each investigated mid-strokes and bellows.

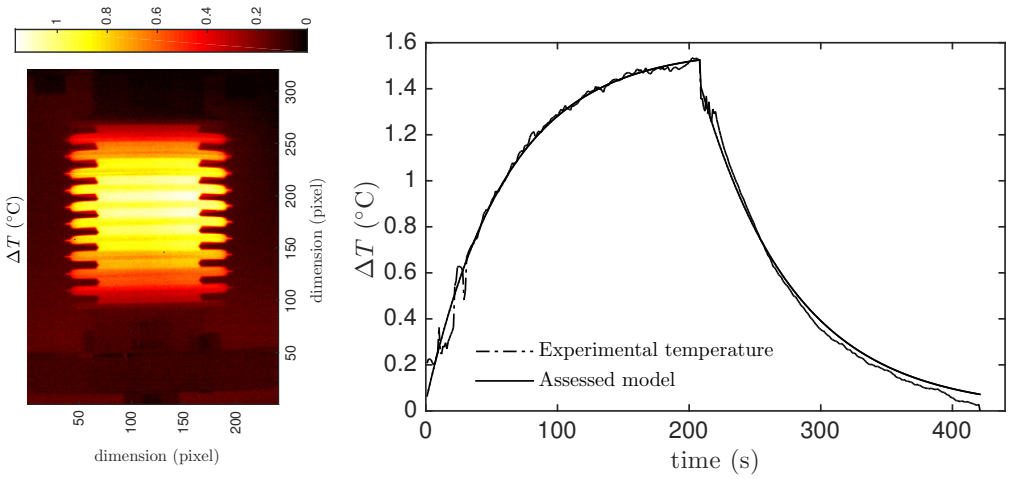


(a) (b)

**Figure 7.9:** (a) Field of temperature difference at $t = 100$ s and (b) temperature difference history processed from the thermal images

Two types of result are obtained, namely, the steady-state temperature and the number of cycles to failure. First, the steady-state temperatures as functions of the chosen mid-stroke are gathered for the four investigated bellows accounting for the two configurations (see Figure 7.10). A unique minimum of steady-state temperature is found in both configurations, but 13-fold bellows dissipate less energy than the 11-fold bellows.

Second, three bellows have failed but only when the mid-stroke was positioned beyond $z_c = 5$ mm. For all cases, the failure occurs at an inner weld. This result is in good agreement with the numerical analysis that revealed that the highest stress level is expected to be in inner welds. However, in this configuration (11 folds and mid-stroke positioned at $z_c = 5$ mm) the bellows is plastically deformed both microscopically and macroscopically but continues to operate without failure for more than one million cycles. This counter-intuitive result originates from its geometry that restrains the crack to propagate from a component side to another by stress inversion. Figure 7.11 shows the principal stresses near an inner weld and reveals that two principal stresses ($\Sigma_{II}$ and $\Sigma_{III}$) have opposite signs and may prevent cracks to propagate.

Last, fractographic observations are carried out to determine the fracture mechanisms for the entire failure history [165]. Figure 7.12 shows post-mortem fractographies SEM of the welded bellows that failed after $3 \times 10^6$ cycles. First, the crack initiates in the region

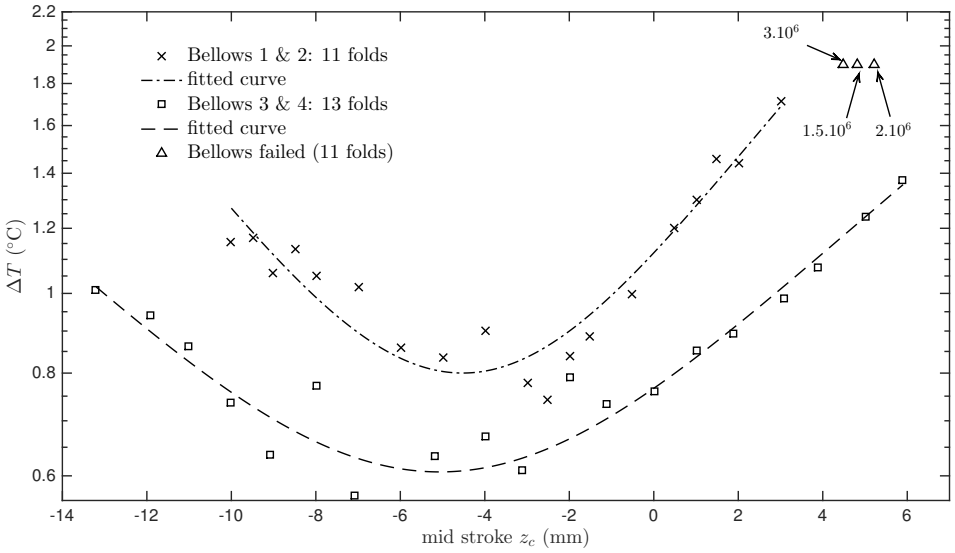


**Figure 7.10:** Experimental results for the variation of the steady-state temperature as a function of the mid-stroke and number of folds. The triangles show three bellows that have failed (the number of cycles to failure are indicated but no steady-state temperature has been measured)

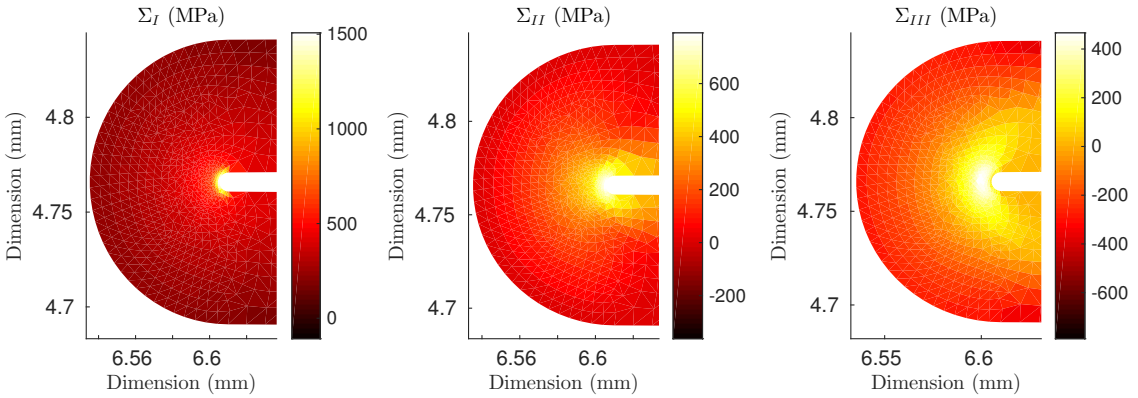


**Figure 7.11:** Principal stress fields near an inner weld. The stresses have opposite signs between the inner and the outer sides of the weld

denoted (a) where numerous striations are seen and are representative of a microscale brittle fracture type. These fractographic features are typical of the fatigue failure initiation for metals. Second, the failure mechanism changes at points (b) to a surface fracture characterized by dimpled zones due to microscale void growth. These features are representative of a microscale ductile fracture regime (see region (c) in Figure 7.12). Last, the bellows fails under a macroscale ductile fracture regime revealed by the important size of

the five shear lips on the fracture surface (see region (d) in Figure 7.12). It is worth noting that the same failure history as encountered for the uniaxial specimen is found.

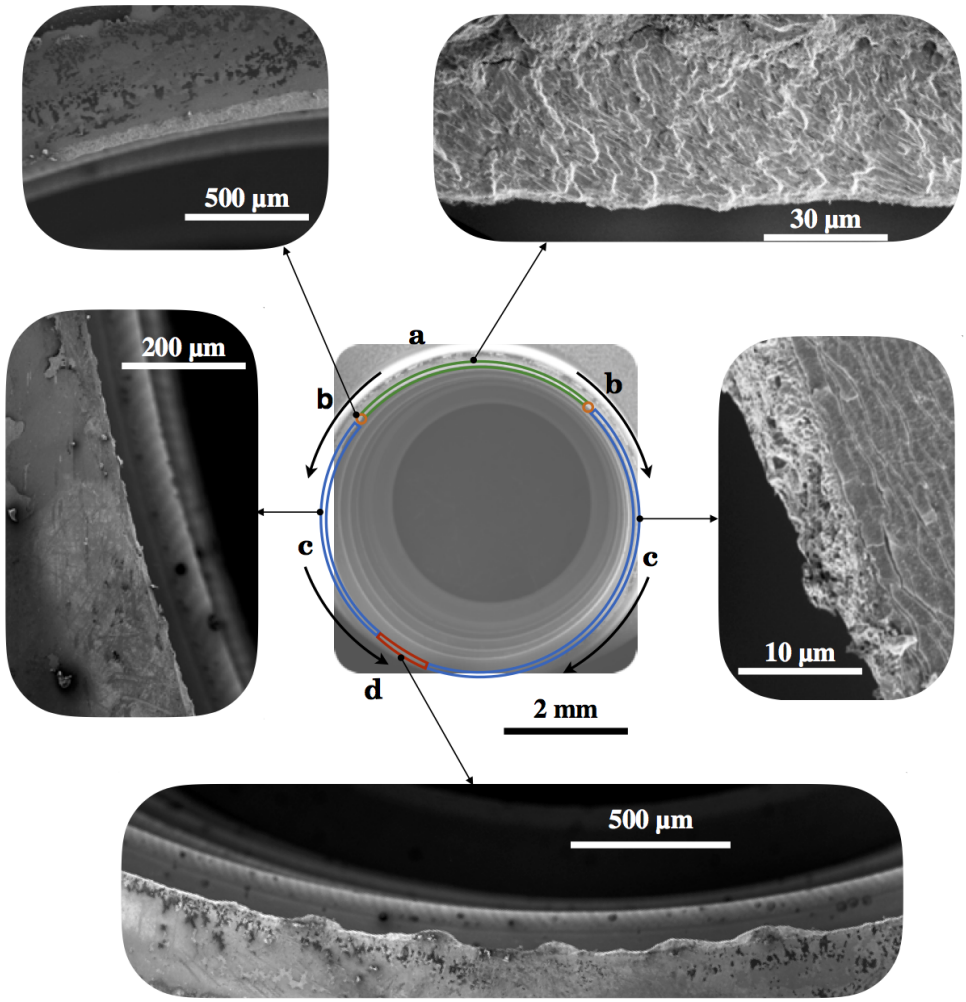


**Figure 7.12:** Secondary electron micrographies showing the complete failure history of one bellows. Three regimes are seen, in the order of appearance: (a) microscopic brittle fracture, (c) microscopic ductile fracture, and (d) macroscopic ductile fracture. (b) indicates the change of regime from (a) to (c)

### 7.4.2 Identification

The probabilistic two-scale model is now extended to describe high-cycle fatigue properties of multiaxial and proportional loadings [19]. This extension consists in the choice of an equivalent activation stress ($\Sigma_a$) that is related to the first and second invariants of the

stress amplitude

$$\Sigma_a = \Sigma_0^{eq}\left(1-\alpha'\left(P_{mean}-\frac{1}{3}\right)\right) \tag{7.24}$$

where $\alpha'$ is a material-dependent parameter, $\Sigma_0^{eq} = J_2(\boldsymbol{\Sigma}_0)$ is the equivalent stress amplitude, and $J_2$ is the second stress invariant. The amplitude of the stress history reads

$$\boldsymbol{\Sigma}_0 = 1/2\left(\boldsymbol{\Sigma}(t_{T.D.C.}) - \boldsymbol{\Sigma}(t_{B.D.C.})\right) \tag{7.25}$$

where $t_{T.D.C.}$ and $t_{B.D.C.}$ are the top dead center ($T.D.C.$) and bottom dead center ($B.D.C.$) strokes, $P_{mean} = \langle 1/3\mathrm{tr}(\boldsymbol{\Sigma})\rangle$ is the mean hydrostatic stress.

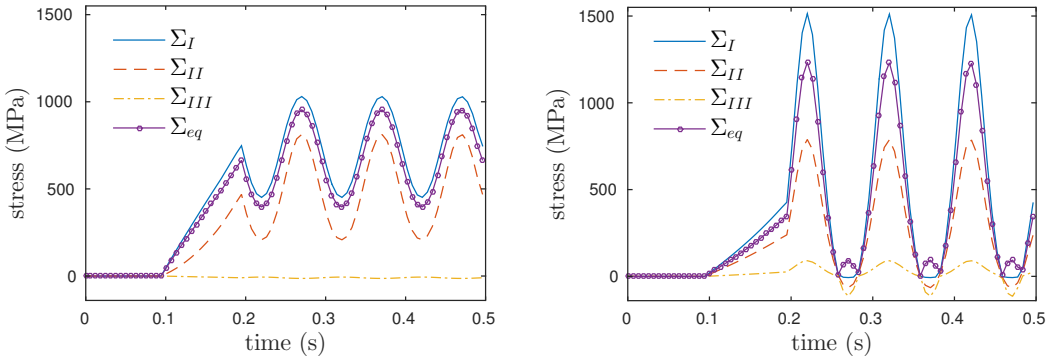


**Figure 7.13:** Histories of the principal stresses and the von Mises equivalent stress ($\Sigma_{eq}$) for two mid-strokes positioned at (a) $z_c = -8$ mm and (b) $z_c = 3$ mm

The parameter identification is performed on the element that undergoes the highest alternating stress amplitude level. Figure 7.13 shows the principal stresses ($\Sigma_I, \Sigma_{II}$, and $\Sigma_{III}$) and the equivalent Von Mises stress ($\Sigma_{eq}$) for this position and for (a) $z_c = -8$ mm and (b) $z_c = 3$ mm. The result is that the mechanical response appears the most severe for a mid-stroke positioned at $z_c = 3$ mm that generates a triaxial tensile stress state. Considering this new equivalent activation stress, the steady-state temperature reads

$$\Delta T = \frac{\eta m}{(m+1)(m+2)}\frac{(\Sigma_0^{eq})^{m+2}}{(S_0)^m}\left(1-\alpha'\left(P_{mean}-\frac{1}{3}\right)\right)^m \tag{7.26}$$

where $S_0$ is the scale parameter assessed from the uniaxial experiment. Looking at the components of the trace of the stress tensor, the hydrostatic stress depends on the mid-stroke value (see Figure 7.14). The result is that, for a mid-stroke positioned at $z_c = -8$ mm, the amplitude and the maximum hydrostatic stress values are smaller than the one obtained for $z_c = 3$ mm. A compressive configuration appears to be less damaging than its tensile counterpart.

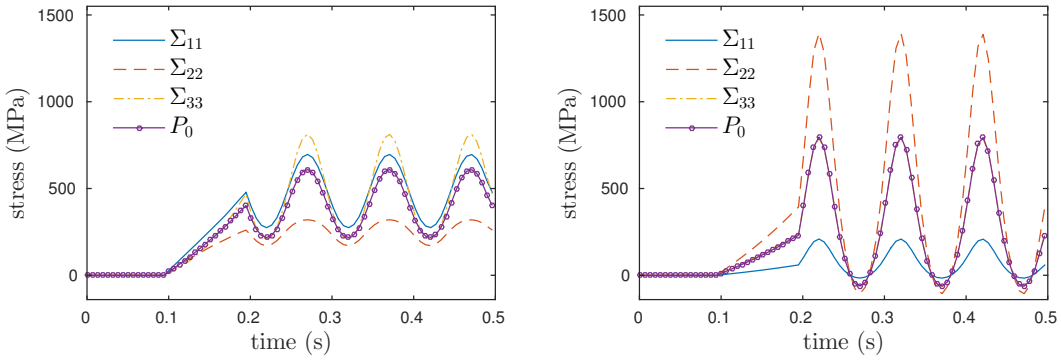


**Figure 7.14:** Components of the trace of the stress tensor and the hydrostatic stress ($P_0 = 1/3\ \mathrm{tr}(\boldsymbol{\Sigma})$) as function of the loading history for (a) $z_c = -8$ mm and (b) $z_c = 3$ mm

The numerical results (the von Mises equivalent stress amplitude ($\Sigma_0^{eq}$) and the mean value of the hydrostatic stress ($P_{mean}$) per cycle) are confronted to the experimentally determined steady-state temperatures. The identification consists of minimizing the temperature difference by finding the best set of the sought material parameters ($m$ and $\alpha'$). Figure 7.15 shows the identified steady-state temperature map based on Equation 7.26 for the 11-fold bellows (*i.e.,* the most severe configuration). The higher the stress-state the higher the steady-state temperature. Yet, a model error remains for low stress levels where the model cannot cope with steady-state temperatures greater than zero. This error originates from the inadequacy between the numerical model and the bellows (see the heterogeneities generated by the manufacturing process in Section 2.4). The boundary between a steady-state temperature remaining null and its fast increase, however, is in agreement with the uniaxial experiment result, *i.e.,* $\Sigma_0^{eq} \approx 400$MPa. The evaluated Weibull modulus ($m$) is significantly different (this result was expected since the component has experienced numerous manufacturing processes that increased its heterogeneity).

Table 7.5 gathers the assessed parameters, the stress heterogeneity factor and the effective volume obtained with the evaluated Weibull modulus and for the optimized mid-stroke ($z_c = -4$ mm). However, the volume $V_0$ has not been assessed because there was not enough bellows available.

**Table 7.5:** Assessed parameters for the probabilistic model

| Name | RMS (°C) | $m$ | $S_0$ (MPa) | $\alpha'$ |
|---|---|---|---|---|
| Value | $2.1 \times 10^{-1}$ | 3.5 | 51 | 0.51 |

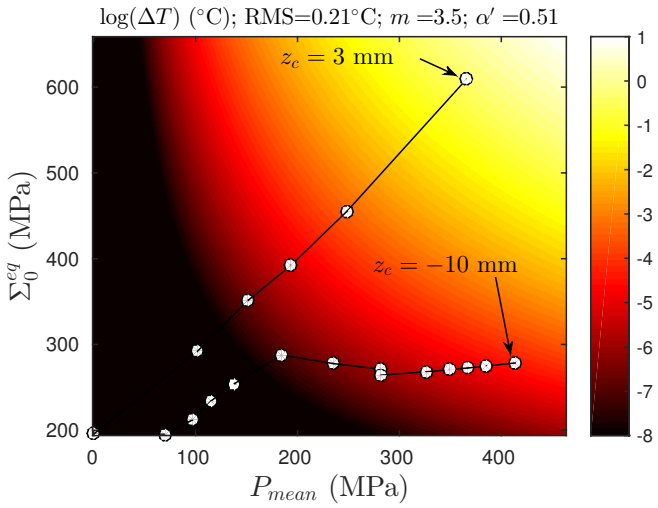


**Figure 7.15:** Steady-state temperature map assessed for the probabilistic multiaxial model. Note the log-scale used on the steady-state temperature

The next section is devoted to analyzing the fatigue data based on Goodman representation [167] and to constructing a dedicated diagram for the fatigue design of the welded bellows based on the coupling of the numerical and experimental results.

### 7.4.3 Goodman diagram

A Goodman diagram is an engineering tool that helps the HCF design of materials and mechanical components [167]. The representation is also useful to study the influence of the mean hydrostatic stress on the fatigue properties [168, 169, 170] or that of the maximum hydrostatic stress [171, 172, 173]. When applied to a uniaxial case it shows the mean stress ($\Sigma_m$) plotted in abscissa and the stress amplitude ($\Sigma$) on the ordinate. A straight “lifeline" is drawn from the equivalent failure stress amplitude $\Sigma_{eq}$ related to the mean failure stress $\Sigma_f$ of $\Sigma_m$. Then for any given mean hydrostatic stress, the endurance limit can be read directly as the ordinate of the lifeline at that value of $\Sigma_m$. Figure 7.16 shows the schematic construction of a Goodman diagram.

In the case of multiaxial stresses, the mean value of the hydrostatic stress ($P_{mean} = \langle 1/3\mathrm{tr}(\boldsymbol{\Sigma})\rangle$) is plotted in abscissa and the von Mises equivalent stress amplitude ($\Sigma_0^{eq}$) on the ordinate. Its simplicity makes it a powerful tool for fatigue design. The Goodman diagram, however, has two down sides [174]: *i*) uncommon damages generated by an extreme loading or an inappropriate material quality are not addressed properly and *ii*) an important part of the diagram is determined by extrapolation of experimental data. The experimental results will be confronted to the Sines [168] and Crossland [171] fatigue criteria. The difference is that, the former uses the mean hydrostatic stress whereas the

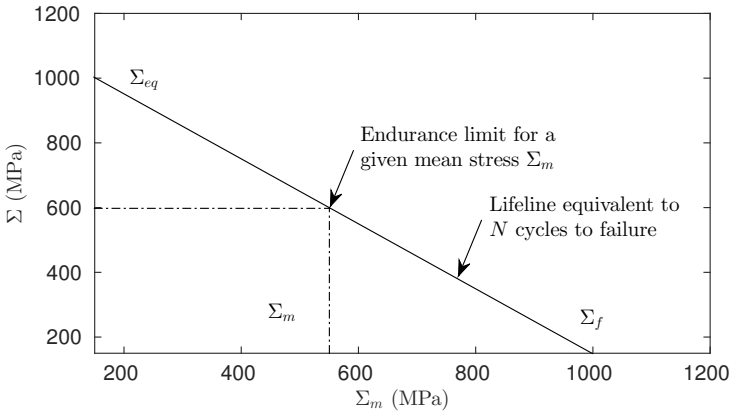


**Figure 7.16:** Construction of Goodman diagram [167]

latter considers its maximum value

$$\text{Sines:} \quad \Sigma_0^{eq} \leq \Sigma_0^S (1 - 3\, b_S\, P_{mean}) \tag{7.27}$$

$$\text{Crosseland:} \quad \Sigma_0^{eq} \leq \Sigma_0^C \frac{1 - 3\, b_C\, P_{max}}{1 - b_C\, \Sigma_0^C} \tag{7.28}$$

where $P_{mean} = \langle 1/3\mathrm{tr}(\boldsymbol{\Sigma}) \rangle$ is the mean value of the hydrostatic stress during a cycle and $P_{max} = \max(1/3\mathrm{tr}(\boldsymbol{\Sigma}))$ its maximum value. The relationship between the equivalent stress amplitude and the mean hydrostatic stress or its maximum value is obtained by fitting an equation of a plane ($\lambda_1 + \lambda_2 \Sigma_0^{eq} + \lambda_3 P = \Delta T$) on the Goodman diagram ($P = P_{mean}$ or $P_{max}$). Then, the Sines and Crosseland parameters are deduced from the parameter set $[\lambda_1, \lambda_2, \lambda_3]$.

Figure 7.17 shows the Goodman diagram for the studied bellows. The larger the mid-stroke the higher the risk of failure. The influence of the mean hydrostatic stress, however, is close to zero, which in contradiction with several studies [174, 168, 169, 170]. Furthermore, when confronted to the Sines criterion, the results show that the failed bellows have a more important mean hydrostatic stress value but a lower equivalent stress amplitude than the result obtained for $z_c = 3$ mm. Therefore, this representation is not adequate for the investigated problem.

Figure 7.18 shows the Goodman diagram relative to the maximum hydrostatic stress. The temperature variation is even lower and both $\Sigma_0^{eq}$ and $P_{max}$ influence the fatigue behavior. The positions of the failed bellows are in agreement with the Crosseland criterion, *i.e.,* located on the $10^6$ cycles fatigue limit. Table 7.6 gathers the assessed parameters of the Sines and Crosseland criteria.

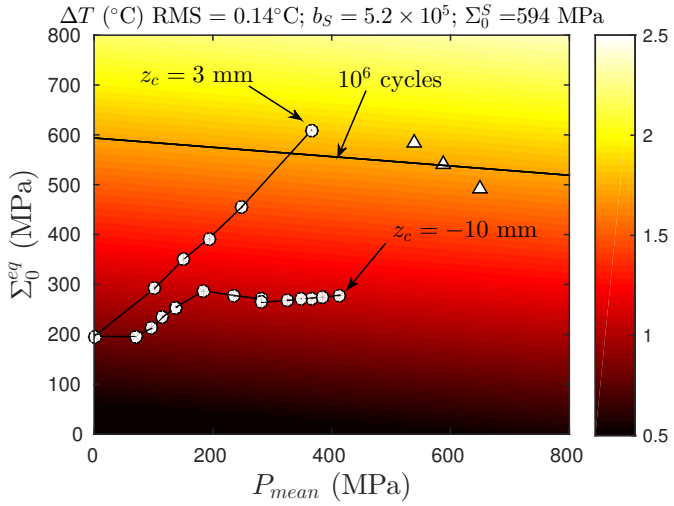


**Figure 7.17:** Goodman diagram assessed with the mean steady-state temperatures, the Sines criterion, and the three failed bellows (triangles)

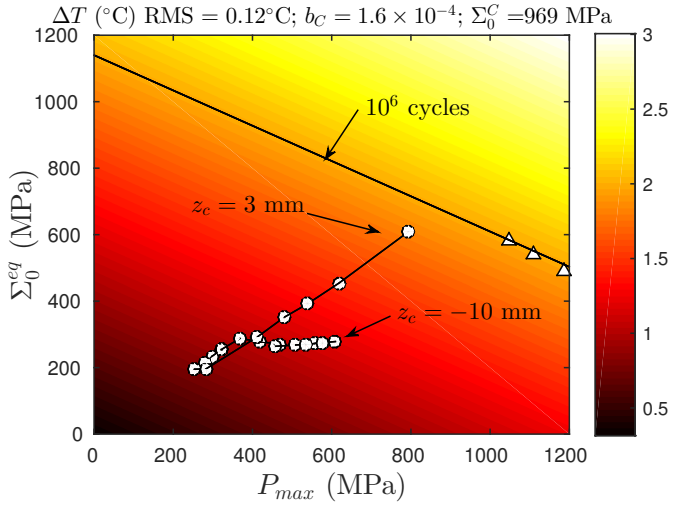


**Figure 7.18:** Modified Goodman diagram assessed with the mean steady-state temperatures, the Crosseland criterion, and the three failed bellows (triangles)

**Table 7.6:** Sines and Crosseland steady-state temperature residuals and corresponding parameters

| Name | $\text{RMS}_{\text{Sines}}$ | $b_S$ | $\Sigma_0^S$ | $\text{RMS}_{\text{Crosseland}}$ | $b_C$ | $\Sigma_0^C$ |
|---|---|---|---|---|---|---|
| dimension | °C | – | MPa | °C | – | MPa |
| Value | $1.4 \times 10^{-1}$ | $5.2 \times 10^{-5}$ | 594 | $1.2 \times 10^{-1}$ | $1.6 \times 10^{-4}$ | 969 |

### 7.4.4 Validation of the 12-fold bellows design

This section aims to validate the fatigue design of the 12-fold welded bellows based on the Goodman plot of Section 7.4.3 and the initial probabilistic fatigue design introduced in Chapter 2. For a 12-fold bellows subjected to an external pressure and for a Weibull modulus evaluated to be $m = 3.5$ the optimal mid-stroke is equal to $z_c = 1.2$ mm. This result is different from the optimal value experimentally assessed for the two investigated configurations but without external pressure ($z_c \approx -4$ mm). This difference originates from the applied pressure and the assumptions (isotropic material, undamaged welds and model geometry) that alter the numerical results.

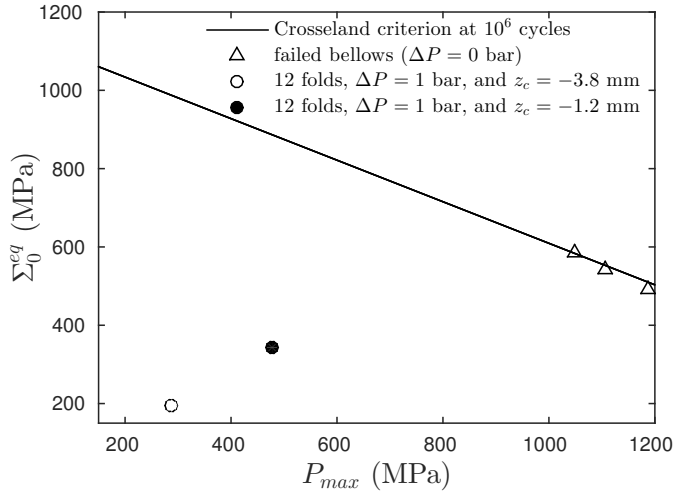


**Figure 7.19:** Modified Goodman diagram of bellows made 17-7 PH grade. The Crosseland criterion is applied to 12-fold bellows where an external pressure equal to $\Delta P = 1$ bar is prescribed

Figure 7.19 shows the maximum stress-states for two mid-strokes ($z_c = -1.2$ mm and $z_c = -3.6$ mm) of the 12-fold bellows with the external pressure on the modified Goodman diagram. The locations of the two optimal mid-strokes are far from the Crossland lifeline. The probabilistic design with a Weibull modulus equal to $m = 3.5$ leads to an optimal mid-stroke different from the deterministic one. Even though their location is identical in the Crossland domain, both predictions are significantly lower than the 'lifeline.' Consequently, the design of the bellows is deemed validated.

## 7.5 Conclusion

The material and the bellows fatigue behaviors have been investigated and the bellows fatigue life has been optimized. Several tools and procedures have been utilized to that

end and the results give several insights into the fatigue properties of the studied material and structure.

First, deterministic and probabilistic models were introduced to describe the fatigue behavior of thin (70 $\mu$m) pre-deformed sheets made of precipitation hardened stainless steel. The material is found to be particularly homogeneous as exhibited by a Weibull modulus of $m = 26$. However, a difference between the ultimate fatigue strengths obtained with the Wöhler approach and the self-heating experiment is observed. This difference originates from the very thin sheet that decreases the stresses in the specimen boundaries and presumably increases its fatigue strength.

Second, a hybrid experimental/numerical analysis of the bellows fatigue behavior was performed. An optimal mid-stroke ($z_c \approx -4$ mm) is obtained thanks to an in-house designed testing machine associated with an infra-red camera. Three bellows have been broken in cyclic fatigue but only for a very large equivalent stress amplitude. Under these severe configurations ($z_c \geq 4$ mm) and for the 11-fold bellows, the lifespan exceeds $10^6$ cycles even if the component is plastically deformed. This result needs to be confirmed with additional experiments. The identification of the probabilistic two-scale model reveals a heterogeneous response ($m = 3.5$) that originates from the two subsequent manufacturing processes (stamping and welding). Unfortunately, too few components were available that prevented the complete validation of the bellows probabilistic model.

Based on the results obtained in Chapter 2 the optimal mid-stroke for a 12-fold bellows subjected to an external 1 bar pressure is equal to $z_c = 1.2$ mm (*i.e.,* different from the deterministic design where $z_c = -3.6$ mm). The modified Goodman diagram validates the fatigue design for a lifespan greater than $10^6$ cycles. Last, it is important to note that the component in its final use will experience a changing environment (various alternating stresses and pressures) and will interact with the coolant. These aspects are not addressed by the Goodman diagram and will negatively affect its fatigue strength [174]. Therefore, the optimized mid-stroke is formulated in terms of an optimized range equal to $z_c \in [-4; 1.2]$ mm and for a lifespan of $10^6$ cycles in standard operating conditions.

# Chapter 8
# General conclusions and recommendations

## 8.1 Conclusions

Many results of this work originate from scientific and engineering collaborations and aim to contribute to meet sustainability standards as introduced in Chapter 1. Chapter 2 gives an initial probabilistic fatigue design based on the weakest link theory that assumes a standard Weibull modulus for stainless steel. Yet, this result is by nature incomplete and a rigorous identification of the mechanical and HCF fatigue properties were the designated objectives. Therefore, the overall thesis relies on a strategy that starts with the identification of the material macroscopic and microscopic mechanical properties and ends with the optimization and the validation of the component probabilistic fatigue design.

Part A addresses the first issue and assesses the material macroscopic and microscopic mechanical behaviors. To that end, Chapter 3 introduces a complete identification procedure from the acquisition of the experimental data to the identification of the sought parameters. The technique embraces all data and their corresponding uncertainties into one single frame via Integrated DIC. To combine these data a weighting that originates from a Bayesian foundation was followed. Consequently each pixel and load cell play the same role, when there respective noise level is accounted for. Using this new procedure, a novel optimization strategy that minimizes the highest uncertainty of the sought parameters is applied to the design of two cruciform geometries for two constitutive laws, *i.e.,* linear elasticity and linear elasticity with linear kinematic hardening.

Chapters 4 and 5 investigate the macroscopic material mechanical behavior. Two experimental devices are used, a servohydraulic tension/compression testing machine and the biaxial testing machine (mini-ASTREE) and four constitutive laws with increasing complexity are investigated. Some of the barriers that have initially prevented the investigation of ultra-thin sheets (50 $\mu$m) with IDIC had be solved with a dedicated anti-wrinkling device. A two-step identification strategy is followed, first an initial sensitivity analysis reveals the adequacy of the raw data with respect to the sought parameters and second the identification problem is addressed with a regularization functional that pre-

vents meaningless parameters to be determined when their influences on the observables are too weak. The study also assesses the limits of the investigated models with four indicators: *i*) gray level residual map, *ii*) displacement residual map, *iii*) load residual, and *iv*) an overall quality indicator $\chi^2$ (see Section 4.5). The latter is based on the IDIC formulation that compares all sensor information inside the Bayesian foundation and gives a quantifiable result of the quality that can provide a constitutive model. These indicators have proven that the investigated material behaves plastically and anisotropically but the result obtained for the elastoplastic model with a linear kinematic hardening was satisfactory enough for low strain amplitudes.

Chapters 6 investigates the micromechanical behavior of a micro-specimen made of IF-steel. Manufacturing and experimental processes based on a triangular prism machined via focused ion beam (FIB) have been designed to perform the identification of the sought hardening parameters. The latter is carried out with integrated-DIC coupled with 3 dimensional finite element simulations where the microstructure has been fully determined with EBSD. Not only are the material parameters being investigated but also the in-depth boundary conditions. Finally, the identification of the sought hardening parameters is achieved with the inclusion of measured reaction forces to the minimization functional.

Part B addresses the second issue via self-heating experiment methodology and a probabilistic multi-scale model. The material and component fatigue properties are evaluated. To that end, a primary analysis of the fatigue behavior of ultra-thin sheets is performed. The result is that the mean endurance limit assessed with deterministic model is equal to 300 MPa. However, this result is lower than the mean endurance limit assessed with the Wölher approach by about 100 MPa. This result originates from the sheet thinness that decreases the stresses in the specimen edges and enhances its mean endurance limit. Then, thanks to the fatigue testing machine designed in collaboration with the engineering company AER the dissipated energy generated in HCF regime by the bellows is estimated. This experimental result has first led to an experimental optimal mid-stroke and second to the determination of the bellows fatigue properties thanks to a dual experimental/numerical analysis. The identification of the probabilistic multi-scale model parameters have revealed a heterogenous component (*i.e.,* the Weibull modulus is equal to $m = 3.5$) far appart from the highly homogeneous raw material ($m = 26$). This result originates from the bellows manufacturing process that increases the variability in the component especially in the welds. The construction of a modified Goodman diagram based on the equivalent stress amplitude and the maximum value of the hydrostatic stress has allowed for the validation of the bellows design.

## 8.2 Recommendations

This research project has met numerous objectives but also many questions have been raised. The recommandations and perspectives presented hereafter are formulated in terms of ideas and concepts that propose new paths to tackle the investigated topics. First, the material parameter identification and its potential future applications are addressed. Second, several perspectives about the characterization of the fatigue properties of ultra-thin steel sheets and components are discussed.

The concept of *the most appropriate* experiment based on full field measurement and Integrated DIC has been investigated. A non-intrusive methodology that proposes a standard and general optimization formulation in solid mechanics has been shown. One result is that the most heterogeneous geometry is not necessarily the most appropriate for a specific constitutive law (see the elastic and elastoplastic optimizations performed in Chapter 3). Its application has led to the determination of four fillet radii for two different laws but a more elaborate optimization procedure of the geometry or even more of the loading path could be performed within the same goal of reducing the identification uncertainty.

The identification methodology relies on a very general formulation that provides a powerful tool to treat raw data and investigate any constitutive models. The IDIC technique can address multidimensional space and time problems, and can be applied to any mechanical experiment aiming to characterize a constitutive law describing a mechanical behavior. Therefore, any problems dealing for example with stereo-correlation [175], infra-red camera [176], scanning electron microscope [134, 133], X-ray diffraction instrument [177], or X-ray tomography [178, 179] can be addressed differently.

So far in this project, raw data are treated post experiment, yet a real time identification of the material properties can be envisioned. Barriers such as computational cost and the direct coupling of numerical and experimental results have started to be confronted [180]. Last, not only the material parameters are the quantities of interest but the boundary conditions can (and should) also be part of the identification problem [181] and even drive the experiment [182].

Regarding the experimental advances dedicated to the characterization of the quasi-static material behavior, mini-ASTREE leads the way to smaller and less expensive experiments, yet still rich enough in raw data. Its efficiency may serve research and industrial objectives by drastically lessening time and specimen costs. However, smaller is usually thinner and a direct investigation of an ultra-thin specimen is unlikely to give results. Therefore, an anti-wrinkling device to prevent out-of-plane displacement has been designed but the interaction between the plexiglas sheets and the specimen needs to be properly characterized. An experiment that measures the displacement fields on both sides (one corresponding to the specimen and one to the plexiglass sheet) would separate both behaviors. Apart from macroscopic characterization, the microscopic experiment

has suffered from two problems, *i*) the lack of load data at the microscopic scale and *ii*) the low image definition. The use of a nano-tensile stage [139] would address the first issue but doing 3 dimensional EBSD pole figures would provide a wealth of information able to cope with the entire microscopic mechanical behavior.

The validation of the constitutive laws remains a key issue and the present study aims to pave the way to design experiments not only to identify but to (in-)validate them. To that end, dedicated indicators help diagnose model errors. The ultimate experiment would start with a set of constitutive laws (so far all candidates) that are ranked in real time from the worst to the most accurate model while the experiment is carried out. The results are the material parameters for each constitutive laws and their corresponding model errors (with respect to the noise level).

Two more issues that have not been addressed herein can enhance the future of IDIC. First, the combination of a robust identification framework associated with a general optimization procedure and an enhanced experimental environment providing a fast, yet precise and faithful characterization and validation device able to reach a wider scientific audience [183] and industry. The start-up EikoSim [184, 185] created by two former Ph.D students and the DICCIT (Digital Image Correlation Comparison Identification Tools) project [186] aim to create a framework for industrial applications that move toward more challenging and interesting geometries. Second, the visualisation of the results is a crucial aspect that would make the analysis of the results easier. The optimal goal would show in real time all results as residual maps and sought parameters.

The characterization of the fatigue properties have been carried out with temperature measurements and a probabilisitic multiaxial model. First, an experiment using infra-red transparent material to prevent the out-of-plane displacement could be envisioned to treat ultra-thin specimens. Second, the key success was gained once the HCF thermal response of the component was acquired. However, the model error originates from differences between the real component and its numerical counterparts. To quantify these errors whose origin is due to the manufacturing process, recommendations are twofold. First perform an experiment with a welded uniaxial specimen, and second assess an exact model of the component with CT-scans. However the large amount of data generated could affect the analysis by leading to new computational challenges.

# Bibliography


[1] The United Nations, The United Nations Conference, The Rio declaration on Environment and Development (1992). (Cited on page 1.)

[2] The United Nations, The united nations conference, The Paris Agreement on Environment and development. Transforming our world: the 2030 Agenda for Sustainable Development (2015). (Cited on page 1.)

[3] M. Berns, A. Townend, Z. Khayat, B. Balagopal, M. Reeves, M. S. Hopkins, N. Kruschwitz, The business of sustainability imperatives, advantages, and actions (2009), BCG.perspectives. (Cited on page 1.)

[4] M. Smits, D. Wald, D. Vismans, E. Huet, An imperative for consumer companies to go green. When social responsibility leads to growth (2014), BCG.perspectives. (Cited on page 1.)

[5] D. Beal, E. Rueda-Sabater, S. L. Heng, Why well-being should drive growth strategies. The 2015 sustainable economic development assessment (2015), BCG.perspectives. (Cited on page 1.)

[6] T. Waring, M. Teisl, E. Manandhar, M. Anderson, On the travel emissions of sustainability science research, Sustainability 6 (5) (2014) 2718. (Cited on page 1.)

[7] European Commission, European aviation environmental report (2016). (Cited on page 1.)

[8] Airbus Group, Annual review, flying efficiently (2014). (Cited on pages 1 and 2.)

[9] Lufthansa Group, Innovation the key to a successful future (2014). (Cited on page 1.)

[10] European Commission, Roadmap to a single european transport area - towards a competitive and resource-efficient transport system (2011). (Cited on page 2.)

[11] J. Tollefson, Car industry: Charging up the future, Nature 456. (Cited on page 2.)

[12] J. Duval, Dossier de soumission THERMOFLUIDE-RT. $14^e$ appel à projets de recherche et développement collaboratifs des ples de compétitivité. (Cited on page 2.)

[13] C. E. Stromeyer, The determination of fatigue limits under alternating stress conditions, Proceedings of the Royal Society of London A: Mathematical, Physical and Engineering Sciences 90 (620) (1914) 411–425. (Cited on pages 3 and 117.)

[14] H. Moore, K. J., Progressive failure or fatigue of metals under repeated stress, Chemical and Metallurgical Engineering 25 (25) 427–434. (Cited on pages 3 and 117.)

[15] L. M. Phong, Infrared thermography of fatigue in metals, Proceding SPIE (1682) 222-233 (1992). (Cited on pages 3, 4, 113, 117 and 122.)

[16] T. Boulanger, A. Chrysochoos, C. Mabru, A. Galtier, Calorimetric analysis of dissipative and thermoelastic effects associated with the fatigue behavior of steels, International Journal of Fatigue 26 (3) (2004) 221 – 229. (Cited on pages 3 and 117.)

[17] C. Doudard, Détermination rapide des propriétés en fatigue à grand nombre de cycles à partir d'essais d'échauffement, Ph.D. thesis, Ecole Normale Supérieure de Cachan (2004). (Cited on pages 3, 4, 22, 118, 119, 121, 122 and 126.)

[18] L. Méric, G. Cailletaud, Single crystal modeling for structural calculations: Part 2 - finite element implementation, Journal of Engineering Materials and Technology 113 (1991) 171–182. (Cited on pages 3, 92, 94 and 102.)

[19] C. Doudard, M. Poncelet, S. Calloch, C. Boué, F. Hild, A. Galtier, Determination of an HCF criterion by thermal measurements under biaxial cyclic loading, International Journal of Fatigue 29 (4) (2007) 748 – 757. (Cited on pages 4, 16, 18, 113, 118, 122 and 132.)

[20] M. Poncelet, C. Doudard, S. Calloch, B. Weber, F. Hild, Probabilistic multiscale models and measurements of self-heating under multiaxial high cycle fatigue, Journal of the Mechanics and Physics of Solids 58 (2010) 578–593. (Cited on pages 4 and 118.)

[21] F. T. Peirce, Tensile tests for cotton yarns - the weakest link theorems on the strength of long and of composite specimens, The Journal of The Textile Institute 17 (1926) 355 – 368. (Cited on pages 5 and 12.)

[22] F. Hild, De la rupture des matériaux à comportement fragile, Ph.D. thesis, Université Paris VI (1992). (Cited on pages 7 and 14.)

[23] AK-Steel, Mechanical characteristics 17-7 PH steel, AK-Steel (2013). (Cited on pages 7, 8, 23, 37, 40, 51, 52, 64, 75, 77, 78, 89, 120, 122 and 127.)

[24] A. Leybold-Herbert, Axial-load fatigue tests on 17-7 PH stainless steel under constant-amplitude loading, NASA TN D-439 62 71013, National Aeronautics and Space Administration, Langley Research Center Langley Field, Va. (October 1960). (Cited on pages 8, 23, 51, 77, 78, 89 and 122.)

[25] H. Mughrabi, H. W. Hoppel, Cyclic deformation and fatigue properties of very fine-grained metals and alloys, International Journal of Fatigue 32 (9) (2010) 1413 – 1427. (Cited on page 8.)

[26] C. Bathias, J. Baïlon, La fatigue des matériaux et des structures, Hermes, France, 1997. (Cited on page 12.)

[27] W. Weibull, A statistical theory of the strength of materials, Ingeniors Vetenskaps Akademien 151-3 (1939) 45–55. (Cited on pages 12, 13 and 118.)

[28] W. Weibull, A statistical distribution function of wide applicability, ASME Journal of Applied Mechanics 18 (1951) 293–297. (Cited on pages 13, 118 and 121.)

[29] R. Hill, A theory of the yielding and plastic flow of anisotropic metals, Proceedings of the Royal Society of London. Series A, Mathematical and Physical Sciences 193 (1033) (1948) 281–297. (Cited on pages 21, 49, 50, 71, 72 and 73.)

[30] I. Wilson, D. J. White, Cruciform specimens for biaxial fatigue tests: An investigation using finite-element analysis and photoelastic-coating techniques, The Journal of Strain Analysis for Engineering Design 6 (1) (1971) 27–37. (Cited on page 21.)

[31] M. W. Brown, K. J. Miller, A theory for fatigue failure under multiaxial stress-strain conditions, Proceedings of the Institution of Mechanical Engineers 187 (1) (1973) 745–755. (Cited on page 22.)

[32] D. A. Kelly, Problems in creep testing under biaxial stress systems, Journal of strain analysis for engineering design 11 (1) (1976) 1–6. (Cited on page 22.)

[33] G. Ferron, A. Makinde, Design and development of a biaxial strenght testing device, Journal of Testing and Evaluation 16 (1988) 253–256. (Cited on page 22.)

[34] A. Makinde, Mise au point d'un dispositif original de traction biaxial: application à l'étude expérimentale de l'écrouissage des métaux sous différents chemins de déformation., Ph.D. thesis, Université de Poitiers (1986). (Cited on page 22.)

[35] A. Makinde, L. Thibodeau, K. Neale, Development of an apparatus for biaxial testing using cruciform specimens, Experimental Mechanics 32 (2) (1992) 138–144. (Cited on page 22.)

[36] T. Kuwabara, S. Ikeda, K. Kuroda, Measurement and analysis of differential work hardening in cold-rolled steel sheet under biaxial tension, Journal of Materials Processing Technology 80-81 (1998) 517 – 523. (Cited on page 22.)

[37] P. Boisse, A. Gasser, G. Hivet, Analyses of fabric tensile behaviour: determination of the biaxial tension-strain surfaces and their use in forming simulations, Composites Part A: Applied Science and Manufacturing 32 (10) (2001) 1395–1414. (Cited on page 22.)

[38] N. Muzyka, Equipment for testing sheet structural materials under biaxial tension. part 2. testing by biaxial loading in the plane of the sheet, Strength of Materials 34 (2) (2002) 206–212. (Cited on page 22.)

[39] M. Teaca, I. Charpentier, M. Martiny, G. Ferron, Identification of sheet metal plastic anisotropy using heterogeneous biaxial tensile tests, International Journal of Mechanical Sciences 52 (4) (2010) 572 – 580. (Cited on pages 22 and 72.)

[40] D. E. Green, Etude expérimentale et numérique du comportement biaxial des tôles minces, Ph.D. thesis, Department of the Faculty of Engineering of the Université de Sherbrooke (janvier 1996). (Cited on pages 22 and 72.)

[41] D. Lecompte, A. Smits, H. Sol, J. Vantomme, D. V. Hemelrijck, Mixed numerical-experimental technique for orthotropic parameter identification using biaxial tensile tests on cruciform specimens, International Journal of Solids and Structures 44 (5) (2007) 1643 – 1656. (Cited on pages 22, 24, 50 and 101.)

[42] T. Kuwabara, Advances in experiments on metal sheets and tubes in support of constitutive modeling and forming simulations, International Journal of Plasticity 23 (3) (2007) 385 – 419. (Cited on page 22.)

[43] T. Kuwabara, Advances of plasticity experiments on metal sheets and tubes and their applications to constitutive modeling, AIP Conference Proceedings 778 (1) (2005) 20–39. (Cited on page 22.)

[44] J. Eftis, D. Jones, H. Liebowitz, Load biaxiality and fracture: Synthesis and summary, Engineering Fracture Mechanics 36 (4) (1990) 537 – 574. (Cited on page 22.)

[45] A. Hannon, P. Tiernan, A review of planar biaxial tensile test systems for sheet metal, Journal of Materials Processing Technology 198 (1-3) (2008) 1 – 13. (Cited on page 22.)

[46] A. Chen, F. Matthews, A review of multiaxial/biaxial loading tests for composite materials, Composites 24 (5) (1993) 395 – 406. (Cited on page 22.)

[47] J. Boehler, S. Demmerle, S. Koss, A new direct biaxial testing machine for anisotropic materials, Experimental Mechanics 34 (1) (1994) 1–9. (Cited on page 22.)

[48] M. Johlitz, S. Diebels, Characterisation of a polymer using biaxial tension tests. part I: Hyperelasticity, Archive of Applied Mechanics 81 (10) (2011) 1333–1349. (Cited on page 22.)

[49] M. Merklein, M. Biasutti, Development of a biaxial tensile machine for characterization of sheet metals, Journal of Materials Processing Technology 213 (6) (2013) 939 – 946. (Cited on page 22.)

[50] E. Hoferlin, A. V. Bael, P. V. Houtte, G. Steyaert, C. D. Maré, Biaxial tests on cruciform specimens for the validation of crystallographic yield loci, Journal of Materials Processing Technology 80 - 81 (1998) 545 – 550. (Cited on pages 22 and 72.)

[51] J. F. Wilson, B. L. Kinsey, Y. P. Korkolis, Development of a biaxial loading frame for sheet metal, Journal of Manufacturing Processes 15 (4) (2013) 580 – 585. (Cited on page 22.)

[52] A. Makinde, L. Thibodeau, K. Neale, D. Lefebvre, Design of a biaxial extensometer for measuring strains in cruciform specimens, Experimental Mechanics 32 (2) (1992) 132–137. (Cited on pages 22 and 72.)

[53] S. Demmerle, J. Boehler, Optimal design of biaxial tensile cruciform specimens, Journal of the Mechanics and Physics of Solids 41 (1) (1993) 143 – 181. (Cited on pages 22 and 72.)

[54] Y. Yu, M. Wan, X.-D. Wu, X.-B. Zhou, Design of a cruciform biaxial tensile specimen for limit strain analysis by {FEM}, Journal of Materials Processing Technology 123 (1) (2002) 67 – 70. (Cited on pages 22 and 72.)

[55] J.-Y. Cognard, V. Feuardent, J.-M. Virely, Optimisation of a structure for biaxial mechanical tests, Integrated Design and Manufacturing in Mechanical Engineering (1997) 495–504. (Cited on pages 22 and 72.)

[56] Y. Hanabusa, H. Takizawa, T. Kuwabara, Numerical verification of a biaxial tensile test method using a cruciform specimen, Journal of Materials Processing Technology 213 (6) (2013) 961 – 970. (Cited on pages 22 and 72.)

[57] E. Lamkanfi, W. V. Paepegem, J. Degrieck, C. Ramault, A. Makris, D. V. Hemelrijck, Strain distribution in cruciform specimens subjected to biaxial loading conditions. Part 2: Influence of geometrical discontinuities, Polymer Testing 29 (1) (2010) 132 – 138. (Cited on pages 22 and 72.)

[58] K. T. Kavanagh, R. W. Clough, Finite element applications in the characterization of elastic solids, International Journal of Solids and Structures 7 (1) (1971) 11 – 23. (Cited on pages 22, 50 and 94.)

[59] S. Avril, M. Bonnet, A.-S. Bretelle, M. Grédiac, F. Hild, P. Ienny, F. Latourte, D. Lemosse, S. Pagano, E. Pagnacco, F. Pierron, Overview of identification methods of mechanical parameters based on full-field measurements, Experimental Mechanics 48 (4) (2008) 381–402. (Cited on pages 22, 49, 50 and 72.)

[60] M. Grédiac, F. Hild, Full-Field Measurements and Identification in Solid Mechanics, ISTE, London, Wiley, 2012. (Cited on pages 22, 49 and 50.)

[61] S. Schmaltz, K. Willner, Comparison of different biaxial tests for the inverse identification of sheet steel material parameters, Strain 50 (5) (2014) 389–403. (Cited on pages 22, 23, 25, 50, 51, 57 and 72.)

[62] H. Leclerc, J. Périé, S. Roux, F. Hild, Integrated digital image correlation for the identification of mechanical properties, Vol. LNCS 5496, Springer, Berlin, 2009, pp. 161–171. (Cited on pages 23, 50, 53, 54, 55, 72, 75, 101 and 107.)

[63] J. Réthoré, A fully integrated noise robust strategy for the identification of constitutive laws from digital images, Int. J. Num. Meth. Eng. 84 (6) (2010) 631–660. (Cited on pages 23, 72 and 75.)

[64] F. Mathieu, H. Leclerc, F. Hild, S. Roux, Estimation of elastoplastic parameters via weighted femu and integrated DIC, Experimental Mechanics 55 (1) (2015) 105–119. (Cited on pages 23, 24, 26, 27, 29, 30, 31, 32, 50, 55, 56, 58, 59 and 67.)

[65] Y. Tick-Hon, Cyclic plasticity of 17-7 precipitation-hardenable semi-austenic stainless steel, Ph.D. thesis, University of Toronto (1998). (Cited on pages 23 and 51.)

[66] A. Tarantola, Inverse Problems Theory. Methods for Data Fitting and Model Parameter Estimation, Elsevier Applied Science, Southampton (UK), 1987. (Cited on pages 24, 34 and 55.)

[67] F. Hild, S. Roux, Comparison of local and global approaches to digital image correlation, Experimental Mechanics 52 (9) (2012) 1503–1519. (Cited on pages 27, 28 and 64.)

[68] G. Besnard, F. Hild, S. Roux, “finite-element" displacement fields analysis from digital images: Application to portevin–le châtelier bands, Experimental Mechanics 46 (6) (2006) 789–803. (Cited on pages 28, 29, 53, 72, 74, 75 and 99.)

[69] R. Gras, H. Leclerc, F. Hild, S. Roux, J. Schneider, Identification of a set of macroscopic elastic parameters in a 3d woven composite: Uncertainty analysis and regularization, International Journal of Solids and Structures 55 (2015) 2 – 16. (Cited on pages 29, 58, 59, 104 and 105.)

[70] W. Prager, A New Method of Analyzing Stresses and Strains in Work-hardening Plastic Solids, Technical report (Brown University. Division of Applied Mathematics), 1955. (Cited on pages 43, 58 and 73.)

[71] ISO, Metallic materials - Tensile testing - Part 1: Method of test at room temperature, International Organization for Standardization (2011). (Cited on pages 49, 50 and 72.)

[72] M. Arcan, Z. Hashin, A. Voloshin, A method to produce uniform plane-stress states with applications to fiber-reinforced materials, Experimental Mechanics 18 (4) (1978) 141–146. (Cited on page 50.)

[73] J. Gelin, O. Ghouati, An inverse method for determining viscoplastic properties of aluminium alloys, Journal of Materials Processing Technology 45 (1–4) (1994) 435 – 440. (Cited on pages 50, 58 and 72.)

[74] O. Ghouati, J. Gelin, Identification of material parameters directly from metal forming processes, Journal of Materials Processing Technology 80–81 (0) (1998) 560 – 564. (Cited on pages 50 and 72.)

[75] M. Sutton, W. Wolters, W. Peters, W. Ranson, S. McNeill, Determination of displacements using an improved digital correlation method, Image and Vision Computing 1 (3) (1983) 133 – 139. (Cited on pages 50 and 72.)

[76] G. Geymonat, F. Hild, S. Pagano, Identification of elastic parameters by displacement field measurement, Comptes Rendus Mécanique 330 (6) (2002) 403 – 408. (Cited on page 50.)

[77] F. Hild, S. Roux, Digital image correlation: from displacement measurement to identification of elastic properties – a review, Strain 42 (2) (2006) 69–80. (Cited on pages 50, 72 and 75.)

[78] D. Lecompte, Elastic and elasto-plastic material parameter identification by inverse modeling of static tests using digital image correlation, Ph.D. thesis, Vrije Universiteit Brussel and Koninklijke Militaire School (March 2007). (Cited on page 50.)

[79] M. Grédiac, F. Pierron, Applying the virtual fields method to the identification of elasto-plastic constitutive parameters, International Journal of Plasticity 22 (4) (2006) 602 – 627. (Cited on page 50.)

[80] F. Latourte, A. Chrysochoos, S. Pagano, B. Wattrisse, Elastoplastic behavior identification for heterogeneous loadings and materials, Experimental Mechanics 48 (4) (2008) 435–449. (Cited on page 50.)

[81] H. Haddadi, S. Belhabib, Improving the characterization of a hardening law using digital image correlation over an enhanced heterogeneous tensile test, International Journal of Mechanical Sciences 62 (1) (2012) 47 – 56. (Cited on page 50.)

[82] J. Réthoré, Muhibullah, T. Elguedj, M. Coret, P. Chaudet, A. Combescure, Robust identification of elasto-plastic constitutive law parameters from digital images using 3d kinematics, International Journal of Solids and Structures 50 (1) (2013) 73–85. (Cited on page 50.)

[83] D. Lindner, F. Mathieu, F. Hild, O. Allix, C. Ha Minh, O. Paulien-Camy, On the evaluation of stress triaxiality fields in a notched titanium alloy sample via integrated digital image correlation, ASME. J. Appl. Mech. 82 (7) (2015) 071014–1–10. (Cited on pages 51, 53 and 55.)

[84] J. Périé, S. Calloch, C. Cluzel, F. Hild, Analysis of a multiaxial test on a c/c composite by using digital image correlation and a damage model, Exp. Mech. 42 (3) (2002) 318–328. (Cited on page 51.)

[85] ISO/IEC, International Vocabulary of Metrology - Basic and General Concepts and Associated Terms, VIM, International Organization for Standardization, Geneva (Switzerland), 2007. (Cited on pages 55 and 59.)

[86] J. Neggers, J. P. M. Hoefnagels, M. G. D. Geers, F. Hild, S. Roux, Time-resolved integrated digital image correlation, International Journal for Numerical Methods in Engineering 103 (3) (2015) 157–182. (Cited on pages 55 and 94.)

[87] C. O. Frederick, P. Armstrong, A mathematical representation of the multiaxial bauschinger effect, Materials at High Temperatures 24 (1) (1966) 1–26. (Cited on pages 58 and 73.)

[88] J. Lemaitre, J. Chaboche, Mechanics of Solid Materials, Cambridge University Press, Cambridge (UK), 1990. (Cited on pages 58, 73 and 118.)

[89] K. Levenberg, A method for the solution of certain non-linear problems in least squares, Quarterly Journal of Applied Mathmatics 2 (2) (1944) 164–168. (Cited on page 58.)

[90] D. Marquardt, An algorithm for least-squares estimation of nonlinear parameters, SIAM Journal of Applied Mathematics 11 (2) (1963) 431–441. (Cited on page 58.)

[91] D. S. Schnur, N. Zabaras, An inverse method for determining elastic material properties and a material interface, International Journal for Numerical Methods in Engineering 33 (10) (1992) 2039–2057. (Cited on page 58.)

[92] COFRAC, Guide technique d'accréditation: Métrologie des forces, lab gta 03 Edition (2003). (Cited on page 61.)

[93] H. Tresca, Mémoire sur l'écoulement des corps solides soumis à de fortes pressions, Compte rendu de l'académie des Sciences, Paris, 1864. (Cited on page 71.)

[94] R. v. Mises, Mechanik der festen Körper im plastisch-deformablen Zustand, Nachrichten von der Gesellschaft der Wissenschaften zu Göttingen, Mathematisch-Physikalische Klasse (1913) 582–592. (Cited on page 71.)

[95] H. W. Babel, D. L. Corn, A Comparison of Methods for Correlating Texturing with the Biaxial Strengths of Titanium Alloys, Metals Eng. 7 (1967) 45–53. (Cited on page 71.)

[96] W. T. Lankford, S. C. Snyder, J. A. Bausher, New criteria for predicting the press performance of deep drawing sheets., Trans. ASM 42 (1950) 1197–1205. (Cited on pages 71 and 80.)

[97] R. L. Whiteley, The importance of directionality in deep drawing quality sheet steel, Trans. Am. Soc. Metals 52 (1960) 154 53 (1960) 154. (Cited on page 71.)

[98] D. H. Lloyd, Metallurgical Engineering in the Pressed-Metal Industry, Sheet Metal Ind. 39 (1962) 82–91. (Cited on page 71.)

[99] J. E. Dorn, Stress-Strain Rate Relations for Anisotropic Plastic Flow, Journal of Applied Physics 20 (1949) 15–20. (Cited on page 71.)

[100] R. Hill, Continuum micro-mechanics of elastoplastic polycrystals, Journal of the Mechanics and Physics of Solids 13 (2) (1965) 89 – 101. (Cited on pages 71 and 93.)

[101] F. Barlat, K. Lian, Plastic behavior and stretchability of sheet metals. part i: A yield function for orthotropic sheets under plane stress conditions, International Journal of Plasticity 5 (1) (1989) 51 – 66. (Cited on page 71.)

[102] G. Taylor, Plastic strain in metals, J. Inst. Metals 62 (1938) 307–325. (Cited on page 72.)

[103] F. Barlat, O. Richmond, Prediction of tricomponent plane stress yield surfaces and associated flow and failure behavior of strongly textured f.c.c. polycrystalline sheets, Materials Science and Engineering 95 (1987) 15 – 29. (Cited on page 72.)

[104] R. H. Wagoner, Comparison of plane-strain and tensile work hardening in two sheet steel alloys, Metallurgical Transactions A 12 (5) (1981) 877–882. (Cited on page 72.)

[105] F. Barlat, H. Aretz, J. Yoon, M. Karabin, J. Brem, R. Dick, Linear transfomation-based anisotropic yield functions, International Journal of Plasticity 21 (5) (2005) 1009 – 1039. (Cited on page 72.)

[106] A. N. Bramley, P. B. Mellor, Plastic flow in stabilized sheet steel, Int. J. Mech. Sci. 8 (1966) 101–114. (Cited on page 72.)

[107] R. Horta, W. Roberts, D. Wilson, Effects of plastic anisotropy on the biaxial stretching performance of low-carbon steels, International Journal of Mechanical Sciences 12 (3) (1970) 231 – 243. (Cited on pages 72 and 92.)

[108] J. Woodthorpe, R. Pearce, The anomalous behaviour of aluminium sheet under balanced biaxial tension, International Journal of Mechanical Sciences 12 (4) (1970) 341 – 347. (Cited on pages 72 and 92.)

[109] A. Bramley, P. Mellor, Plastic anisotropy of titanium and zinc sheets, International Journal of Mechanical Sciences 10 (3) (1968) 211 – 219. (Cited on pages 72 and 92.)

[110] A. Andrade-Campos, S. Thuillier, P. Pilvin, F. Teixeira-Dias, On the determination of material parameters for internal variable thermoelastic-viscoplastic constitutive models, International Journal of Plasticity 23 (8) (2007) 1349 – 1379. (Cited on page 72.)

[111] K. M. Zhao, J. K. Lee, Inverse estimation of material properties for sheet metals, Communications in Numerical Methods in Engineering 20 (2) (2004) 105–118. (Cited on page 72.)

[112] R. Mahnken, E. Stein, Parameter identification for viscoplastic models based on analytical derivatives of a least-squares functional and stability investigations, International Journal of Plasticity 12 (4) (1996) 451 – 479. (Cited on page 72.)

[113] R. Kreißing, U. Benedix, U.-J. Görke, M. Lindner, Identification and estimation of constitutive parameters for material laws in elastoplasticity, GAMM-Mitteilungen 30 (2) (2007) 458–480. (Cited on page 72.)

[114] T. Pottier, Constitutive parameter identification using finite element updating method associated with kinematic and thermal full field measurements, Ph.D. thesis, Université de Savoie (Oct. 2010). (Cited on page 72.)

[115] 3M, Structural Adhesive Film, AF 126 - AF 126 FR, Tech. rep., 3M (September 2002). (Cited on page 76.)

[116] G. C. Ramos, M. Stout, R. Bolmaro, J. Signorelli, P. Turner, Study of a drawing-quality sheet steel. i: Stress/strain behaviors and lankford coefficients by experiments and micromechanical simulations, International Journal of Solids and Structures 47 (17) (2010) 2285 – 2293. (Cited on page 81.)

[117] D. J. Steigmann, Tension field theory, Proceedings of the Royal Society of London A: Mathematical, Physical and Engineering Sciences 429 (1876) (1990) 141 – 173. (Cited on page 87.)

[118] G. D. Piero, Constitutive equation and compatibility of the external loads for linear elastic masonry-like materials, Meccanica 24 (1989) 150–162. (Cited on page 87.)

[119] O. Mahmood, B. Audoly, S. Roux, Cracks in tension field theory, preprint, 2016. (Cited on page 87.)

[120] J. D. Eshelby, The determination of the elastic field of an ellipsoidal inclusion, and related problems, Series A, Mathematical and Physical Sciences 241 (1957) 376–396. (Cited on pages 93 and 119.)

[121] Z. Hashin, S. Shtrikman, A variational approach to the theory of the elastic behaviour of multiphase materials, Journal of the Mechanics and Physics of Solids 11 (2) (1963) 127 – 140. (Cited on page 93.)

[122] P. Franciosi, A. Zaoui, Multislip in $f.c.c.$ crystals a theoretical approach compared with experimental data, Acta Metallurgica 30 (8) (1982) 1627 – 1637. (Cited on page 93.)

[123] A. M. Cuitino, M. Ortiz, Computational modelling of single crystals, Modelling and Simulation in Materials Science and Engineering 1 (3) (1993) 225. (Cited on page 93.)

[124] L. Tabourot, M. Fivel, E. Rauch, Generalised constitutive laws for $f.c.c.$ single crystals, Materials Science and Engineering: A 234-236 (0) (1997) 639 – 642. (Cited on page 93.)

[125] D. Raabe, M. Sachtleber, Z. Zhao, F. Roters, S. Zaefferer, Micromechanical and macromechanical effects in grain scale polycrystal plasticity experimentation and simulation, Acta Materialia 49 (17) (2001) 3433 – 3441. (Cited on page 94.)

[126] A. Musienko, A. Tatschl, K. Schmidegg, O. Kolednik, R. Pippan, G. Cailletaud, Three-dimensional finite element simulation of a polycrystalline copper specimen, Acta Materialia 55 (12) (2007) 4121 – 4136. (Cited on page 94.)

[127] R. Martins, C. Ohms, K. Decroos, Full 3D spatially resolved mapping of residual strain in a 316L austenitic stainless steel weld specimen, Materials Science and Engineering: A 527 (18 - 19) (2010) 4779 – 4787. (Cited on page 94.)

[128] T. Hoc, J. Crépin, L. Gélébart, A. Zaoui, A procedure for identifying the plastic behavior of single crystals from the local response of polycrystals, Acta Materialia 51 (18) (2003) 5477 – 5488. (Cited on page 94.)

[129] O. Dmitrieva, P. W. Dondl, S. Maoeller, D. Raabe, Lamination microstructure in shear deformed copper single crystals, Acta Materialia 57 (12) (2009) 3439 – 3449. (Cited on page 94.)

[130] C. Tasan, J. Hoefnagels, M. Geers, Microstructural banding effects clarified through micrographic digital image correlation, Scripta Materialia 62 (11) (2010) 835 – 838. (Cited on page 94.)

[131] D. Raabe, M. Sachtleber, H. Weiland, G. Scheele, Z. Zhao, Grain-scale micromechanics of polycrystal surfaces during plastic straining, Acta Materialia 51 (6) (2003) 1539 – 1560. (Cited on page 94.)

[132] E. Héripré, M. Dexet, J. Crépin, L. Gélébart, A. Roos, M. Bornert, D. Caldemaison, Coupling between experimental measurements and polycrystal finite element calculations for micromechanical study of metallic materials, International Journal of Plasticity 23 (9) (2007) 1512 – 1539. (Cited on page 94.)

[133] C. Tasan, M. Diehl, D. Yan, C. Zambaldi, P. Shanthraj, F. Roters, D. Raabe, Integrated experimental-simulation analysis of stress and strain partitioning in multiphase alloys, Acta Materialia 81 (0) (2014) 386 – 400. (Cited on pages 94 and 143.)

[134] A. Guery, F. Latourte, F. Hild, S. Roux, Identification of crystal plasticity law parameters using kinematic measurements in polycrystals, in: WCCM XI - 11th World Congress on Computational Mechanics, Barcelona, Spain, 2014. (Cited on pages 94 and 143.)

[135] S. Roux, F. Hild, Digital image mechanical identification (DIMI), Experimental Mechanics 48 (4) (2008) 495–508. (Cited on page 94.)

[136] S.-H. Lee, H. Utsunomiya, T. Sakai, Microstructures and mechanical properties of ultra low carbon interstitial free steel severely deformed by a multi-stack accumulative roll bonding process, Materials transactions 45 (7) (2004) 2177–2181. (Cited on page 96.)

[137] K. Han, M. Ciccotti, S. Roux, Measuring nanoscale stress intensity factors with an atomic force microscope, EPL (Europhysics Letters) 89 (6) (2010) 66003. (Cited on page 99.)

[138] J. Neggers, J. Hoefnagels, F. Hild, S. Roux, M. Geers, Direct stress-strain measurements from bulged membranes using topography image correlation, Experimental Mechanics 54 (5) (2014) 717–727. (Cited on page 99.)

[139] L. Bergers, J. Hoefnagels, M. Geers, On-wafer time-dependent high reproducibility nano-force tensile testing, Journal of Physics D: Applied Physics 47 (49) (2014) 495306. (Cited on pages 99, 111, 112 and 144.)

[140] P. Franciosi, Glide mechanisms in *b.c.c.* crystals: An investigation of the case of α-iron through multislip and latent hardening tests, Acta Metallurgica 31 (9) (1983) 1331 – 1342. (Cited on page 103.)

[141] D. D. Tjahjanto, S. Turteltaub, A. S. J. Suiker, S. van der Zwaag, Modelling of the effects of grain orientation on transformation-induced plasticity in multiphase carbon steels, Modelling and Simulation in Materials Science and Engineering 14 (4) (2006) 617. (Cited on page 103.)

[142] H. David, Comportements élastoviscoplastiques mono et polycristallins, R5.03.11 - Code_Aster (2014) 1–58. (Cited on page 103.)

[143] G. L. Rosa, A. Risitano, Thermographic methodology for rapid determination of the fatigue limit of materials and mechanical components, International Journal of Fatigue 22 (1) (2000) 65 – 73. (Cited on pages 117 and 122.)

[144] A. Wöhler, On the strength tests with iron and steel, Zeitschrift für Bauwesen 20 (1870) 73–1106. (Cited on pages 117 and 121.)

[145] E. Charkaluk, A. Constantinescu, Dissipative aspects in high cycle fatigue, Mechanics of Materials 41 (5) (2009) 483 – 494. (Cited on page 117.)

[146] F. Maquin, F. Pierron, Heat dissipation measurements in low stress cyclic loading of metallic materials: From internal friction to micro-plasticity, Mechanics of Materials 41 (8) (2009) 928 – 942. (Cited on page 117.)

[147] A. Ezanno, C. Doudard, S. Calloch, J.-L. Heuzé, A new approach to characterizing and modeling the high cycle fatigue properties of cast materials based on self-heating measurements under cyclic loadings, International Journal of Fatigue 47 (2013) 232 – 243. (Cited on page 117.)

[148] R. Munier, C. Doudard, S. Calloch, B. Weber, Determination of high cycle fatigue properties of a wide range of steel sheet grades from self-heating measurements, International Journal of Fatigue 63 (2014) 46 – 61. (Cited on page 117.)

[149] L. G. Mayorga, S. Sire, B. Plu, Understanding fatigue mechanisms in ancient metallic railway bridges: A microscopic study of puddled iron, Procedia Engineering 114 (2015) 422 – 429. (Cited on page 118.)

[150] F. Lahuerta, R. Nijssen, F. van der Meer, L. Sluys, Experimental-computational study towards heat generation in thick laminates under fatigue loading, International Journal of Fatigue 80 (2015) 121 – 127. (Cited on page 118.)

[151] N. Ranc, D. Wagner, P. Paris, Study of thermal effects associated with crack propagation during very high cycle fatigue tests, Acta Materialia 56 (15) (2008) 4012 – 4021. (Cited on page 118.)

[152] C. Doudard, S. Calloch, P. Cugy, A. Galtier, F. Hild, A probabilistic two-scale model for high cycle fatigue life predictions, Fatigue & Fracture of Engineering Materials & Structures 28 (2005) 279–288. (Cited on pages 118, 119, 121 and 125.)

[153] B. F. Langer, Design of pressure vessels for low-cycle fatigue, Trans. ASME 84(3) (1962) 389–399. (Cited on page 118.)

[154] M. Tanaka, Fatigue life estimation of bellows based on elastic-plastic calculations, International Journal of Pressurize vessels and piping 2 (1973) 51–68. (Cited on page 118.)

[155] C. Becht, Fatigue of bellows, a new design approach, International Journal of Pressure Vessels and Piping 77 (2000) 843–850. (Cited on page 118.)

[156] T. Nagamachi, T. Mishiba, K. Katsuki, Deformation and fatigue characteristics of large welded bellows with inclined external edge, Materials Transactions 49 (6) (2008) 1249–1255. (Cited on page 118.)

[157] P. Germain, Q. Son Nguyen, P. Suquet, Continuum Thermodynamics, Journal of Applied Mechanics 50 (1983) 1010–1020. (Cited on page 118.)

[158] P. Rosakis, A. Rosakis, G. Ravichandran, J. Hodowany, A thermodynamic internal variable model for the partition of plastic work into heat and stored energy in metals, Journal of the Mechanics and Physics of Solids 48 (3) (2000) 581 – 607. (Cited on page 119.)

[159] A. Chrysochoos, H. Louche, An infrared image processing to analyse the calorific effects accompanying strain localisation, International Journal of Engineering Science 38 (16) (2000) 1759 – 1788. (Cited on page 119.)

[160] J. Simo, C. Miehe, Associative coupled thermoplasticity at finite strains: Formulation, numerical analysis and implementation, Computer Methods in Applied Mechanics and Engineering 98 (1) (1992) 41 – 104. (Cited on page 119.)

[161] P.-J. Cunat, Aciers inoxydables, propriétés et résistance à la corrosion, Techniques de l'ingénieur M4 541. (Cited on page 120.)

[162] P. Cugy, G. A., Microplasticity and temperature increase in low carbon steel, Proceedings of the 8th International Fatigue Conference, Stockolm (2002). (Cited on page 119.)

[163] D. Davies, The statistical approach to engineering design in ceramics, Proc. Brit. Ceram. Soc. 22 (1973) 429–452. (Cited on page 121.)

[164] F. Hild, R. Billardon, D. Marquis, Hétérogénéité des contraintes et rupture des matériaux fragiles, C. R. Acad. Sci. Paris t. 315 (Série II) (1992) 1293–1298. (Cited on page 121.)

[165] W. Becker, S. Lampman, Fracture appearance and mechanisms of deformation and fracture, Materials Park, OH: ASM International, 2002. (2002) 559–586. (Cited on pages 123 and 130.)

[166] E. Reissner, The effect of transverse shear deformation on the bending of elastic plates, ASME Journal of Applied Mechanics 12 (1945) 68–77. (Cited on page 127.)

[167] J. Goodman, Mechanics Applied to Engineering, Longmans, Green, & Co., London, 1899. (Cited on pages 135 and 136.)

[168] G. Sines, J. Waisman, Behavior of metals under complex static and alternating stresses., Metal Fatigue. (1959) 145–469. (Cited on pages 135 and 136.)

[169] D. J. White, B. Crossland, J. L. M. Morrison, Effect of hydrostatic pressure on the direct-stress fatigue strength of an alloy steel, Journal of Mechanical Engineering Science 1 (1) (1959) 39–49. (Cited on pages 135 and 136.)

[170] D. Kujawski, F. Ellyin, A unified approach to mean stress effect on fatigue threshold conditions, International Journal of Fatigue 17 (2) (1995) 101 – 106. (Cited on pages 135 and 136.)

[171] B. Crosseland, Effect of large hydrostatic pressure on the torsional fatigue strength of an alloy steel., Proc. Int. Conf. on Fatigue of Metals (1956) 138–149. (Cited on page 135.)

[172] D. J. Burns, J. S. C. Parry, Effect of Large Hydrostatic Pressures on the Torsional Fatigue Strength of two Steels, Journal of Mechanical Engineering Science 6 (3) (1964) 293–310. (Cited on page 135.)

[173] J. L. M. Morrison, B. Crossland, J. S. C. Parry, Fatigue under Triaxial Stress: Development of a Testing Machine and Preliminary Results, Proceedings of the Institution of Mechanical Engineers 170 (1) (1956) 697–712. (Cited on page 135.)

[174] T. Nicholas, J. Zuiker, On the use of the Goodman diagram for high cycle fatigue design, International Journal of Fracture 80 (1996) 219–235. (Cited on pages 135, 136 and 139.)

[175] J.-E. Dufour, F. Hild, S. Roux, Shape, displacement and mechanical properties from isogeometric multiview stereocorrelation, The Journal of Strain Analysis for Engineering Design 50 (7) (2015) 470–487. (Cited on page 143.)

[176] A. Charbal, J.-E. Dufour, A. Guery, F. Hild, S. Roux, L. Vincent, M. Poncelet, Integrated digital image correlation considering gray level and blur variations: Application to distortion measurements of IR camera, Optics and Lasers in Engineering 78 (2016) 75 – 85. (Cited on page 143.)

[177] B. Voillot, F. Hild, R. Billardon, J. Lebrun, XRD stress analysis combing insitu tests and integrated approaches, 2016, ICRS2016 International Conference on Residual Stresses. (Cited on page 143.)

[178] T. Taillandier-Thomas, C. Jailin, S. Roux, F. Hild, Measurement of 3D displacement fields from few tomographic projections, Proc. SPIE 9896 (2016) 98960L–98960L–12. (Cited on page 143.)

[179] A. Buljac, M. Shakoor, J. Neggers, M. Bernacki, P.-O. Bouchard, L. Helfen, T. F. Morgeneyer, F. Hild, Numerical Validation Framework for Micromechanical Simulations based on Synchrotron 3D Imaging, Comput. Meth. Appl. Mech. Eng., submitted. (Cited on page 143.)

[180] A. Carpiuc, Innovative tests for characterizing mixed-mode fracture of concrete: from pre-defined to interactive and hybrid tests, Ph.D. thesis, École Normale Supérieure de Cachan. (Cited on page 143.)

[181] M. Bertin, C. Du, J. P. Hoefnagels, F. Hild, Crystal plasticity parameter identification with 3d measurements and integrated digital image correlation, Acta Materialia 116 (2016) 321 – 331. (Cited on page 143.)

[182] V. P. Ionut, Experimental analysis and modeling of the behavior of Inco718DA in multiaxial fatigue, Ph.D. thesis, École Normale Supérieure de Cachan. (Cited on page 143.)

[183] J. Neggers, On a DIC framework for research - The philosophy behind Correli 3.0, Materials Science Sector weekly meeting (February 2016). (Cited on page 144.)

[184] SATT-Paris Saclay, Press release (18 December 2015). (Cited on page 144.)

[185] J.-F. Preveraud, EikoSim rapproche simulation numérique et essais physiques, Industrie technologique (4 January 2016). (Cited on page 144.)

[186] F. Mathieu, F. Hild, J. Bellec, Le projet diccit: des outils pour la comparaison essai/calcul et l'identification, S11 Couplage modélisation/expérimentation en mécanique des matériaux, mesure de champs. (Cited on page 144.)

# Appendix A
# Operation manual of mini-Astrée and its environnement

Co-authored by: Morgan Bertin, Xavier Pinelli, Remy Legroux, and François Hild *Design of an enhanced experimental environment for Mini-ASTREE*, LMT-Cachan, 2015


## Abstract

This manual introduces the rules, methods and tools related to the mini-ASTREE environment, the new biaxial machine available at LMT Cachan. It shows the methods related to in-situ experimentation with the dedicated digital camera PCO-edge. It also gives installation and starting instructions both related to the experimental system and the software. To ensure the safety both of the machine and the user these instructions must be followed. If a problem is encountered contact the chief engineer. For other uses, *i.e.,* in-situ experiment with the Scanning Electron Microscope (SEM), in-situ experiment with the X-ray diffraction set-up, and the load cell installation procedure, please refer to the dedicated manual inside the moving storage cabinet.


## A.1 Installation instructions

- Read this user-manual entirely and open the workbook.
- Check if all the tools and systems are inside the moving storage cabinet.
- Check if no cables are connected outside the moving storage cabinet.

**List 1:** First use instructions

All instructions as shown above must be followed. All the other issues, *i.e., i*) change of the load cells, *ii*) perform a test in SEM, and *iii*) perform a test in the X-ray diffraction device, are available in the aluminum *Deben* folder inside the moving storage cabinet. Please collect back the latter inside the folder when you have finished.

### A.1.1 Experimental tools

mini-ASTREE is a compact biaxial experimental device with a dedicated environment composed of two parts. First, a moving storage cabinet dedicated to carry and drive the system. The usual locations are at LMT Cachan, *i*) the microscopic investigation room (level $-1$), and *ii*) the X-ray diffraction device in the experimental platform (level 0), and at the d'Alembert Institute (IDA), *iii*) the Scanning Electron Microscopy (SEM) room. Second, an experimental platform and dedicated tools have been designed. All the cameras, sensors, and other materials are stored inside the moving storage cabinet. Figure A.1 shows the moving storage cabinet in its carrying configuration.

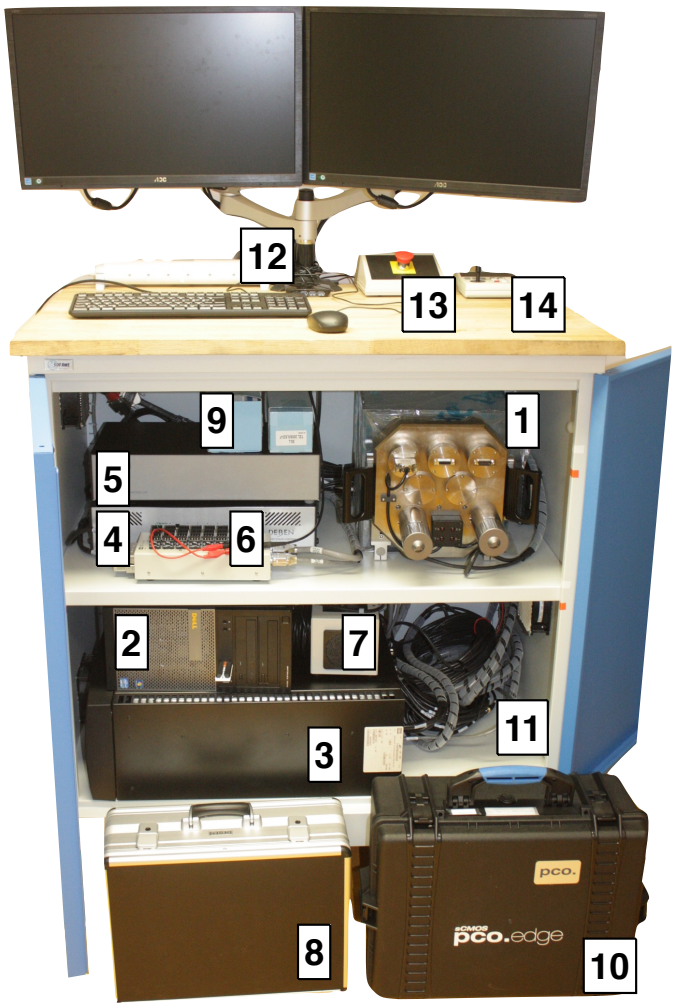


**Figure A.1:** The mini-ASTREE moving storage cabinet with its parts

| When finished, collect all the equipment inside the moving storage cabinet |
|---|

You can access the connections on the sides and behind the moving storage cabinet. The inflated wheels allow to move the moving storage cabinet easily. However, secure the wheels with the incorporated brakes before performing an experiment. All the devices are controlled from one computer thanks to the USB 3.0 PCO-edge camera. The equipment, cables and their positions inside the moving storage cabinet are gathered in List 2.

1. The displacement stage with the door dedicated to the SEM.
2. The command computer for both mini-ASTREE and the digital camera.
3. The electrical and electronic controller.
4. The control bay for all electrical engines.
5. The control bay for the SEM door displacement stage.
6. The electronic MTS output unit.
7. The power unit.
8. The mini-ASTREE folder with other guides.
9. The optics.
10. The camera PCO-edge folder.
11. The connection outlets.
12. The USB 3.0 connectors.
13. The emergency button.
14. The stage controller.

**List 2:** Systems and their corresponding locations

Figure A.2 shows the experimental platform. The latter is composed of one digital camera (PCO-edge), two LED pattern projectors, a support frame that carries the optical mounting system. Two pins on the platform can be seen in Figure A.2. They allow for a reliable positioning of the machine over time and to set the platform reference. The connections, one male and one female, are visible and must be secured with the screws available on the connectors. The optical mounting system is an in-house designed device to set quickly, precisely, and faithfully the position of the camera. Several electrical outlets are available under the platform to power any electrical systems that one may use on it.

Connect the platform power cable to a mural electrical outlet.

Figure A.3(a) shows the connections between the moving storage cabinet and the experimental platform. The cables are stored outside the moving storage cabinet and the electronic outlets are located on the left side of the moving storage cabinet (when you are in front of the latter).

**Figure A.2:** Optical mounting system and the PCO-edge camera

| Do not access or modify the connections inside the moving storage cabinet. |
|---|

From the moving storage cabinet, connect the cable to the corresponding connector "trigger in" under the platform. From the connector "trigger out" connect the cable to the digital camera at connector "1". Figure A.3 shows the connections on the digital camera: 1. the power outlet, 2. the trigger, and 3. the USB 3.0 connection.

| Before turning on the digital camera, connect all the cables. |
|---|

### A.1.2 Material setting instructions

The machine is small, fragile, and expensive. Therefore, you must strictly follow the written instructions and comply at any time with the two following rules.

1. Complete all the instructions before starting a test.
2. Do not remove the protective cover unless necessary.


**Figure A.3:** Connections on the digital camera

The installation instructions are described and must be followed in the same order as presented in List 3.

1. Place mini-ASTREE with its protective cover on the platform.
2. Connect mini-ASTREE.
3. Place the camera and the optical mounting system.
4. Connect the camera.
5. Turn on all the elements as follows:
   (a) The moving storage cabinet power unit.
   (b) The platform power unit.
   (c) The command computer.
   (d) The camera and LEDs.

**List 3:** mini-ASTREE installation instructions on the experimental platform

When all the elements have been switched on, a small blinking red light appears on the panel of the electrical engine command bay. The following instruction aims to initialize the connection between the command computer, the electrical and electronic control MTS bay and the machine.

1. Launch the Station Manager (Figure A.4).
2. Open project 1.
3. Choose the reference calibration file in Mini_Astree/calibration/.

**List 4:** Preliminary software instructions

The experimental machine and the command computer are now connected to each other and synchronized. If a load cell appears to be outside of its operating range, a red light will appear on the electrical engine control bay panel. Before going further, the incriminated load cell has to be moved back inside its operating range. Figure A.5 shows the MTS command window.


**Figure A.4:** Station Manager icon

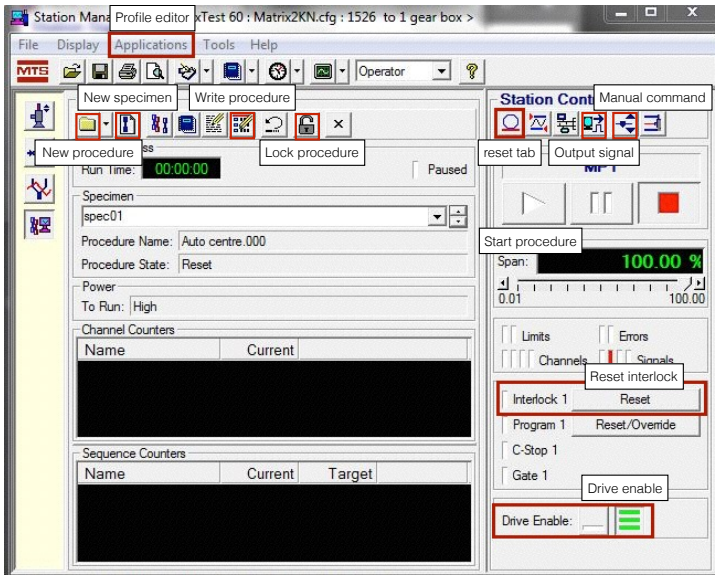


**Figure A.5:** MTS window and specific features highlighted

Figure A.6 shows the manual command window with four different tabs: *i*) A1 Tension, *ii*) A1 Translation, *iii*) A2 Tension, and *iv*) A2 Translation. First, A1 corresponds to the loading direction of the load cells 1 and 3. Each number is visible on the machine itself. Similarly A2 corresponds to the loading direction of the load cells 2 and 4. Secondly,"Tension" corresponds to the prescribed displacement ("Ext") or load ("Force"). The second tab option shows the functions A1 and A2 "translation". It prescribes the symmetry condition for each directions. For example, when the command "A1 translation" and "A2 translation" are equal to zero and the control mode is set to "Ext", the displacements are symmetric and centered about the machine reference. To move the incriminate load cell, apply a negative or a positive load with A*i* "tension" in load control "Force" and wait that the load cell reaches its operating range. Furthermore, apply the symmetry condition by defining A1 and A2 "translation"+"Ext" equal to zero. To unlock the system and to enable the motion of the load cells follow the instruction enumerated in List 5.

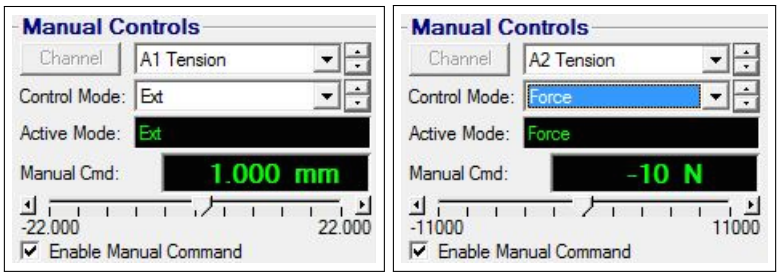


(a) (b)

**Figure A.6:** (a) "Ext" or (b) "Force" control mode in the window "Manual command"

1. Click on reset interlock.
2. Click on drive enable (the blinking red light stops).
3. Click on manual command.
4. Enable manual command on the window.
5. Set A1 translation and A2 translation in Control Mode "Ext".
6. Indicate in Manual Cmd the value 0.0 mm.
7. Set A1 tension and A2 tension in Control Mode "Ext".
8. Indication in Manual Cmd the value 1.0 mm.

**List 5:** Enable the motion of the load cells

In that case and when the displacement of 1 mm is prescribed, the displacement between the two grips is increased by 1mm. However, each grip moved by about 0.5mm

symmetrically because of the prescribed symmetry condition. Figure A.7 shows the panel of the electrical engine control bay. The green lights are activated and indicate that the engines are fully operational. When an engine is activated, an orange light in front of "DRIVE" switches on to indicate which engine(s) is(are) activated. Finally, to set all the measured loads equal to zero click on the "reset" tab and reset all the load measurements (Figure A.8).

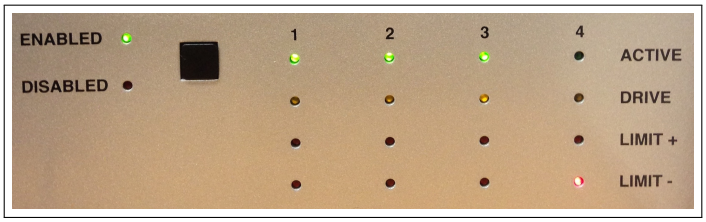


**Figure A.7:** View of the panel of the electrical engine control bay. The buttons enabled and disabled are on the left, the green lights indicate the engines available, the orange lights indicate which engines are activated and the red lights indicate which engines are outside of their operating range

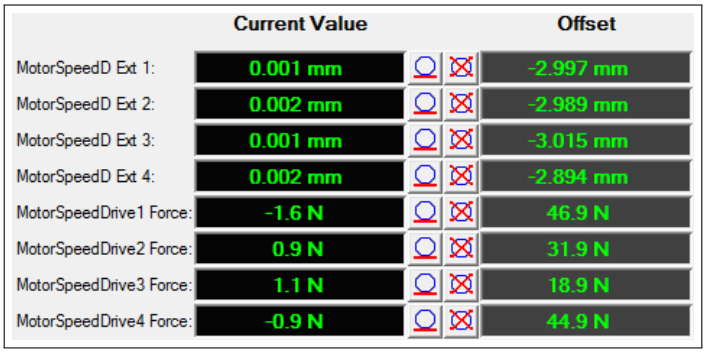


**Figure A.8:** Reset tab window and load measurement

You have now finished the initial settings. The next section presents the camera setting. A specific section shows the load cell calibration procedure that has to be performed with an LMT staff. Finally, the instructions regarding the specimen alignment and the experiment itself will be presented. Before going further, please comply with the simple rule:

| Do not remove the mini-ASTREE protective cover unless it is necessary. |
|---|

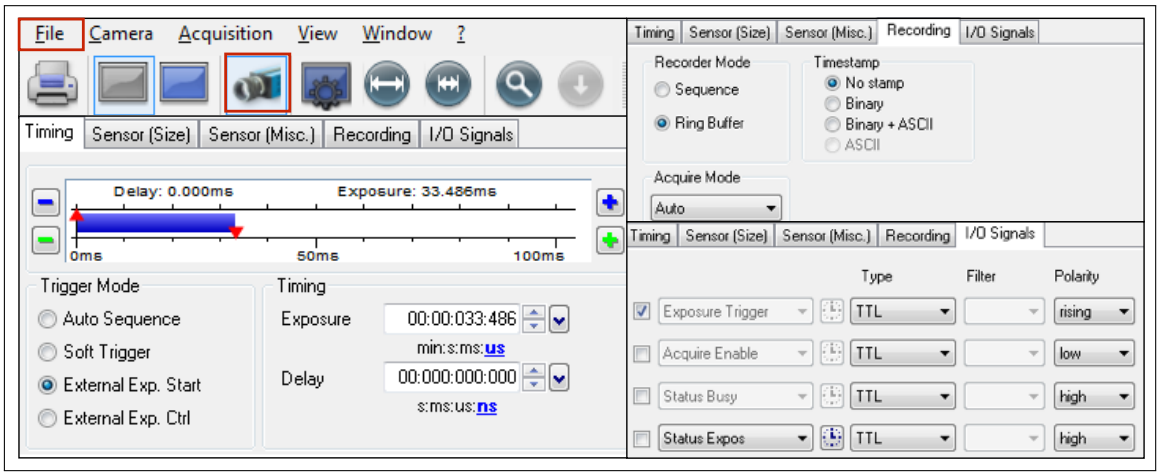


**Figure A.9:** Configuration of the CamWare software to trigger the camera by the MTS software

## A.2 Digital camera instructions

The digital camera is controlled with the "CamWare" software. The camera can be used alone or can be triggered using the MTS control software. In the latter configuration all the connections must be set and the biaxial machine must be turned on. Before turning on the software the camera must be turned on and plugged in using the USB 3.0 port. To set the camera software ready to be triggered by MTS, refer to the instructions of List 6.

1. Click on the tab with the sketch of a camera.
2. On timing tab, select External Exp Start and the correct exposure.
3. On Recording tab, select Ring buffer and Auto.
4. On I/O signals, only enable exposure trigger.
5. On file, choose direct record to file, select single .tiff file.

**List 6:** CamWare and MTS synchronization software instructions

Figure A.9 shows several windows of the CamWare software to fill in before running MTS. In MTS panel select the output signal tab (Figure A.5) and when CamWare is ready, click on the green tab to create an impulse that triggers the camera. The procedure to automatically trigger the digital camera during a test is introduced in Section A.4.3.

# A.3 Load cell calibration procedure

## A.3.1 Introduction

The load cells have been designed for the biaxial machine, and their measurements vary with respect to the specimen thickness. Therefore, the load cells have to be calibrated and Section A.3.2 shows the calibration procedure. However, if the thickness has already been investigated, the calibration file already exists and is available at "Desktop\mini-ASTREE\Calibration\".

## A.3.2 Calibration procedure

To create a new calibration, firstly, create a new file by copying and pasting on the folder "Computer/OS(C)/MTS793/Calibration Files" the reference file 2KN.cfg. Close the software at this point and open it again and chose the new calibration file.

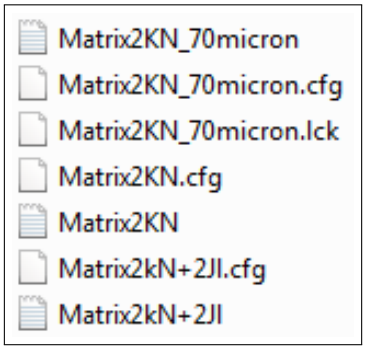


Second, the new four calibration files for the corresponding configuration file have to be created. On the folder "Computer/OS(C)/MTS793/Controllers/MTS FlexTest 60/Config" copy and past the four load cell files denoted CH*i* 2kN, *i* being the load cell number. Then name the new file with the corresponding thickness.

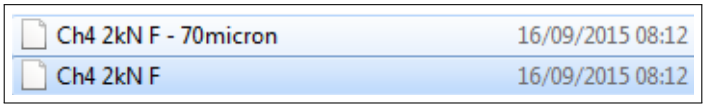


On the main command page of MTS, click on the calibration tab, the password is empty and then click on the station setup tab.

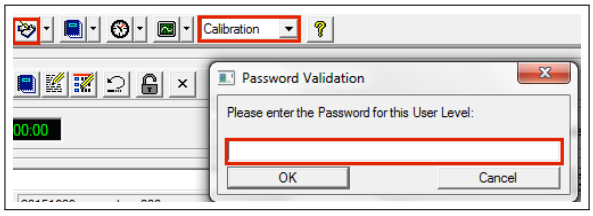

Finally, open the tab Station Setup. On the left part all names of the input and output signals are listed. In order to choose another load cell calibration, click on the Auxiliary Inputs tab and choose the corresponding load cell. The latter is denoted on the software as "MotorSpeedDrive*i* Force", *i* being the number of the load cell. Then on the tab Sensor, you can chose the new calibration file that you previously created. Once the calibration file has been selected, modify the gain with your value and click on the tab "Assign" to end the procedure. Repeat the latter for all load cells. The calibration procedure is now ended.

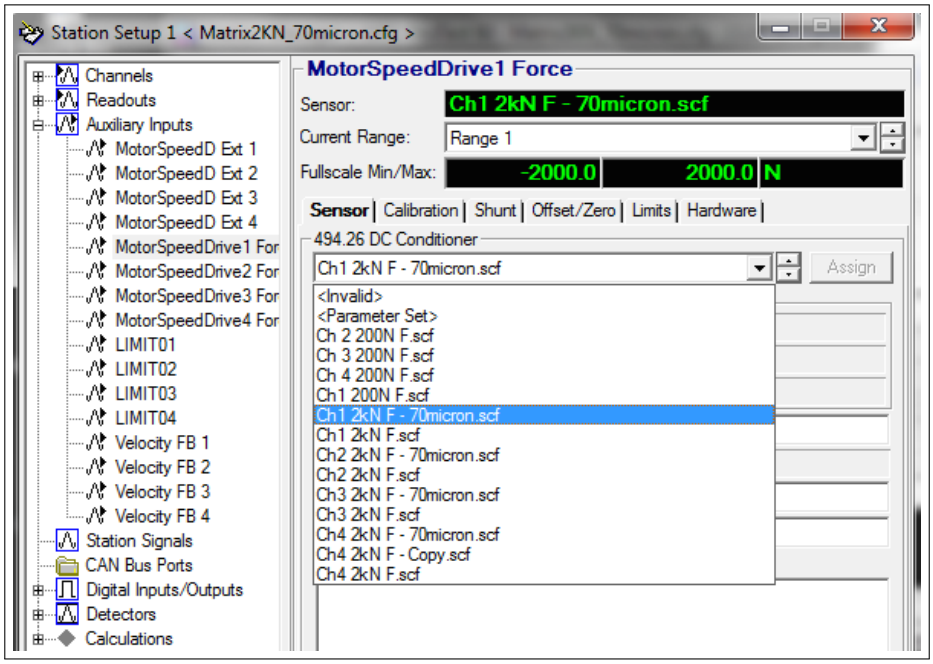


# A.4 Experimental instructions

## A.4.1 Design of the specimen

The machine specifications are available in the appendices. Figure A.10 shows the geometrical features that can be used. Four holes with a diameter greater than 3 mm are necessary to let pass the four pins through the specimen. The maximum specimen thickness is 3 mm. However, prefer a thickness less than 1mm. Other indications are available in the MICROTEST manual.

## A.4.2 Specimen alignment procedure

First, the specimen has to be validated or adapted to fit the positioning pins inside the machine. A reamer dedicated to adapt the size of the four holes is available (the process

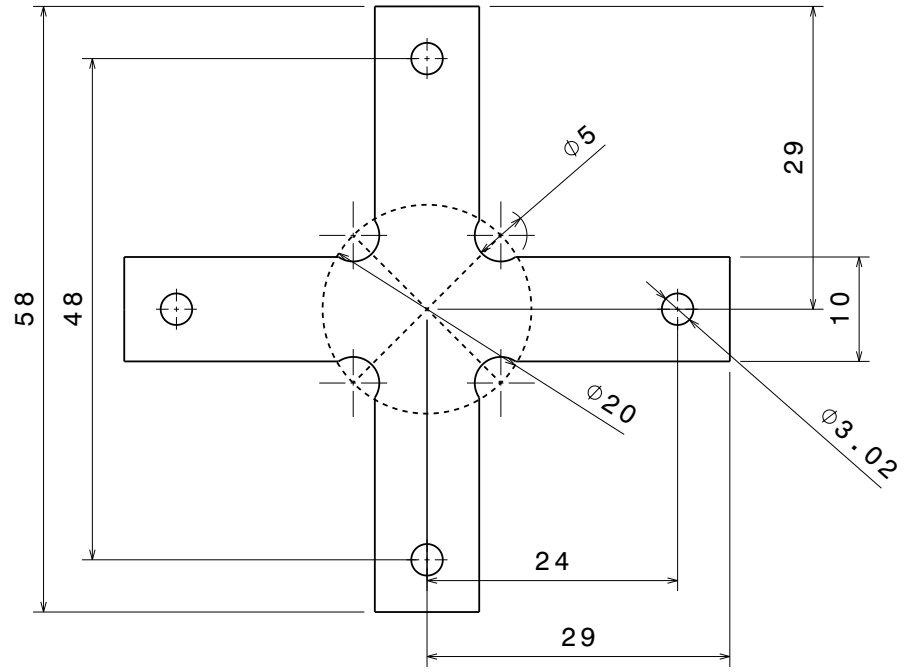


**Figure A.10:** Exemple of a specimen geometry

of enlarging the hole is called reaming, https://en.wikipedia.org/wiki/Reamer). Validate the hole dimensions and if necessary ream them until the valid dimension is reached.

1. Ream the specimen with the dedicated reamer.
2. Remove the mini-ASTREE protective cover.
3. Unclench the clamps and put them down aside.
4. Check the hole sizes with the positioning pins.

**List 7:** Instructions to validate the size of the positioning holes

Figure A.11 shows the unclench instruction. Remove all the screws with the dedicated Allen wrench. After the specimen positioning and when you start to tight the clamps, tight successively and alternatively all the screws until the Allen wrench starts to band.

Figure A.12 shows the four clamps of the machine without the specimen and with the specimen put on top of the four positioning pins. The instructions in List 7 indicate how to fit the specimen within the machine. The routine called “auto-centre” seeks to align

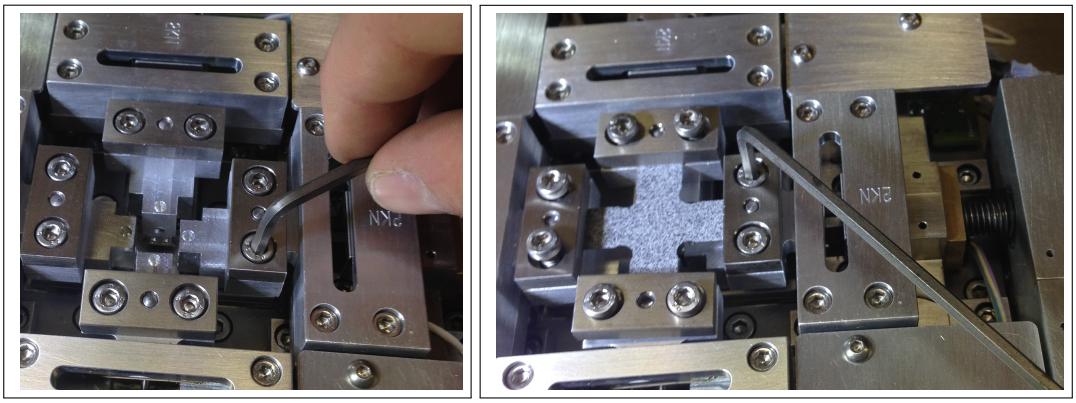

(a) (b)

**Figure A.11:** To tighten and to release, stop when the Allen wrench starts to band

the specimen as much as possible, to set the displacements to zero and to keep the loads equal to zero.

1. Select the tab “Manual Commands”.
2. Select “A1 Translation - Ext” and “A2 translation - Ext” equal to zero.
3. Select “A1 tension - Ext” and “A2 tension - Ext”.
4. Move successively with small steps the load cells until the specimen fits.
5. Select “A1 tension - Force” and “A2 tension - Force” equal to zero.
6. Tighten the clamps and check the symmetry of all grips.
7. Open the procedure “Mini_Astree\procedures\auto_centre” and “lock”.
8. Start the procedure and wait for 2 minutes.

**List 8:** Fitting and alignement specimen instructions

### A.4.3 Running an experiment

The specimen is now positioned and the loading history can be designed and implemented. The first step is to create a new project and a new specimen (Figure A.5). Then, two different files must be created, a profile and a procedure. The profile corresponds to the loading history and a procedure is the code that will run all the test. Some templates are already available and greatly facilitate the design of the latter. To find them go to “desktop\Mini_Astree\procedure\”. Figure A.13 shows a procedure that has been created. It shows all the information used during the test, *i.e.,* the data collection, the triggering of the digital camera and the prescribed loading history (the profile). The latter

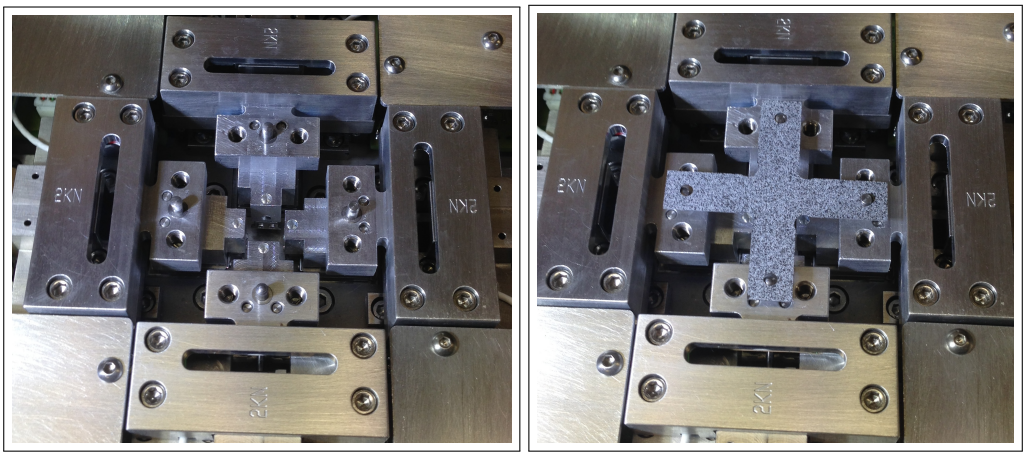

(a) (b)

**Figure A.12:** View of the machine without the upper clamps, (a) without and (b) with the specimen before the alignement instructions

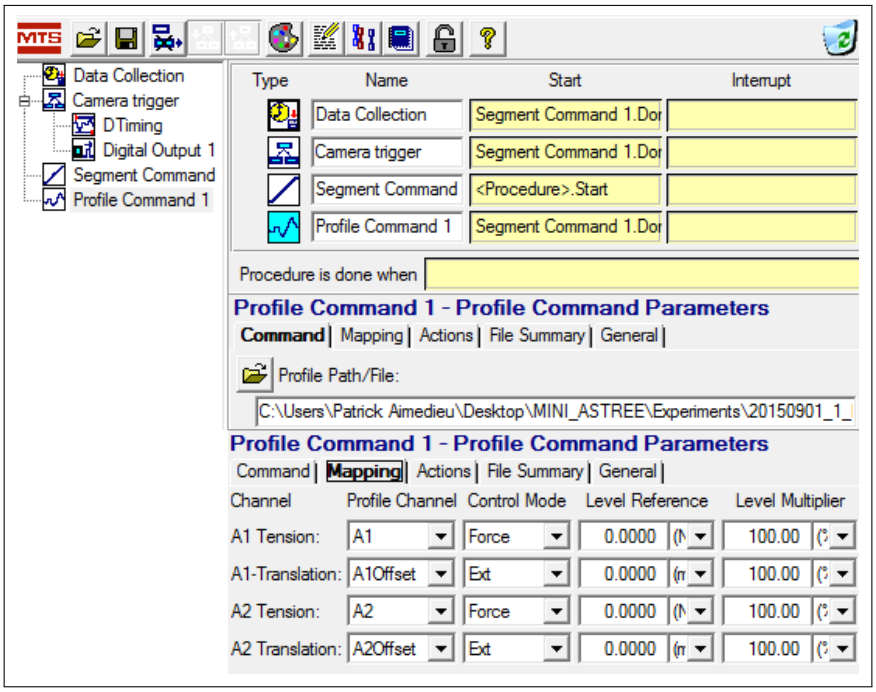


**Figure A.13:** How to create an MTS procedure?

is saved under the tab Profile Command 1. To create one profile select application and profile editor. As before, some examples are available. Once the profile is created and saved, on the procedure click on the tab in blue (Figure A.13) next to Profile Command 1 and select the file. Then, map all the channels with their counterparts in the profile file

(Figure A.13).

To save the data two instructions have to be followed. First, the computer is not dedicated to store all the acquired images. A specific feature is here to help you to save easily all your images on one hard-drive. Connect the latter to the specific connection on the top of the moving storage cabinet below the computer screens. Second, to save the experimental data create a folder as "\desktop\Mini_ Astree\aaaammjj_ n_ last_name_ first_name\...".

At this point, everything is ready to start the test, lock the procedure and click on the white arrow to start. At the end write all the important data of your test in the monitoring workbook stored inside the moving storage cabinet.

## A.5 Digital Image Correlation

DIC is available at LMT Cachan with several tools. Lately, you can perform the computation on any computer with Matlab and Correli 3.0. In a computer of the computation center, type in the terminal:

```
yourname@computer:~ cd /u/dic
yourname@computer:/u/dic scp -r Correli/ /ul/yourname/.
yourname@computer:~ cd /ul/yourname/Correli
yourname@computer:~ ./matlab-preload &
```

From this point you can learn to perform a Digital Image Correlation analysis with the tutorials. Have fun!

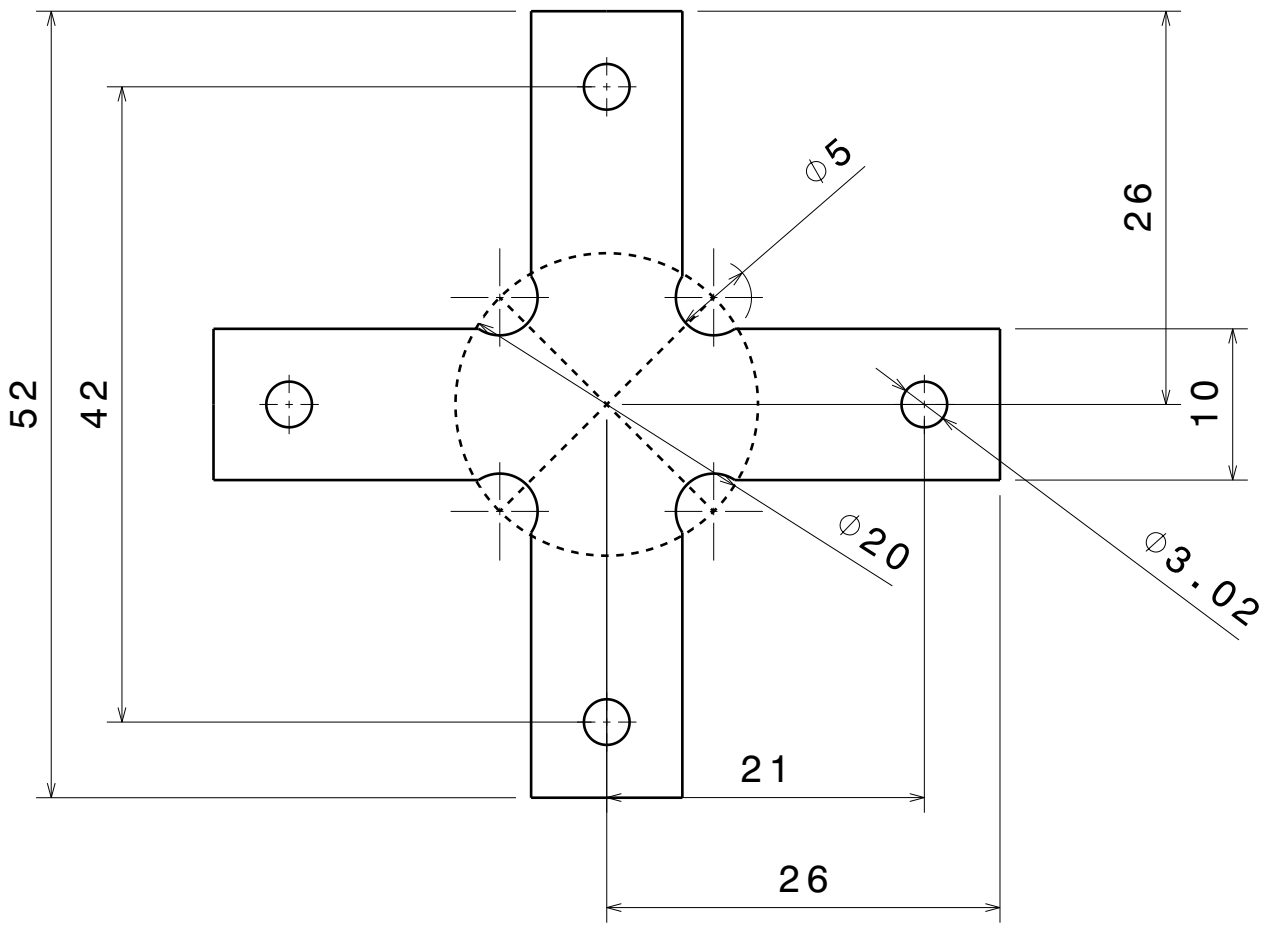


Epaisseur 0,3 mm

THICKNESS 0,3 mm

| | | | | |
|---|---|---|---|---|
| DESIGNED BY: Bertin Morgan<br>DATE: 21/01/2014 | LMT - CACHAN | | | I _ |
| CHECKED BY:<br>DATE: | | | | H _ |
| | | | | G _ |
| | | | | F _ |
| SIZE A4 | BIAXIAL SAMPLE | | | E _ |
| | | | | D _ |
| SCALE 2:1 | WEIGHT (kg) 0,00 | DRAWING NUMBER NOMINAL SAMPLE | SHEET 1/1 | C _ |
| | | | | B _ |
| | | | | A _ |

# Appendix B
# Draft of a testing machine for bellows and temperature measurement in HCF

Co-designed by: Morgan Bertin and AER-Atmostat, 2015

## Design objectives

The design of the fatigue testing machine originates from a partnership between LMT-Cachan and AER-Atmostat. Four objectives were sought, *i*) prescribe a fixed alternating displacement amplitude, *ii*) reach a 20-Hz loading frequency, *iii*) capture thermal images with an infra-red camera, and *iv*) adapt the bellows mid-stroke. To that end the fatigue machine relies on a crankshaft mechanism linked to the electrical engine using an elastic coupling. The rotation speed of the electrical engine is controlled to correspond to the infra-red camera acquisition rate. Two sensors (load and gauge length) are positioned to monitor the experiment. In order to position the mid-stroke a mechanism based on an unequal threaded stud and two nuts is associated with the piston rod. Last, the machine frame is designed to be put on the mini-ASTREE experimental platform in order to avoid external vibrations and to stabilize the latter.

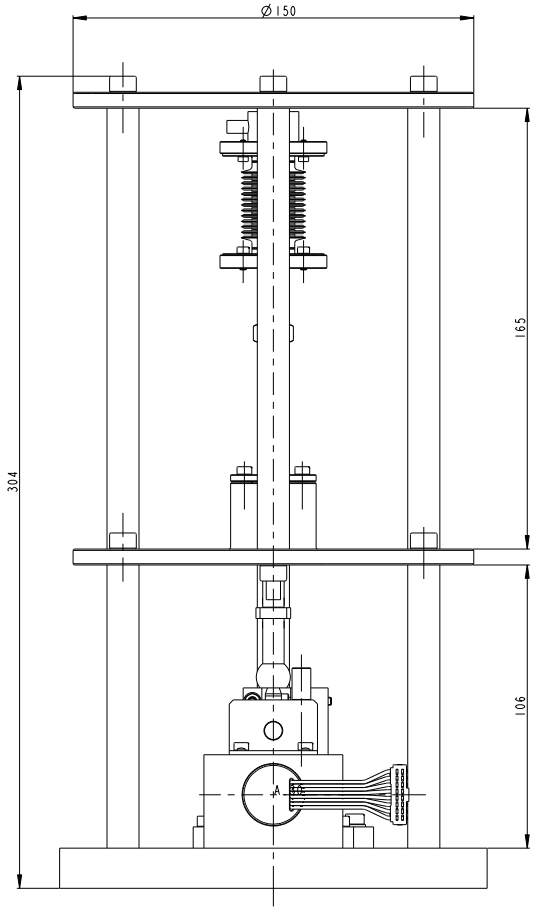


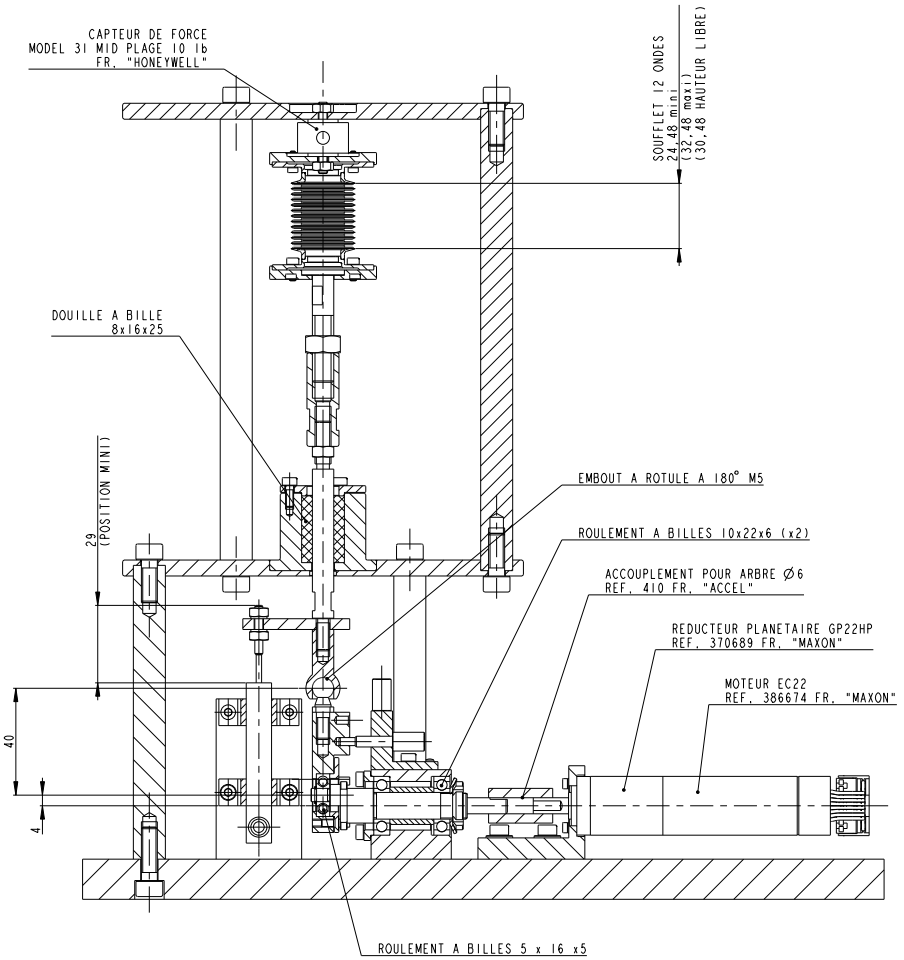


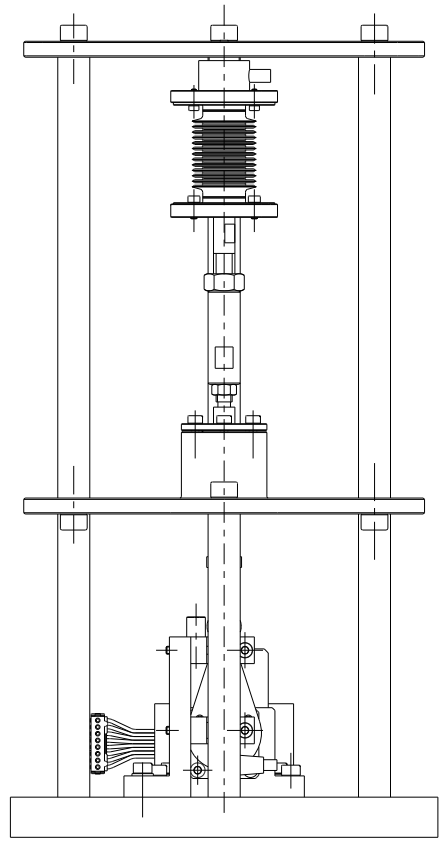

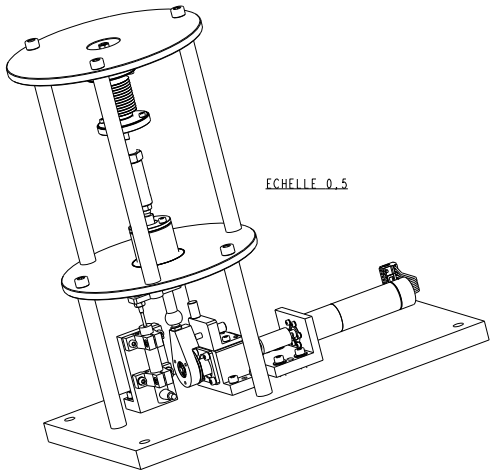


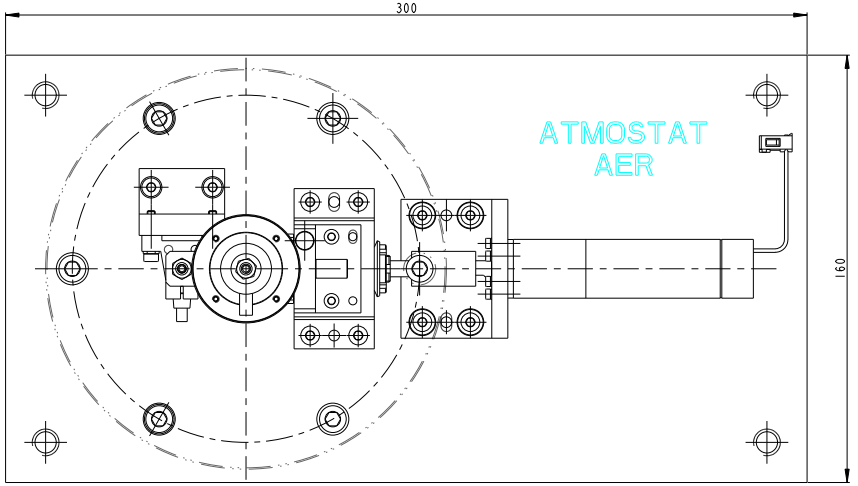


| Indice | Date | MODIFICATIONS | Etabli par | Verifie par |
|---|---|---|---|---|
| E | - | - | - | - |
| D | - | - | - | - |
| C | - | - | - | - |
| B | - | - | - | - |
| A | 08/08/2014 | Edition originale | FERE | |

CONTRAINTES GENERALES (sauf indications contraires)

TOLERANCES GENERALES D'USINAGE: ISO 2768-fH (Toutes les cotes < à 0,5 tol. ±0,05)

Matiere: -

TEMPERATURE DE REFERENCE : 20°C

Traitements: -

QUALITE FILETAGE : 6g

QUALITE TARAUDAGE : 6H

RUGOSITE GENERALE Ra 1,6 MAXI

Protection: -

Rayon d'outil Maxi = 0.2

Ebavurage = 0.2 Maxi x 45°

**AER**

Immeuble "LE FLAMMARION"
106, Rue du
Lieutenant Petit Leroy
94550 CHEVILLY LARUE
Tél. : 01.56.70.79.79.

ENSEMBLE: BANC SOUFFLET

DESIGNATION: AVANT PROJET

| Echelle | Projections | Masse | Approbation | Format | | Indice | Folio |
|---|---|---|---|---|---|---|---|
| 1 | | - | | A1 | XXXXXXXX | A | 1/1 |



A-241-01